Modeling structural behavior of fiber reinforced composite parts by considering draping effects

Zur Erlangung des akademischen Grades eines

DOKTORS DER INGENIEURWISSENSCHAFTEN
(Dr.-Ing.)

von der KIT-Fakultät für Maschinenbau
des Karlsruher Instituts für Technologie (KIT)

angenommene

DISSERTATION

von

Dipl.-Ing. Siegfried Galkin

Tag der mündlichen Prüfung: 14.02.2022

Hauptreferentin: Dr.-Ing. Luise Kärger
Korreferent: Prof. Dr.-Ing. habil. Robert Böhm
Korreferent: Prof. Dr.-Ing. Frank Henning

Trust in the LORD *with all your heart,*
And lean not on your own understanding;
In all your ways acknowledge Him,
And He shall direct your paths.
Do not be wise in your own eyes;
Fear the LORD *and depart from evil.*
It will be health to your flesh,
And strength to your bones.
Honor the LORD *with your possessions,*
And with the firstfruits of all your increase;
So your barns will be filled with plenty,
And your vats will overflow with new wine.

Proverbs 3:5-10

Vorwort

Die vorliegende Arbeit entstand im Rahmen meiner Tätigkeit als wissenschaftlicher Mitarbeiter am Institut für Fahrzeugsystemtechnik (FAST) des Karlsruher Instituts für Technologie (KIT).

Mein besonderer Dank gilt Dr.-Ing. Luise Kärger für die Übernahme des Hauptreferats, sowie für die kontinuierliche Unterstützung, die wertvollen Anmerkungen und das entgegengebrachte Vertrauen. Des Weiteren bedanke ich mich bei Prof. Dr.-Ing. habil. Robert Böhm für die Übernahme des Koreferats und für die wertvollen Diskussionen zur vorliegenden Arbeit. Ebenso bedanke ich mich bei Prof. Dr.-Ing. Frank Henning für die Übernahme des Koreferats und die Unterstützung in allen Fragen. Zudem gilt mein Dank Univ.-Prof. Dr.-Ing. Dr. h. c. Albert Albers für die Übernahme des Prüfungsvorsitzes.

Bei meinen Kollegen vom FAST möchte ich mich für die anregenden Diskussionen, Ratschläge und die uneingeschränkte Hilfsbereitschaft bedanken. Meinem langjährigem Bürokollegen Alexander Bernath danke ich für die freundschaftliche Atmosphäre, die spannenden Diskussionen und das konstruktive Feedback.

Darüber hinaus gebührt mein Dank den Kollegen vom Fraunhofer Institut für Chemische Technologie (ICT), den Kollegen vom Institut für Angewandte Materialien am KIT (IAM) und den Kollegen vom Institut für Leichtbau und Kunststofftechnik in Dresden (ILK) für die umfangreiche Unterstützung zur Herstellung von Proben und bei der Durchführung der experimentellen Untersuchungen. Besonders hervorheben möchte ich hier Eckart Kunze und Dr.-Ing. Wilfried Liebig. Außerdem möchte ich den von mir betreuten Abschlussarbeitern und Hilfswissenschaftlern für das Engagement und die gute Zusammenarbeit danken.

Die Inhalte dieser Arbeit wurden großteils im Rahmen des Projektes „Experimentelle und virtuelle Analyse von Drapiereffekten und deren Auswirkungen auf das strukturmechanische Verhalten von Faserverbundkomponenten “ sowie

im Rahmen der Young Investigator Group (YIG) „Green Mobility “ erarbeitet. Für die finanzielle Unterstützung möchte ich mich bei der Deutschen Forschungsgemeinschaft (DFG) sowie bei der Vector Stiftung bedanken.

Nicht zuletzt bedanke ich mich von ganzem Herzen bei meiner lieben Frau Olga, meinen Kindern, meiner Familie und meinem Heiland für den kompromisslosen Rückhalt, die Entbehrungen und die große Unterstützung während der letzten Jahre.

Karlsruhe, im Februar 2022 *Siegfried Galkin*

Abstract

Fiber reinforced composites are ideal lightweight materials. Particularly in the automotive sector, fiber reinforced composites are increasingly used for geometrical complex components. Depending on the complexity of the component, different semi-finished products are suitable for forming into the final preform. If dry semi-finished products with continuous fibers are used, such as unidirectional noncrimp fabrics (UD-NCF), draping effects occur during forming. These effects are relevant to structure mechanical properties and are manifested in the variation of the fiber orientation, the local change of the fiber volume content and in areas with fiber waviness. If these effects are not taken into account in the design of components, the quality of the numerical prediction decreases. To account for draping effects in structural simulation, the relevant information can be taken from draping simulation. In a previous work, a material model for forming UD-NCF semi-finished products was developed. However, new material models are needed to capture the draping effects in the structural simulation of consolidated components. The requirements for the development of a material model are derived from the experimental observations. In an extensive experimental campaign, the impact of individual draping effects on the material behavior is investigated. It is found that, in addition to the generally known influence of fiber orientation, other material-specific properties come to light. If large shear strains are applied, the fiber orientation changes. Although the fiber orientation significantly influences the mechanical properties, its change under shear has hardly been considered so far. Furthermore, it is shown that the initial transverse material axis is also subjected to deformation. By considering only the change in fiber direction, while the transverse material axis remains orthogonal, an incorrect failure mechanism can be predicted. In this work, a suitable strain measure is presented, with which the change of the material axes can be accounted. The comparison between experimental and numerical results shows a very good agreement with respect to the deformation of each material axis. To consider the fiber volume content, experimental investigations are carried out to determine the elastic material parameters, as well as the different material strengths and material nonlinearities for varying fiber volume contents. The elastic properties and the strengths are modeled using analytical approaches. On the basis of tests, a fiber volume content-dependent failure criterion for fiber failure and inter-fiber failure is derived. It is shown that for inter-fiber failure, the material strengths are influenced differently by the fiber volume content. The numerical prediction, which considers fiber volume content, shows a very good agreement with experimental results. Fiber waviness is considered as another draping effect. Here, the most significant impact on the mechanical properties is observed. In order to investigate the influence of fiber volume content and fiber waviness in detail, microscopic scale modeling is performed. This method shows clearly the influence of the matrix on the effective material properties of the composite and on the failure behavior. In another numerical study, the influence of draping effects on component level is investigated. In particular, the influence of the laminate lay-up becomes apparent when draping effects are taken into account.

Kurzfassung

Faserverbundwerkstoffe eignen sich als ideale Leichtbauwerkstoffe. Besonders im Automobilsektor werden zunehmend Faserverbundwerkstoffe für geometrisch komplexe Bauteile verwendet. Je nach Bauteilkomplexität eignen sich unterschiedliche Halbzeuge für die Umformung zur finalen Preform. Werden trockene Halbzeuge, wie zum Beispiel UD-NCF verwendet, entstehen während der Umformung strukturmechanisch relevante Drapiereffekte. Diese äußern sich in der Variation der Faserorientierung, der lokalen Änderung des Faservolumengehaltes und in Bereichen mit Faserwelligkeiten. Werden diese Effekte bei der Auslegung von Bauteilen nicht berücksichtigt, sinkt die numerische Prognosegüte. Für die Erfassung der Drapiereffekte in der Struktursimulation können die Informationen aus der Drapiersimulation entnommen werden. In einer vorangegangenen Arbeit wurde ein Materialmodell zur Umformung von UD-NCF Halbzeugen entwickelt. Um jedoch die Drapiereffekte in der Struktursimulation zu erfassen, bedarf es neuer Materialmodelle. Die Anforderungen an das zu entwickelnde Materialmodell leiten sich aus den experimentellen Beobachtungen ab. In einer umfangreichen Versuchskampagne wurde der Einfluss von einzelnen Drapiereffekten auf das Materialverhalten untersucht. So zeigte sich, dass neben dem im Allgemeinen bekannten Einfluss der Faserorientierung, weitere materialspezifische Eigenschaften zum Vorschein treten. Wird eine Belastung aufgeprägt, ändert sich die Faserorientierung. Obwohl die Faserorientierung maßgeblich die mechanischen Eigenschaften beeinflusst, wird deren Änderung in der Modellierung kaum berücksichtigt. Darüber hinaus zeigte sich, dass die initial transversale Materialachse ebenso einer Deformation unterliegt. Wird nur die Änderung der Faserorientierung berücksichtigt, kann ein falscher Versagensmechanismus prognostiziert werden. Um die Änderung der Materialachsen zu berücksichtigen, wird ein geeignetes Dehnungsmaß vorgestellt. Der Vergleich zwischen experimentellen und numerischen Ergebnissen zeigt eine sehr gute Übereinstimmung hinsichtlich der Deformation der einzelnen Materialachsen. Zur Berücksichtigung des Faservolumengehaltes wurden experimentelle Untersuchungen zur Bestimmung der elastischen

Materialparameter, sowie der unterschiedlichen Materialfestigkeiten und Materialnichtlinearitäten durchgeführt. Die Modellierung der elastischen Eigenschaften und der Festigkeiten erfolgt mithilfe von analytischen Ansätzen. Auf Basis der Versuche konnte ein faservolumengehaltsabhängiges Versagenskriterium für Faserbruch und Zwischenfaserbruch eingeführt werden. Es zeigt sich, dass für den Zwischenfaserbruch die Materialfestigkeiten unterschiedlich vom Faservolumengehalt beeinflusst werden. Die numerische Vorhersage bei Berücksichtigung des Faservolumengehaltes zeigt eine sehr gute Übereinstimmung mit experimentellen Ergebnissen. Als weiterer Drapiereffekt wird die Faserwelligkeit berücksichtigt. Hier zeigt sich der signifikanteste Einfluss auf die mechanischen Eigenschaften. Um den Einfluss des Faservolumengehaltes und der Faserwelligkeit im Detail zu untersuchen wurden Modellierungen auf der mikroskopischen Skala durchgeführt. Hierbei zeigt sich deutlich der Einfluss der Matrix auf die Materialeigenschaften des Verbundes und dessen Versagensverhalten. In einer weiteren numerischen Studie wurde der Einfluss von Drapiereffekten an einem Bauteil untersucht. Insbesondere tritt der Einfluss des Laminataufbaus bei der Berücksichtigung von Drapiereffekten zum Vorschein.

Table of Contents

Nomenclature

Acronyms

CFRP	Carbon Fiber Reinforced Plastics
DIC	Digital image correlation
FE	Finite element
FEA	Finite element analysis
FF	Fiber failure
FRP	Fiber-reinforced Plastics
FVC	Fiber Volume Content
HCCF	Hydraulic Composites Compression Fixture
IFF	Inter-fiber failure
NCF	Non-Crimp Fabric
OAC	Off-axis compression
OAT	Off-axis tension
RTM	Resin Transfer Molding
RVE	Representative volume element
SRVE	Statistical representative volume element
UD	Unidirectional
VTK	Visualization Toolkit

Greek Symbols

α	Plastic volumetric flow control	-
α^{TI}	Transversely isotropic stiffness tensor invariant	GPa
α_{ap}	Action plane yield surface slope	-

β^{TI}	Transversely isotropic stiffness tensor invariant	GPa
β_{ap}	Action plane dilatancy coefficient	-
$\Delta\theta$	Fiber rotation	$^\circ$
δ_{c}	Crack density	mm^{-1}
δ_{ij}	Kronecker delta	-
Γ	Gibbs free energy	$\mathrm{J\,m}^{-3}$
$\boldsymbol{\lambda}$	Deformed wavelength direction vector	mm
$\boldsymbol{\lambda}^{\mathrm{init}}$	Initial wavelength direction vector	mm
$\Delta\lambda_{\mathrm{ap}}$	Action plane plastic multiplier	-
$\Delta\lambda_{\mathrm{d}}$	Damage multiplier	-
$\Delta\lambda_{\mathrm{pl}}$	Plastic multiplier	-
λ	Waviness wavelength	mm
λ^{init}	Initial wavelength	mm
λ^{TI}	Transversely isotropic stiffness tensor invariant	GPa
λ_0^+, λ_0^-	Fiber damage tension and compression initiation factor	-
μ	Viscoplasticity viscosity parameter	s
μ_{d}	Damage viscosity coefficient	s
$\mu_{\mathrm{L}}^{\mathrm{TI}}$	Invariant transversely isotropic longitudinal shear modulus	GPa
$\mu_{\mathrm{T}}^{\mathrm{TI}}$	Invariant transversely isotropic transverse shear modulus	GPa
$\bar{\phi}/\gamma_{\mathrm{y}}$	Longitudinal fiber compressive strength parameter	-
ν	Isotropic Poisson's ratio	-
ν_{12}	Major Poisson's ratio	-
$\nu_{12}^{\mathrm{f,init}}$	Static major Poisson's ratio of a carbon fiber	-
ν_{12}^{f}	Fiber major Poisson's ratio	-
ν_{13}	Major transverse Poisson's ratio	-
ν_{21}	Minor Poisson's ratio	-
ν_{23}	Major through-thickness Poisson's ratio	-
ν_{31}	Minor transverse Poisson's ratio	-
ν_{32}	Minor through-thickness Poisson's ratio	-
ν_{m}	Poisson's ratio of the matrix	-

ν_{pl}	Plastic Poisson's ratio	-
ν_{xy}	Effective major Poissons's ratio in the (x,y)-plane	-
Φ_{ap}	Action plane yield surface	MPa
Φ_{d}	Damage surface	MPa
Φ_{pl}	Yield surface	MPa^2
Ψ	Angle between τ_{n1} and τ_{nt}	$^\circ$
ψ	HELMHOLTZ free energy	$\mathrm{J\,m^{-3}}$
ψ_{d}	Damage part of the specific HELMHOLTZ free energy	$\mathrm{J\,m^{-3}}$
ψ_{el}	Elastic part of the specific HELMHOLTZ free energy	$\mathrm{J\,m^{-3}}$
ψ_{pl}	Plastic part of the specific HELMHOLTZ free energy	$\mathrm{J\,m^{-3}}$
ρ_{f}	Fiber density	$\mathrm{g\,cm^{-3}}$
$\hat{\sigma}_{\mathrm{n}}$	Effective action plane normal stress	MPa
σ_{n}	Action plane normal stress	MPa
$\hat{\boldsymbol{\sigma}}$	Effective stress tensor	MPa
$\boldsymbol{\sigma}^{+}, \boldsymbol{\sigma}^{-}$	Positive and negative part of the sress tensor	MPa
$\boldsymbol{\sigma}^{(\mathrm{f})}$	Fiber-parallel frame stress	MPa
$\boldsymbol{\sigma}^{(\mathrm{GN})}$	GREEN-NAGHDI frame stress	MPa
$\boldsymbol{\sigma}^{(O)}$	Stress in the initial/global coordinate system	MPa
$\boldsymbol{\sigma}_{\mathrm{ap}}$	Action plane stress tensor	MPa
$\boldsymbol{\sigma}_{\mathrm{x}}$	NYE stress in global coordinate system	MPa
$\boldsymbol{\sigma}_{i}$	NYE stress in local coordinate system of section *i*	MPa
$\hat{\boldsymbol{\sigma}}_{\mathrm{x}}$	NYE effective stress in global coordinate system	MPa
$\hat{\boldsymbol{\sigma}}_{i}$	NYE stress in local coordinate system of section *i*	MPa
$\hat{\boldsymbol{\sigma}}_{\mathrm{ap}}$	Effective action plane stress tensor	MPa
$\bar{\sigma}$	Equivalent stress	MPa
$\bar{\sigma}_{\mathrm{s}}$	Saturation tension or compression flow stress	MPa
$\bar{\sigma}_{\mathrm{ap}}$	Equivalent action plane plasticity stress	MPa
$\boldsymbol{\sigma}_{i}^{\mathrm{x}}$	Effective stress in section *i* of the wave	MPa
σ_{0}	Failure initiation stress	MPa
$\sigma_{\mathrm{I}}, \sigma_{\mathrm{II}}, \sigma_{\mathrm{III}}$	Principal stress values	MPa

$\sigma_{\mathrm{t,c}}$	Tension or compression yield function	MPa
σ_{vm}	von Mises stress	MPa
σ_{y}	Yield stress	MPa
σ_{ij}	Local stress tensor components	MPa
$\sigma_{ij}^{\mathrm{OAT/OAC}\theta^\circ}$	Failure stress components of an OAT or OAC test	MPa
σ_{xy}	Global stress components	MPa
$\bar{\sigma}_{0\mathrm{t}}, \bar{\sigma}_{0\mathrm{c}}$	Initial tension and compression yield stress	MPa
$\hat{\tau}_{\mathrm{n1}}$	Effective action plane shear stress	MPa
$\hat{\tau}_{\mathrm{nt}}$	Effective action plane shear stress	MPa
τ_{n1}	Action plane shear stress	MPa
τ_{nt}	Action plane shear stress	MPa
τ_{y}	Action plane plasticity hardening law	MPa
$\tau_{\mathrm{y}}^{\mathrm{init}}$	Action plane plasticity yield onset	MPa
θ	Fiber orientation angle	$^\circ$
θ_0	Initial fiber orientation angle	$^\circ$
θ_{12}	Angle between first and second material axes	$^\circ$
$\theta_{12}^{\mathrm{init}}$	Initial angle between material axes	$^\circ$
θ_{ap}	Angle of the action plane	$^\circ$
θ_{fp}	Fracture plane angle	$^\circ$
θ_{max}	Maximum waviness misalignment angle	$^\circ$
$\theta_{i,\mathrm{max}}$	Maximum waviness misalignment angle in section *i*	$^\circ$
$\theta_{i,\mathrm{max}}^{\mathrm{init}}$	Initial maximum waviness misalignment angle in section *i*	$^\circ$
$\hat{\boldsymbol{\varepsilon}}$	Effective strain tensor	-
$\hat{\boldsymbol{\varepsilon}}_i$	Effective local Nye strain in section *i*	-
$\boldsymbol{\varepsilon}^{(\mathrm{f})}$	Fiber-parallel frame strain	-
$\boldsymbol{\varepsilon}^{(\mathrm{GN})}$	Green-Naghdi frame strain	-
$\boldsymbol{\varepsilon}^{(O)}$	Strain in the initial/global coordinate system	-
$\boldsymbol{\varepsilon}_1$	Nye strain in local coordinate system	-
$\boldsymbol{\varepsilon}_{\mathrm{dev}}$	Deviatoric strain tensor	-
$\boldsymbol{\varepsilon}_{\mathrm{el}}$	Elastic strain tensor	-

$\boldsymbol{\varepsilon}_{\mathrm{pl,ap}}$	Action plane plastic strain tensor	-
$\boldsymbol{\varepsilon}_{\mathrm{pl}}$	Plastic strain tensor	-
$\boldsymbol{\varepsilon}_{\mathrm{x}}$	Nye strain in global coordinate system	-
$\bar{\varepsilon}_{\mathrm{pl,ap}}$	Equivalent action plane plastic strain	-
$\bar{\varepsilon}_{\mathrm{pl}}$	Equivalent plastic strain	-
ε_0	Failure initiation strain	-
$\varepsilon^{\mathrm{f}}_{11,\mathrm{max}}$	Longitudinal fiber tensile failure strain	-
ε_{f}	Strain at full damage of the material point	-
$\varepsilon_{\mathrm{vol}}$	Volumetric strain	-
ε_{ij}	Local strain tensor components	-
φ	Fiber volume content	-
φ_0	Initial fiber volume content	-
φ_{v}	Void volume content	-
ζ_i	Halpin-Tsai parameters for $i \in \{E_2, G_{12}, G_{23}\}$	-

Latin Symbols

A	Waviness amplitude	mm
A_0	Cross section prior to damage	m^2
A_{D}	Damage surface	m^2
A_{f}	Deformed fabric reference area	m^2
$A^{\mathrm{init}}_{\mathrm{f}}$	Fabric reference area	m^2
A_{t}, A_{c}	Rate of hardening tension and compression parameter	MPa
$\boldsymbol{A}$	Deformed amplitude direction vector	mm
$\boldsymbol{a}$	Normal vector to the plane of transverse isotropy	-
$\boldsymbol{A}^{\mathrm{init}}$	Initial amplitude direction vector	mm
$\boldsymbol{b}$	Fiber-parallel transformation matrix	-
$\boldsymbol{B}_{\mathrm{F}}$	Left Cauchy-Green tensor	-
$\bar{\boldsymbol{C}}$	Effective material stiffness matrix	GPa
$\boldsymbol{C}$	Stiffness matrix	GPa
$\boldsymbol{C}_{\mathrm{D}}$	Damaged material stiffness matrix	GPa

$\boldsymbol{C}_{\mathrm{F}}$	Right CAUCHY-GREEN tensor	-
$\mathbb{C}$	Fourth order material elasticity tensor	GPa
$\mathbb{C}^{\mathrm{TI}}$	Transversely isotropic fourth order stiffness tensor	GPa
C_{ij}	Stiffness matrix components	MPa
d	Damage variable	-
d^{+}, d^{-}	Positive and negative isotropic damage variable	-
d_{v}	Viscous damage variable	-
d_{V}	Percentage of the damaged matrix volume	%
d_{12}, d_{13}, d_{23}	Composite shear damage variables	-
$d_{1}, d_{\mathrm{m2}}, d_{\mathrm{m3}}$	Composite normal damage variables	-
$d_{\mathrm{exp}}, d_{\mathrm{const}}$	Exponential and constant stress damage evolution	-
$d_{\mathrm{n}}^{+}, d_{\mathrm{n}}^{-}$	Damage variables in normal direction to the action plane	-
$\boldsymbol{e}_{i}$	Material axis direction	-
$\boldsymbol{e}_{1}, \boldsymbol{e}_{2}, \boldsymbol{e}_{3}$	Principal stress direction vectors	-
$\hat{\boldsymbol{e}}_{i}$	Deformed material axes directions	-
$\hat{\boldsymbol{e}}_{1},\hat{\boldsymbol{e}}_{2},\hat{\boldsymbol{e}}_{3}$	Deformed local direction vectors	-
E	Isotropic Young's modulus	GPa
$E_{1}^{\mathrm{f,init}}$	Fiber direction static modulus	GPa
E_{1}^{f}	Fiber longitudinal modulus	GPa
E_{2}^{f}	Fiber transverse modulus	GPa
E_{1}	Longitudinal modulus	GPa
E_{2}	Transverse modulus	GPa
E_{2}^{init}	Initial transverse modulus	GPa
E_{3}	Though-thickness modulus	GPa
e_{ap}	Action plane yield surface ellipticity	-
E_{m}	Modulus of the matrix	GPa
E_{x}	Effective stiffness along x-axis	GPa
E_{y}	Effective stiffness along y-axis	GPa
$\boldsymbol{e}_{\mathrm{x}},\boldsymbol{e}_{\mathrm{y}},\boldsymbol{e}_{\mathrm{z}}$	Deformed global direction vectors	-
$\boldsymbol{F}$	Deformation gradient	-

$\boldsymbol{f}_1$	Fiber orientation vector ($\hat{1}$-axis)	-
$\boldsymbol{f}_1^{\mathrm{init}}$	Initial fiber orientation vector (1-axis)	-
$\boldsymbol{f}_1^{\mathrm{proj}}$	Projected fiber orientation vector	-
$\boldsymbol{f}_2$	Transverse orientation vector ($\hat{2}$-axis)	-
$\boldsymbol{f}_2^{\mathrm{init}}$	Initial transverse orientation vector (2-axis)	-
f_{ap}	Action plane plastic flow rate coefficient	-
$f_{\mathrm{FF}}^{+}, f_{\mathrm{FF}}^{-}$	Tension and compression composite fiber failure index	-
f_{IFF}	Failure index for inter-fiber failure	-
$f_{\mathrm{IFF}}^{\mathrm{init}}$	Failure index for inter-fiber failure w/o f_{FF} impact	-
f_{M}	Matrix failure index	-
$f_{\mathrm{t}}, f_{\mathrm{c}}$	Tensile and compressive fiber failure criterion	-
G	Isotropic shear modulus	GPa
g	Total enery release rate	$\mathrm{J\,m^{-2}\,m^{-1}}$
g_0	Energy prior to failure initiation	$\mathrm{J\,m^{-2}\,m^{-1}}$
G_{12}	In-plane shear modulus	GPa
G_{12}^{f}	Fiber in-plane shear modulus	GPa
G_{13}	Transverse shear modulus	GPa
G_{23}	Through-thickness shear modulus	GPa
G_{23}^{f}	Fiber through-thickness shear modulus	GPa
g_{ap}	Action plane flow potential	MPa
g_{d}	Damage energy	$\mathrm{J\,m^{-2}\,m^{-1}}$
$g_{\mathrm{d}}^{+}, g_{\mathrm{d}}^{-}$	Tension and compression damaged energy	$\mathrm{J\,m^{-2}\,m^{-1}}$
G_{f}	Energy release rate due to failure	$\mathrm{J\,m^{-2}}$
G_{Ic}	Mode I fracture toughness	$\mathrm{J\,m^{-2}}$
G_{m}	Shear modulus of the matrix	GPa
g_{pl}	Nonassociative flow potential	MPa
G_{xy}	Effective shear modulus in the (x,y)-plane	GPa
h	Viscoplasticity rate sensitivity	-
$H_{0\mathrm{t}}, H_{0\mathrm{c}}$	Tension and compression hardening modulus	MPa
$\boldsymbol{I}$	Second order identity tensor	-

$\boldsymbol{l}$	Material axes transformation matrix	-
$\mathbb{I}^{\mathrm{s}}$	Symmetric fourth order identity tensor	-
I_1	First invariant of the stress tensor	MPa
J_2	Second invariant of the deviatoric stress tensor	MPa^2
K	Bulk modulus	GPa
K_{m}	Bulk modulus of the matrix	GPa
L_{C}	Characteristic finite element length	mm
$\mathbb{M}$	Fourth order damage tensor	-
$\mathbb{M}^{+}, \mathbb{M}^{-}$	Positive and negative fourth order damage tensor	-
m, s	Parameters affecting the impact of f_{FF} on f_{IFF}	-
m_0	Square meter fabric weight	g
m_{f}	Carbon fiber specific modulus slope over strain	GPa
$m_{\mathrm{t}}, m_{\mathrm{c}}$	Tension and compression hardening law balance	-
m_{w}	Fabric area weight	$\mathrm{g\,m^{-2}}$
$\boldsymbol{N}_{\mathrm{pl}}$	Plastic flow rule	MPa
$\boldsymbol{n}$	Crack normal direction	-
n_{L}	Number of plies of a laminate	-
$n_{\mathrm{t}}, n_{\mathrm{c}}$	Tension and compression decrement of hardening	-
$\mathbb{P}^{+}, \mathbb{P}^{-}$	Positive and negative fourth order projection tensor	-
p	Hydrostatic pressure	MPa
$p^{\mathrm{t}}_{\mathrm{n1}}, p^{\mathrm{c}}_{\mathrm{n1}}$	Tension and compr. inclination parameter $(n, n1)$-plane	-
$p^{\mathrm{t}}_{\mathrm{nt}}, p^{\mathrm{c}}_{\mathrm{nt}}$	Tension and compr. inclination parameter (n, nt)-plane	-
$\boldsymbol{R}$	Rigid body motion	-
$\boldsymbol{R}_{\mathrm{ap}}$	Action plane rotation matrix	-
$\boldsymbol{R}_{\mathrm{w}}$	Waviness rotation matrix	-
$\boldsymbol{R}_{i,\mathrm{max}}$	Waviness section i rotation matrix	-
r_{y}	Ratio of damage driving forces	-
r_{g}	Ratio of energy prior to failure g_0 and damage energy g_{d}	-
R_{pl}	Viscoplastic consistency condition	-
$\bar{\boldsymbol{S}}$	Effective compliance matrix	GPa^{-1}

$\boldsymbol{S}$	Material compliance matrix	GPa^{-1}
$\boldsymbol{S}_\mathrm{D}$	Damaged material compliance matrix	GPa^{-1}
$\mathbb{S}$	Fourth order compliance tensor	GPa^{-1}
S_{12}	In-plane shear strength	MPa
S_{23}^ap	Shear resistance of the action plane against τ_nt	MPa
s_λ	Arc length of a wave	mm
S_m	Matrix shear strength	MPa
$\boldsymbol{T}^{(\mathrm{f})}$	Fiber-parallel transformation matrix	-
$\boldsymbol{T}_i, \tilde{\boldsymbol{T}}_i$	Forward and backwards waviness rotation matrix of section i	-
t	Time	s
t_L	Laminate/Ply thickness	mm
$\boldsymbol{U}$	Right stretch tensor	-
$\boldsymbol{V}$	Left stretch tensor	-
$\boldsymbol{v}_\mathrm{n}$	Element normal direction vector	-
$\boldsymbol{v}_\mathrm{n}^\mathrm{cp}$	Cutting plane normal direction vector	-
$\boldsymbol{x}$	Deformed global x-axis	-
$\boldsymbol{x}_0$	Initial global x-axis	-
$\boldsymbol{x}_i$	Deformed fiber direction vector in section i	-
$\boldsymbol{x}_i^\mathrm{init}$	Initial fiber direction vector in section i	-
X_C	(Longitudinal) compressive strength	MPa
X_T	(Longitudinal) tensile strength	MPa
X_T^f	Longitudinal fiber tensile strength	MPa
$\boldsymbol{y}_i$	Deformed transverse direction vector in section i	-
$\boldsymbol{y}_i^\mathrm{init}$	Initial transverse direction vector in section i	-
Y	Damage driving force	MPa
Y^+, Y^-	Positive and negative damage driving force	MPa
Y_0	Damage driving force at failure initiation	MPa
Y_C	Transverse compressive strength	MPa
$Y_\mathrm{D}^+, Y_\mathrm{D}^-$	Positive and negative isotropic damage hardening function	MPa
Y_T	Transverse tensile strength	MPa

$Y_{\mathrm{T}}^{\mathrm{f}}$	Transverse fiber tensile strength	MPa
$z_1, z_2, \hat{z}$	Deformed through-thickness direction vector in section i	-
$\hat{\boldsymbol{x}}, \hat{\boldsymbol{y}}, \hat{\boldsymbol{z}}$	Deformed global direction vectors	-

1 Introduction

1.1 Motivation

Fiber composites are among the most common group of lightweight materials found in nature. In particular, these are characterized by their excellent specific material properties. Natural fiber composites, such as wood or bones, also have the special property of adapting to the load condition. Animated by the advantages of this natural group of materials, the development of fiber-reinforced plastics (FRPs) has been strongly promoted in recent decades. Such material systems are especially well suited to minimize the weight of future vehicles over land, water, and air. The low density of continuous FRPs combined with very good mechanical properties makes them ideal lightweight materials, which are useful to reduce the weight of vehicles. This is important to achieve the required reduction of CO_2 emissions. Since the weight of a vehicle directly determines its maximum range, minimizing vehicle weight can make an enormous contribution to reduce CO_2 emissions while increasing the operating range. In particular, carbon fiber reinforced plastics (CFRP) have very good mechanical potential. The use of CFRP is widespread, but the challenge is to apply the load in the fiber direction as much as possible to achieve the highest lightweight potential.

Besides careful design of components, which include the final geometry and laminate layup, the mechanical properties are also determined by the manufacturing process. If a component is manufactured in an infiltration process (e.g., RTM process), the forming process precedes it. During the forming of the dry semi-finished product, the fiber orientation and the distribution of the fiber bundles in the later component is determined. There are different semi-finished products that can be draped differently well. Among others, unidirectional non-crimp fabrics (UD-NCF) offer a high degree of drapability. Compared to other fabric types UD-NCF show very good mechanical properties in fiber direction. The resulting fiber orientation after the forming determines the preferred load direction of the material and is therefore one of the most important factors for component behavior. Likewise, fiber waviness can occur locally, which significantly influences the material properties. After forming, the local fiber volume content (FVC) is mainly defined by the areal weight of the fabric for a given laminate thickness. To obtain a solid component the fabric needs to be infiltrated. During the infiltration step the FVC can be changed, if the cavity of the tool leads to a different laminate thickness than initially defined. The FVC determines in particular the stiffness and strength of the resulting laminate. The subsequent curing and cooling of the component may introduce additional residual stresses to the component. The characteristics resulting from the draping process, such as fiber orientation, fiber waviness and FVC, are called draping effects.

In order to capture the entire manufacturing process numerically, the development of appropriate methods for the individual process steps has been pursued [1]. This virtual process chain is characterized by the fact that the information from the individual process steps is passed on to the subsequent process steps (cf. Figure 1.1). In addition, virtual design offers a decisive advantage with regard to holistic component optimization. For the different load cases, an optimal material and stress distribution can be achieved in the final component by such optimization. On the one hand, this is achieved by a process-specific optimization, on the other hand an optimization of the component geometry can be achieved throughout the entire process chain.

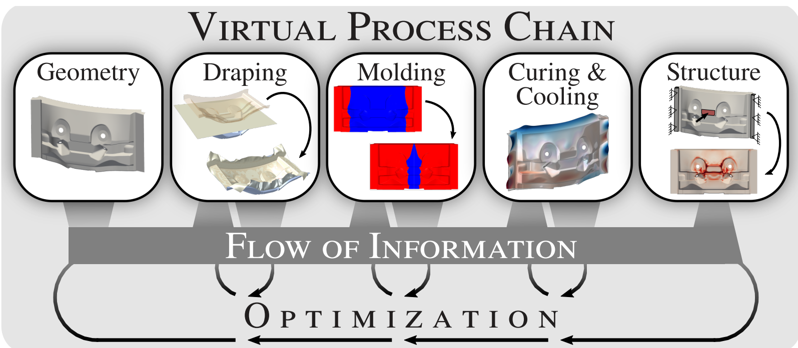

Figure 1.1: Schematic representation of a continuous virtual process chain for an automotive component

For the completeness of the process chain, new material models are needed to calculate the structure mechanical behavior under consideration of draping effects. Moreover, the models need to be able to process the information on draping effects that result from the manufacturing process. Generally, a largely homogeneous distribution of the material properties in the component is often used in the state-of-the-art structure simulation. However, by using such an approach the full potential of the composite part cannot be achieved. One reason for using such a simplified approach is that the necessary information is not available or that the effort, which is required to acquire them experimentally, would be too high. On the other hand, if preimpregnated fibers (so-called prepregs) are used, they have already a defined fiber direction and FVC. Such materials limit the possible part complexity and dry fabrics with a high drapeability need to be used. In contrast to prepregs, UD-NCFs undergo a completely different deformation process and require reliable knowledge of the deformed fabric to ensure component quality. Up to now, the large-scale measurement of the fiber orientation can only be carried out on the surface of the component. The distribution of the fiber orientation of the inner layers is hardly known. Furthermore, only a homogenized distribution of the fiber orientation can be experimentally determined. Additional information that results from the deformation of the dry semi-finished product, such as the local area weight (from which the resulting FVC is derived), occurring gaps or waviness, are not available. Fortunately, the validated numerical draping models can provide valuable information to describe the material behavior of UD-NCFs [2–4]. From a structure mechanical point of view, even if the fiber orientation distribution is available, its rotation with increasing load is generally neglected. If a constant fiber orientation is used for the calculation, the material nonlinearity that occurs can be incorrectly projected onto other mechanisms. Under certain circumstances, completely different stress states may be present in the material, leading to different material failures. Likewise, due to lack of information regarding material failure at different fiber volume contents, trade-offs in the quality of numerical prediction are often accepted. In general, the systematic analysis of the material behavior with respect to the FVC-dependent stiffnesses and strengths is lacking, especially for loads that cause inter-fiber failure (IFF). When the waviness of unidirectional FRPs is considered, most studies focus on the compressive failure of the material. However, waviness under tension has just as much influence on stiffness and strength. The impact of FVC on the failure of wavy areas has yet to be determined. The lack of reliable experimental tests can be named as a possible reason for the current state of research. Although analytical and numerical approaches exist that describe the material behavior under draping effects, their validation is still pending. If these approaches are not reliable, the foundation for a holistic view of the virtual process chain cannot be laid.

1.2 Thesis Objectives

The present work is dedicated to consider draping effects resulting from the forming of UD-NCFs. In particular, the draping effects relevant from a structure mechanical point of view are to be incorporated into the realistic modeling of FRP components by using the virtual process chain. Therefore, the obtained information from the draping process need to be transferred to the structure mechanical model. The required methods for transferring the relevant data are to be implemented. For the modeling of the material behavior, a material model that takes into account the information on the draping effects is to be developed. The input data that comes from draping simulation shall be processed and provides an appropriate set of material parameters to model the local distribution of draping effects. Based on this set of material parameters, the linear and the nonlinear material behavior as well as the failure initiation and the degradation of the material, need to be determined. The material model shall also be used for component design. Accordingly, the material behavior has to be homogenized and modeled on a macroscopic scale. Several influencing factors, such as fiber rotation, FVC-dependent strengths for fiber and inter-fiber failure, or the homogenized consideration of fiber waviness, are to be implemented. Since the material model needs a set of basic material parameters, corresponding material characterization experiments need to be performed. For the validation of the developed material model, different stress states have to be generated within experiments, which will then be remodeled accordingly. Since not every structure mechanical impact of draping effects can be considered experimentally, additional virtual material tests are necessary. For this purpose, the material behavior must be observed on a microscopic scale. Thus, the impact of FVC or fiber waviness, as well as the resulting nonlinear material behavior and fracture can be analyzed in detail. The general observations and conclusions are to be formed as recommendations for material characterization to virtually evaluate composite parts.

1.3 Layout of Thesis

As a first point, the individual draping effects are investigated experimentally in Chapter 2. The manufacturing of the coupons to determine the material properties on the macro as well as on the micro-scale is described first. Since the evaluation of the experiments requires new methods, the advanced method to determine strains from digital image correlation, among others, is discussed. For virtual material characterization, the material properties of the matrix are determined. To model the composite on micro-scale, the geometric characteristics of the fiber, such as the fiber diameter and its distribution, are obtained. The coupon tests of the composite are carried out on both unidirectional and angle-ply laminates. In addition to laminates with straight fibers, the experimental results of tests with fiber waviness are investigated.

The modeling of the material behavior is a focus of this work and is thoroughly described in Chapter 3. A general consideration of a suitable strain measure for the resulting stress components comes first. To model the composite material behavior on micro-scale, material models for the fiber and matrix are presented subsequently. Both material models take into account the material-specific nonlinearities, as well as failure initiation and damage evolution. The macroscopic material model that considers the draping effects, is developed based on the experimental observations. The nonlinearities resulting from the fiber and matrix are incorporated into the material model. The composite-specific material behavior, such as failure initiation and damage evolution, is presented. Additionally, the dependency on FVC is incorporated into the material model. Based on the developed model, an extension for areas with waviness is presented.

The developed methods for gathering and mapping, in order to transfer the information from the draping simulation to the structural simulation, are described in Chapter 4. This is followed by the application and validation of the developed material models in Chapter 5. First, the simulation results of the micro-scale models are compared with experimental results. The issues that are still open from experimental investigation, are addressed here. Second, the developed macroscopic material model is used to perform a side-by-side comparison of the numerical and experimental results. Here the prediction accuracy of the developed material model is evaluated. Finally, the prediction quality of the draping simulation is evaluated and the virtual process chain is used on an automotive component. Here the impact of the draping effects is evaluated on a component level. Based on the gained knowledge, a general evaluation of the draping effects and the most important material parameters, which should be determined, are presented in Chapter 6. The thesis ends with a summary and an outlook on possible further work in Chapter 7.

2 Experimental Tests to Consider the Influence of Draping Effects

2.1 Literature Review

The deformation of the fabric during the draping process contributes significantly to the mechanical behavior of the consolidated component. To enable the consideration of these effects in the design, reliable experimental results are needed to reproduce these phenomena. Since the characteristics of the draping effects are strongly dependent on the type of fabric used, the parameters such as fiber orientation, fiber volume content, and the degree of fiber waviness, are to be investigated. For the analysis of the individual effects, coupon tests are suitable, which can reproduce a representative material behavior. For example, the fiber angle can be systematically varied to analyze the influence of fiber orientation on the mechanical material behavior. The experimental results available in the literature so far focus only on one influencing parameter (e.g., fiber orientation) whereas the others are considered constant or negligible. Since the fiber orientation plays a dominant role for fiber composites with continuous fiber reinforcement, its influence has been extensively investigated [5–11]. If a load is not applied exactly in the fiber direction or transverse to it, fiber rotation occurs [10–15]. Previous experimental studies on fiber rotation have mainly used angle-ply laminates, as these allow a simple correlation between fiber rotation and the resulting strain. It could be shown that neglecting the fiber rotation leads to completely different stress states and thus makes the interpretation of failure mechanisms more difficult [11, 16]. However, if off-axis tests are carried out to determine the reorientation of the fibers, this is more challenging due to the unbalanced laminate layout. Such laminate structures create a coupling between normal and shear distortions and thus a highly inhomogeneous strain distribution in the sample. For a reliable analysis of the change in fiber orientation, the deformation gradient $\boldsymbol{F}$ should therefore be used, as it provides all the necessary information. In literature such an analysis has not yet been performed. Likewise, only the change in fiber orientation is analyzed, and the other material axes are always assumed to be perpendicular to it. Therefore, an analysis of the rotation of initially perpendicular material axes and the resulting stress distribution need to be investigated. This is especially important for the selection of a suitable material model for the reliable design of fiber composite laminates.

In addition to the fiber orientation, the FVC is also considered to be an essential factor for the resulting stiffness and strength of the composite. The experimental results available on this subject are mainly directed towards the resulting stiffness [17–20]. For the stiffness in fiber direction E_1 a parallel connection of fiber and matrix can be assumed, which corresponds to a linear increase in stiffness over the FVC. When determining E_1 as a function of the FVC, a distinction must be made between different fiber materials. For example, carbon fibers show an increase or decrease of the modulus with increasing load in fiber direction [21–23], while glass fibers do not show such an effect. The slope of the modulus is thus part of the FVC dependent modulus. This correlation is rarely used so far in the design of continuous fiber reinforced laminates. The transverse stiffness E_2 and the in-plane shear stiffness G_{12} show a nonlinear correlation between FVC and the resulting homogenized stiffness [17–19]. For a complete description of the transversely isotropic material behavior, the in-plane Poisson's ratio ν_{12} and the transverse shear modulus G_{23} over the FVC are also required. Thereby ν_{12} can be determined via a parallel connection of fiber and matrix [17]. For the shear modulus G_{23} no experimental study varying the FVC is known and has yet to be evaluated. The impact of the FVC on strength has only been studied rarely so far. In general, a linear relationship between FVC and tensile strength X_T in fiber direction is assumed. As with stiffness, this assumption is based on a parallel connection model and has been experimentally confirmed [17]. In contrast, for the compressive strength X_C in fiber direction the distribution over the FVC is clearly nonlinear [24–26]. This can be attributed to the fact that the fibers are never ideally straight, but can contain undulations. These lead to a shear failure, including local buckling and kinking, rather than fiber breakage as under tensile loading. Regardless of the direction of loading, a trend towards higher strengths with increasing FVC is discernible for fiber-dominant loading. For a reliable statement regarding the dependence of the matrix-dominant strengths, such as the transverse tensile strength Y_T, the transverse compressive strength Y_C and the in-plane shear strength S_{12}, at least three different FVCs must be investigated. There are only few experimental studies in the literature that investigate the matrix dominant strengths as a function of the FVC [18, 27–29]. For example, there is no uniform trend for the transverse tensile strength that can be derived from the experimental tests. This can be attributed to the fact that the experimental results are dependent on the manufacturing process, the type of specimen used (coupon or hoop wound), or the fiber-matrix interface. However, the shear strength seems to be independent of the FVC [18]. This would reduce the number of material parameters to be determined. Based on the work of Brunbauer [28] the transverse compressive strength seems to increase with increasing FVC. Furthermore, an attempt was made to draw conclusions of the existing transverse compressive strength on the basis of angle-ply laminates and a varying FVC [27]. An experimental validation on unidirectional UD90° samples has not yet been carried out. If the uniaxial failure strengths are known, the suitability of failure criteria can be evaluated with varying FVC and, if necessary, their extension by the dependence on the FVC can be considered.

In addition to fiber orientation and fiber volume content, fiber waviness is another factor which influences the mechanical behavior of FRP laminates. A pronounced waviness has an impact on the effective stiffness and strength of the composite [27, 30–35]. Due to the fiber waviness the FVC changes also locally [36]. According to the current state of the art, there are two ways to characterize waviness. One describes the maximum angle deviation θ_{max} compared to the ideal fiber orientation [37], the other relates the present amplitude A to the wavelength λ [38]. Both possibilities can be converted into each other. Since the influence of waviness significantly reduces the buckling stability of UD0° laminates, the effective fiber compressive strength X_{C} decreases [39]. When samples are loaded with a fiber waviness in tension, the decrease in fiber tensile strength X_{T} seems to be dependent on the fiber material used. While FRP laminates with glass fibers at an amplitude to wavelength ratio of $A/\lambda = 0.05$ show a decrease of 18 % compared to UD0° reference samples [32], carbon fibers at $A/\lambda = 0.03$ already show a decrease of 35 % [27]. Loading a wavy area changes also the local fiber orientation. Thus, this has a direct effect on the amplitude and wavelength. This fact has already been considered in the modeling of waviness [33, 38, 40]. However, an experimental analysis of this effect is still lacking, since the measuring methods using extensiometers or strain gauges are not sufficient to determine the fiber rotation.

The material properties determined from coupon tests reflect the effective properties of the laminate. In any case, the material response is determined by the mechanical behavior of the individual components. Likewise, damage mechanisms occur on the micro-scale, which determine the global material behavior. For example, the strength of the matrix has an influence on the resulting composite strength [18]. To analyze the influence of matrix and fiber on the effective material properties, the corresponding material properties of the individual constituents are required. The characterization of the fiber and matrix properties is a major challenge, since these are subject to the size effect with respect to strength [17, 41, 42]. The determined characteristics of constituents can then be used to model the microscopic material behavior. For example, plane and wavy samples with varying FVC can be analyzed in detail. Likewise, individual material parameters, whose influence cannot be determined experimentally, can be analyzed.

Since the measurement methods used to determine the deformation are essential for the analysis of the observed effects, a possibility of generating reliable measurement results with a modified test setup is necessary. Digital image correlation (DIC) is best suited for a detailed analysis of the deformation behavior, since here a full-field strain distribution can be determined. This is especially important if the change of the fiber orientation has to be investigated. There are several commercially DIC methods available. Nevertheless, the extension or adaptation of these systems is not easily possible. There are numerous open source codes available that allow a reliable DIC analysis [43–46]. These tools also allow an individual adaptation to the given experimental environment. Furthermore, it is possible to precisely analyze the loss of facets during the measurement and make improvements to the algorithms. The use of DIC methods for the analysis of fiber rotation has so far only been based on the resulting strains [11]. This approach will be enhanced by the use of the deformation gradient $\boldsymbol{F}$ in order to perform in-depth experimental analyzes.

2.2 Manufacturing Coupons with Draping Effects and Test Setup

In order to investigate the material behavior of fiber composites under the presence of draping effects, representative samples are suitable. These samples can be taken from plane sheets and characterized experimentally. Draping effects, such as varying local fiber orientation, local fiber volume content, and existing fiber waviness, are examined more closely, as these have the most impact on the mechanical properties. The focus is on the influence of draping effects on stiffness, nonlinear material behavior, fiber rotation during loading, the resulting composite strength, and the associated degradation after damage initiation. Primarily, the material behavior of unidirectional and angle-ply laminates will be investigated, since the findings can be transferred to other ply orientation combinations. In this chapter the used materials, the manufacturing process, the experimental test scope, and the corresponding test setup are presented.

2.2.1 Materials and Manufacturing Process

Using continuous FRPs allow to achieve a very high lightweight potential. Especially in combination with fabric types that allow a high degree of deformation almost ideal lightweight component structures can be manufactured. For this purpose a unidirectional non-crimp fabric is analyzed. The UD-NCF fabric from Zoltek Panex 35 with an areal weight of $330\,\mathrm{g\,m^{-2}}$ is used for this purpose. According to the manufacturer, the fabric is composed of 93 % carbon fiber rovings, 3 % glass fiber rovings as a carrier material, 2 % polyester sewing thread to tie the carbon fibers to the glass fiber rovings, and 2 % of pre-applied binder to fix the layers in a preform. The rovings have a width of 5 mm and the not compacted fabric has a thickness of 0.5 mm (see Appendix A.5). The rovings are connected by a tricot loop type stitching which forms the characteristic zigzag pattern on one side of the fabric. Further, the glass fiber rovings are oriented perpendicular to the carbon fiber direction. Both sides of the fabric are shown in Figure 2.1. As matrix system the Sika Biresin CR170 epoxy resin with Biresin CH150-3 hardener is used. The equipment and machines of the Fraunhofer ICT in Pfinztal are used to cut and to stack the individual fabric plies to form the different laminates. Furthermore, the high pressure RTM process at the Fraunhofer ICT is chosen to produce plates [48, 49]. The dimensions of the plates are $900 \times 550\,\mathrm{mm}^2$. To adjust the FVC, the thickness of the plates and the number of laminate plies are varied. The thickness of the consolidated plates is between 4 mm to 4.4 mm. In addition to the fiber composite plates, pure resin plates are produced for mechanical characterization

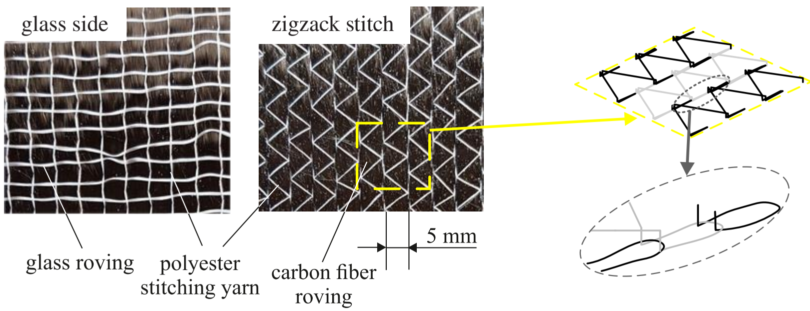

Figure 2.1: Both sides of the Zoltek PX35 unidirectional non-crimp carbon fiber fabric [47]

of the resin system. After the manufacture of the plates, composites and resin, they are tempered in an oven according to the manufacturer's specifications. All process parameters are summarized in Table 2.1.

To analyze the impact of the FVC that results from different deformations of the fabric and different fiber waviness ratios on the mechanical properties, separate preforms are produced at the ILK in Dresden using specially developed

Table 2.1: Manufacturing parameters of the RTM-process

Process Parameter	**Value**
Mix ratio by volume-resin:hardener	100:29
Resin temperature-resin/hardener	$\approx 80\,°C/\approx 30\,°C$
Mix head pressure-resin/hardener	≈ 120 bar/120 bar
Tool temperature	$\approx 120\,°C$
Tool closing force	4000 kN to 5000 kN
Evacuation time	60 s
Resin flow rate	$30\,g\,s^{-1}$ to $100\,g\,s^{-1}$
Curing time	10 min
Post cure	4 h @ 140 °C

tools [50]. The same fabric and resin system as described before is used. The plates contain six plies, while the FVC is adjusted by varying the laminate thickness. The specimens that are used to characterize the strength with varying fiber volume content and fiber waviness ratio have a thickness of 1.8 mm to 2.3 mm. As for the production of the plates at the Fraunhofer ICT, the plates are also manufactured using the high-pressure RTM process in order to maintain the comparability of the experimental results. A detailed description of the manufacturing process is published by Kunze et al [47].

2.2.2 Laminates with Draping Effects and Experimental Plan

For the experimental characterization of the basic mechanical properties of unidirectional laminates, several material parameters have to be determined to define the stiffness and strength. Different standards can be used for this purpose. For example, tensile tests can be performed according to or based on the DIN EN ISO 527-5 standard. From these tests the stiffness in fiber and transverse direction E_1 and E_2, as well as the Poisson's ratio ν_{12}, the fiber tensile strength X_T and the transverse tensile strength Y_T can be determined. Many standards (e.g., DIN EN ISO 14126 or ASTM D 6641) exist to perform compression tests. The different fixtures of each standard provides a way to induce force into the specimens and simultaneously minimize the buckling tendency. In particular, the compressive strength in fiber direction X_C and in transverse direction Y_C can be determined from these tests. To determine the shear properties, there are standardized tests (DIN EN ISO 14129 or ASTM D 7078) as well as new approaches with improved testing devices [51]. Although all approaches provide very reliable results for the in-plane shear stiffness G_{12}, the determination of the shear strength S_{12} is more challenging. This difficulty is due to the challenge of creating a homogeneous stress state in the sample, in which the actual shear strength can be measured. For example, the determined shear strength according to the ASTM D 7078 standard represents a lower bound, since the involved notch stress favors premature failure of the composite. A complete description of the material properties requires also the transversal isotropic shear stiffness G_{23}. For this purpose, Iosipescu shear tests can be carried out [52]. Assuming an isotropic relationship between the transverse modulus E_2 and the shear modulus G_{23} in the transverse isotropic plane, only the through-thickness Poisson's ratio ν_{23} needs to be determined to obtain the shear modulus G_{23}. Since ν_{23} is defined as the negative ratio of the laminate thickness strain ε_{33} to the transverse strain ε_{22}, it can be determined from tension or compression tests on UD90° laminates. The relationship between E_2, G_{23} and ν_{23} is defined by

$$G_{23} = \frac{E_2}{2\,(1 + \nu_{23})}. \tag{2.1}$$

In addition to the basic stiffnesses and strengths, other factors that influence the material behavior must be taken into account. When carbon fibers are loaded in fiber direction, the modulus increases under tensile stress and decreases under compressive stress loads [21–23]. This has an impact on the composite properties in fiber direction. The corresponding increase or decrease of the modulus ${}^{\mathrm{d}E_1}/_{\mathrm{d}\varepsilon_{11}}$ can be determined from tensile or compression tests on UD0° laminates. For this purpose, the secant modulus is plotted against the strain and subsequently the slope of the secant modulus is determined. Since the magnitude of the slope is very similar for both loading directions [21], this material property can be determined more easily from tensile tests than from compression tests. The nonlinear material behavior due to shear stress, σ_{12} or σ_{13}, is assumed as a result of plastic deformation. As a result of the transverse isotropy, the hardening due to plasticity can be assumed to be the same for both σ_{12} and σ_{13} stresses. The resultant hardening curves for these shear stresses can be obtained as a by-product of the shear strength tests. It is well known that under transverse compressive loading of FRPs a fracture angle of about 50° to the loading direction occurs [53]. If the stress state is rotated into this action plane, a shear stress through the thickness (comparable to the σ_{23} stress) occurs. The nonlinearity that occurs for transverse compression loads can therefore be attributed to this shear stress. Since a combined stress state is present here, the hardening curve cannot be directly extracted from UD90° compressive tests. However, depending on the used plasticity model this stress state can be captured.

To analyze the impact of FVC on the stiffness and strength in the different load directions, coupon samples with varying FVC are produced and tested. The test results obtained serve as a requirement for the corresponding material models, which take into account the fiber volume content dependent material behavior. The FVC is adjusted in two ways: by the number of plies at a given laminate thickness and by the thickness of the laminate at a constant number of plies. If the FVC influences the matrix-dominant strengths, this will have an impact on the used failure criterion. It has been shown that off-axis coupon tests can be used to generate combined stress states and thus provide support points for a failure criterion in the $(\sigma_{22}, \sigma_{12})$-plane [54]. Therefore, off-axis tensile and compression tests (OAT and OAC) are performed with varying fiber orientation and varying FVC. The experimentally obtained stress values $\sigma_{22}^{\mathrm{OAT/OAC}\,\theta^\circ}$ and $\sigma_{12}^{\mathrm{OAT/OAC}\,\theta^\circ}$ at failure can be used to determine a FVC specific inter-fiber failure envelope. In addition to the resulting stiffness and strength as a function of the FVC, the hardening under a shear load is analyzed in order to draw conclusions on the required modeling approach. Besides the FVC, the stiffness and strength is significantly dependent on the existing waviness. If a load is applied perpendicular to the fiber waviness, a combined stress state is created that leads to a matrix dominant failure. A load parallel to the fiber waviness, on the other hand, leads to reduced buckling stability in the case of a compressive load and to a significant reduction in tensile strength in the case of a tensile load [47]. Here the impact of the waviness on the effective stiffness E_{x} and the resulting strength is investigated at two different amplitude to wavelength ratios.

In addition to the basic material properties, such as FVC and fiber waviness as well as the resulting stiffnesses and strengths, a nonlinear material behavior is created solely by the rotation of the material axes. The occurring fiber rotation $\Delta\theta$ and the resulting angle θ_{12} between the fiber direction and the initial transverse direction is directly linked to the deformation of the material. Therefore, off-axis and angle-ply laminates are tested and the resulting rotation of the material axes is determined. The entire scope of the experiments is summarized in Table 2.2. Additionally, the individual material parameters obtained from each experiment are presented.

It should be noted that due to forming of the UD-NFC two other possible deformation mechanisms have an impact on the local FVC [50]. By applying a tension transverse to the roving bundles, the textile tends to develop gaps or lower filament density. On the other hand, a shear deformation, as in a picture frame, leads to a transverse compaction of the rovings. While gaps lead to a lower FVC, the compaction of the rovings increases the FVC. By comparing the resulting E_2 and G_{12} stiffness values at the same FVC but different deformation approaches (adjusting the laminate thickness vs. applying tension

Table 2.2: Experimental plan and the resulting material parameters from each test series

Test series	Number of plies	Laminate thickness	Fiber volume content	Material parameter
UD0°*	6	1.80 mm 2.00 mm 2.25 mm	48 % 54 % 60 %	E_1, ν_{12}, $^{\mathrm{d}E_1}/_{\mathrm{d}\varepsilon_{11}}$, X_T, X_C
UD90°*	6	1.80 mm 2.00 mm 2.25 mm	48 % 54 % 60 %	$Y_\mathrm{T}, Y_\mathrm{C}$
UD90°	12 12 14	4.30 mm 4.00 mm 4.00 mm	50 % 55 % 60 %	E_2, ν_{23}, Y_C
Double V-Notch Rail shear*	6	1.80 mm 2.00 mm 2.25 mm	48 % 54 % 60 %	S_{12}
OAC/OAT $\theta°$, $\theta \in \{10, 20, 30, 45, 50, 75\}$	12	4.00 mm	55 %	$\sigma_{22}^{\mathrm{OAT/OAC}\,\theta°}$ $\sigma_{12}^{\mathrm{OAT/OAC}\,\theta°}$ G_{12}
OAC $\theta°$, $\theta \in \{30, 50\}$	12 14	4.30 mm 4.00 mm	50 % 60 %	$\sigma_{22}^{\mathrm{OAC}\,\theta°}$ $\sigma_{12}^{\mathrm{OAC}\,\theta°}$
OAT $\theta°$, $\theta \in \{30, 45, 75\}$	12 14	4.30 mm 4.00 mm	50 % 60 %	$\sigma_{22}^{\mathrm{OAT}\,\theta°}$ $\sigma_{12}^{\mathrm{OAT}\,\theta°}$ G_{12}
Angle-ply $\pm\theta°$, $\theta \in \{30, 40, 45, 50, 60, 75\}$	12	4.00 mm	55 %	$\Delta\theta, \theta_{12}$
$^{A}/_{\lambda} \approx 0.03$* $^{A}/_{\lambda} \approx 0.06$*	6	2.00 mm	54 %	$E_\mathrm{x}, X_\mathrm{T}, X_\mathrm{C}$

* test series are manufactured and tested at ILK in Dresden [47]

or shear to the fabric) no significant difference could be observed. However, both deformation mechanisms have an impact on the inter-fiber failure related strength values ($Y_\mathrm{T}, Y_\mathrm{C}$ and S_{12}) of the composite [47]. As the resulting strength values change the shape of the failure envelope, a deformation mode specific adaptation of the material model can be performed to capture these deformation mechanisms. Unfortunately, current draping models allow only an evaluation of the in-plane fabric area weight change, rather than the volumetric ratio change, to predict the resulting FVC. Therefore, a clear difference between the actual effect of the FVC and the impact of the fabric deformation on the strength cannot be clearly differentiated. In order to predict the resulting strength values further experimental tests are required and also more advanced draping methods need to be developed [55–57].

2.2.3 Test Setup

All tests carried out at the KIT are performed on the testing machines of IAM-WK. A Zwick universal testing machine with a 100 kN load cell is used. To carry out the tests, the tensile and compression tests are provided with end-tabs for better force introduction. A hydraulic fixture is used as clamping device for the tensile tests. For compression tests the Hydraulic Composites Compression Fixture (HCCF) is used. DIC is used to measure the deformation to determine the local strain. For this purpose a speckle pattern is applied to the specimen and the displacements of individual facets are recorded. The image acquisition is performed from two perspectives: on the front side and sideways onto the specimen (see Figure 2.2). The measurement of the SLR cameras must be synchronized with the force measurement. Therefore, a separate testing

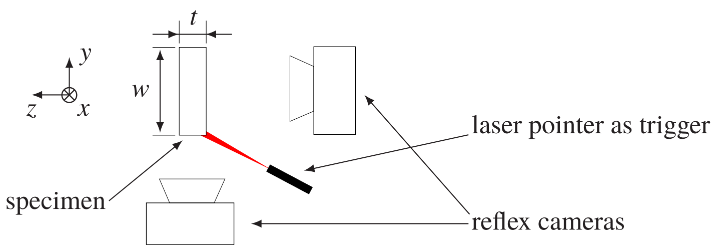

Figure 2.2: Top view of the schematic representation of the test setup with two reflex cameras and a laser pointer as trigger for synchronization

program is written, which triggers a laser pointer pointing at the specimen and is recorded by both cameras when the test is started. A DIC algorithm is further developed to process the video recording (see next section).

2.3 Development of Digital Image Correlation Algorithm for Strain Measurement

The acquisition of the deformation of a sample using DIC is widely used nowadays. If the deformation is known, the local strain can be determined. The advantages are the full-field acquisition of the strain, the possibility to directly compare the strains with numerical results and the robustness of the system. There is a variety of commercially available measurement systems, but these systems do not allow user defined modifications to prevent facet loss during the measurement or any other adaptations. In addition, the experimental effort increases if two sides of a sample have to be captured. For these reasons, existing DIC algorithms [43, 45] have been further developed to be able to determine the fiber rotation directly for each facet. The further developed methods and algorithms have already been successfully used for the measurement of hybrid material systems and dry and impregnated materials [2, 58, 59]. The method to determine the resulting strain described in the following is applied to all performed experiments.

2.3.1 Data Acquisition

After applying a speckle pattern to the two sides of the specimen, the specimen is clamped in the testing machine and loaded to a specific pre-load. Each camera records a video with a resolution of 1920 px × 1080 px@24 fps. When the experiment is started, the laser pointer is switched off and marks a point in time at which the DIC takes place. After recording, the videos are split into individual images and these are converted into gray scale images. Subsequently, a region of interest is defined and individual tracking points in this region are defined. The points define the center of the image section (so-called facet), whose displacement is tracked. The size of the facet defines the area to be tracked. Based on the coordinates of the center of the facet, the search area in the source image is also defined. This area is usually four times as large as the facet itself. To determine the displacement of the facet in the search area, the `normxcorr2` function available in MATLAB is used, which performs a normalized 2 -D cross-correlation. The offset is determined in the subpixel range with an accuracy of 0.001 px. Basically, a correlation coefficient is calculated for a cross-correlation that indicates the center of the facet to the search area. The process is similar to a puzzle search: the overall picture is known, but the position of each piece of the puzzle has yet to be found. The whole process of image correlation is shown in Figure 2.3. After each processed image, the displacement of each facet is calculated and stored. Thus, a link between the position of each facet at the corresponding time is known. Based on each center of a facet a mesh is generated. With the help of the shape function for the corresponding mesh element, the deformation gradient $\boldsymbol{F}$ is calculated. This gradient is the starting point for the calculation of the resulting strain over the analyzed element. Likewise, the local deformation of the fiber orientation can be analyzed by utilizing the deformation gradient.

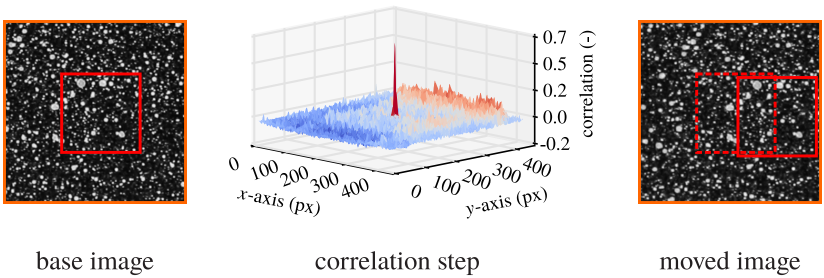

Figure 2.3: Digital image correlation process from the origin facet (initial position) over the cross-correlation step to the actual facet (deformed position)

2.3.2 Data Export and Strain-Stress Synchronization

To compare the numerical and experimental results, the evaluated strains and stresses must be the same in both cases. Since digital image correlation provides a full-field strain distribution, but a scalar strain value for each time stamp is needed, the strain field is averaged over the whole range. The choice of the measuring range is decisive here, since this has a significant influence on the resulting stiffness and the nonlinear behavior. To minimize measurement errors, the range should be as large as possible and the strain distribution as homogeneous as possible. Inhomogeneous strain distribution occurs for unbalanced laminates, which correspond to OAT or OAC tests. In this case, it is advisable to determine the effective longitudinal strain ε_{xx} from the side of the sample.

Since the strain is measured optically, but the force is measured via load cell, both measuring systems must be synchronized. In both systems the common factor is the measuring time. Since the laser pointer, which is used in the test setup, switches off at the beginning of the test, this determines the start of the measuring time. The difference between strain and force measurement is $^1/_{24}$ s, which results from the frame rate of the video. In case of quasi-static tests, which can last several minutes, the time difference between the two signals is negligible. To detect the time when the laser pointer goes off, a comparison of the current image with the next one is performed. Since the position of the laser point can differ from experiment to experiment, either the position must be redefined each time in the evaluation software or detected automatically in a different way. Here a semi-automatic method is chosen and implemented. As long as no load is applied to the sample and the laser pointer is active, only a background image noise can exist between two consecutive frames. If the two images are subtracted from each other pixel by pixel and the variance of this difference is then formed, this quantity represents a measure of the background noise. When the laser pointer switches off, the variance between two images increases significantly (see Figure 2.4). This marks a point in time when the user has to confirm that the laser pointer has gone off. If the start point of the image correlation is known, the force signal can be interpolated to

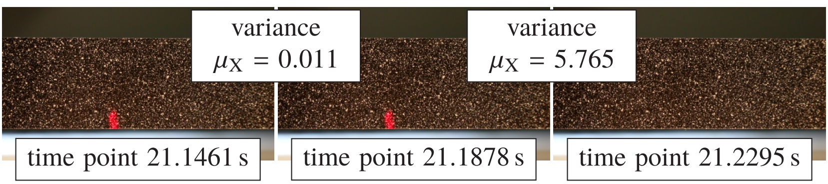

Figure 2.4: Semiautomatic detection of the time point at which the laser pointer turns off

the individual frames. Afterwards, the whole data set is written out and can be used for comparison or validation of the simulation results with experimental results.

2.4 Material Parameters for Micro Structure Models

Numerical micro-scale models can be used to analyze the damage mechanisms of FRPs with present draping effects. Each constituent of the composite (fiber and matrix) can be modeled separately. The nonlinear material behavior of the composite as well as its failure and damage evolution can be analyzed in detail. The use of microscopic models enables a basic understanding of the material and the crack propagation within the rovings. Since the filaments have a significantly higher stiffness than the matrix, they act like notches, which trigger the failure initiation. In such case the strain in the matrix can be increased by a factor of 20 [60]. Micro-scale models offer a simple possibility to systematically analyze the fiber volume content as draping effect. In order to model the material behavior of the individual constituents, the corresponding material properties are required. To experimentally characterize the matrix, a set of tensile and compression tests is performed. In order to consider rate-dependent material behavior, the tests are carried out at different strain rates. The mechanical properties of the fibers are more difficult to determine. The stiffness and strength in fiber direction can be determined by single fiber tensile tests [61–63]. Furthermore, mechanical properties of the fiber, such as ν_{12}^{f}, E_2^{f}, G_{12}^{f} or G_{23}^{f}, cannot directly be obtained from experiments. Therefore, well-founded assumptions or using reverse engineering these can be obtained from composite coupon tests.

2.4.1 Matrix Material Behavior

Epoxy matrix systems show a temperature, rate and size dependent material behavior [64–66]. Likewise, nonlinear material behavior occurs due to plastic deformation. Since the coupon tests with draping effects are all performed at room temperature, the mechanical properties of the matrix are also determined at room temperature. To keep the experimental effort low, three different strain rates ($\dot{\varepsilon} \in [1 \times 10^{-4}\,\mathrm{s}^{-1}, 1 \times 10^{-3}\,\mathrm{s}^{-1}, 1 \times 10^{-1}\,\mathrm{s}^{-1}]$) are chosen to determine the rate-dependent material behavior. The dimensions of the specimens correspond to the standard DIN EN ISO 527-2 for tensile tests on molded plastics. For compression tests, test specimens with a width of 20 mm and a thickness of 4 mm are tested on the HCCF test fixture with a free length of 15 mm. Since the material behavior of the matrix is influenced by the size effect [64], it can be faced by taking into account that the experimentally obtained strength values represent the lower limit. For the use of micro-scale models this effect needs to be kept in mind. The results of the experimental tests are shown in Figure 2.5. For both loading directions the modulus is determined to $E_{\mathrm{m}} = 2.8\,\mathrm{GPa}$, which is very close to the value provided by the manufacturer (cf. Appendix A.5). The determined modulus is independent of the strain rates. As the matrix is an isotropic material, the Poison's ratio ν_{m} is additionally needed to define the elastic behavior. By analyzing the results of ν_{m} a difference between tensile and compressive tests can be observed. The Poison's ratio yield to $\nu_{\mathrm{m}} = 0.4$ for tensile tests and is independent of the applied strain rate. On the other hand, under compression loads the determined Poison's ratio shows an increase towards higher strain rates ($\nu_{\mathrm{m}}|_{\dot{\varepsilon}=1\mathrm{e}-4} = 0.44$, $\nu_{\mathrm{m}}|_{\dot{\varepsilon}=1\mathrm{e}-4} = 0.46$, and $\nu_{\mathrm{m}}|_{\dot{\varepsilon}=1\mathrm{e}-4} = 0.47$).

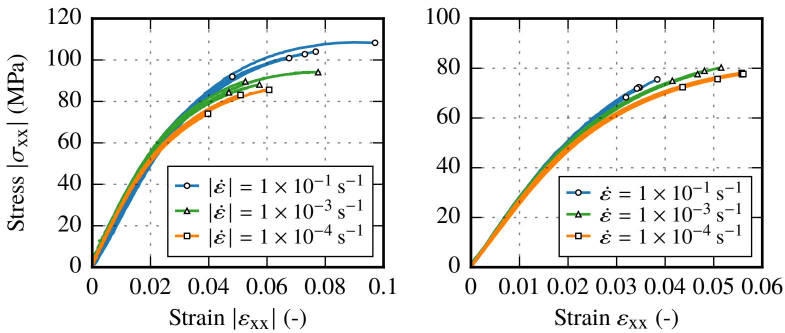

Figure 2.5: Matrix test results under compressive (left) and tensile load (right) for three different strain rates

With increasing strain rate an impact on the nonlinear material behavior can be observed. Here the determined tensile strengths of the matrix seem to be independent of the actual strain rate. The tensile strength yields $X_T = 75\,\text{MPa}$. In contrast, the compressive strengths show a trend towards higher values with increasing strain rate ($X_C|_{\dot{\varepsilon}=1e-4} = 86\,\text{MPa}$, $X_C|_{\dot{\varepsilon}=1e-3} = 91\,\text{MPa}$ and $X_C|_{\dot{\varepsilon}=1e-1} = 105\,\text{MPa}$). The compression tests themselves tend to buckle (cf. Figure 2.6). Thus, the stress maxima determined in the compression tests can be interpreted as the lower bound compressive strength values. For comparison, according to the manufacturer the tensile strength of the matrix yields 87 MPa and the compressive strength to 120 MPa (see Appendix A.5). In general the actual strength values are difficult to determine, since the size effect plays a major role, which affects the resulting strength values [41].

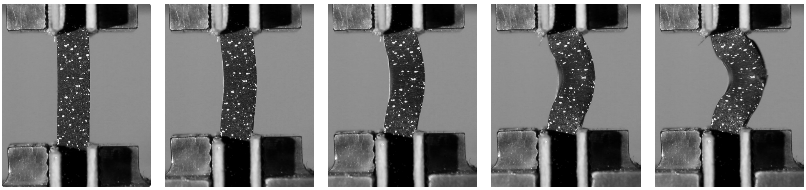

(a) $\varepsilon_{xx} = 6.8\,\%$ (b) $\varepsilon_{xx} = 10.2\,\%$ (c) $\varepsilon_{xx} = 13.0\,\%$ (d) $\varepsilon_{xx} = 14.9\,\%$ (e) $\varepsilon_{xx} = 19.3\,\%$

Figure 2.6: Resulting buckling of the matrix under compression loads prior to the stress maximum

2.4.2 Filament Size and Distribution

Besides the mechanical properties of the fiber and the matrix, the geometry of the filaments and their distance to each other within the roving is relevant to create the micro-scale models. According to the manufacturer, the used carbon fiber has a diameter of 7 µm. However, this specification assumes a circular cross section, which does not necessarily have to be present [61]. In addition, the diameter is measured on a few filaments and only the average value is given. Hence, a prediction of the standard deviation is missing and must be determined. To determine the diameter of the filaments and their standard deviation, an evaluation method is developed in MATLAB (see Figure 2.7). For this purpose, a microscopic image of the cross section of a

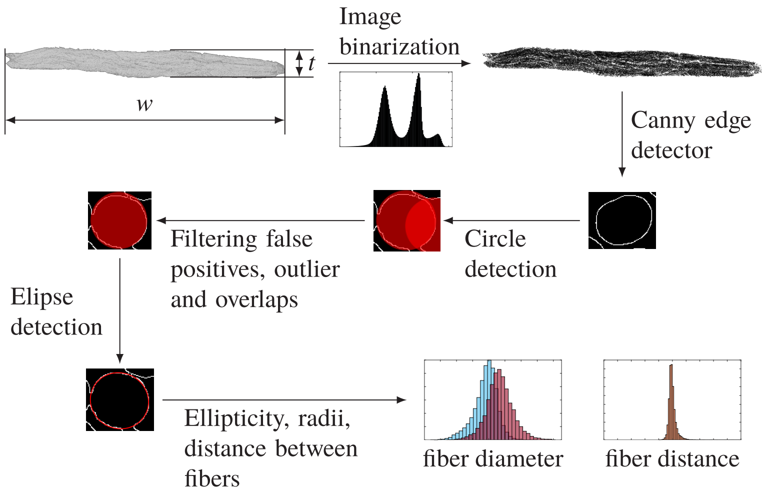

Figure 2.7: Algorithm to determine the geometrical microstructure fiber properties

roving in an infiltrated UD90° laminate is made. The cross section is prepared in several grinding steps. The dimensions of the examined roving area are 4.6 mm × 0.39 mm. Since the cross section contains several thousand individual filaments, a very reliable statement about the statistical fiber cross section and its distribution is possible. The cross section represents the composition of individual images, which are taken under the microscope at a magnification of 500 times. This results in a diameter of a filament of about 70 px. In the first step, the gray scale distribution of the image is created. This step allows to separate the filaments from the matrix. The gray value distribution should have two significant peaks. The local minimum between the peaks is used as a threshold to distinguish between fiber and matrix. This means that all gray values below the threshold are colored white and all gray values above the threshold are colored black. Using the modified image a binarization is performed and can be used for edge detection by using the Canny algorithm. Afterwards the detection of the circles follows. The first step is to determine the position and diameter of the filaments. Then the results must be filtered to remove overlaps, false positives and outliers. This reduces the number of detected circles from about 30k to about 20k valid results. Based on the center coordinates of the circles, the second step is performed to determine the cross section of the filaments. In this step, the individual ellipses are determined by using Hough transform [67]. The final step provides the distribution of the major and minor radius of the ellipses (see Figure 2.8 left). The determined axes indicate a clearly elliptical shape of the filaments. If the distance between the centers of two nearest neighbor filaments is determined, the minor radii of the respective filaments can be subtracted to obtain the filament distance distribution (cf. Figure 2.8 right). By using this method, the mean distance is close to zero, what indicates that the filaments are touching each other.

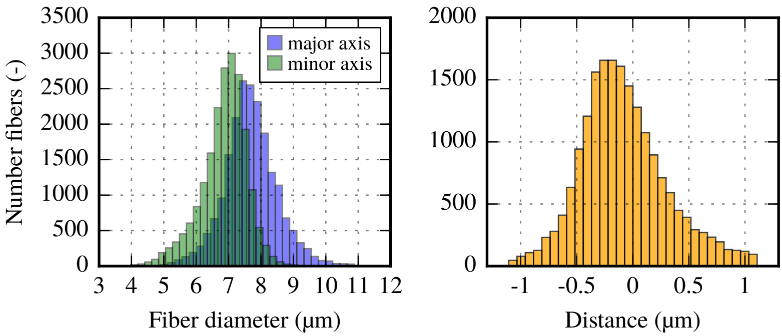

Figure 2.8: Resulting fiber diameter distribution using the major or minor axis of the detected ellipses (left) and fiber distance distribution using results of the filtered circle detection (right)

2.5 Testing and Evaluation of Coupons with Draping Effects

2.5.1 Unidirectional Coupon Tests with varying FVC

2.5.1.1 Elastic Material Parameters

Draping effects affect the FVC and the corresponding material properties significantly [47, 50]. Therefore, a special focus on the impact of the FVC on the mechanical properties of the composite is evaluated. For this purpose the resulting stiffness and strength are investigated on unidirectional coupons. The identification of the material parameters from the tests is carried out according to the test series from Table 2.2. For all tests the resulting FVC is calculated based on the average areal weight of $m_\mathrm{w} = 331\,\mathrm{g\,m^{-2}}$ (for tests at ILK $m_\mathrm{w} = 338\,\mathrm{g\,m^{-2}}$) and the measured coupon thickness. Based on the areal weight m_w, the number of plies n_L and the laminate thickness t the fiber volume content can be deduced by

$$\varphi = \frac{m_\mathrm{w} n_\mathrm{L}}{\rho_\mathrm{f} t}, \tag{2.2}$$

where ρ_f corresponds to density of the fiber. The mechanical properties that describe the elastic material behavior can be divided into fiber-dominant properties, such as E_1 and ν_{12}, and matrix-dominant properties, such as E_2, G_{12}, and ν_{23}. The impact of the FVC on the elastic quantities for plane loads is generally known and has been studied in detail [17–19, 27]. The carbon fiber-specific increase or decrease of the modulus in fiber direction due to the misorientation of the crystallites in carbon fibers and their dependence on the FVC as well as the transverse material properties, G_{23} or ν_{23}, have not been considered so far. All determined dependencies of the material stiffness parameters on the FVC are shown in Figure 2.9 and discussed below.

In order to determine the stiffness in fiber direction UD0° samples are used. Due to nonlinear stress-strain relation, a distinction between the static modulus E_1^init and the increase in modulus over strain ${}^{\mathrm{d}E_1}/{}_{\mathrm{d}\varepsilon_{11}}$ must be made. The static modulus defines the initial modulus if no load is applied. To determine these quantities the secant E_1^S is evaluated. Using the origin point as reference the secant yields

$$E_1^\mathrm{S} = \frac{\sigma_{11}}{\varepsilon_{11}}. \tag{2.3}$$

By plotting the secant modulus over each strain value, a constant slope ${}^{\mathrm{d}E_1}/{}_{\mathrm{d}\varepsilon_{11}}$ can be extracted. Based on this slope the intersection with the E_1^S-axis can be determined and the static module $E_1^\mathrm{S}|_{\varepsilon_{11}=0} = E_1^\mathrm{init}$ is obtained. The results show a significant increase of the static modulus E_1^init over the FVC, whereas the increase of the modulus ${}^{\mathrm{d}E_1}/{}_{\mathrm{d}\varepsilon_{11}}$ in the examined FVC range seems to be rather constant (see Figure 2.9a and 2.9b). The results are plausible, since the material properties result from a parallel connection of fiber and matrix. Only the Poisson's ratio ν_{12} decreases with increasing FVC (see Figure 2.9e). This

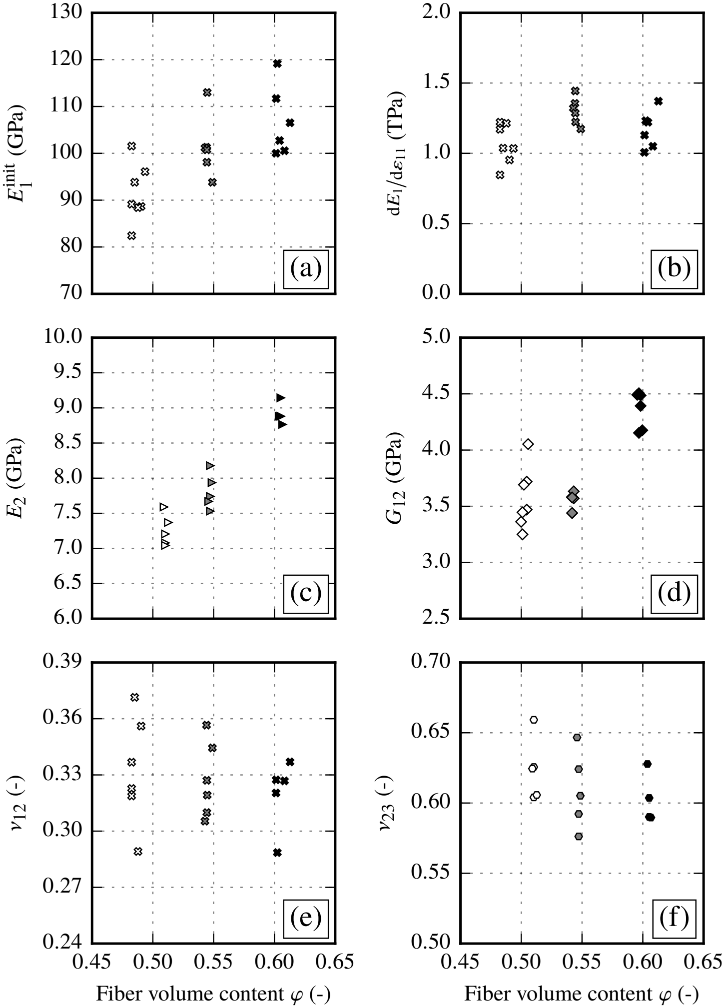

Figure 2.9: Material properties at different fiber volume contents: (a) static modulus E_1^{init}, (b) slope of the E_1 modulus, (c) transverse modulus E_2, (d) in-plane shear modulus G_{12}, (e) major Poisson's ratio ν_{12} and (f) major through-thickness Poisson's ratio ν_{23} (experimental tests results for E_1^{init}, $\mathrm{d}E_1/\mathrm{d}\varepsilon_{11}$ and ν_{12} are provided by the ILK in Dresden)

indicates that the Poisson's ratio of the fiber is smaller than that of the matrix. Material properties of the fiber, which are available in the literature, confirm this observation [17, 68–70]. The transverse stiffness E_2 and the Poisson's ratio ν_{23} are determined from compression tests on UD90° samples. As expected, the E_2 modulus increases significantly with FVC, since the influence of the matrix stiffness decreases with increasing FVC (see Figure 2.9c). The increase of the modulus is clearly nonlinear and shows an increasing gradient towards higher FVC values. On the other hand, the Poisson's ratio ν_{23} shows a decreasing trend with increasing FVC (see Figure 2.9f). Since ν_{23} is a combination of the transverse modulus E_2 and the shear modulus G_{23}, it can be concluded that the shear modulus G_{23} also increases over the FVC.

To determine the shear modulus G_{12} at different FVC, OAT45° tests are carried out. For this purpose the local shear stress σ_{12} and the shear strain γ_{12} are required. As the force is applied in the longitudinal direction of the specimen, σ_{xx} is the only nonzero component of the global stress tensor in an OAT45° test. To calculate the local shear strain γ_{12} the global in-plane strains $\varepsilon_{\mathrm{xx}}$, $\varepsilon_{\mathrm{yy}}$ and γ_{xy} are required. Since σ_{xx} is the only nonzero component, the local shear stress and shear distortion can generally be calculated using the following transformation

$$
\begin{aligned}
\sigma_{12} &= \frac{-\sin(\theta+\theta_{12})\sin(\theta)}{\sin^2(\theta_{12})}\sigma_{\mathrm{xx}} \\
\gamma_{12} &= -\frac{1}{\sin^2(\theta_{12})}\left(2\sin(\theta)\sin(\theta+\theta_{12})\,\varepsilon_{\mathrm{xx}}\right. \\
&\quad \left. +2\cos(\theta)\cos(\theta+\theta_{12})\,\varepsilon_{\mathrm{yy}} - \sin(2\theta+\theta_{12})\,\gamma_{\mathrm{xy}}\right),
\end{aligned}
\tag{2.4}
$$

where θ is the off-axis angle and θ_{12} is the angle between the material axes (see Figure 2.10). If $\theta = 45°$ and $\theta_{12} = 90°$ are used as angles, the shear stress is exactly half of the applied stress σ_{xx} and the shear strain is reduced to half of the difference between $\varepsilon_{\mathrm{yy}}$ and $\varepsilon_{\mathrm{xx}}$. However, due to the deformation of the specimen, the initial fiber orientation changes and must be taken into account to calculate the local stresses and strains. The corresponding fiber orientation can be calculated using the deformation gradient $\boldsymbol{F}$ at any point in time. From the optical strain measurement, the deformation gradient is known. The initial fiber orientation $\boldsymbol{f}_1^{\mathrm{init}}$ is defined by the angle θ_0 from the undeformed $\boldsymbol{x}$-axis (here $\boldsymbol{x}_0$-axis). The fiber orientation angle θ in Equation (2.4) results from the

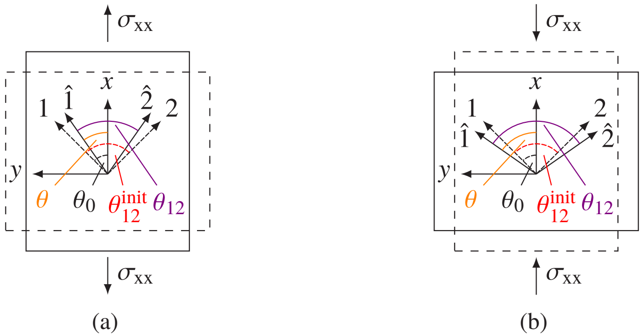

Figure 2.10: Schematic representation of the change of initial fiber orientation θ_0 to the deformed fiber orientation θ and the initial angle between material axes $\theta_{12}^{\mathrm{init}}$ to the angle after deformation θ_{12} for (a) tension and (b) compression loads

scalar product between the deformed $\boldsymbol{x}$-axis and the current fiber orientation vector $\boldsymbol{f}_1$

$$\theta = \arccos \frac{\boldsymbol{f}_1 \cdot \boldsymbol{x}}{\|\boldsymbol{f}_1\| \|\boldsymbol{x}\|} \tag{2.5}$$

with

$$\boldsymbol{x} = \boldsymbol{F}\boldsymbol{x}_0 = \begin{pmatrix} F_{11} & F_{21} \end{pmatrix}^\top \tag{2.6}$$

and

$$\boldsymbol{f}_1 = \boldsymbol{F}\boldsymbol{f}_1^{\mathrm{init}} = \begin{pmatrix} F_{11} \cos\theta_0 + F_{12} \cos\left(\theta_0 + \theta_{12}^{\mathrm{init}}\right) \\ F_{21} \cos\theta_0 + F_{22} \cos\left(\theta_0 + \theta_{12}^{\mathrm{init}}\right) \end{pmatrix}. \tag{2.7}$$

The initial angle between the material axes is $\theta_{12}^{\mathrm{init}} = 90°$. The acting angle θ_{12} can also be calculated via

$$\theta_{12} = \arccos \frac{\boldsymbol{f}_1 \cdot \boldsymbol{f}_2}{\|\boldsymbol{f}_1\| \|\boldsymbol{f}_2\|} \tag{2.8}$$

with

$$\boldsymbol{f}_2 = \boldsymbol{F}\boldsymbol{f}_2^{\mathrm{init}} = \begin{pmatrix} F_{11} \sin\theta_0 + F_{12} \sin\left(\theta_0 + \theta_{12}^{\mathrm{init}}\right) \\ F_{21} \sin\theta_0 + F_{22} \sin\left(\theta_0 + \theta_{12}^{\mathrm{init}}\right) \end{pmatrix}, \tag{2.9}$$

where $\boldsymbol{f}_2^{\text{init}}$ and $\boldsymbol{f}_2$ define the initial and the deformed second material axes. Using the updated angles θ and θ_{12}, the shear stress σ_{12} and γ_{12} can be obtained. The ratio of these stresses allow to determine the shear modulus in the linear elastic region. The shear modulus shows the large increase with increasing FVC compared to the other material stiffness values (see Figure 2.9d). The pronounced increase in the shear modulus results from the decrease in the volume fraction of the matrix. At high FVC the fiber shear stiffness contributes more to the transfer of the shear stress as the matrix. The fibers usually have a shear modulus G_{12}^{f} which is 15 to 50 times as large as the shear modulus G_{m} of the matrix [68–70]. In comparison, the ratio of the transverse modulus of carbon fibers E_2^{f} to the modulus of the matrix E_{m} is between 5 to 7.

2.5.1.2 Hardening due to Plasticity

The determined material constants are used to model the elastic behavior. In general, nonlinear material behavior (such as plasticity) is expected for different loads. At uniaxial stress conditions, the strain can be divided into an elastic and a plastic component. The uniaxial plastic strain over the corresponding uniaxial stress defines the hardening due to plasticity. Additionally, the FVC can be varied to determine the impact on the hardening. For this purpose, tests according to the V-Notched Rail Shear Method (ASTM D7078) are carried out at the ILK. The resulting hardening curves for varying FVC are shown in Figure 2.11. It can be seen that despite increasing shear modulus, the hardening due to plasticity is independent of the FVC. This simplifies the modeling, since only one single hardening curve has to be specified for the evaluated FVC range.

2.5.1.3 Material Strength Values

To describe the failure behavior, the uniaxial strengths of the composite must be known. This includes the strengths in fiber direction and transverse to it. A further distinction needs to be made between tensile and compressive strengths. The dependencies of the tensile and compressive fiber strengths (X_{T} and X_{C}) on the FVC was already proven [17–19, 24, 26–29]. Matrix-dominant strengths, such as the transverse tensile and compressive strength (Y_{T} and Y_{C}), have barely been investigated so far. Thus, there are two different findings regarding the

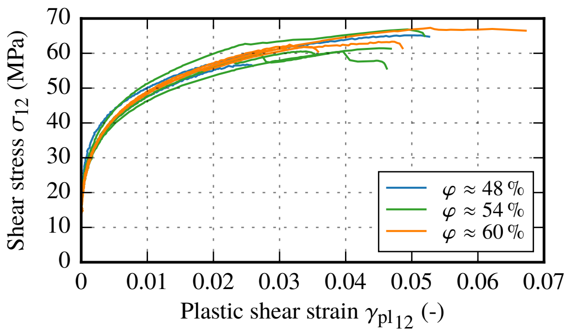

Figure 2.11: Hardening curves from V-Notched Rail Shear Method experimental results at different fiber volume contents $\varphi \approx \{48\,\%, 54\,\%, 60\,\%\}$ (all experiments performed at ILK in Dresden)

transverse tensile strength and its dependence on the FVC: a direct dependence on the FVC [18] and no dependence at all [27]. On the other hand, the interface between fiber and matrix has a significant impact on the resulting transverse tensile strength [18]. Experimental studies do exist, but they only compare two FVCs and have a maximum FVC of 50 % [27, 28]. Furthermore, for the analysis of the strength gradient more than two support points over the FVC are required. Additionally, the material characteristics at higher FVC values are generally needed for the component level. The experimentally determined material strengths are shown in Figure 2.12.

By analyzing the experimental results, the composite strengths in fiber direction X_T and X_C increase significantly over the FVC. As expected, there is a linear relationship across the FVC for tensile strength in fiber direction (Figure 2.12a). The compressive strength in fiber direction is about 35 % lower than the corresponding tensile strength (Figure 2.12b). Similarly, the increase in compressive strength is significantly lower towards higher FVC than for the tensile strength. In comparison to the tensile strength, the compressive strength shows a large spread. These tests involve a stability failure that is caused by the material intrinsic fiber misalignment. The transverse compressive strength Y_C shows also an increase towards higher FVC values. Furthermore, a linear relationship in the analyzed FVC range can be observed (Figure 2.12d).

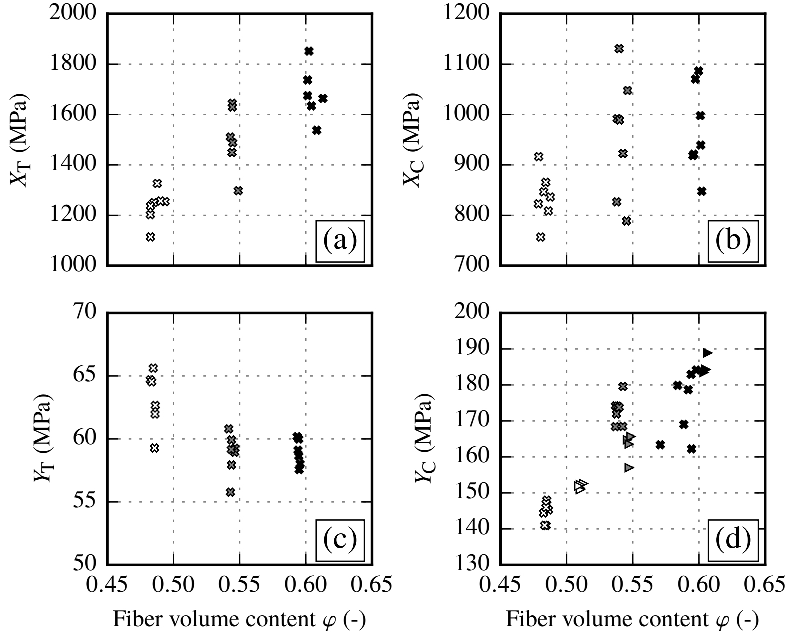

Figure 2.12: Experimentally obtained strength values at different fiber volume contents (all experiments performed at ILK in Dresden have cross markers): Longitudinal tensile strength X_T (a), longitudinal compressive strength X_C (b), transverse tensile strength Y_T (c) and transverse compressive strength Y_C (d)

Thereby, the experiments at $\varphi \approx 60\,\%$ for samples with a thickness of 4 mm (black triangles) show a significantly lower scattering than the samples with a thickness of 1.8 mm (black crosses). The transverse tensile strengths Y_T show no clear trend (Figure 2.12c). The results indicate that the transverse tensile strength tends to remain constant independent of the FVC. A possible reason for this condition is the fact that with increasing FVC the distance between the filaments decreases and thus the weakest link determines the strength of the composite [71]. Considering the results, the assumption of a constant transverse tensile strength seems to be the most suitable approach.

The determination of the shear strength S_{12} represents a special challenge. Ideally, hoop wound specimens are well suited to determine the shear strength. However, such samples are difficult to manufacture and there is always an overlapping area that creates an inhomogeneous stress state. There is also no standardized procedure for the production of such samples, which makes it more difficult to compare the results. So far the shear strength with varying FVC has been only determined on round samples [18]. No obvious correlation between FVC and shear strength could be observed. The experimental analysis on samples according to the V-Notched Rail Shear Method (ASTM D 7078) shows a slight increase towards higher shear strengths with increasing FVC (cf. Figure 2.13). As mentioned in Section 2.2.2, this type of test provides a conservative estimate of the shear strength, since a multiaxial stress state is created near the notch, which can induce premature failure.

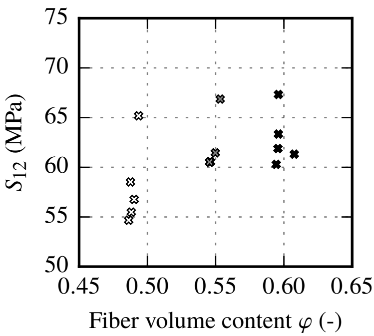

Figure 2.13: Shear strength results at different fiber volume contents using the V-Notched Rail Shear Method (all experiments performed at ILK in Dresden)

2.5.1.4 Failure Envelopes

Failure envelopes are needed to model the failure behavior under combined stress loads. Based on experimental results of combined σ_{22}-σ_{12} load cases, failure criteria have been developed for fiber composites that can be transferred to three-dimensional stress states [72, 73]. A possibility to analyze different σ_{22}-σ_{12} stress ratios can be achieved by off-axis tension and compression tests

[53, 54]. The global failure stress σ_{xx} is therefore transformed into the local stresses σ_{22} and σ_{12}, while the deformation of the material axes is taken into account. The calculation of the angles θ and θ_{12}, as well as the local shear stress σ_{12} is given in Equations (2.4) to (2.8). Since σ_{xx} is the only nonzero component, the local stress σ_{11} and σ_{22} can be calculated as follows:

$$\sigma_{11} = \frac{\sin^2(\theta + \theta_{12})}{\sin^2 \theta_{12}} \sigma_{xx} \quad \text{and} \quad \sigma_{22} = \frac{\sin^2 \theta}{\sin^2 \theta_{12}} \sigma_{xx}. \tag{2.10}$$

Thus, to determine a failure envelope, individual support points are needed. As the failure envelope defines the brittle failure of unidirectional laminates, the failure stresses from OAT and OAC tests $\sigma_{22}^{\mathrm{OAT/OAC}\theta^\circ}$ and $\sigma_{12}^{\mathrm{OAT/OAC}\theta^\circ}$, as also from UD90° tests, are used. A total of six different off-axis angles are experimentally investigated under tensile and compressive loading. The initial fiber orientation angles for the OAT and OAC tests are given in Table 2.2. In addition to the uniaxial tests on UD90° samples, the V-Notched Rail Shear Method tests, which provide support points along the σ_{22} and σ_{12} axes, are used to provide a more holistic overview of the available test data. The result of the off-axis tests provides in total twelve additional support points in the $(\sigma_{22}, \sigma_{12})$-plane. The resulting support points are given in Figure 2.14. All OAT and OAC samples have an FVC of approximately $\varphi \approx 55\,\%$. To investigate the impact of the FVC on the failure envelope, additional selected OAT and OAC tests are performed at different FVC values ($\varphi \approx 50\,\%$ and

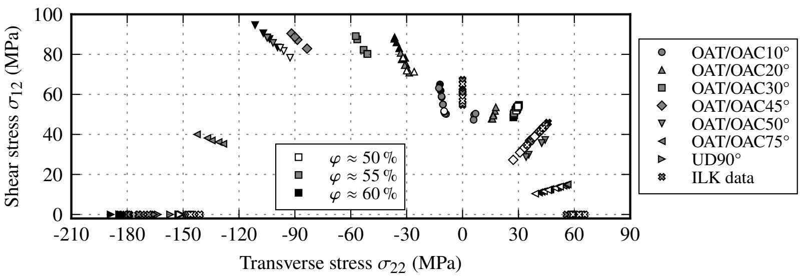

Figure 2.14: Failure envelope in the $(\sigma_{22}, \sigma_{12})$-plane for different fiber volume content values $\varphi \approx \{50\,\%, 55\,\%, 60\,\%\}$ (ILK experimental data at $\varphi \approx \{48\,\%, 54\,\%, 60\,\%\}$)

$\varphi \approx 60\,\%$). As for uniaxial transverse compression tests, an expansion of the support points can be observed. This means that these failure stresses are also dependent on the FVC. By a detailed analysis some test results (such as OAC10°, OAC20°, OAT10° and OAT20°) show a higher deviation from an overall failure envelope trend. The OAC tests with an angle $\theta \in \{10°, 20°\}$ have a much higher local shear stress σ_{12} compared to the transverse stress σ_{22}. Although these specimens should have a shear dominant failure behavior, the specimens fail due to buckling. Therefore, the failure results from the local stress in the fiber direction rather than from a shear stress failure. Thus, the support points of these tests in the $(\sigma_{22}, \sigma_{12})$-plane represent a lower limit of the actual failure stress. The OAT tests of specimens with the same angles ($\theta \in \{10°, 20°\}$) show a significantly lower failure stress than the V-Notched Rail Shear Method tests or the OAT30° specimens. A possible explanation is that with decreasing angle, the local stress in the fiber direction σ_{11} increases significantly and thus causes an interaction with the local stresses σ_{22} and σ_{12}, which leads to premature failure. This phenomenon has already been observed in experimental tests and is considered by analytical failure criteria [74].

2.5.1.5 Experimental Off-Axis Tests on Unidirectional Coupons for Validation of Numerical Models

The parameterization of simulation models is done on uniaxial experiments. To validate the developed model, OAT and OAC tests with complex stress states can be used. These tests can be used to compare the resulting deformation behavior and failure. The measured stress-strain curves for different OAT and OAC tests at $\varphi \approx 55\,\%$ are shown in Figure 2.15. For a better comparison, the results are plotted by using the global stress σ_{xx} and the strain in longitudinal direction ε_{xx}. The test results show distinct nonlinear behavior. As expected, the maximum stress and stiffness decreases with increasing off-axis angle. It can also be observed that for OAC tests significantly larger deformations are achieved.

In addition to the deformation behavior, stiffness and strength, the fiber rotation $\Delta\theta$ can be used as an essential factor in validation. If the fiber orientation angle θ is calculated according to Equation (2.5) and the initial angle θ_0 is subtracted, the fiber rotation $\Delta\theta$ can be plotted over the acting strain ε_{xx}. The resulting fiber rotation for different OAT and OAC tests is given in Figure 2.16.

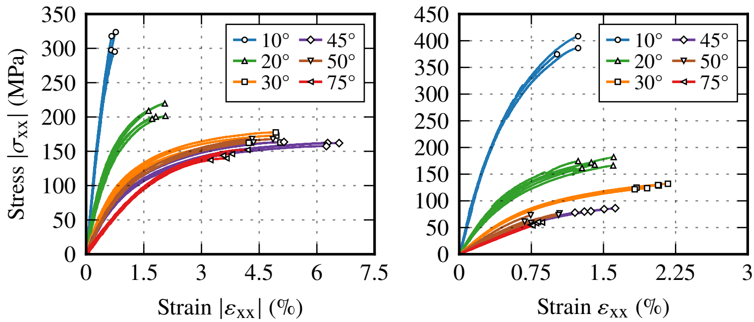

Figure 2.15: Compression (left) and tension (right) coupons tests at different off-angles (failure points are denoted by markers)

The results are taken from samples with a FVC $\varphi \approx 55\,\%$. It should be noted that the fiber rotation $\Delta\theta$ is given as an absolute value to allow a direct comparison between tensile and compression tests. In general, $\Delta\theta$ is negative in tensile tests and positive in compression tests (see Figure 2.10). Fiber

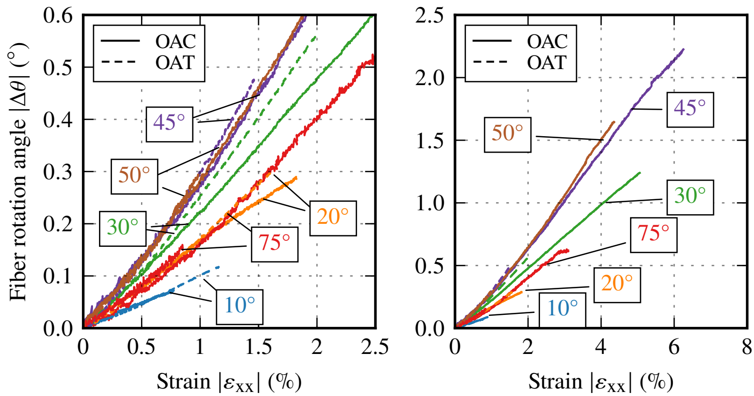

Figure 2.16: Fiber rotation over strain during off-axis compression and tension tests (corresponding off-axis angles are annotated): small strain area (left) and large strain area (right)

rotation occurs under both tensile and compressive loading. For small strains and for samples with the same off-axis angle, the fiber rotation is independent of the loading direction. Only tests at an angle of $\theta \in \{20°, 30°\}$ show larger deviations between tensile and compressive loads. High shear strains do not lead to maximum fiber rotation for OAT/OAC tests, which is the case for OAT/OAC10° tests. Instead, the maximum fiber rotation angle occur for laminates with $\theta \approx 45°$. By comparing tensile and compressive tests, large difference in the maximum achievable fiber rotation can be observed. In tensile tests with angles of $\theta > 20°$ the maximum fiber rotation is significantly smaller than for compression tests. This can be attributed to the fact that the strains until failure are also higher than in compression tests. In other words, higher strain values allow the specimens to undergo greater deformation. For OAC10° and OAC20° tests, the fiber rotation is less than or equal to the OAT tests, since these tests fail by buckling rather than shear failure. It is noticeable that the sensitivity of the fiber rotation around $\theta \approx 45°$ is small. Thus, the results for OAT/OAC45° and OAT/OAC50° tests are almost identical.

In addition to the fiber rotation, the deformation of the initially transverse material axis can be analyzed. In this case the deformation can lead to different rotation angles as for the fiber direction. The angle θ_{12} is determined from the performed OAC and OAT tests and can be used as a measure for the change of the second material axis. The results are given in Figure 2.17. It can be observed that for all tensile tests the angle θ_{12} becomes smaller and for all compression tests larger than 90°. The slope of the angle θ_{12} is dependent on the off-axis angle. The slope increases from small angles to larger ones. For OAT tests up to 30° a maximum angle of $\theta_{12} \approx 87°$ seems to be reached independently on the strain at failure. Compared to OAC tests, such a correlation cannot be observed. One possible explanation yields from different failure modes (e.g., OAC10° and OAC20° tend to buckle). It is particularly noteworthy that for OAC30° tests, the maximum angle yields $\theta_{12} \approx 96°$, while at the same point the fiber rotation reach an angle of $\theta \approx 1.2°$. This condition leads to the consequence, that the second material axis changes by an angle of 4.8°, which is four times larger as the fiber rotation.

One special note should be mentioned regarding the acting stress in combination with rotation of material axes. By using the initial orthogonal material coordinate system and the global stress σ_{xx}, the resulting local stress values can be totally different compared to the local stress values by us-

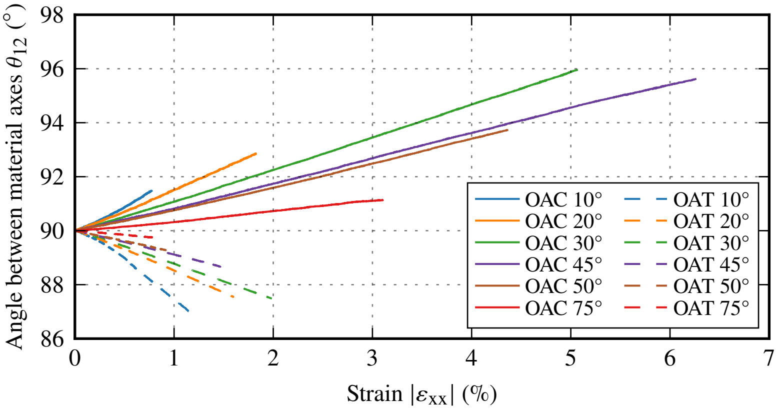

Figure 2.17: Angle between material axes over strain for different off-axis tension and compression coupon tests

ing the deformed material axes instead. Previous investigations concerning the fiber rotation on coupon tests show a maximum change of the angle by about $\Delta\theta \approx 8°$ for $\pm 45°$ angle-ply laminates [11]. Here, with unidirectional laminates a maximum fiber rotation of $\Delta\theta \approx 2.3°$ at OAC45° occurs. This means that the acting global stress σ_{xx} at an initial angle $\theta_0 = 45°$ and $\theta_{12}^{\text{init}} = 90°$ is equally distributed to the local stress components $\sigma_{11} = 0.5\sigma_{xx}, \sigma_{22} = 0.5\sigma_{xx}, \sigma_{12} = -0.5\sigma_{xx}$. If the deformation of the material axes is not taken into account, this distribution remains unchanged. On the other hand, by calculating the local stresses along the deformed material axes, the stress components yields $\sigma_{11} = 0.36\sigma_{xx}, \sigma_{22} = 0.55\sigma_{xx}, \sigma_{12} = -0.44\sigma_{xx}$ using $\Delta\theta = 2.3°$ and $\theta_{12} = 96°$. This produces a stress difference of 8.5 % to 38.5 % compared to the results of an orthogonal coordinate system. Therefore, when modeling composite materials, special attention should be paid to the reference coordinate system in which the stress is evaluated.

In addition to stiffness, strength and the resulting deformation of the material axes, the variation of the fiber volume content can be used for a model validation. For selected OAC and OAT experiments (see Table 2.2), the fiber volume content is varied to analyze its impact on the nonlinear material behavior. In contrast, uniaxial tests such as UD90° tension or compression tests show a difference in nonlinear behavior. Tension tests show a linear elastic material response. On the other hand, compression tests show a pronounced nonlinear stress-strain curve. Therefore, UD90° compression tests with varying fiber volume content are chosen to validate the developed material model. The experimental results are given in Figure 2.18. As the fiber volume content increases, the degree of nonlinearity decreases. This can be explained by the fact that the dominance of the fiber increases and that the plastic deformation, which results from the matrix, plays a reduced role. Another observation regarding nonlinearity can be observed with the increase of the off-axis angle. For example, the OAT75° tests show an approximately linear trend. This observation correlates with tensile tests on UD90° samples, where the σ_{22} is the dominant stress component.

2.5.2 Angle-ply Coupons

Due to the different load cases unidirectional laminates are only suitable for precisely known load paths. For this reason, laminates with different orientations are used to withstand forces from different directions. In addition to the validation of deformation and nonlinear behavior of unidirectional laminates, different angle-ply laminates can be also used. For this purpose, tests are carried out at different angle-ply angles $\pm\theta$ (see Table 2.2). The results of the stress-strain curves are given in Figure 2.19. The FVC of the laminates is $\varphi \approx 55\,\%$. Regardless of the load direction, the initial stiffness of the specimens with the same angle $\pm\theta$ is equal. It is noticeable that for ±30° and ±40° laminates, the failure stress of tensile loads is significantly higher than the failure stress of compression loads. For all other angle combinations, the strength under tension is lower than compression strength. By comparing unidirectional laminates with angle-ply laminates, it is primarily noticeable that the achievable strengths and maximum strains differ. For example, OAT30° achieves a strength of 130 MPa and a maximum strain of approximately 2 %. In contrast, a ±30° laminate achieves a tensile strength of 230 MPa and a maximum strain just below 1 %. The difference appears even more significant if the results of OAT45° and ±45° angle-ply tests are compared. The maximum strain differs by at least a factor of four. The reason for this is that occurring cracks in angle-ply laminates do not cause complete failure of the laminate and further load can be applied. Both fiber orientations in an angle-ply laminate continue

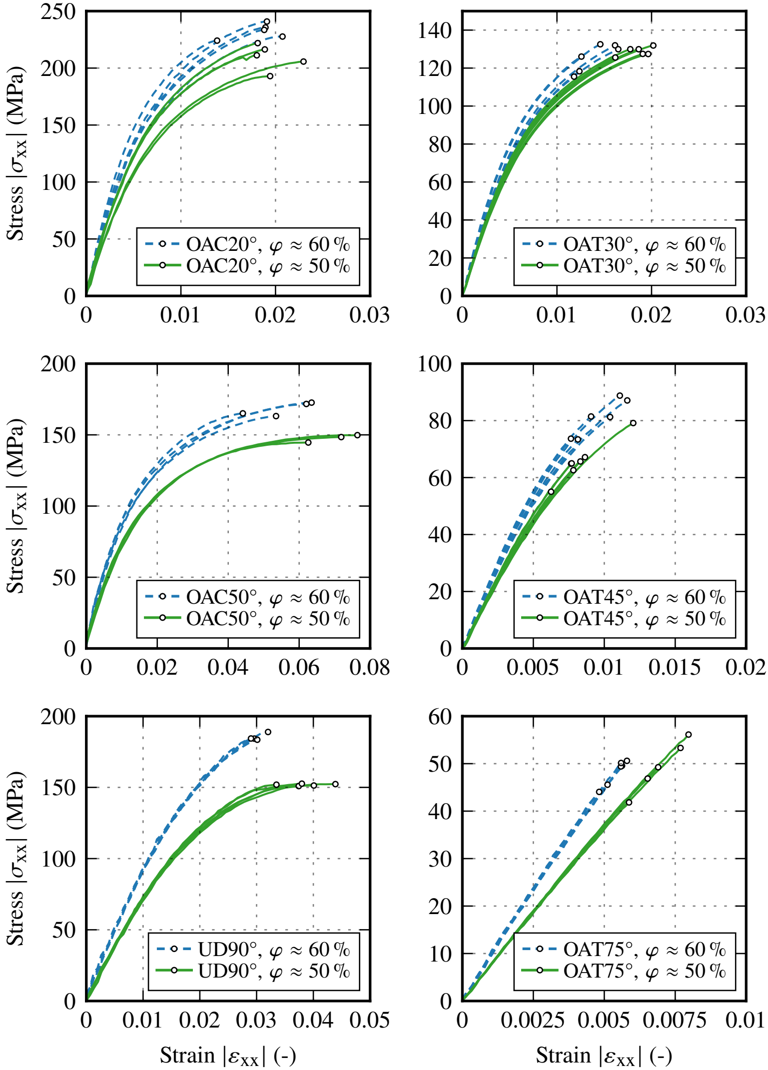

Figure 2.18: Stress-strain curves of selected off-axis compression (OAC) and off-axis tension (OAT), and UD90° compression tests at different fiber volume contents

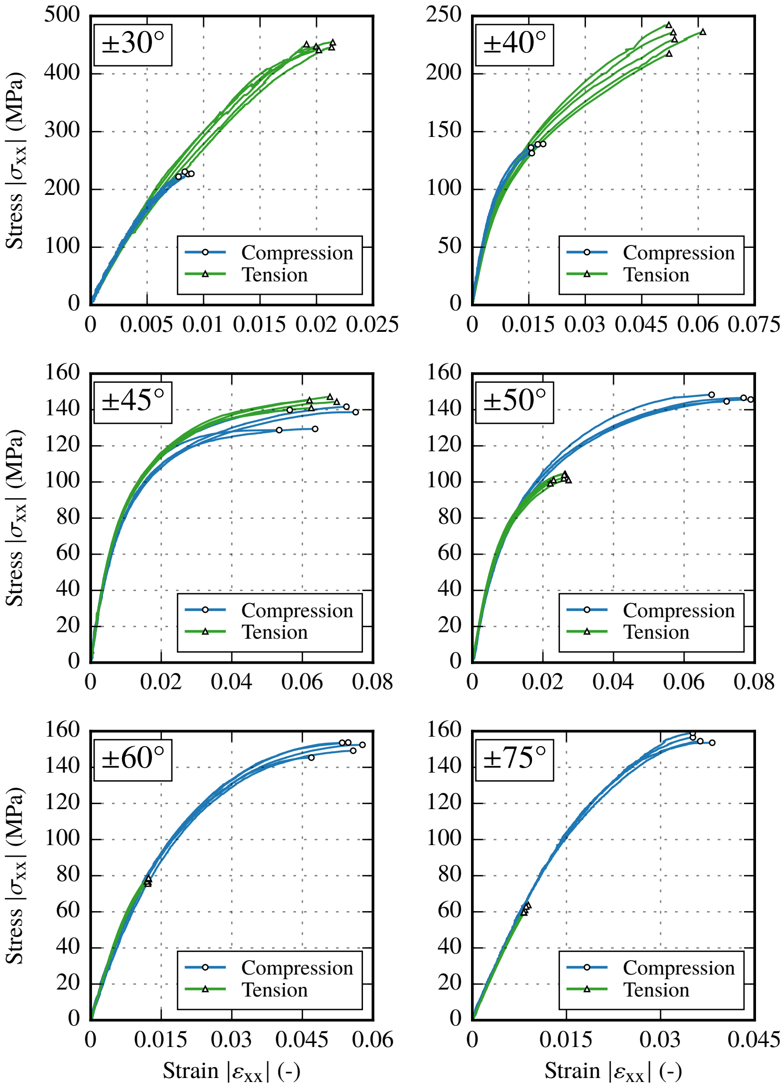

Figure 2.19: Experimental results for angle-ply laminates at $\varphi \approx 55$ % under tension and compression loads (angle-ply angles are annotated)

to contribute to the integrity of the laminate. A sequential formation of cracks can be observed in tests (see Figure 2.20). It is known that for unidirectional laminates with increasing compressive transverse stress σ_{22} the fracture plane changes [72]. This correlation could also be observed for angle-ply laminates. Compression loads on angle-ply laminates with an angle $\theta \geq 45°$ lead to a fracture angle $\theta_{\text{ap}} \neq 0°$. However, the exact value of the fracture angle is difficult to be determined from experiments. Large uncertainties can arise as the fracture angle is determined after unloading the test specimen. In contrast to OAT and OAC tests, where failure is primarily matrix dominant, angle-ply tests can be divided into three failure categories. Loads up to an angle of ±30° exhibit high stresses in fiber direction and show also fiber dominant failure behavior. For angles between ±40° and ±50° a high reorientation of the fiber direction is observed. After the maximum stress value is reached, the stress decreases while the test samples do not fail. A complete separation of the coupons is primarily not observed. Such material behavior suggests a shear dominant failure. Laminates with an angle of ±60° and ±75° show a matrix dominant failure, which leads to a sudden failure, as for unidirectional coupon tests.

As for unidirectional laminates, a fiber rotation $\Delta\theta$ can also be observed for angle-ply laminates. The resulting fiber rotation for each test is shown in

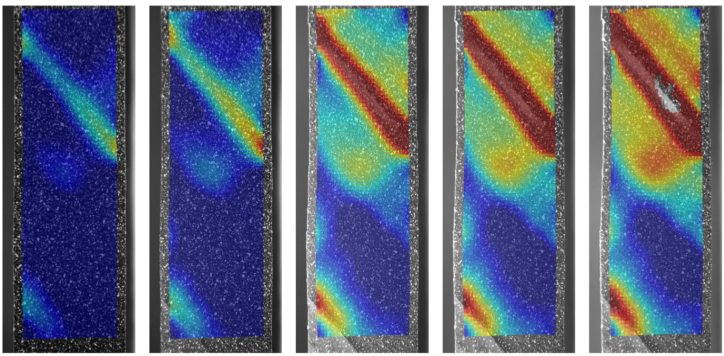

(a) $\varepsilon_{\text{xx}} = 4.8\,\%$ (b) $\varepsilon_{\text{xx}} = 5.2\,\%$ (c) $\varepsilon_{\text{xx}} = 6.0\,\%$ (d) $\varepsilon_{\text{xx}} = 6.3\,\%$ (e) $\varepsilon_{\text{xx}} = 6.5\,\%$

Figure 2.20: Global strain distribution and the formation of cracks during tensile loading of an ±45° angle-ply laminate at different strain states

Figure 2.21. For angle-ply laminates a maximal fiber rotation of $\Delta\theta \approx 4.5°$ for the compression test on a ±45° laminate can be observed. Similar to OAT and OAC tests, the change of the fiber orientation is independent of the load direction. Concerning ±30° laminates a parallel trend of the curves can be observed, but the horizontal offset between the tensile and compression tests could not be clarified conclusively. For larger deformations, only ±45° laminate tests show a difference between tensile and compression tests. Here the change of the angle θ, described in Figure 2.10, can be observed: under tension the angle becomes smaller while under compression it becomes larger. As in unidirectional coupon tests, an approximately linear progression of fiber rotation versus strain can be observed for each angle-ply angle combination. This leads to the conclusion that the geometric deformation has a greater impact on the fiber rotation than the material behavior itself. For unidirectional samples the fiber rotation through the sample can be assumed to be constant. On the other hand, angle-ply laminates have an alternating fiber orientation, which raises the question whether fiber rotation is the same for each ply. Since $\boldsymbol{F}$ describes the global deformation of the sample and the deformation of the individual layers is coupled, it can be assumed that the same fiber rotation

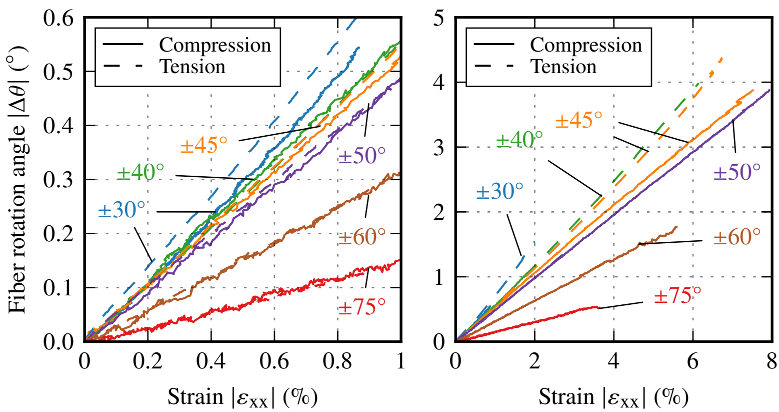

Figure 2.21: Fiber rotation over strain for various angle-ply coupon tests (angle-ply laminate angles are annotated): small strain area (left) and large strain area (right)

occurs in the inner plies. A further difference to the unidirectional coupon tests can be observed by comparing the slope of fiber rotation versus strain. In OAT and OAC tests, the largest slope is observed at an angle of $\theta \approx 45°$. In addition, the slope increases with increasing angle and then decreases again after reaching $\theta \approx 45°$. The slope of the fiber rotation of angle-ply laminates decreases continuously with increasing angle.

Just as in unidirectional laminate tests, the angle between the material axes θ_{12} is undergoing a continuous change. Using the deformation gradient $\boldsymbol{F}$ the angle θ_{12} for angle-ply laminates is determined. The results are summarized in Figure 2.22. The slope of θ_{12} versus strain decreases from small angles to larger ones. This observation is comparable with unidirectional laminate tests. Compared to OAT and OAC tests, an even more significant change of the angle between the material axes occur. The ±45° and ±50° angle-ply laminates show the largest change of θ_{12}.

A direct deduction to the local stresses σ_{11}, σ_{22} and σ_{12} as in the unidirectional laminate tests cannot be made without further ado. In case of angle-ply laminates in addition to the global stress σ_{xx}, which can be determined from the force measurement, the global shear stress σ_{xy} is also present in each

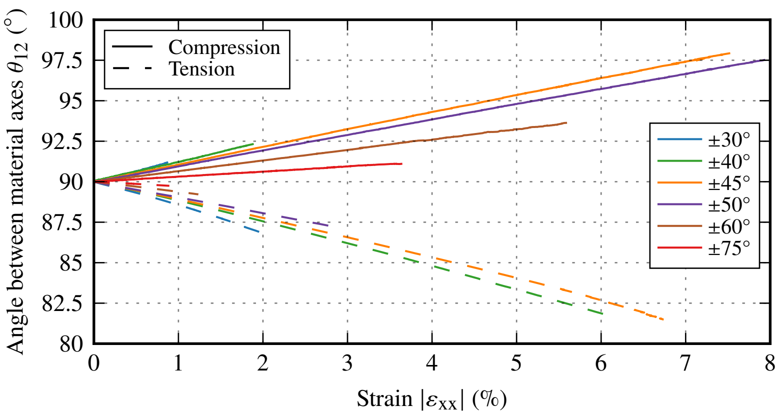

Figure 2.22: Angle between material axes over strain for angle-ply coupon tests at $\varphi \approx 55$ %

layer. However, the global shear stress is not known and cannot be determined without knowledge of the material stiffness. As the absolute value of σ_{xy} is the same in all layers, they cancel each other out due to the alternating angles. Nevertheless, on the basis of unidirectional coupon tests it can be concluded that the fiber rotation $\Delta\theta$ and the angle θ_{12} for angle-ply laminates have an even greater impact on the local stress. If this composite specific condition is neglected, the validity of the numerically determined stress and the resulting failure behavior of the material can be questioned.

2.5.3 Coupons with Waviness

Due to the draping process, areas with waviness may occur. The mechanical properties in these areas also change significantly. Waviness and its impact on the compression failure of composites has been analyzed in numerous investigations [27, 30–35]. Usually, waviness is the result of shearing or running length difference that can occur between two parallel running rovings. Such effects occur close to multiple curved regions, since fibers running parallel to each other have to follow different path lengths. Another possible cause of waviness is an applied compressive load in fiber direction. To reduce complexity, an occurring waviness can be approximated as sinusoidal. For this purpose, the following wave definition is used

$$y = A \sin \frac{2\pi x}{\lambda}. \tag{2.11}$$

An occurring waviness in an area with previously straight fibers leads to an increase of the local fiber length. The length of the fiber in a wavy area can be determined from the arc length s_λ of the sinusoidal waviness

$$s_\lambda = \int_0^\lambda \sqrt{1 + \left(\frac{\mathrm{d}y}{\mathrm{d}x}\right)^2}\, \mathrm{d}x = \int_0^\lambda \sqrt{1 + \left(\frac{2\pi A}{\lambda} \cos \frac{2\pi x}{\lambda}\right)^2}\, \mathrm{d}x. \tag{2.12}$$

It is obvious that with an amplitude $A = 0$ the fiber length is exactly the wavelength of the wave $s_\lambda = \lambda$. This means that for the arc length of the fiber the condition $s_\lambda \geq \lambda$ must apply. To solve such an integral, the following substitution is made

$$u = \frac{2\pi x}{\lambda} \quad \text{and} \quad \frac{\mathrm{d}u}{\mathrm{d}x} = \frac{2\pi}{\lambda}\mathrm{d}x. \tag{2.13}$$

This simplifies the integral to

$$s_\lambda = \frac{\lambda}{2\pi} \int_0^{2\pi} \sqrt{1 + \left(\frac{2\pi A}{\lambda} \cos u\right)^2} \mathrm{d}u = \frac{2\lambda}{\pi} E \left(2\pi \sqrt{-\left(\frac{A}{\lambda}\right)^2} \right), \tag{2.14}$$

where E describes the elliptic integral of the second kind. In the case of an existing waviness, the maximum angle deviation from the ideal state can also be determined. These occur at the inflection points of the wave. Only the amplitude A and the wavelength λ are required to determine the maximum waviness misalignment angle

$$\theta_{\max} = \arctan \frac{2\pi A}{\lambda}. \tag{2.15}$$

Due to material flow in an area with waviness the local fabric weight is increased [50]. As a result, the FVC increases and can be estimated as

$$\varphi = \varphi_0 \frac{s_\lambda}{\lambda} \tag{2.16}$$

where the initial FVC φ_0 can be determined from Equation (2.2). Due to the condition that the length of the roving can only increase, the FVC can also only increase. This correlation has already been experimentally proven [50]. For a constant wavelength λ and an initial FVC of $\varphi_0 = 0.55$, the resulting FVC corresponding for each A/λ ratio can be calculated using Equations (2.14) and (2.16). This relationship is shown in Figure 2.23. The FVC rises significantly nonlinear with increasing A/λ ratio. For an initial FVC of $\varphi_0 = 0.55$ and a waviness ratio $A/\lambda \approx 0.1$ the FVC only increases by 5 %. For a further increase of the FVC by 5 % it only takes a ratio of $A/\lambda \approx 0.15$. The relation between FVC and A/λ ratio can be compared to the reduction of the laminate thickness $\Delta t/t$ (cf. Figure 2.23). In both cases the sensitivity of the FVC is strongly dependent on the present waviness ratio.

Using the manufacturing tools developed at the ILK in Dresden [50], two different waviness ratios, $A/\lambda \approx \{0.03, 0.06\}$, under tensile and compressive loads are analyzed (see Table 2.2). The stress-strain curves determined are given in Figure 2.24. The thickness of the coupon samples lead to a FVC of $\varphi_0 \approx 55\,\%$. For the examined A/λ ratios, the FVC increases again to $\varphi \approx 55.5\,\%$ and $\varphi \approx 56.9\,\%$. To deduce the impact of the waviness on the

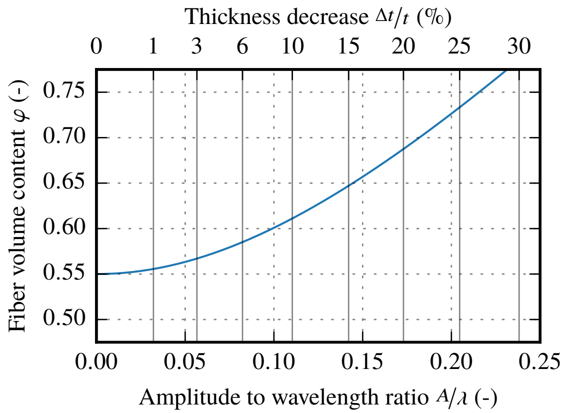

Figure 2.23: Analytical solutions of the resulting fiber volume content with increasing amplitude to wavelength ratio A/λ or percentual decrease of the laminate thickness t

stiffness and strength, UD0° coupons with a FVC of $\varphi \approx 55\,\%$ are used. The resulting stiffness and strength values are specified in Table 2.3. By comparing the resulting stiffness E_x no difference between the tensile and compressive loads is found. As expected the stiffness drops significantly by up to 60 %. The resulting strength values are even more affected by the waviness. The tensile strength of UD0° samples yields approximately $X_T = 1500\,\text{MPa}$. At

Table 2.3: Comparison of experimental results at different A/λ ratios (all experiments performed at ILK in Dresden)

Waviness ratio A/λ /–	Stiffness E_x /GPa	Tensile strength X_T /MPa	Compressive strength X_C /MPa
0	100.9	1500	988.8
0.03	70.3	568.2	307.9
0.06	41.2	231.1	277.0

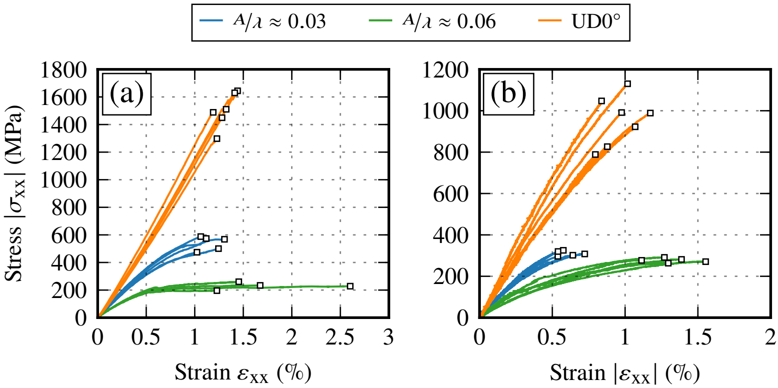

Figure 2.24: Experimental results for coupons with imposed waviness under tension (a) and compression (b) loads [47]

$A/\lambda \approx 0.03$ the strength yields $X_T = 568.2\,\text{MPa}$, which corresponds to a reduction of 62 %. With increasing waviness ratio, the tensile strength drops even further. Here, the strength is only 15 % of the tensile strength of UD0° coupon samples. Similar results are obtained for the compression tests. The ratio $A/\lambda \approx 0.03$ leads to a 69 % reduction and $A/\lambda \approx 0.06$ to 72 % lower strength value. By analyzing the damage evolution of coupons with waviness, a load direction specific pattern can be observed (cf. Figure 2.25a-e). For

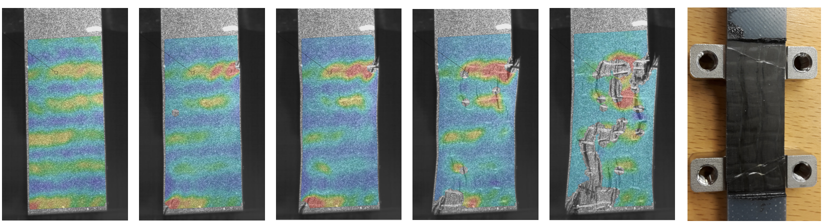

(a) $\varepsilon = 0.2\,\%$ (b) $\varepsilon = 0.75\,\%$ (c) $\varepsilon = 1.1\,\%$ (d) $\varepsilon = 1.7\,\%$ (e) $\varepsilon = 2.0\,\%$ (f) compression

Figure 2.25: Evolution of deformation under tensile load for an amplitude to wavelength ratio of $A/\lambda \approx 0.06$ (a)–(e) and resulting crack after compression for $A/\lambda \approx 0.03$ (f) [47]

tensile loads, initial cracks are formed at the edges of the coupons. Next, these cracks develop further until they reach the point, where the normal direction of the crack is perpendicular to the loading direction. At the same time, cracks at turning points of the wave all over the sample start to form. Finally, the cracks continue to grow until these are connected and the sample fails. On the other hand, samples under compression loads fail with a single crack formation (cf. Figure 2.25f). An in depth discussion of the experimental tests is published by Kunze/Galkin et al [47].

Based on the experimental results an amplitude to wavelength ratio dependent tensile and compressive strength formulation in fiber direction could be found [47]. As shown in Figure 2.25, for tensile loads inter-fiber failure occur. Using a well established failure criteria for inter-fiber failure by Puck [72], the corresponding failure stress can be determined for each stress state. This criterion requires local stress values as input. The acting global stress σ_{xx} of samples with waviness can be rotated to the local fiber direction to obtain the local stress components σ_{11}, σ_{22} and σ_{12}. The angular difference between global direction and local fiber direction is defined by the maximum misalignment angle θ_{max}. As the local stress components are functions of θ_{max}, the global stress $\sigma_{xx}^{IFF} = f(\theta_{max})$ defining the failure for different amplitude to wavelength ratios can be calculated using Puck's failure criterion. For small misalignment angles $\theta_{max} < 5^\circ$ ($A/\lambda \approx 0.014$) the dominance of the fiber direction is more pronounced. Therefore, a case dependent waviness strength formulation is used

$$X_{T,C} = \min\{\sigma_{xx}^{IFF}, X_{T,C}^{UD0^\circ}\}, \tag{2.17}$$

where $X_{T,C}^{UD0^\circ}$ is the tensile or compressive strength in fiber direction of nonundulated UD0° laminates. Such formulation shows a very good correlation with experimental results for tensile strength. However, this formulation must be extended for compressive strength as a transition from an inter-fiber failure to a fiber failure is reached. The tensile and compressive strength for samples with waviness can be finally defined as follows

$$\begin{aligned} X_T &= \min\{\sigma_{xx}^{IFF}, X_T^{UD0^\circ}\} \\ X_C &= \begin{cases} \frac{2X_C^{UD0^\circ} S_{12}}{2S_{12}\cos^2\theta_{max} - X_C^{UD0^\circ}\sin 2\theta_{max}}, & \theta_{max} < 10^\circ \\ \min\{X_C|_{\theta_{max}=10^\circ}, \sigma_{xx}^{IFF}\}, & \theta_{max} \geq 10^\circ \end{cases}, \end{aligned} \tag{2.18}$$

where $X_C^{UD0°}$ correspond to the compressive strength of nonundulated UD0° laminates, S_{12} is the in-plane shear strength, and $X_C|_{\theta_{max}=10°}$ is the resulting waviness compressive strength at $\theta_{max} = 10°$. The detailed derivation of the analytical strengths for different amplitude to wavelength ratios is described by KUNZE/GALKIN et al [47].

As already observed for unidirectional and angle-ply coupons, a fiber rotation also occurs in case of waviness. As a result, a continuous change of the waviness ratio takes place. A schematic representation of the fiber angle change is shown in Figure 2.26. The initial maximum angles $\theta_{1,max}^{init}$ and $\theta_{2,max}^{init}$ thus change to $\theta_{1,max}$ and $\theta_{2,max}$ during an applied deformation. The developed DIC algorithms (see Section 2.3) are used to analyze this phenomenon. The resolution of the DIC measurement is about 24 px/mm and allows a very detailed evaluation. To calculate the fiber rotation along the wavelength λ, the start and end coordinates of the wave within the strain field must be known. If the coordinates are known, the displacements of each point along the wave can be used to determine the fiber direction change. Since a speckle pattern is applied to the sample, the periodic waves can no longer be visually determined. However, the individual waves can be determined by the displacements of the facets. If a specimen is stretched, the largest displacement occurs in areas where the fiber orientation is parallel to the loading direction. These positions correspond exactly to the minima and maxima of a wave. Since the amplitude to wavelength ratio is known, the deformation of a wave function between these points can be evaluated. The resulting fiber rotation due to straightening of the roving is shown in Figure 2.27. It can be observed that the fiber rotation increases with increasing ε_{xx} strain. The position of the maximum reached

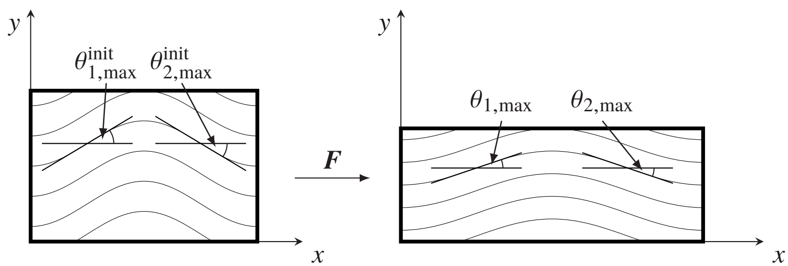

Figure 2.26: Schematic representation of the fiber orientation change due to deformation

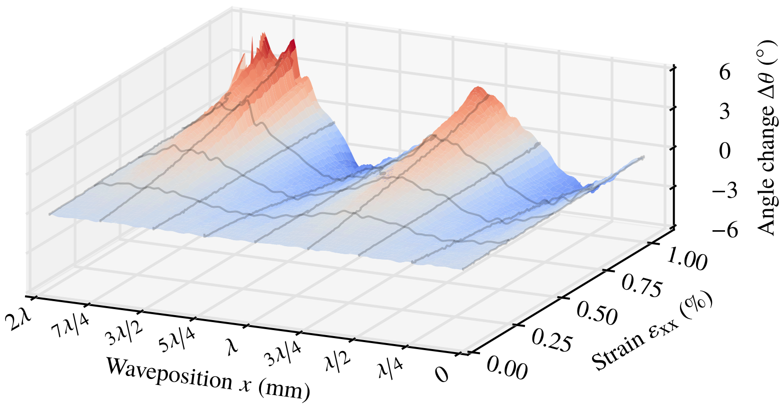

Figure 2.27: Experimental result of fiber orientation change for coupons with an imposed waviness of $A/\lambda \approx 0.03$

fiber rotation angles correspond to the turning points of the wave. The regions where the fiber and loading direction are parallel, the fiber rotation remains zero. In the examined area the change of the angle is mostly homogeneous. The formation of spikes between λ and 2λ results from local crack formation, which pronounces the fiber rotation even more. The average fiber rotation for a waviness ratio $A/\lambda \approx 0.03$ ranges between $-4.3\,°$ to $4\,°$. This condition shows again the importance of considering the local change of the fiber orientation in the numerical simulation of composite materials.

3 Constitutive Modelling of Fiber Reinforced Plastics Considering Draping Effects

3.1 Literature Review

Despite the comprehensive research in the field of fiber reinforced composites, the material behavior, especially as a result of forming, is still under ongoing research. In most cases, the influence of the manufacturing process is considered in a simplified way. This includes the projection of the global fiber orientation onto the component, the use of a constant FVC and the assumption of perfectly straight fibers. This leads to fiber orientations deviating from the real ones which significantly influence the mechanical response of fiber reinforced composites [1, 75–77]. The use of virtual process chains that transfer information from the manufacturing process to the structure mechanical component simulation creates the possibility of a more realistic design of FRP components. In addition to the forming related effects, the structure mechanical material behavior from the initial state to failure needs to be considered accurately. This includes some further material-specific characteristics, for example fiber rotation due to shear deformation. This aspect has not yet been taken into account in commercially available material models for FRP materials. The corresponding publications only consider the fiber orientation itself and neglect the rotation of the other material axes [10–15, 78–80]. In addition to this, the carbon fiber specific material property (increase or decrease of the modulus in fiber direction [21–23, 81]) is largely neglected. For example various publications [82, 83] report a tension-compression asymmetry of the stiffness of CFRPs, which is actually caused by the nonlinear behavior of carbon fibers [21] and the initially not perfectly straight fibers. While numerous analytical and semi-empirical models [17, 84–88] exist to determine the FVC-dependent material stiffnesses in different directions, the variety of models for the FVC-dependent strengths is limited [20, 88–90]. For example, the tensile strength in the fiber direction is determined by the Voigt rule of mixture using fiber and matrix tensile strength. On the other hand, the FVC-dependent compressive strength in fiber direction results from a micro mechanical stability failure and therefore cannot be determined in the same way. An extensive study [25] showed that the model according to Rosen [91] clearly overestimates the compressive strength. The reason for the deviation are idealistic assumptions which neglect the presence of possible imperfections. However, further models showed better agreement if the fiber misalignment is considered [73, 92]. Currently, there are no validated models predicting the strength transverse to the fiber direction or the shear strength at different fiber volume contents. On the other hand, there are many validated failure criteria [73, 93–95] that reliably predict the material-specific interaction of stresses for inter-fiber failure for a constant FVC. For example, the fracture angle can be predicted for an inter-fiber failure, which in turn can be considered in the damage evolution. The extension of these criteria by FVC-dependent strengths has received little attention so far.

Until failure initiation, the nonlinear material behavior is influenced not only by the used fiber but also by the matrix itself. In most cases FRPs are manufactured by using a thermoset matrix system. The matrix behaves viscoplastic at moderate strain rates and viscoelastoplastic at very high strain rates. To model the plastic behavior of FRPs there are numerous approaches available [96–101]. Hereby the hydrostatic sensitivity of the matrix in a composite determines the load dependent initial yield stress. In some cases it is not possible to distinguish between plasticity and diffuse micro damage. Therefore, there are approaches which consider the nonlinear material behavior until failure by degradation [102–106]. The influence of the FVC on the nonlinear material behavior has not been considered so far.

Over the past years, intensive research has been conducted on damage modeling occurring after failure initiation and the results have been compared in a worldwide competition [107]. Although the models have similarities such as the usage of energy release rates to model the damage evolution process, they differ in the number of required material parameters which in the worst case cannot be measured. In order to provide real measured intralaminar energy release rates to model damage, several experimental methods are available to determine the energy release rates for different load directions [108–112].

The dependence of these intralaminar energy release rates on the FVC is still unknown. In contrast to intralaminar failure, the interlaminar failure and the resulting energy release rate as a function of the FVC were analyzed at an early stage [113–117]. The results show that there is no apparent relationship between the energy release rate and the FVC, which allows to use a constant value over a certain range of the FVC.

In addition to the effect of fiber orientation and FVC-dependent strengths, local waviness is a further effect which reduces stiffness and strength. An existing waviness has in particular an impact on the compressive strength along the effective fiber direction [30, 32, 33, 118]. In order to determine the effective stiffnesses analytical solutions can be used [33, 38, 118–120]. In addition, there are numerical approaches that use representative volume elements (RVE) at the micro scale to analyze the material behavior more precisely [121–123]. On this scale, the influence of the FVC on the stiffness of the composite with a present waviness was also investigated. Thus, a nonlinear relationship between the present waviness and the resulting stiffness was found when the FVC was varied. This RVE method, initially presented by Karami and Garnich [121–123] can reliably predict the stiffness and is therefore also suitable for the analysis of the resulting strength at different fiber volume contents. However, a suitable material model for each constituent, fiber and matrix, must be developed beforehand. In addition, the strength for flat nonundulated RVEs at different loads can be investigated in order to improve the understanding of the observed experimental results for different fiber volume contents. For example, the matrix material strength can be varied or other parameters which affects the failure initiation and damage progression. In contrast to meso-scale models, where the roving and the matrix are discretized separately, the use of micro-scale models to determine the strength of a composite is particularly suitable, since with decreasing distance between adjacent fibers an increase of the globally applied strain in the matrix is induced. The ratio between the stiffness of fiber and matrix can increase the local strain by a factor of 20, leading to failure initiation [60]. However, the influence of initial or deformed geometry of the preform is not captured in micro-scale models. For this purpose meso-scale models are suitable that consider this geometry dependency and provide a deeper understanding of the acting mechanisms. The gained knowledge from micro- and meso-scale models can be considered in the development of homogenized macro models.

The combination of fiber orientation, FVC and waviness has not yet been considered in a single material model on macroscopic scale. Only experimental analyses of these factors and the assumption of a constant FVC for structural simulation of FRP parts are available [27]. In addition, the waviness is realized by fiber orientation, which in turn leads to a mesh-dependent waviness. Whether these simplifications can be made, must be analyzed in detail for each new composite configuration, since with increasing isotropy of the laminate or geometrical stiffness the influence of the manufacturing process can turn out differently. Based on the state of the art and on the findings described above, a material model that can consider forming dependent draping effects must meet the following requirements:

- Consideration of the rotation of the material axes and the resulting strain and stress
- Consideration of the carbon fiber specific material behavior in fiber direction
- Consideration of the hydrostatic sensitivity of the matrix, which affects the plastic flow behavior in a composite
- Prediction of the failure initiation including the fracture angle
- FRP specific damage evolution based on the fracture angle and the associated direction-dependent material effort
- Processing of information from the forming process, such as local fiber orientation, local FVC and local waviness
- Determination of the effective stiffness and strength based on the local FVC
- Use of effective stiffnesses resulting from waviness present

For the analysis of the FVC- and waviness-dependent strength on the micro scale, additional material models for the matrix and the fiber are needed. The constitutive equation for the matrix should cover the viscoplastic material behavior, a physical failure criterion and damage evolution. The fiber model has to consider the nonlinear material behavior for carbon fibers, has to reliably predict the failure in fiber direction and has to be able to model resulting damage evolution. In the following section, the question of a suitable strain measure that correctly considers the rotation of material axes is addressed first. Subsequently, the constitutive equations for matrix, fiber and composite that meet the requirements are presented.

3.2 Strain Measures

To define a constitutive model for any material describing the relationship between strains and stresses, an appropriate strain measure for the specific material needs to be defined. Dependent on the used strain measure, the resulting stresses and therefore the failure and damage propagation are highly affected. In this section different approaches of strain measures are compared regarding physical meaning, their effect on the resulting stresses, failure initiation and damage propagation. This section is by no means complete, for more detailed explanation the reader is referred among others to the work of Belytschko et al. [124] or Willems [125].

3.2.1 Kinematics of a Material Point

In a three-dimensional space the position of a material point $\boldsymbol{X}$ at time t is defined by:

$$\boldsymbol{x} = \chi\left(\boldsymbol{X}, t\right). \tag{3.1}$$

The displacement of the material point is then defined by the vector field $\boldsymbol{u}$

$$\boldsymbol{u} = \chi\left(\boldsymbol{X}, \boldsymbol{t}\right) - \boldsymbol{X}. \tag{3.2}$$

Utilizing the displacement gradient of the vector field $\boldsymbol{u}$, the deformation gradient of the material point $\boldsymbol{X}$ is defined as

$$\boldsymbol{F} = \boldsymbol{I} + \nabla \boldsymbol{u}, \tag{3.3}$$

where $\boldsymbol{I}$ is the second order identity tensor. The deformation gradient has a significant role in the definition of a strain measure. For instance, it is possible to distinguish between the rigid body motion $\boldsymbol{R}$ and the symmetric right or left stretch tensor ($\boldsymbol{U}$ or $\boldsymbol{V}$) of the material point by utilizing the polar decomposition

$$\boldsymbol{F} = \boldsymbol{R}\boldsymbol{U} = \boldsymbol{V}\boldsymbol{R}. \tag{3.4}$$

$\boldsymbol{U}$ and $\boldsymbol{V}$ are both positive definite and symmetric. It is important to note that the information about stretching or shortening (in general volume change) of the material body is contained by $\boldsymbol{U}$ or $\boldsymbol{V}$ (cf. Figure 3.1). By squaring the left or right stretch tensor, the right and left CAUCHY-GREEN tensors and their relation to $\boldsymbol{F}$ are obtained

$$\boldsymbol{C}_{\mathrm{F}} = \boldsymbol{U}^2 = \boldsymbol{F}^{\top}\boldsymbol{F} \quad \text{and} \quad \boldsymbol{B}_{\mathrm{F}} = \boldsymbol{V}^2 = \boldsymbol{F}\boldsymbol{F}^{\top}. \tag{3.5}$$

The right CAUCHY-GREEN tensor $\boldsymbol{C}_{\mathrm{F}}$ is used for instance to describe finite strains, so called GREEN-LAGRANGE strain, $\boldsymbol{E}_{\mathrm{GL}} = {}^1\!/_2\,(\boldsymbol{C}_{\mathrm{F}} - \boldsymbol{I})$. The physical meaning of $\boldsymbol{E}_{\mathrm{GL}}$ can be interpreted as follows: strain components on the main diagonal are functions of the engineering strain along the material direction $\boldsymbol{e}_i$. The off-diagonal components represent the shear strain based on the change of the angle between two material directions in conjunction with the engineering strain along those material directions.

Using curvilinear vectors, such as covariant base vectors $\boldsymbol{G}_i$ (or contravariant base vectors $\boldsymbol{G}^i$) in the initial space and the covariant vectors $\boldsymbol{g}_i$ defining the

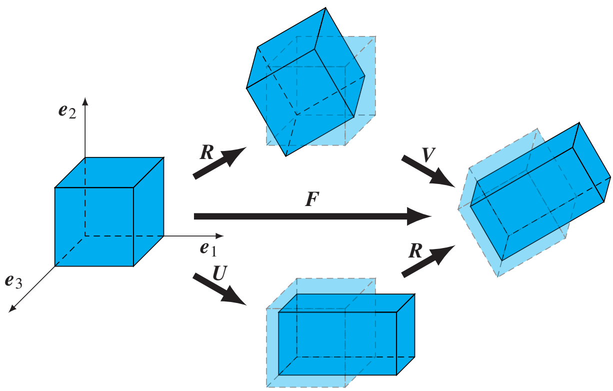

Figure 3.1: Deformation of a body and the differentiation between each component of the deformation gradient

tangent space (or contravariant vectors $\boldsymbol{g}^i$ defining the cotangent space), a further formulation of the deformation gradient can be defined by

$$\boldsymbol{F} = \boldsymbol{g}_i \otimes \boldsymbol{G}_i \quad \text{or} \quad \boldsymbol{F} = \boldsymbol{g}_i \otimes \boldsymbol{G}^i, \tag{3.6}$$

since $\boldsymbol{G}_i$ and $\boldsymbol{G}^i$ are equivalent in the initial space. The relation between the covariant vectors $\boldsymbol{g}_i$ and the covariant base vectors $\boldsymbol{G}_i$ are especially important for materials with distinct material behavior along their material axes. Such materials are e.g., dry fabrics or continuous fiber reinforced plastics [125]. Further connection between the co- and contravariant vectors can be summarized in the following equations:

$$\boldsymbol{g}_i = \boldsymbol{F} \cdot \boldsymbol{G}_i, \quad \boldsymbol{G}_i = \boldsymbol{F}^{-1} \cdot \boldsymbol{g}_i, \quad \boldsymbol{g}^i = \boldsymbol{F}^{-\top} \cdot \boldsymbol{G}^i \quad \text{and} \quad \boldsymbol{G}^i = \boldsymbol{F}^{\top} \cdot \boldsymbol{g}^i. \tag{3.7}$$

It is important to note that the dyadic product of co- and contravariant vectors results in the identity tensor $\boldsymbol{I}$

$$\boldsymbol{I} = \boldsymbol{g}_i \otimes \boldsymbol{g}^i = \boldsymbol{g}^i \otimes \boldsymbol{g}_i. \tag{3.8}$$

This relation is also valid for the base curvilinear vectors $\boldsymbol{G}_i$ and $\boldsymbol{G}^i$.

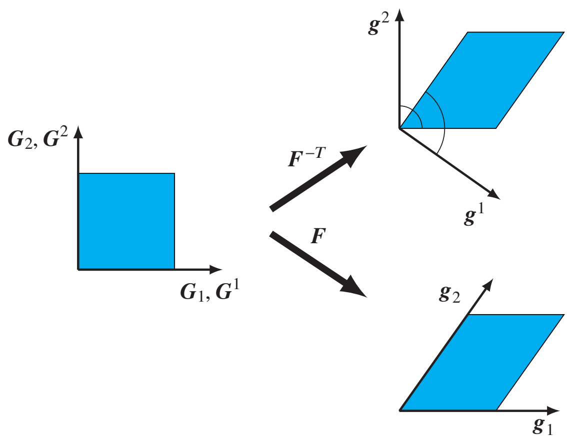

Figure 3.2: Relation between the initial space and the tangent or respectively the cotangent space

3.2.1.1 Material Strains Family

There are several approaches to obtain material strains utilizing the deformation gradient. Based on the work of Seth [126] and Hill [127] the different strain measures can be combined in a generalized Seth-Hill family of strain tensors

$$\boldsymbol{E}_{(m)} = \begin{cases} \frac{1}{2m}\left(\boldsymbol{U}^{2m} - \boldsymbol{I}\right), & m \neq 0 \\ \ln \boldsymbol{U}, & m = 0 \end{cases} \tag{3.9}$$

where the parameter m determines the resulting strain measure. For instance $m = 1$ results in Green-Lagrange strain tensor and $m = 0$ in the Hencky strain tensor (aka Logarithmic or True strain). The Seth-Hill family of strain tensors are expressed as a function of the right stretch tensor $\boldsymbol{U}$, since $\boldsymbol{U}$ represents the stretch in the material coordinate system. These strains can be also expressed as function of the left stretch tensor $\boldsymbol{V}$. The relationship between $\boldsymbol{U}$ and $\boldsymbol{V}$ can be derived from the deformation gradient $\boldsymbol{F}$. Using Equation (3.4) it is obvious that by multiplying $\boldsymbol{R}^\top$ from the right side and considering that $\boldsymbol{R}\boldsymbol{R}^\top = \boldsymbol{I}$, the relationship between $\boldsymbol{U}$ and $\boldsymbol{V}$ is given as

$$\boldsymbol{U} = \boldsymbol{R}^\top \boldsymbol{V} \boldsymbol{R}. \tag{3.10}$$

Therefore, the left stretch tensor $\boldsymbol{V}$ is expressed in the initial configuration and is rotated to the material coordinate system.

According to Onaka [128] the different strain measures can be defined in the scope of their application. Dependent on the application each strain measure can therefore be defined as a function of strain and rotation. For small rotation and strain the infinitesimal (or linearized) strain is sufficient. On the other hand, for large rotation and small strain the Green-Lagrange is more recommended. However, for large strain and rotation the Hencky strain suits better.

Besides the used strain measure, it is required to use the proper definition and utility of the stress, stress rate, the work-conjugate strains and strain rates [129]. For example the finite element analysis software Abaqus uses Green-Naghdi and Jaumann stress rates, which both are work-conjugate to Cauchy stress and Hencky strain.

3.2.2 Influence of Material Axis Rotation on the Strain Measure

For materials with distinct material axes, such as FRPs, the resulting strain from the right stretch tensor $\boldsymbol{U}$ does not always coincide with the initial material axis after deformation. For instance the true stress in fiber direction is only achieved, if either the strain is rotated into the material axis coordinate system or the material stiffness itself. The following example demonstrates the problem. Let's assume a hexahedral cube body with unit edge length (see Figure 3.3). If a deformation is applied only along the material axes the deformation gradient $\boldsymbol{F}_1$ equals

$$\boldsymbol{F}_1 = \begin{pmatrix} 1+x & 0 & 0 \\ 0 & 1+y & 0 \\ 0 & 0 & 1+z \end{pmatrix}. \tag{3.11}$$

To calculate the actual material strain (in this case $\boldsymbol{\varepsilon} = \ln \boldsymbol{U}$) a polar decomposition of the deformation gradient needs to be performed. Since $\boldsymbol{C}_\mathrm{F} = \boldsymbol{U}^2$ and $\boldsymbol{C}_\mathrm{F}$ is a function of $\boldsymbol{F}$ (see Equation (3.5)) only the square root of $\boldsymbol{C}_\mathrm{F}$ needs to be calculated to obtain the right stretch tensor $\boldsymbol{U}$. Using the orthogonal relation of the eigenvalues λ_i and eigenvectors $\boldsymbol{v}_i$ a symmetric $N \times N$ matrix can be decomposed as

$$\boldsymbol{C}_\mathrm{F} = \boldsymbol{Q}\boldsymbol{\Lambda}\boldsymbol{Q}^\top, \tag{3.12}$$

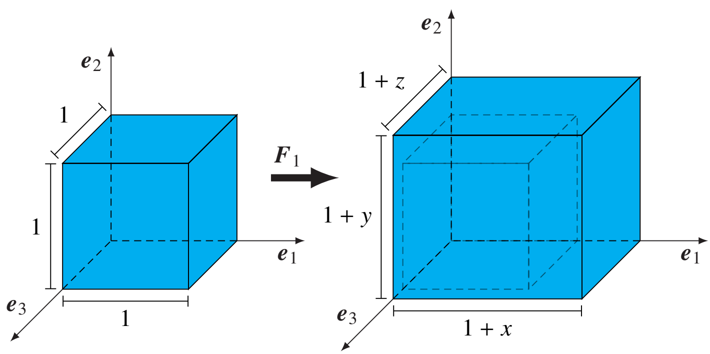

Figure 3.3: Simple deformation along each material axis

where $\boldsymbol{\Lambda} = \operatorname{diag}(\lambda_1, \ldots, \lambda_n)$ and the columns of $\boldsymbol{Q}$ are the eigenvectors $\boldsymbol{v}_i$. Since $\boldsymbol{C}_{\mathrm{F}}$ is symmetric per definition and the square root of a diagonal matrix corresponds to the square root of each value along the diagonal $\sqrt{\boldsymbol{\Lambda}} = \operatorname{diag}\left(\sqrt{\lambda_1}, \ldots, \sqrt{\lambda_n}\right)$ the right stretch tensor $\boldsymbol{U}$ equals

$$\boldsymbol{U} = \sqrt{\boldsymbol{C}_{\mathrm{F}}}^{+} = \boldsymbol{Q}\sqrt{\boldsymbol{\Lambda}}^{+}\boldsymbol{Q}^{\top}. \tag{3.13}$$

It should be noted that only the positive square roots of $\boldsymbol{C}_{\mathrm{F}}$ are taken into account, since the eigenvalues are real and nonnegative and therefore the square roots can be chosen as real and nonnegative. In the same manner as the right stretch tensor $\boldsymbol{U}$ the strain $\boldsymbol{\varepsilon}$ can be calculated by using Equation (3.13)

$$\boldsymbol{\varepsilon} = \ln \boldsymbol{U} = \boldsymbol{Q} \ln\left(\sqrt{\boldsymbol{\Lambda}}^{+}\right)\boldsymbol{Q}^{\top}, \tag{3.14}$$

where the natural logarithm is calculated from the square roots of the eigenvalues of $\boldsymbol{C}_{\mathrm{F}}$.

In the given case of $\boldsymbol{F}_1$ each component on the main diagonal correspond to a square root of each eigenvalue and therefore the only nonzero strain components result to $\varepsilon_{ii} = \ln F_{ii}$. Furthermore, the rigid body motion $\boldsymbol{R}$ results here to identity tensor $\boldsymbol{I}$. Therefore, the material axes remain the same and the strains are also applied only along the material axes.

Now consider a simple shear deformation where the material axis $\boldsymbol{e}_2$ is deformed. The other material axes $\boldsymbol{e}_1$ and $\boldsymbol{e}_3$ remain the same (cf. Figure 3.4). The deformation is defined by the deformation gradient $\boldsymbol{F}_2$

$$\boldsymbol{F}_2 = \begin{pmatrix} 1 & 1/\sqrt{2} & 0 \\ 0 & 1 & 0 \\ 0 & 0 & 1 \end{pmatrix}. \tag{3.15}$$

In this case $\boldsymbol{\Lambda}$ and $\boldsymbol{Q}$ are equal to

$$\boldsymbol{\Lambda}_2 = \begin{pmatrix} 1 & 0 & 0 \\ 0 & 2 & 0 \\ 0 & 0 & 0.5 \end{pmatrix} \quad \text{and} \quad \boldsymbol{Q}_2 = \frac{1}{3}\begin{pmatrix} 0 & \sqrt{3} & -\sqrt{6} \\ 0 & \sqrt{6} & \sqrt{3} \\ 3 & 0 & 0 \end{pmatrix}. \tag{3.16}$$

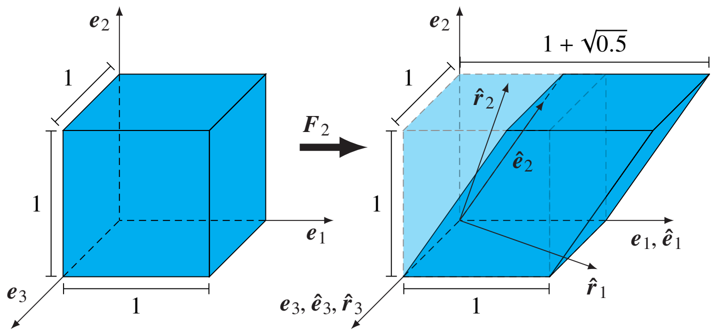

Figure 3.4: Simple shear deformation with resulting material and rigid body coordinate systems

From $\boldsymbol{\Lambda}_2$ and $\boldsymbol{Q}_2$ the left stretch tensor $\boldsymbol{U}_2$ and the rigid body motion $\boldsymbol{R}_2$, by utilizing the relationship $\boldsymbol{R}_2 = \boldsymbol{F}_2\boldsymbol{U}_2{}^{-1}$, are calculated to

$$\boldsymbol{U}_2 = \frac{1}{6}\begin{pmatrix} 4\sqrt{2} & 2 & 0 \\ 2 & 5\sqrt{2} & 0 \\ 0 & 0 & 6 \end{pmatrix} \quad \text{and} \quad \boldsymbol{R}_2 = \frac{1}{6}\begin{pmatrix} 4\sqrt{2} & 2 & 0 \\ -2 & 4\sqrt{2} & 0 \\ 0 & 0 & 6 \end{pmatrix}. \tag{3.17}$$

Now it becomes obvious that the deformed material axis $\hat{\boldsymbol{e}}_2$ corresponds to $\hat{\boldsymbol{e}}_2 = \boldsymbol{F}_2\boldsymbol{e}_2 = (1/\sqrt{2}, 1, 0)^\top$, while the axis $\hat{\boldsymbol{r}}_2$ corresponding to the rigid body motion $\boldsymbol{R}_2$ (and therefore to $\boldsymbol{U}_2$) equals $\hat{\boldsymbol{r}}_2 = \boldsymbol{R}_2\boldsymbol{e}_2 = \left(1/3, 2\sqrt{2}/3, 0\right)^\top$. Thus $\hat{\boldsymbol{e}}_2$ and $\hat{\boldsymbol{r}}_2$ are totally different (cf. Figure 3.4). Another observation is that the axes of $\boldsymbol{R}_2$ are all perpendicular to each other, which is not the case for $\hat{\boldsymbol{e}}_1$ and $\hat{\boldsymbol{e}}_2$. If the strain is now calculated from $\boldsymbol{U}_2$, it does not correspond to the strain along the true physical material axes which has also an effect on the resulting stresses.

The previous observations show that the usage of the HENCKY strain is not useful, if the strain along the deformed material axes of FRPs need to be considered. Further, in contrast to the orthogonal coordinate system of the HENCKY strain, the deformed material axes can create a new nonorthogonal coordinate system. The HENCKY strain and the strain from the deformed material axes correspond only for a special case (cf. example using $\boldsymbol{F}_1$). In such case only the length of the axes change, while the initial axes direction remains the same. For arbitrary deformations the true strain along the current material axes can also be calculated directly. This can be done by calculating the natural logarithm of the length of the deformed material axes $\hat{\boldsymbol{e}}_i$ (cf. example using $\boldsymbol{F}_1$). Note that the initial material axes must have a length of one $\|\boldsymbol{e}_i\| = 1$. In this initial state the strain along the material axes corresponds to $\varepsilon_{ii} = \ln \|\boldsymbol{e}_i\| = \ln 1 = 0$. When the material axes are deformed, the strain along these axes is always known from $\varepsilon_{ii} = \ln \|\hat{\boldsymbol{e}}_i\|$. However, the shear strains cannot be directly calculated from the deformed material axes. Nevertheless, it is possible to obtain the shear strains by using a hypoelastic approach. Here the strain within the material axes frame can be incrementally determined. The following section show the methods to determine the strains based on hypoelastic material behavior and its impact on failure and damage behavior.

3.2.3 Calculation of Strains in a Hypoelastic Material

There are different approaches available to determine the material stress response to a given deformation. For instance constitutive laws for hyperelastic materials define the stress-strain relationship derived from a strain energy density function. As these types of materials undergo large deformations such constitutive laws can reliably predict the stress response. For constutive models using hyperelastic strain, such as Green-Lagrange strain, is defined in the initial configuration and is independent of the increment size. On the other hand hypoelastic materials require incremental steps to ensure the prediction of accurate stress states. A further difference between hyperelastic and hypoelastic materials is the fact that hypoelastic materials are not derived from the strain energy density function, but from the relation between stress rate and strain rate. This also implies that for the same deformation different loading paths are possible between these two material types. Both material types follow the material axes deformation. However, the hypoelastic material models are simpler to be implemented. If failure is initiated and damage occurs, the further loading path is highly dependent on the acting stress. In this case small increments are required to capture the damage evolution. Hypoelastic constitutive laws are capable of considering large deformations and material nonlinearity such as plasticity [130, 131]. Such constitutive equations have been widely used [124, 132–134]. In hypoelastic approaches, the stresses for each increment are given in a rotated objective frame. This type of constitutive laws is based on rate constitutive equations, which are often used in finite element analysis. For instance in Abaqus the Green-Naghdi and Jaumann objective frames are used. Both frames represent the mean values of the actual material axes. Although the usage of mean values within such frames is reasonable for isotropic materials, for direction-dependent materials such as FRPs the strains should be evaluated in the material frame itself. However, the stress objectivity must be kept in order to avoid nonphysical results for large rigid body motions.

Generally speaking for hypoelastic materials a stress rate $\dot{\boldsymbol{\sigma}}$ depends on the strain rate $\dot{\boldsymbol{\varepsilon}}$ by a constitutive stiffness tensor $\mathbb{C}$. The stress rate $\dot{\boldsymbol{\sigma}}$ is defined as the objective derivative which fixes an observer with respect to the material. By this definition the objective stress rate is not affected by rigid body rotations. The relation between stress rate and strain rate can be written as

$$\dot{\boldsymbol{\sigma}} = \mathbb{C} : \dot{\boldsymbol{\varepsilon}}, \tag{3.18}$$

where the stress rate $\dot{\boldsymbol{\sigma}}$ can be obtained by using $\boldsymbol{l}$ as the material rotation matrix

$$\dot{\boldsymbol{\sigma}} = \boldsymbol{l}\left(\frac{\mathrm{d}}{\mathrm{d}t}\left(\boldsymbol{l}^{\top}\boldsymbol{\sigma}\boldsymbol{l}\right)\right)\boldsymbol{l}^{\top} = \mathring{\boldsymbol{\sigma}} + \boldsymbol{\sigma}\boldsymbol{\Omega} - \boldsymbol{\Omega}\boldsymbol{\sigma}. \tag{3.19}$$

Here $\boldsymbol{\sigma}$ defines the Cauchy stress and $\mathring{\boldsymbol{\sigma}}$ its rate. By using $\boldsymbol{\Omega} = \dot{\boldsymbol{R}}\boldsymbol{R}^{\top}$, where $\boldsymbol{R}$ represent the rigid body rotation from the polar decomposition of the deformation gradient, the stress rate $\dot{\boldsymbol{\sigma}}$ corresponds to the Green-Naghdi rate of the Cauchy stress. The rotation of the objective frame is here defined by $\boldsymbol{R}$. On the other hand if $\boldsymbol{\Omega} = \boldsymbol{w}$, where $\boldsymbol{w}$ is the spin tensor, the Jaumann rate of the Cauchy stress is defined.

To calculate the true material strain, each strain increment $\Delta\boldsymbol{\varepsilon}^{(O)}$ defined in the initial coordinate system, is transformed to the corresponding deformed material axes. It should be noted that the initial coordinate system, denoted by (O), coincides with the initial material axes ($\boldsymbol{e}_i^{(O)} = \boldsymbol{e}_i$). The strain increment $\Delta\boldsymbol{\varepsilon}^{(O)}$ is calculated from the incremental left stretch tensor $\Delta\boldsymbol{V}$, which is obtained from polar decomposition of the incremental deformation gradient $\Delta\boldsymbol{F}$

$$\Delta\boldsymbol{\varepsilon}^{(O)} = \ln\Delta\boldsymbol{V} = \ln\sqrt{\Delta\boldsymbol{F}\Delta\boldsymbol{F}^{\top}}. \tag{3.20}$$

The left stretch tensor is used since it defines the stretch of the material body in the initial coordinate system. The incremental deformation gradient itself is obtained from the deformation gradient at the start t and at the end $t + \Delta t$ of the time increment

$$\Delta \boldsymbol{F} = \boldsymbol{F}_{t+\Delta t} \boldsymbol{F}_t^{-1}. \tag{3.21}$$

To transform the strain $\Delta \boldsymbol{\varepsilon}^{(O)}$ to the true material strain $\Delta \boldsymbol{\varepsilon}$ a suitable transformation matrix $\boldsymbol{l}$ is needed. This matrix can be calculated from the initial and the deformed material axes $\boldsymbol{e}_i$ and $\hat{\boldsymbol{e}}_i$. The components of $\boldsymbol{l}$ are defined by the dot product of the target axis with the initial axis

$$l_{ij} = \hat{\boldsymbol{e}}_i \cdot \boldsymbol{e}_j. \tag{3.22}$$

It should be noted that here the vectors $\hat{\boldsymbol{e}}_i$ and $\boldsymbol{e}_j$ are normalized. Otherwise, if the transformation matrix $\boldsymbol{l}$ would be calculated from nonnormalized vectors additional strain would be created. Therefore, $\hat{\boldsymbol{e}}_i$ is defined as follows:

$$\hat{\boldsymbol{e}}_i = \frac{\boldsymbol{F}_{t+\Delta t} \boldsymbol{e}_i}{\|\boldsymbol{F}_{t+\Delta t} \boldsymbol{e}_i\|}. \tag{3.23}$$

The transformation of the strain increment $\Delta \boldsymbol{\varepsilon}$ is achieved by a simple tensor transformation

$$\Delta \varepsilon_{ij} = l_{ik} l_{jl} \Delta \varepsilon_{kl}^{(O)} \quad \text{or} \quad \Delta \boldsymbol{\varepsilon} = \boldsymbol{l} \Delta \boldsymbol{\varepsilon}^{(O)} \boldsymbol{l}^{\top}. \tag{3.24}$$

3.2.3.1 Influence of the Number of Material Axes Used for a Strain Transformation

According to Equation (3.24) all three material axes are used to perform the strain transformation. However, materials such as unidirectional FRPs have only one distinct material orientation. The question arises whether all material axes or only the material-specific ones should be transformed. The necessity of transforming all axes is shown by following example. Consider two different unidirectional laminates with 0° (UD0°) and 90° (UD90°) orientation. Both laminates are applied to simple shear (cf. Figure 3.5). Since unidirectional laminates have one distinct direction, one can assume that transforming the strain only to the fiber direction, while the other directions are perpendicular to the fiber direction, would be sufficient. From observation of the resulting deformation in case of UD0° no fiber strain $\varepsilon_{\mathrm{f}} = 0$ is observed. In contrast, the deformed transverse direction is stretched, which leads to a positive strain

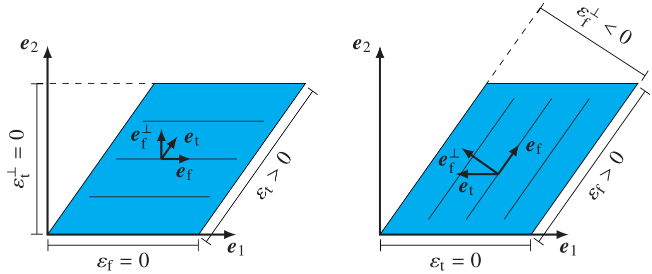

Figure 3.5: Simple shear examples for UD0° (left) and UD90° (right) laminates with corresponding strains

along this material axis $\varepsilon_t > 0$. For the UD90° case it is quite the opposite. On the other hand, strains along the $\boldsymbol{e}_f^\perp$ axis differs considerably. In case of UD0° it yields zero, while for UD90° a negative strain is produced. This phenomenon will result in different stresses which cause different interpretation of the material behavior. In conclusion ε_t and $\varepsilon_f^\perp$ are considerable different for both cases and only ε_t corresponds to the material frame.

Considering only the fiber direction and rotating the strain to this direction has been used in several publications [10–15, 78–80]. In most cases fiber rotation is only considered as an in-plane deformation. Additionally, instead of using the deformed fiber axis, the fiber rotation is expressed as the angle resulting from the current strain state. For instance using the pure geometrical relationship between the applied strain and initial fiber orientation of a ±45° laminate the resulting fiber angle is calculated by

$$\theta = \arctan \frac{1 + \varepsilon_{yy}}{1 + \varepsilon_{xx}}. \tag{3.25}$$

Using a more general case to determine the resulting fiber angle can be expressed by

$$\begin{aligned} \theta = \theta_0 + \arctan \Big(& -\sin(\theta_0)\cos(\theta_0)\left(\varepsilon_{xx} - \varepsilon_{yy}\right) \\ & + \frac{1}{2}\left(\cos^2(\theta_0) - \sin^2(\theta_0)\right)\varepsilon_{xy}\Big) \end{aligned} \tag{3.26}$$

where θ_0 is the initial fiber orientation of the ply. The term inside arc tangent function equals the rotation of the global strains ($\varepsilon_{\mathrm{xx}}$, $\varepsilon_{\mathrm{yy}}$ and $\varepsilon_{\mathrm{xy}}$) to obtain the local shear strain ε_{12}. The assumption to rotate the global strain by a certain angle resulting from the local shear strain is legitimate within an objective frame, since this frame represents the mean values of the material axes. However, several experimental studies [11, 16, 78] reported very high transverse stress σ_{t} for ±45° laminates, if only the fiber axis deformation is considered. At the same time, almost all appearing cracks are perpendicular to the local transverse direction. According to well-established failure criteria, damage models and experimental results for FRPs [72, 135–139] at high transverse stress σ_{t} the occurring failure plane is no longer perpendicular, but rather tilted to the local transverse direction. While knowing this phenomenon for FRPs, the discrepancy between experimentally observed crack direction can be solved by transforming both material axes. In this case the transverse strain ε_{t} for the ±45° laminate remains positive and therefore also the transverse stress σ_{t}.

3.2.3.2 Hypoelastic Strain Dependency on the Number of Increments

The result of rate dependent approaches, such as hypoelastic constitutive laws, are highly affected by the number and length of increments to reach a specific deformation. Generally the result of a rate dependent constitutive law is dependent on the grade of deformation itself. Large deformations need more increments to achieve accurate results. If no rigid body motion occurs, the results within the objective frame are not affected by the number of increments. However, as soon as shear strains occur, a certain number of increments are needed to achieve reliable results. To quantify a certain number is difficult because of the high conjunction with the deformation itself. Nevertheless, a range of necessary number of increments can be estimated for specific cases such as simple shear alone or with superimposed tension. The following in-plane deformations are evaluated

$$\boldsymbol{F}_{\mathrm{sh}} = \begin{pmatrix} 1 & 0 \\ 1 & 1 \end{pmatrix} \quad \text{and} \quad \boldsymbol{F}_{\mathrm{tsh}} = \begin{pmatrix} 2 & 0 \\ 1 & 1 \end{pmatrix}, \tag{3.27}$$

where sh denotes simple shear and tsh denotes tension with simple shear. The influence of the number of increments N for both deformations is evaluated for $N = \{1, 2, 10, 20, 50, 100, 1000\}$. For the strain components ε_{11} and ε_{22}

an exact solution can be calculated via $\varepsilon_{ii} = \ln\|\boldsymbol{F}\boldsymbol{e}_i\|$. The results of each strain component from $\boldsymbol{F}_{\mathrm{sh}}$ and $\boldsymbol{F}_{\mathrm{tsh}}$ are shown in Figure 3.6. The given deformation results at very high strain (cf. $\varepsilon_{11} = 0.7$ for $\boldsymbol{F}_{\mathrm{tsh}}$). These examples are specifically chosen to evaluate the convergence of the strain components for large deformations. For smaller deformations the convergence of the strain components will require a lower number of increments, since the axes rotations are also smaller. From the results it can be inferred that the hypoelastic strains itself are a source of nonlinear behavior of the material (cf. ε_{11} for $\boldsymbol{F}_{\mathrm{sh}}$). Further, the evaluated deformations converge above a certain number of increments to the exact solutions. Depending on the required accuracy of each strain component it can be derived that in case of simple shear only $\boldsymbol{F}_{\mathrm{sh}}$ the highest number of increments $N = 1000$ are needed to achieve convergence of the strain component ε_{22}. All other strain components require only 50 to 100 number of increments to achieve convergence. But even for small number of increments (e.g., at $N = 10$) the accuracy of the strain components, besides ε_{22} from $\boldsymbol{F}_{\mathrm{sh}}$, are very high. From the results of ε_{12} at $\boldsymbol{F}_{\mathrm{sh}}$ and ε_{11} at $\boldsymbol{F}_{\mathrm{tsh}}$ it can be also observed that in some cases the convergence is almost not effected by the number of increments. Additionally, it should be noted that the results are not affected by the chosen objective frame. However, to transform the Green-Naghdi or Jaumann strain increments, the knowledge of the rotated frame is needed. Since the strain increments of both objective frames are derived from the same strain increment $\Delta\boldsymbol{\varepsilon}^{(O)}$, the calculation of the hypoelastic strains would only result in a higher computational effort compared to the direct transformation of the strain increment $\Delta\boldsymbol{\varepsilon}^{(O)}$ itself. In conclusion, it can be recommended to perform a study for a given deformation to determine the necessary number of increments. In this work all numerical simulations are performed with at least 100 increments.

3.2.3.3 Resulting Errors from an Inaccurate Incrementation of the Transformed Strain

The calculation of resulting stresses of constitutive laws can be defined in two ways. The first option is by using each strain increment $\Delta\boldsymbol{\varepsilon}$ to compute the corresponding stress increment $\Delta\boldsymbol{\sigma}$, which is added to the stress $\boldsymbol{\sigma}_t$ to obtain the resulting stress $\boldsymbol{\sigma}_{t+\Delta t}$ at the end of the increment. This option correspond to the stress response using a hypoelastic approach. The second way uses directly the total strain $\boldsymbol{\varepsilon}_{t+\Delta t}$ to compute the resulting stress $\boldsymbol{\sigma}_{t+\Delta t}$. Such

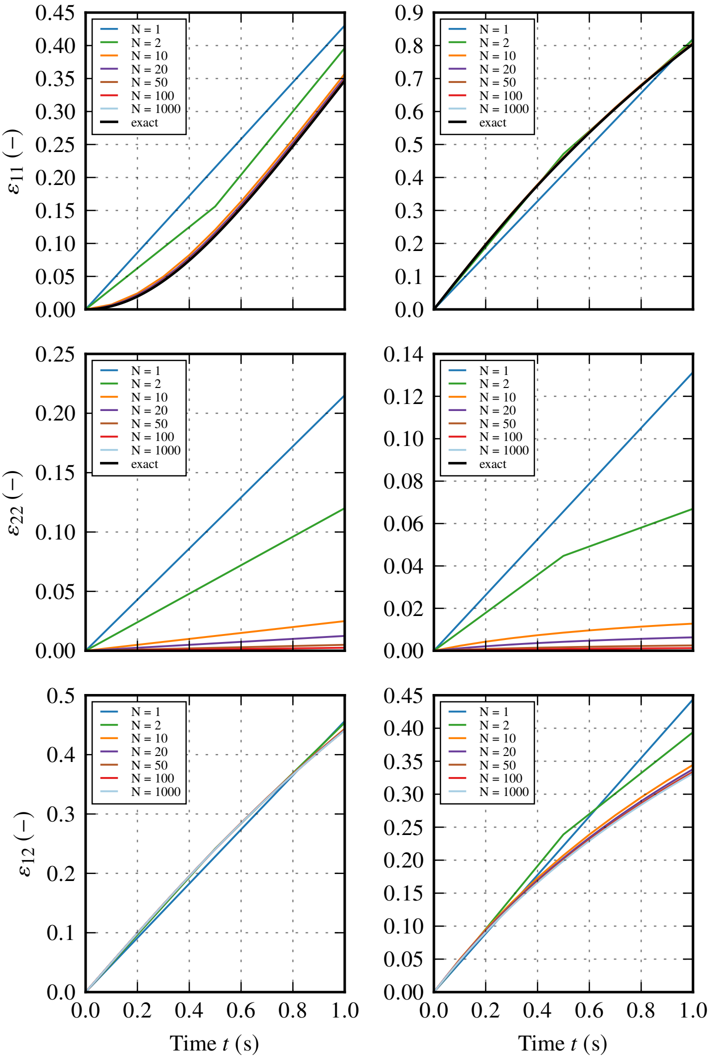

Figure 3.6: Resulting strain components ε_{11}, ε_{22} and ε_{12} at different number of increments for the deformations $\boldsymbol{F}_{\text{sh}}$ (simple shear, left) and $\boldsymbol{F}_{\text{tsh}}$ (tension with simple shear, right)

way represents the hyperelastic modeling approach. However, by using a rate dependent approach to consider material axes rotations, huge errors can arise by an inaccurate incrementation of the strain and therefore also the stress. For example, Badel et al. [133] analyzed two different approaches to accumulate stresses of hypoelastic constitutive equations. In their study the rotation of the fiber material axis is considered, while the other material axes are perpendicular to the fiber direction, which corresponds to the Green-Naghdi frame. The first approach updates stresses of the rotated Green-Naghdi frame via

$$\boldsymbol{\sigma}_{t+\Delta t}^{(\mathrm{GN})} = \boldsymbol{\sigma}_{t}^{(\mathrm{GN})} + \boldsymbol{T}^{(\mathrm{f})}\boldsymbol{C}\boldsymbol{T}^{(\mathrm{f})\top}\Delta\boldsymbol{\varepsilon}^{(\mathrm{GN})}, \tag{3.28}$$

where $\boldsymbol{T}^{(\mathrm{f})}$ defines the 6×6 transformation matrix to the fiber direction and $\boldsymbol{C}$ the stiffness matrix for a transversely isotropic material. In this case only the material stiffness is rotated to the fiber direction. Besides the Green-Naghdi frame also the Jaumann frame can be used in the same way to determine the resulting stress. The second approach uses a rotated frame defined by the fiber direction itself. Here the stress of the objective Green-Naghdi frame are obtained from the transformed stress of the fiber-parallel frame. This stress update procedure is defined by the following equation

$$\boldsymbol{\sigma}_{t+\Delta t}^{(\mathrm{GN})} = \boldsymbol{b}^{\top}\boldsymbol{\sigma}_{t+\Delta t}^{(\mathrm{f})}\boldsymbol{b} = \boldsymbol{b}^{\top}\left(\boldsymbol{\sigma}_{t}^{(\mathrm{f})} + \boldsymbol{C}\boldsymbol{b}\Delta\boldsymbol{\varepsilon}^{(\mathrm{GN})}\boldsymbol{b}^{\top}\right)\boldsymbol{b}, \tag{3.29}$$

where $\boldsymbol{b}$ is the transformation matrix from the Green-Naghdi frame to the fiber direction and $\boldsymbol{\sigma}^{(\mathrm{f})}$ denotes the stress in the fiber-parallel frame. It should be noted that the transformation matrix $\boldsymbol{T}^{(\mathrm{f})}$ is derived from $\boldsymbol{b}$. Both approaches have been applied to four different load cases with varying fiber orientation. The load cases are summarized in Figure 3.7. All loads have been applied to a unit cube where the fiber orientation corresponds to one axis of the cube. Since only the fiber stress should be evaluated, all materials constants besides the fiber direction modulus has been set to zero. The resulting stresses of both approaches have been evaluated regarding their feasibility. Since only the modulus in fiber direction is used, only the fiber stress should be present at the end of each load case. Using the first approach, rotation the stiffness to the fiber direction, the load cases (a) and (b) lead to feasible results. However, both other load cases (c) and (d) lead to transverse and shear stresses which are spurious stresses. On the other hand the second approach, rotation of the fiber frame stresses, leads in all cases to satisfying results. Therefore, only the incrementation within the fiber-parallel frame is reliable for evaluating rotated

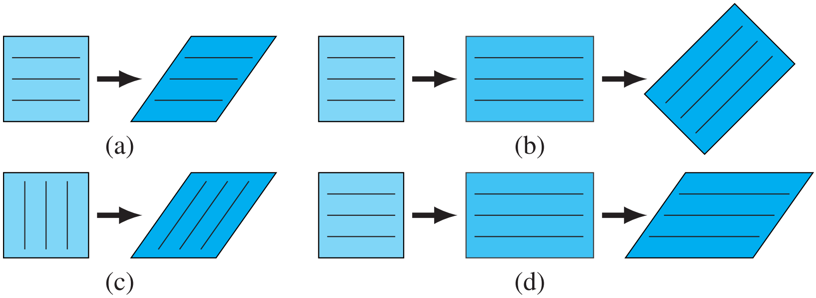

Figure 3.7: Four different load cases according to [133]: UD0° simple shear (a), UD0° tension and rigid body rotation (b), UD90° simple shear (c) and UD0° tension and simple shear (d)

fiber stress. According to Badel et al. the inaccuracy of the first approach arise from the initial stress $\boldsymbol{\sigma}_t^{(\mathrm{GN})}$. Here the rotation of rigid body $\boldsymbol{R}$, which correspond to the Green-Naghdi frame, differs from the fiber frame $\boldsymbol{b}$. The erroneous stresses at the end of the load cases are only resolved if both frames are equal $\boldsymbol{R} = \boldsymbol{b}$.

Both approaches have been also used in several publications [12, 79, 80, 140–142] by rotating the total strain $\boldsymbol{\varepsilon}_{t+\Delta t}$ to the fiber direction, instead of using the strain increment. However, if the total strain is used to calculate fiber-parallel stress $\boldsymbol{\sigma}_{t+\Delta t}$ a similar error, compared to the first approach used by Badel et al. (cf. Equation (3.28)), occur in both cases. Since the error is equal for both approaches the source of this error is shown based on the fiber frame approach. In this case the fiber-parallel stress can be expressed as

$$\boldsymbol{\sigma}_{t+\Delta t}^{(\mathrm{f})} = \boldsymbol{C}\boldsymbol{\varepsilon}_{t+\Delta t}^{(\mathrm{f})} = \boldsymbol{C}\boldsymbol{b}\boldsymbol{\varepsilon}_{t+\Delta t}^{(\mathrm{GN})}\boldsymbol{b}^{\top}. \tag{3.30}$$

The transformation of the fiber parallel stress $\boldsymbol{\sigma}^{(\mathrm{f})}$ to the Green-Naghdi frame is conducted according to Equation (3.29). Here the total strain can be split up into the initial strain $\boldsymbol{\varepsilon}_t^{(\mathrm{GN})}$ and the strain increment $\Delta\boldsymbol{\varepsilon}^{(\mathrm{GN})}$. If the latter expression is expanded, then the rotation matrix $\boldsymbol{b}$ will be also applied to the initial strain

$$\boldsymbol{\sigma}_{t+\Delta t}^{(\mathrm{f})} = \boldsymbol{C}\boldsymbol{b}\boldsymbol{\varepsilon}_{t+\Delta t}^{(\mathrm{GN})}\boldsymbol{b}^{\top} = \boldsymbol{C}\boldsymbol{b}\boldsymbol{\varepsilon}_{t}^{(\mathrm{GN})}\boldsymbol{b}^{\top} + \boldsymbol{C}\boldsymbol{b}\Delta\boldsymbol{\varepsilon}^{(\mathrm{GN})}\boldsymbol{b}^{\top}. \tag{3.31}$$

However, the rotation matrix $\boldsymbol{b}$ rotates the initial strain $\boldsymbol{\varepsilon}_t^{(\mathrm{GN})}$ from the *current* Green-Naghdi frame to the fiber-parallel frame. As the initial deformation at t can have a different rigid body rotation, compared to the rigid body rotation in the current increment $t+\Delta t$, this will lead to an incorrect strain accumulation in the current increment. This means that the definition of the rotation matrix $\boldsymbol{b}$ is not suited to be applied to the initial total strain $\boldsymbol{\varepsilon}_t^{(\mathrm{GN})}$. Using the total strain will correspond to the hypoelastic approach with only one increment (cf. Figure 3.6).

Since in the present work not only the fiber axis but all material axes are transformed to the nonorthogonal fiber-parallel frame, special care needs to be taken for the forward and backward transformation of the strain and stress. In general a rotation from one orthogonal coordinate system to another using the rotation matrix $\boldsymbol{R}$ satisfies the condition $\boldsymbol{R}^{-1} = \boldsymbol{R}^{\top}$. For example, if the strain increment is rotated forward from the origin frame (O) to the rotated frame (R) ($\Delta\boldsymbol{\varepsilon}^{(R)} = \boldsymbol{R}\Delta\boldsymbol{\varepsilon}^{(O)}\boldsymbol{R}^{\top}$), then the backward rotation of the corresponding stress can be performed by using the inverse or transposed rotation matrix ($\Delta\boldsymbol{\sigma}^{(O)} = \boldsymbol{R}^{\top}\Delta\boldsymbol{\sigma}^{(R)}\boldsymbol{R}$). However, this is not the case for nonorthogonal (curvilinear) coordinate systems, which is obvious the case by using all deformed material axes as the material frame. By using the relation between co- and contravariant vectors from Equation (3.7) and the condition that the transformation matrix should not add any stretch to the deformed vectors, results in definition of a transformation matrix according to Equation (3.22) by utilizing the normalized deformed vectors from Equation (3.23). Since the stress tensor σ^{ij} is a contravariant second-order tensor, it is connected to the covariant strain tensor ε_{kl}, according to Hooke's law, by the stiffness tensor C^{ijkl} ($\sigma^{ij} = C^{ijkl}\varepsilon_{kl}$) or the other way around by the compliance tensor S_{klij} ($\varepsilon_{kl} = S_{klij}\sigma^{ij}$). The stiffness and the compliance tensor are both forth-order tensors. Using the relationship between the strain and stress tensors and also the relation between co- and contravariant vectors, the transformation rules and the resulting constitutive equation using a nonorthogonal material frame is summarized and visualized in Figure 3.8. For a reliable determination of the strains and stresses in the fiber-parallel frame, the following approach has been chosen in the present work:

- First the deformed normalized material axes $\hat{\boldsymbol{e}}_i$ and the corresponding transformation matrix $\boldsymbol{l}$ is determined from the deformation gradient

$$
\begin{tikzcd}[column sep=huge, row sep=huge]
\boldsymbol{e}_i, \Delta\boldsymbol{\varepsilon}^{(O)} \arrow[r, shift left, "\boldsymbol{l}"] & \hat{\boldsymbol{e}}_i, \Delta\boldsymbol{\varepsilon}^{(\mathrm{f})} \arrow[l, shift left, "\boldsymbol{l}^{-1}"] \arrow[d, shift right, "\boldsymbol{C}"'] \\
\boldsymbol{e}^i, \Delta\boldsymbol{\sigma}^{(O)} \arrow[r, shift right, "\boldsymbol{l}^{-\top}"'] & \hat{\boldsymbol{e}}^i, \Delta\boldsymbol{\sigma}^{(\mathrm{f})} \arrow[l, shift right, "\boldsymbol{l}^{\top}"'] \arrow[u, shift right, "\boldsymbol{S}"']
\end{tikzcd}
$$

Figure 3.8: Transformation procedure for normalized curvilinear vectors and the corresponding constitutive equation

$\boldsymbol{F}_{t+\Delta t}$ at the end of the increment $t + \Delta t$ (see Equations (3.22) and (3.23)).

- Next the strain increment $\Delta\boldsymbol{\varepsilon}^{(O)}$ based on the incremental left stretch tensor $\Delta\boldsymbol{V}$ is obtained from the deformation gradient increment $\Delta\boldsymbol{F}$ (see Equations (3.20) and (3.21)).
- Utilizing the strain increment $\Delta\boldsymbol{\varepsilon}^{(O)}$ and the transformation matrix $\boldsymbol{l}$, the strain increment $\Delta\boldsymbol{\varepsilon}^{(\mathrm{f})}$ in the material axes frame is calculated (see Equation (3.24)).
- The total strain $\boldsymbol{\varepsilon}^{(\mathrm{f})}_{t+\Delta t}$ is obtained from the initial strain $\boldsymbol{\varepsilon}^{(\mathrm{f})}_{t}$ in the material axes frame and the current strain increment $\Delta\boldsymbol{\varepsilon}^{(\mathrm{f})}$. It should be noted that the initial strain is equal to zero prior to the first deformation. After the first increment the total strain needs to be stored for the calculation of the next increment.
- From the total strain $\boldsymbol{\varepsilon}^{(\mathrm{f})}_{t+\Delta t}$ the resulting material stress $\boldsymbol{\sigma}^{(\mathrm{f})}_{t+\Delta t}$ is determined by utilizing the material stiffness $\boldsymbol{C}$.
- Finally, the material stress $\boldsymbol{\sigma}^{(\mathrm{f})}_{t+\Delta t}$ is transformed back to the stress of the original frame $\boldsymbol{\sigma}^{(O)}_{t+\Delta t}$ by using the transposed transformation matrix $\boldsymbol{l}^{\top}$

It should be noted that Abaqus provides the deformation gradient only for nonlinear calculations (Nlgeom=On). In this case an objective frame (Green-Naghdi or Jaumann) is used. Therefore, special care needs to be taken as the stress needs to be provided in the correct frame. In this work the parameters for the solver are set in a way, that the resulting stress should always be transformed to the global coordinate system.

3.2.3.4 Influence of the of Hypoelastic Material Modeling on the Failure and Damage Behavior

If the strain from a hypoelastic material model is used, the failure initiation and the damage behavior are highly affected by the material axes. This condition has a significant effect on the interpretation of failure and damage propagation from experimental results. To demonstrate the effect on the failure resulting from using hypoelastic strain compared to a Green-Naghdi strain, the stress of an isotropic material is determined and the von Mises stress is evaluated. The examples of a simple shear and a tension-superposed simple shear test from Section 3.2.3.2 are used as load cases to analyze the effect of the hypoelastic strain. To achieve an accurate result for the hypoelastic strain the number of increments is set to $N = 1000$. To calculate the isotropic material stiffness a Young's modulus $E = 3\,\mathrm{GPa}$ and a Poisson's ratio $\nu = 0.3$ is used. The resulting von Mises stress for the Green-Naghdi frame and the material axes frame ($\sigma_{\mathrm{vm}}^{(\mathrm{GN})}$ and $\sigma_{\mathrm{vm}}^{(\mathrm{f})}$) and the ratio $\sigma_{\mathrm{vm}}^{(\mathrm{f})}/\sigma_{\mathrm{vm}}^{(\mathrm{GN})}$ are shown in Figure 3.9. For both examples the usage of hypoelastic strains lead to an increase of the von Mises stress. If this circumstance is taken into account the failure initiation for a certain failure stress is reached earlier compared to the von Mises stress resulting in the Green-Naghdi frame. It is particularly remarkable that this condition applies to isotropic direction-independent materials. It should be noted that the ratio $\sigma_{\mathrm{vm}}^{(\mathrm{f})}/\sigma_{\mathrm{vm}}^{(\mathrm{GN})}$ is dependent on the deformation itself. Isotropic materials with intrinsically brittle material behavior, such as an epoxy matrix system, tend to a sudden failure which complicates the analysis of the damage behavior in conjunction with hypoelastic strains. A transversely isotropic material with the same brittle matrix system can sustain cracks within the matrix transverse to the fiber direction. The increase of the crack density of ±45° and ±50° laminates is evaluated by Taubert [78] based on the material IM7-8552. It is found that the first cracks appear for the ±45° laminate at 2 ‰ and for the ±50° laminate at 1.3 ‰ strain in specimen direction. With increasing strain the crack density rises and additionally, according to Mandel [11], the fiber direction also changes. For example, for the ±45° laminate the rotation of the fiber from 0 ‰ to 2 ‰ strain equals to 1.1°, but at failure the total fiber

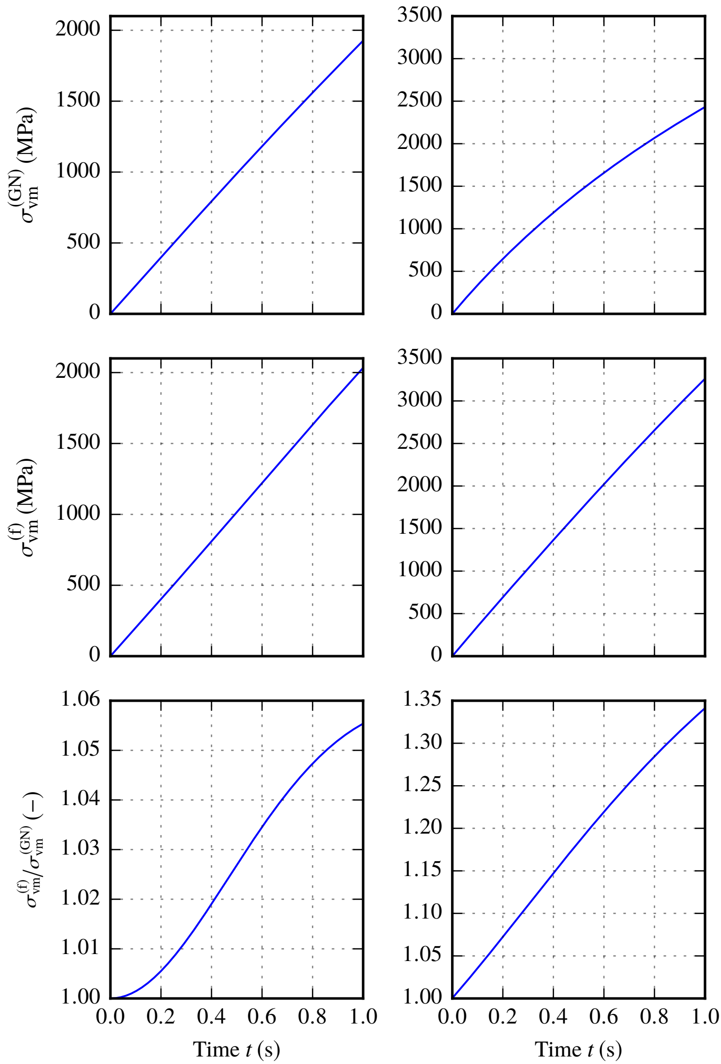

Figure 3.9: Comparison of von Mises stress in the Green-Naghdi frame, the material axes frame and the ratio of both values for two different load cases, simple shear (left) and simple shear with tension (right)

rotation reach 7.8°. The difference of additional 6.7° in fiber rotation need to be taken into account during damage propagation. This condition reveals the benefit of using a hypoelastic (or hyperelastic) model within deformed material axes rather than using strain in an orthogonal coordinate system.

3.3 Constitutive Matrix Model

The capabilities of micro or meso mechanical simulations allow analyzing and understanding the material behavior of composites more precisely. At this modeling levels, fiber (or roving) and matrix need to be modeled separately. Therefore, a constitutive model is developed for each constituent. In this section the material model for the matrix is described. The model captures viscoplastic material behavior and during damage evolution it can distinguish between damage caused by tension or compression. The presented viscoplastic material is based on a published plasticity model [143–146] which is extended by strain-rate dependency [147, 148]. The viscoplastic model is combined with a failure initiation utilizing the yield surface proposed by Tschoegel [149] and a damage surface [150]. Although the failure criterion cannot distinguish between tensile and compressive failure, the damage model used can do so by decomposing the stress. In total the combined model covers all major aspects of the matrix material behavior. As described in Section 3.2 the strain measure is crucial for an accurate and physical reliable result of the material stress. Therefore, the hypoelastic model is used to determine the resulting material stress of the matrix. In the following the used strain is always defined in the material axes.

3.3.1 Elasto-Viscoplasticity Model

In general isotropic polymer matrix systems tend to develop a nonlinear stress response over an increasing load. Such material behavior can be captured sufficient by plasticity models if no damage is present. There are several plasticity models available for different kind of materials. A more detailed overview and the phenomenological aspects of the plasticity theory are given in [151, 152]. Furthermore, if a time dependency of the material is present, which is the case for polymers, this behavior can be modeled by using time dependent viscous models. For such a case two major model types are commonly used: viscoelastic or viscoplastic models. As the name suggests viscoelastic covers the elastic region of the material by additionally considering the time dependency. On the other hand viscoplastic can capture permanent deformations within the material. A combination of both model types is also possible. The difference between both approaches can be observed during the unloading phase. For a pure elastic-viscoplastic approach the stress response during unloading is linear. In combination with a viscoelastic model, a time dependent nonlinear stress response is possible. An example for a pure viscoplastic material response is given in Figure 3.10.

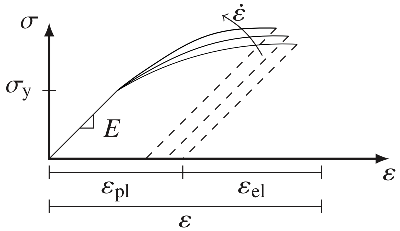

Figure 3.10: Example for a viscoplastic material behavior of uniaxial tensile test

3.3.1.1 Elastic Behavior

Assuming linear elastic material behavior of isotropic materials, the relationship between the stress tensor $\boldsymbol{\sigma}$ and elastic strain tensor $\boldsymbol{\varepsilon}_{\mathrm{el}}$ is defined by

$$\boldsymbol{\sigma} = \mathbb{C} : \boldsymbol{\varepsilon}_{\mathrm{el}} \tag{3.32}$$

where $\mathbb{C}$ is the fourth order material elasticity tensor. For isotropic materials the elasticity tensor can be defined by only two distinct material property constants. Dependent on the constitutive model this two constants can be defined in terms of Lamé parameters μ and λ, in terms of bulk modulus K and shear modulus G or in terms of engineering constants Young's modulus E and Poisson's ratio ν. Using bulk modulus K and shear modulus G the linear elastic stress tensor can also be defined as follows

$$\boldsymbol{\sigma} = 2G\boldsymbol{\varepsilon}_{\mathrm{dev}} + 3K\varepsilon_{\mathrm{vol}}\boldsymbol{I} \tag{3.33}$$

where $\boldsymbol{\varepsilon}_{\text{dev}}$ represents the deviatoric strain tensor, $\varepsilon_{\text{vol}} = {}^1\!/\!{}_3 tr(\boldsymbol{\varepsilon}_{\text{el}})$ is the volumetric strain and $\boldsymbol{I}$ is the identity tensor. If the material elasticity tensor $\mathbb{C}$ is used instead it can be expressed in index notation as follows

$$C_{ijkl} = 2GI^{\text{dev}}_{ijkl} + K\delta_{ij}\delta_{kl} \tag{3.34}$$

with

$$I^{\text{dev}}_{ijkl} = I^{\text{s}}_{ijkl} - \frac{1}{3}\delta_{ij}\delta_{kl} \quad \text{and} \quad I^{\text{s}}_{ijkl} = \frac{1}{2}\left(\delta_{ik}\delta_{jl} + \delta_{il}\delta_{jk}\right). \tag{3.35}$$

3.3.1.2 Yield Function

During loading, besides elastic strain $\boldsymbol{\varepsilon}_{\text{el}}$, plastic strain can occur (cf. Figure 3.10). In such case at a specific stress σ_{y} yielding of the material begins. From this point the plastic strain increases and to determine the resulting material stress the elastic strain must be known. To obtain the current elastic strain the total strain can be decomposed in its elastic and plastic part

$$\boldsymbol{\varepsilon} = \boldsymbol{\varepsilon}_{\text{el}} + \boldsymbol{\varepsilon}_{\text{pl}}. \tag{3.36}$$

The elastic and the plastic part of the total strain under uniaxial load can be directly determined from the stress-strain curve by knowledge of the Young's modulus. However, to determine the acting plastic strain in a three-dimensional space a yield surface Φ_{pl} and the corresponding plastic flow rule $\boldsymbol{N}_{\text{pl}}$ must be defined. In general the yield surface must satisfy the condition:

$$\Phi_{\text{pl}}\left(\boldsymbol{\sigma}, \boldsymbol{q}\right) = 0, \tag{3.37}$$

where $\boldsymbol{q}$ defines the hardening variables. This surface defines the elastic region for $\Phi_{\text{pl}} < 0$, and at $\Phi_{\text{pl}} = 0$ each point on the surface corresponds to plastic region. A suitable definition of the yield surface is dependent on the material itself. There are several yield surfaces which have been developed in past century. Among others the Mohr-Coulomb, Tresca, von Mises or Drucker-Prager are the most well-known yield criteria. From experimental studies [41, 153–157] it is observed that for epoxy polymers the uniaxial tension and compression strength differ. This condition indicates that epoxy materials have a hydrostatic pressure dependency which also affects the yielding. Therefore, yield criteria which have no hydrostatic pressure dependency, such as TRESCA or VON MISES, are not suited for epoxy materials. Additionally, yielding can be strain rate dependent and need to be considered by the yield criteria. In his work, MELRO [143] concludes that a good yield criterion for epoxy polymers must have the following characteristics:

- Hydrostatic pressure dependency - allows considering yielding at different stress states.
- Different yield strengths in tension and compression - enables failure prediction for epoxy materials.
- Strain rate dependency - considering change of the yield surface based on the strain rate.

Although yield criteria such as MOHR-COULOMB or DRUCKER-PRAGER meet the requirements, special care must be taken because these surfaces are not free of edges or vertices. This condition creates difficulties since they are not differentiable in all of its domain and therefore the implementation into a constitutive model is more complex. To avoid such inconvenience based on experimental observations FIEDLER [41, 155] suggests the usage of a paraboloidal criterion. A parabolic shaped expression of a yield or failure criterion is first introduced by TSCHOEGEL [149]. This criterion is a quadratic modified version of the VON MISES criterion and is defined as

$$\Phi_{\mathrm{pl}} = 6J_2 + 2I_1\left(\sigma_{\mathrm{c}} - \sigma_{\mathrm{t}}\right) - 2\sigma_{\mathrm{c}}\sigma_{\mathrm{t}} = 0 \tag{3.38}$$

where J_2 is the second invariant of the deviatoric stress tensor, I_1 is the first invariant of the stress tensor and $\sigma_{\mathrm{t,c}}$ are the yield functions or failure strengths in tension and compression, respectively. If the strengths σ_{c} and σ_{t} are equal the expression is reduced to a VON MISES criterion. A visualization of this criterion is shown in Figure 3.11. An intensive study for different polymer materials using this criterion is performed by RAGHAVA et al [158]. In general, an excellent agreement with experimental results is found using such paraboloidal criterion. Using the yield surface the resulting plastic strain can be derived. To do so two different ways are possible using an associative or nonassociative flow rule. In the next section it is shown that only a nonassociative flow rule leads to feasible results.

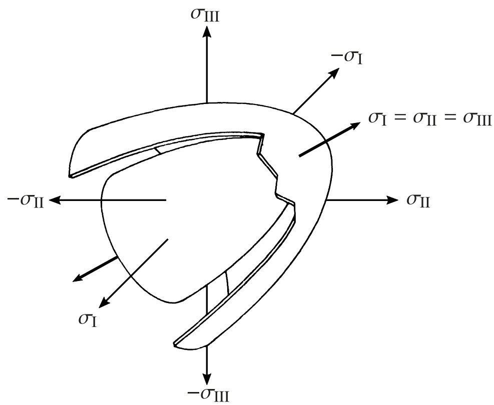

Figure 3.11: Paraboloidal yield (inner surface) and failure (outer surface) criterion in the principal stress space according to TSCHOEGEL [149]

3.3.1.3 Plastic Flow Rule

If a stress state exceeds the yield surface $\Phi_{\mathrm{pl}} > 0$ a return mapping scheme needs to be solved to satisfy the condition $\Phi_{\mathrm{pl}} = 0$. In order to perform the return mapping the actual plastic strain needs to be determined. Based on the current stress state $\boldsymbol{\sigma}$ the flow tensor $\boldsymbol{N}_{\mathrm{pl}}$, which defines the direction of the plastic flow, can be directly obtained from the yield surface:

$$\boldsymbol{N}_{\mathrm{pl}} = \frac{\partial \Phi_{\mathrm{pl}}}{\partial \boldsymbol{\sigma}} = 6\boldsymbol{\sigma}_{\mathrm{dev}} + 2\left(\sigma_{\mathrm{c}} - \sigma_{\mathrm{t}}\right)\boldsymbol{I}, \tag{3.39}$$

where $\boldsymbol{\sigma}_{\mathrm{dev}}$ is the deviatoric stress tensor, $\boldsymbol{I}$ is the identity tensor and σ_{t} and σ_{c} are the yield stresses in tension and compression direction, respectively. By using such definition of the flow tensor, an associative flow rule of the plastic strain increment is given by

$$\Delta\boldsymbol{\varepsilon}_{\mathrm{pl}} = \Delta\lambda_{\mathrm{pl}}\boldsymbol{N}_{\mathrm{pl}} = \Delta\lambda_{\mathrm{pl}}\frac{\partial \Phi_{\mathrm{pl}}}{\partial \boldsymbol{\sigma}}, \tag{3.40}$$

where $\Delta\lambda_{\mathrm{pl}}$ is the plastic multiplier which defines the length of the flow tensor. Since $\boldsymbol{N}_{\mathrm{pl}}$ is self-dependent on $\Delta\boldsymbol{\varepsilon}_{\mathrm{pl}}$ the backward Euler scheme is being used to solve such an equation. More important is that $\Delta\lambda_{\text{pl}}$ in conjunction with the yield surface Φ_{pl} satisfies the condition for the plastic domain

$$\Delta\lambda_{\text{pl}}\Phi_{\text{pl}} = 0. \tag{3.41}$$

If the stress state does not exceed the yield surface $\Phi_{\text{pl}} < 0$, the plastic multiplier results to $\Delta\lambda_{\text{pl}} = 0$. Further, since the direction of the plastic flow is defined by flow tensor $\boldsymbol{N}_{\text{pl}}$, this leads to the condition $\Delta\lambda_{\text{pl}} \geq 0$. These conditions are known as the KUHN-TUCKER conditions, which define the evolution of the plastic domain

$$\Phi_{\text{pl}} \leq 0, \quad \Delta\lambda_{\text{pl}} \geq 0 \quad \text{and} \quad \Delta\lambda_{\text{pl}}\Phi_{\text{pl}} = 0. \tag{3.42}$$

If an associative flow rule is used special care needs to be taken since non-physical results can occur. As shown by MELRO if the associative flow rule given in Equation (3.40) is used in conjunction with hydrostatic pressure $\sigma_{11} = \sigma_{22} = \sigma_{33} < 0$, the resulting plastic strain $\Delta\boldsymbol{\varepsilon}_{\text{pl}}$ leads to values greater zero which seems to be not feasible for negative stress values. Therefore, a nonassociative flow potential proposed by [144–146] is used

$$g_{\text{pl}} = \sqrt{\sigma_{\text{vm}}^2 + \alpha p^2}, \tag{3.43}$$

where σ_{vm} is the VON MISES stress, p is the hydrostatic stress and α controls plastic volumetric flow. The corresponding flow rule is then defined as

$$\begin{aligned} \Delta\boldsymbol{\varepsilon}_{\text{pl}} &= \Delta\lambda_{\text{pl}}\frac{\partial g_{\text{pl}}}{\partial\boldsymbol{\sigma}} = \Delta\lambda_{\text{pl}}\frac{\partial\sqrt{\sigma_{\text{vm}}^2 + \alpha p^2}}{\partial\boldsymbol{\sigma}} \\ &= \frac{\Delta\lambda_{\text{pl}}}{2g_{\text{pl}}}\left(2\sigma_{\text{vm}}\frac{\partial\sigma_{\text{vm}}}{\partial\boldsymbol{\sigma}} + 2\alpha p\frac{\partial p}{\partial\boldsymbol{\sigma}}\right) = \frac{\Delta\lambda_{\text{pl}}}{2g_{\text{pl}}}\left(3\boldsymbol{\sigma}_{\text{dev}} - \frac{2}{3}\alpha p\boldsymbol{I}\right). \end{aligned} \tag{3.44}$$

The parameter α can be determined from a uniaxial load. In such a case the stress tensor, the corresponding deviatoric stress tensor and the hydrostatic stress result to

$$\boldsymbol{\sigma} = \begin{pmatrix} \sigma & 0 & 0 \\ 0 & 0 & 0 \\ 0 & 0 & 0 \end{pmatrix}, \quad \boldsymbol{\sigma}_{\text{dev}} = \begin{pmatrix} \frac{2}{3}\sigma & 0 & 0 \\ 0 & -\frac{1}{3}\sigma & 0 \\ 0 & 0 & -\frac{1}{3}\sigma \end{pmatrix} \quad \text{and} \quad p = -\frac{\sigma}{3}. \tag{3.45}$$

For a uniaxial tensile load the acting stress σ is positive and the nonassociative flow potential yields

$$g_{\mathrm{pl}} = \sigma\sqrt{1 + \frac{\alpha}{9}}. \tag{3.46}$$

Substituting these results into the nonassociative flow rule the plastic strain is given as

$$\Delta\boldsymbol{\varepsilon}_{\mathrm{pl}} = \Delta\lambda_{\mathrm{pl}}\frac{1}{2\sqrt{1 + \alpha/9}}\left(\begin{pmatrix} 2 & 0 & 0 \\ 0 & -1 & 0 \\ 0 & 0 & -1 \end{pmatrix} + \frac{2\alpha}{9}\begin{pmatrix} 1 & 0 & 0 \\ 0 & 1 & 0 \\ 0 & 0 & 1 \end{pmatrix}\right). \tag{3.47}$$

Since for a uniaxial tension load in isotropic material the plastic strain in transverse direction is defined by

$$\Delta\varepsilon_{\mathrm{pl}_{22}} = \Delta\varepsilon_{\mathrm{pl}_{33}} = -\nu_{\mathrm{pl}}\Delta\varepsilon_{\mathrm{pl}_{11}}, \tag{3.48}$$

where ν_{pl} is the plastic Poisson's ratio, the volumetric plastic strain $\Delta\varepsilon_{\mathrm{pl}_{\mathrm{vol}}} = tr(\Delta\boldsymbol{\varepsilon}_{\mathrm{pl}})$ can also be defined by:

$$\Delta\varepsilon_{\mathrm{pl}_{\mathrm{vol}}} = \left(1 - 2\nu_{\mathrm{pl}}\right)\Delta\varepsilon_{\mathrm{pl}_{11}}. \tag{3.49}$$

Furthermore, if the volumetric plastic strain and the plastic strain $\Delta\varepsilon_{\mathrm{pl}_{11}}$ are used from Equation (3.47) and by replacing the components of Equation (3.49), the relation between the parameter α and the plastic Poisson's ratio is obtained:

$$\begin{aligned} \Delta\varepsilon_{\mathrm{pl}_{\mathrm{vol}}} &= \left(1 - 2\nu_{\mathrm{pl}}\right)\Delta\varepsilon_{\mathrm{pl}_{11}} \\ \Leftrightarrow \Delta\lambda_{\mathrm{pl}}\frac{\alpha}{3\sqrt{1 + \alpha/9}} &= \left(1 - 2\nu_{\mathrm{pl}}\right)\Delta\lambda_{\mathrm{pl}}\sqrt{1 + \alpha/9} \\ \Leftrightarrow \alpha &= \frac{9}{2}\frac{1 - 2\nu_{\mathrm{pl}}}{1 + 2\nu_{\mathrm{pl}}}. \end{aligned} \tag{3.50}$$

The plastic Poisson's ratio can be determined from uniaxial tests and therefore the parameter α is fully defined. Furthermore, it can be noted that in case of incompressible materials with $\nu_{\mathrm{pl}} = 0.5$, the parameter α yields to zero and the flow potential g_{pl} is reduced to a simple von Mises yield criterion.

3.3.1.4 Hardening Law

In case of uniaxial loads with one active stress component, the hardening or softening of the material can be defined by a simple scalar function. However, in a more general case this definition must also be valid for a multiaxial load case. To accomplish this validity, a definition of a hardening law based on equivalent stress $\bar{\sigma}$ and equivalent plastic strain $\bar{\varepsilon}_{\mathrm{pl}}$ is used. In this case an arbitrary stress state and the corresponding strain is represented by a scalar. Generally the definition of a certain analytical function of a hardening law is dependent on the material behavior itself. Well known laws such as VOCE [159] or SWIFT [160] are used to model plasticity of metals. A broad overview of different hardening laws have been analyzed by LAROUR [161]. However, such functions can also be applied to polymer matrix systems. In the present model a combination of the VOCE and SWIFT hardening law is used (cf. Figure 3.12). Since the hardening can differ in tension and compression, the direction-dependent parameters are denoted by t or c and the hardening law is given by

$$\begin{aligned}\bar{\sigma}_{\mathrm{t,c}} &= m_{\mathrm{t,c}} A_{\mathrm{t,c}} \left(\bar{\varepsilon}_{0\mathrm{t,c}} + \bar{\varepsilon}_{\mathrm{pl}}\right)^{n_{\mathrm{t,c}}} \\ &\quad + \left(1 - m_{\mathrm{t,c}}\right) \left(\bar{\sigma}_{\mathrm{st,c}} + \left(\bar{\sigma}_{0\mathrm{t,c}} - \bar{\sigma}_{\mathrm{st,c}}\right) e^{-\frac{\bar{\varepsilon}_{\mathrm{pl}}}{k_{\mathrm{t,c}}}}\right),\end{aligned} \tag{3.51}$$

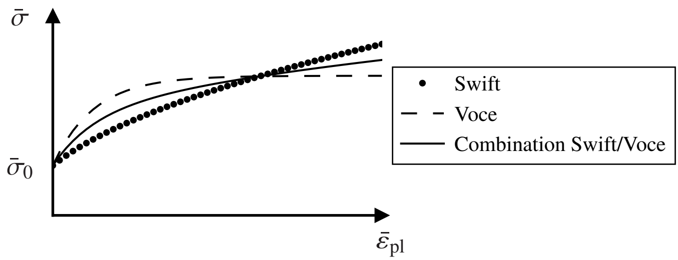

Figure 3.12: Hardening law definitions of VOCE, SWIFT and the combined version

where $\bar{\varepsilon}_{0\text{t,c}}$ and $k_{\text{t,c}}$ are defined as

$$\bar{\varepsilon}_{0\text{t,c}} = \left(\frac{\bar{\sigma}_{0\text{t,c}}}{A_{\text{t,c}}}\right)^{\frac{1}{n_{\text{t,c}}}} \quad \text{and} \quad k_{\text{t,c}} = \frac{\bar{\sigma}_{\text{st,c}}}{H_{0\text{t,c}}}. \tag{3.52}$$

Here the term $m_{\text{t,c}}$ balances the weight of the Voce and Swift hardening laws on the combined hardening law. In case of $m_{\text{t,c}} = 1$ only the Swift hardening law is used and in case of $m_{\text{t,c}} = 0$ the Voce hardening law is recovered. Each hardening law requires only two parameters. For example, Swift defines the parameter A as a general measure of the rate of hardening and n as the decrement of this hardening. On the other hand Voce uses saturation flow stress $\bar{\sigma}_{\text{s}}$ and a parameter k which is defined as a slope in the logarithmic stress ratio vs. logarithmic strain space. Here the parameter k is redefined as a quotient of the saturation flow stress and the hardening modulus H_0. Since for tension and compression the initial yield stress $\bar{\sigma}_0$ is known, the remaining five parameters can be identified by a least square fit based on experimental results of uniaxial tension and compression tests. In case of plasticity, the acting equivalent plastic strain $\bar{\varepsilon}_{\text{pl}}$ at the end of each increment is not known. To determine the equivalent plastic strain, it can be decomposed into the equivalent plastic strain at the end of the last increment and the current equivalent plastic strain increment

$$\bar{\varepsilon}_{\text{pl}} = \bar{\varepsilon}^{t}_{\text{pl}} + \Delta\bar{\varepsilon}_{\text{pl}}. \tag{3.53}$$

The incremental equivalent plastic strain is defined here as

$$\Delta\bar{\varepsilon}_{\text{pl}} = \sqrt{k \Delta\boldsymbol{\varepsilon}_{\text{pl}} : \Delta\boldsymbol{\varepsilon}_{\text{pl}}} \tag{3.54}$$

where k depends on the plastic Poisson's ratio ν_{pl}. For example, in case of von Mises yield criterion and $\nu_{\text{pl}} = 0.5$ the parameter k results to $2/3$. To determine the general definition of k a uniaxial load case is used. Here the equivalent plastic strain is reduced to:

$$\Delta\bar{\varepsilon}_{\text{pl}} = \sqrt{k \left(\Delta\varepsilon_{\text{pl}}{}^2_{11} + \Delta\varepsilon_{\text{pl}}{}^2_{22} + \Delta\varepsilon_{\text{pl}}{}^2_{33}\right)} \tag{3.55}$$

and by substituting Equation (3.48) into the equation above, while enforcing $\Delta\bar{\varepsilon}_{\mathrm{pl}} = \Delta\varepsilon_{\mathrm{pl}_{11}}$ then the parameter k is defined by

$$k = \frac{1}{1 + 2\nu_{\mathrm{pl}}}. \tag{3.56}$$

3.3.1.5 Strain-Rate Dependent Material Behavior

To extend the yielding behavior of the matrix by a strain-rate dependency, several approaches are possible. For example, it is suitable to define the hardening law based on the strain-rate or by scaling the yield surface itself. A broad overview of different viscoplastic models is given by Souza Neto et al. [162]. A definition of a strain-rate dependent plastic multiplier $\Delta\lambda_{\mathrm{pl}}$ has been proposed by Perzyna [147, 148]. Such viscoplastic model is defined by

$$\dot{\lambda} = \begin{cases} \frac{1}{\mu}\left(\frac{\Phi_{\mathrm{pl}}}{2\sigma_{\mathrm{t}}\sigma_{\mathrm{c}}}\right)^{\frac{1}{h}}, & \Phi_{\mathrm{pl}} \geq 0 \\ 0, & \Phi_{\mathrm{pl}} < 0 \end{cases} \tag{3.57}$$

where μ is the viscosity-related parameter and h is the rate sensitivity. Here $\dot{\lambda}$ defines the change due to a rate and can be discretized by $\dot{\lambda} = {}^{\Delta\lambda_{\mathrm{pl}}}/_{\Delta t}$. In case $\Phi_{\mathrm{pl}} \geq 0$ Equation (3.57) can be repositioned to

$$\frac{\Delta\lambda_{\mathrm{pl}}}{\Delta t} = \frac{1}{\mu}\left(\frac{\Phi_{\mathrm{pl}}}{2\sigma_{\mathrm{t}}\sigma_{\mathrm{c}}}\right)^{\frac{1}{h}} \Leftrightarrow R_{\mathrm{pl}} = \left(\frac{\Delta\lambda_{\mathrm{pl}}\mu}{\Delta t}\right)^{h} - \frac{\Phi_{\mathrm{pl}}}{2\sigma_{\mathrm{t}}\sigma_{\mathrm{c}}} = 0, \tag{3.58}$$

where R_{pl} defines the viscoplastic consistency condition of the yield surface Φ_{pl}. It should be noted that in case of $\mu = 0$ and $h \neq 0$ the function R_{pl} is reduced to a strain-rate independent formulation. To identify the parameters μ and h, experimental tension and compression tests at different strain-rates are needed. Special care needs to be taken by determining the parameters of the hardening law. Since these parameters are different for each strain-rate, the definition of the hardening laws from Equation (3.58) represent the limit case at $\mu \to 0$. Since the plastic strain from experimental tests is known, the plastic multiplier $\Delta\lambda_{\mathrm{pl}}$ can be directly derived from Equation (3.47) by solving to $\Delta\varepsilon_{\mathrm{pl}_{11}}$. In this case the plastic multiplier $\Delta\lambda_{\mathrm{pl}}$ is only dependent on the parameter α and therefore on ν_{pl}. Using experimental test results, the stress at every time step is known and the viscoplasticity parameters or the hardening law parameters in Equation (3.58) can be obtained by using a parameter optimization algorithm. To solve the viscoplastic consistency condition for $\Delta\lambda_{\mathrm{pl}}$ a return mapping algorithm is used. The full derivation of the return algorithm is given in Appendix A.1.1.1. Using the obtained solution for $\Delta\lambda_{\mathrm{pl}}$ the stress state for a present strain state is defined and can be returned to the solver. In addition to stress, the derivative of stress with respect to strain (also known as the consistent tangent operator) is needed to achieve rapid convergence. The required tangent operator is derived in Appendix A.1.1.1.

3.3.2 Damage Initiation and Evolution

Besides nonlinear behavior due to plasticity of the epoxy a further nonlinearity results from progressive damage. To determine the initiation point of progressive damage a failure criterion is used. Typically, damage is activated if the value of a failure criterion is above one. For example, a uniaxial load leads to a stress σ which cause damage above the material strength X. Therefore, if $\sigma/X > 1$ progressive damage is activated. For polymer materials the yield surface proposed by TSCHOEGEL [149] can also be used as a failure surface by replacing the hardening variables $\sigma_{\mathrm{t,c}}$ with the macroscopic material strengths X_{T} and X_{C} respectively. The failure index f_{M} is then defined as follows

$$f_{\mathrm{M}} = \frac{6J_2 + 2\left(X_{\mathrm{C}} - X_{\mathrm{T}}\right) I_1}{2X_{\mathrm{T}}X_{\mathrm{C}}}. \tag{3.59}$$

It should be noted that if the material strengths X_{T} and X_{C} are equal, the failure initiation surface falls back to a simple VON MISES failure criterion. Typically, polymers such as epoxy are strain rate sensitive. This material behavior has been shown in Figure 2.5. This strain rate sensitivity of the strengths is not observed from experimental tests in Section 2.4.1 for the used epoxy system. In other words the tensile and compressive strength of the epoxy is assumed to be constant at different strain rates. After the failure criterion exceeds the value of one, damage is initiated. There are several ways to model damage evolution. The resulting stress is based on the actual value of the damage variables. By using damage evolution laws two main groups are available: isotropic and anisotropic damage (cf. Figure 3.13). In the case of isotropic damage, the damage surface is represented by a sphere. On the other hand anisotropic

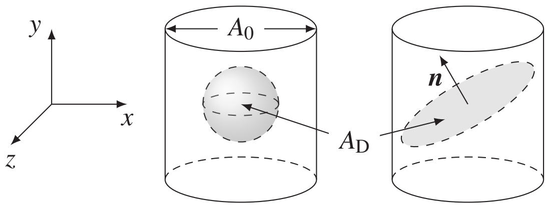

Figure 3.13: Schematically understanding of isotropic (left) and anisotropic (right) damage within an extracted cylindrical continuum

damage laws define slit damage surfaces, which account for different loading directions and therefore cause a direction-dependent material response. This behavior results from the assumption of the cross section area reduction due to damage. If the initial cross section area A_0 is reduced by the damage surface A_D, in case of isotropic damage the remaining cross section area remains the same in each direction, even if the cylindrical continuum is rotated (cf. Figure 3.13). However, in the case of anisotropic damage the remaining surface depends on the orientation of the slit. For example, in transverse direction to $\boldsymbol{n}$, which represent the direction of the damage surface A_D, the cross section of the continuum equals the initial cross section area A_0. Generally the effective stress $\hat{\boldsymbol{\sigma}}$, which represents the trial stress based on the current elastic strain, is used to calculate the actual acting nominal stress $\boldsymbol{\sigma}$. The relation between the effective stress and the nominal stress can be expressed via a damage tensor $\mathbb{M}$ which is a forth-order tensor,

$$\boldsymbol{\sigma} = \mathbb{M} : \hat{\boldsymbol{\sigma}}. \tag{3.60}$$

Using $\mathbb{M}$ an isotropic or an anisotropic damage model can be defined. As discussed in Section 3.1 there are several published damage models available. Here a simplified isotropic damage model is used to define the progressive damage of the epoxy material. In the case of isotropic damage the damage factor $\mathbb{M}$ is defined as follows

$$\mathbb{M} = (1 - d)\,\mathbb{I}^{s}, \tag{3.61}$$

where d is the isotropic damage variable. Combining Equations (3.60) and (3.61) leads to a formulation of the constitutive equation using isotropic damage evolution

$$\boldsymbol{\sigma} = \mathbb{M} : \hat{\boldsymbol{\sigma}} = \mathbb{M} : \mathbb{C} : \boldsymbol{\varepsilon}_{\mathrm{el}} = \mathbb{C}_{\mathrm{D}} : \boldsymbol{\varepsilon}_{\mathrm{el}}. \tag{3.62}$$

3.3.2.1 Stress Decomposition

If an initial crack is created due to a tension load, the resulting crack will have a direct effect on the stiffness of the isotropic material. However, if the load is reversed and a compressive load is applied, the crack closes and full stiffness of the material is recovered. Considering this effect at least two separate damage variables need to be used to distinguish between positive and negative damage. One of the main challenges modeling damage of an isotropic material is to determine these two damage variables from a given stress load. Simo [163, 164] proposed an approach to separate the strain load into a positive and a negative part. The same approach can also be used to determine the positive and the negative stress part. Such approach has been used in several publications [150, 165–168]. It is assumed that a stress state can be decomposed as follows

$$\boldsymbol{\sigma} = \boldsymbol{\sigma}^{+} + \boldsymbol{\sigma}^{-}, \tag{3.63}$$

where the subscript denotes the positive and negative stress tensor. To distinguish between these, a projection tensor $\mathbb{P}$ is used. Due to symmetry of the stress tensor, such projection tensor must also be symmetric. The relation between the positive and the negative stress part can then be expressed as

$$\boldsymbol{\sigma}^{+} = \mathbb{P}^{+} : \boldsymbol{\sigma} \quad \text{and} \quad \boldsymbol{\sigma}^{-} = \mathbb{P}^{-} : \boldsymbol{\sigma} \tag{3.64}$$

where $\mathbb{P}^{-}$ is defined as follows

$$\mathbb{P}^{-} = \mathbb{I}^{\mathrm{s}} - \mathbb{P}^{+}. \tag{3.65}$$

To determine the projection tensor the principal stresses $\sigma_{\mathrm{I}}, \sigma_{\mathrm{II}}$ and σ_{III} with the corresponding principal direction vectors $\boldsymbol{e}_1, \boldsymbol{e}_2$ and $\boldsymbol{e}_3$ are utilized. The positive projection tensor $\mathbb{P}^+$ can then be expressed in index notation as

$$P^+_{ijkl} = \sum_{m=1}^{3} H\left(\sigma_m\right) e_{mi} e_{mj} e_{mk} e_{ml}, \tag{3.66}$$

where $H\left(\cdot\right)$ is the Heaviside step function. For a better understanding of such projection tensor let's assume a triaxial load along each axis of the coordinate system. In such case the stress tensor values along the main diagonal are equal to the principal stresses. The corresponding principal directions yields the axis of the coordinate system of the stress tensor. Here the following stress state is assumed $\sigma_{\mathrm{I}} > 0$, $\sigma_{\mathrm{II}} > 0$ and $\sigma_{\mathrm{III}} < 0$. Now if the positive and the negative stress part are calculated, both positive stress components are the only nonzero components along the main diagonal of $\boldsymbol{\sigma}^+$. On the other hand σ_{III} is the only nonzero component along the main diagonal of $\boldsymbol{\sigma}^-$. It should be noted that for both tensors, all off-diagonal components are zero. The sum of both stress tensors result to the initial stress tensor containing positive and negative components. If the trial stress tensor is decomposed into its positive and negative part and by utilizing the relation between the nominal and the trial stress tensor (cf. Equation (3.60)) the resulting damage stress can be expressed by

$$\boldsymbol{\sigma} = \mathbb{M}^+ : \hat{\boldsymbol{\sigma}}^+ + \mathbb{M}^- : \hat{\boldsymbol{\sigma}}^-, \tag{3.67}$$

where the damage tensors $\mathbb{M}^+$ and $\mathbb{M}^-$ are dependent on the damage variables d^+ and d^- respectively. By using these damage variables, stiffness recovery can be modeled for isotropic materials after damage initiation. It should be noted in case $d^+ < d^-$, the damage due to compression affects also the damage variable due to tension. Therefore, the positive damage variable is updated by the following rule:

$$d^+ = \max\left\{d^-, d^+\right\}. \tag{3.68}$$

If the positive and negative stress (cf. Equation (3.64)) and the definition of the trial stress $\hat{\boldsymbol{\sigma}}$ from Equation (3.60) is substituted into Equation (3.67), a definition of the damage factor $\mathbb{M}$ based on the positive and negative damage factors $\mathbb{M}^{+}$, and $\mathbb{M}^{-}$ can be obtained

$$\begin{aligned} &\boldsymbol{\sigma} = \mathbb{M}^{+} : \hat{\boldsymbol{\sigma}}^{+} + \mathbb{M}^{-} : \hat{\boldsymbol{\sigma}}^{-} \Leftrightarrow \mathbb{M} : \hat{\boldsymbol{\sigma}} = \mathbb{M}^{+} : \mathbb{P}^{+} : \hat{\boldsymbol{\sigma}} + \mathbb{M}^{-} : \mathbb{P}^{-} : \hat{\boldsymbol{\sigma}} \\ &\quad \Rightarrow \mathbb{M} = \mathbb{M}^{+} : \mathbb{P}^{+} + \mathbb{M}^{-} : \mathbb{P}^{-}. \end{aligned} \tag{3.69}$$

3.3.2.2 Damage Surface

To model damage it is necessary to ensure thermodynamic consistency. This means that in case of damage the dissipated energy due to damage must be positive and consistent with the amount of elastic energy loss. Following the work of Cicekli [150] the definition of the specific Helmholtz free energy can be decomposed to

$$\psi = \psi_{\mathrm{el}} + \psi_{\mathrm{pl}} + \psi_{\mathrm{d}}, \tag{3.70}$$

where ψ_{el}, ψ_{pl} and ψ_{d} represent the elastic, plastic and damage parts respectively. The elastic Helmholtz free energy is determined from the damaged material stiffness, which is dependent on the damage variables, and is given as

$$\psi_{\mathrm{el}} = \frac{1}{2}\boldsymbol{\varepsilon}_{\mathrm{el}} : \mathbb{C}_{\mathrm{D}} : \boldsymbol{\varepsilon}_{\mathrm{el}} = \frac{1}{2}\boldsymbol{\sigma} : \boldsymbol{\varepsilon}_{\mathrm{el}} = \frac{1}{2}\left(\boldsymbol{\sigma}^{+} + \boldsymbol{\sigma}^{-}\right) : \boldsymbol{\varepsilon}_{\mathrm{el}}. \tag{3.71}$$

By utilizing the definition of stress decomposition (cf. Equation (3.63)) and the relation between trial and resulting stress using damage tensor $\mathbb{M}$ (cf. Equation (3.60)), a further simplification can be made

$$\psi_{\mathrm{el}} = \frac{1}{2}\mathbb{M} : \hat{\boldsymbol{\sigma}} : \boldsymbol{\varepsilon}_{\mathrm{el}}. \tag{3.72}$$

To obtain thermodynamic consistent damage evolution the dissipated energy has to be positive. The rate of damage energy dissipation based on the damage rate is given as:

$$Y^{+}\dot{d}^{+} + Y^{-}\dot{d}^{-} \geq 0, \tag{3.73}$$

where Y denote the positive and the negative thermodynamic forces, which are the driving forces of the damage progression. Since the damage rate has to be positive for further damage evolution, the rate of damage energy leads to the condition that the driving forces Y has also to be positive. The thermodynamic forces are defined by the derivative of the elastic Helmholtz free energy to the damage variables

$$Y^{\pm} = -\frac{\partial \psi_{\mathrm{el}}}{\partial d^{\pm}} = -\frac{1}{2}\frac{\partial \mathbb{M}}{\partial d^{\pm}} : \hat{\boldsymbol{\sigma}} : \boldsymbol{\varepsilon}_{\mathrm{el}} = \frac{1}{2}\mathbb{P}^{\pm} : \hat{\boldsymbol{\sigma}} : \boldsymbol{\varepsilon}_{\mathrm{el}}. \tag{3.74}$$

Furthermore, by using Y a definition of the damage surface can be formulated. For each damage variable the damage surface is defined as

$$\Phi_{\mathrm{d}}^{\pm} = Y^{\pm} - Y_{\mathrm{D}}^{\pm} \leq 0, \tag{3.75}$$

where Y_{D} defines the positive or negative damage isotropic hardening function. It should be noted that Y_{D} is interpreted as the driving force to d and can be also derived from the damage part of the Helmholtz free energy ψ_{d}. The derivative of ψ_{d} to d yield then to

$$\frac{\partial \psi_{\mathrm{d}}}{\partial d} = Y_{\mathrm{D}}. \tag{3.76}$$

3.3.2.3 Damage Evolution

Comparable to the plasticity model the evolution of the damage variables can be obtained from the derivative of the damage surface Φ_{d} to the driving forces. Since the damage hardening function Y_{D} is considered as a history term and therefore not dependent on the current acting driving forces Y the damage increment is given as:

$$\Delta d^{\pm} = \Delta\lambda_{\mathrm{d}}^{\pm} \frac{\partial \Phi_{\mathrm{d}}^{\pm}}{\partial Y^{\pm}} = \Delta\lambda_{\mathrm{d}}. \tag{3.77}$$

The Kuhn-Tucker conditions must be also fulfilled for damage evolution,

$$\Phi_{\mathrm{d}} \leq 0, \quad \Delta\lambda_{\mathrm{d}} \geq 0 \quad \text{and} \quad \Delta\lambda_{\mathrm{d}}\Phi_{\mathrm{d}} = 0. \tag{3.78}$$

It is obvious that damage progression occurs only in the case of $\Phi_{\mathrm{d}} \geq 0$ and the damage increment is positive since $\Delta\lambda_{\mathrm{d}}$ has to be positive per definition.

3.3.2.4 Isotropic Damage Hardening Law

Damage evolution defines the stress softening after failure initiation. Similar to plasticity the evolution can be defined by a hardening law. In this case the evolution of the equivalent damage variable over the damage driving force is defined. While the damage variable increases (hardening), at the same time the stress response decreases (softening). For example, the simplest way to model damage evolution is achieved with a linear softening of the stress over the strain. Other damage models can model an exponential softening of the resulting stress or even a constant stress, which is the limit case for all damage models (cf. Figure 3.14). The general procedure to derive a damage model is presented using the linear stress softening damage model. In Figure 3.15 a 1D linear elastic path of the stress is given. This path can be separated into an area prior to damage initiation g_0 and afterwards g_d. The total area sums up to the total available energy g of the material. In general the energy of the material g can be experimentally determined. By calculating the energy g_0 prior to damage initiation, the available energy g_d for damage evolution can be determined. Prior to failure initiation at σ_0 the damage variable d is equal to zero. Here the stress σ_0 can be interpreted as the material strength. After failure initiation, the damage variable starts to grow until the strain ε_f is reached. A certain strain ε_1 leads to σ_1 as a response of the reduction of the initial material stiffness C by the factor $1 - d$. The gradient of d is dependent on g_d. It is obvious that in case of $d = 1$ for any strain state the stress will remain zero. To determine the evolution of the damage variable d based on the

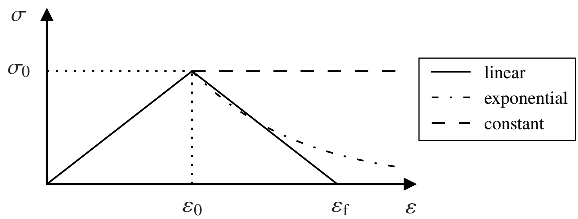

Figure 3.14: Schematic representation of different damage models with linear, exponential and a constant stress softening

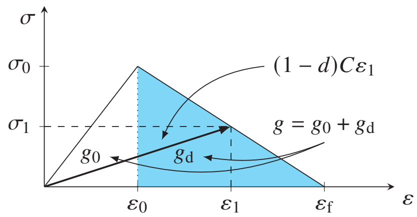

Figure 3.15: Stress path of a triangular damage model based on the damage variable d

strain ε in conjunction with g_d (and by noticing that $C = \sigma_0/\varepsilon_0$) the following relation between the resulting stress and the stress path is used:

$$
\begin{aligned}
\sigma = (1-d)C\varepsilon &\overset{!}{=} -\frac{\sigma_0}{\varepsilon_f - \varepsilon_0}(\varepsilon - \varepsilon_f) \\
\Leftrightarrow (1-d)\frac{\cancel{\sigma_0}}{\varepsilon_0}\varepsilon &= -\frac{\cancel{\sigma_0}}{\varepsilon_f - \varepsilon_0}(\varepsilon - \varepsilon_f) \Leftrightarrow d = \frac{\varepsilon_f(\varepsilon - \varepsilon_0)}{\varepsilon(\varepsilon_f - \varepsilon_0)},
\end{aligned}
\tag{3.79}
$$

where the total failure strain ε_f is defined as a function of g_d

$$
\varepsilon_f = \varepsilon_0 + \frac{2g_d}{\sigma_0}. \tag{3.80}
$$

The definition of the damage variable for the 1D stress path can also be used for the 3D stress state. This is permissible because the 1D stress path can be derived from the 3D stress state. However, the acting strain tensor $\boldsymbol{\varepsilon}$ needs to be reduced to a scalar in order to be used as input for damage variable evolution. This definition of d is only valid within the damage evolution region. Since the damage variable d is calculated only after failure initiation and up to total failure strain ε_f, a full definition of the damage variable d using a piecewise function of d is given as:

$$
d = \begin{cases} 0, & \varepsilon \leq \varepsilon_0 \\ \frac{\varepsilon_f(\varepsilon - \varepsilon_0)}{\varepsilon(\varepsilon_f - \varepsilon_0)}, & \varepsilon_0 \leq \varepsilon \leq \varepsilon_f \\ 1, & \varepsilon \geq \varepsilon_f. \end{cases} \tag{3.81}
$$

Using the same procedure the damage evolution of the exponential and the constant stress softening can be obtained:

$$d_{\text{exp}} = 1 - \frac{\varepsilon_0}{\varepsilon} \exp\left(-\frac{\sigma_0}{g_{\text{d}}} (\varepsilon - \varepsilon_0)\right) \tag{3.82}$$

$$d_{\text{const}} = 1 - \frac{\varepsilon_0}{\varepsilon}. \tag{3.83}$$

If the damage evolution function (cf. Equation (3.75)) is used to determine the damage propergation a relation between the damage driving force Y and the damage variable d is needed. In general the following definition is applied to the positive and the negative damage evolution law. In the following a uniaxial tensile load $\sigma_{11} > 0$ where $\boldsymbol{\varepsilon} = \boldsymbol{\varepsilon}_{\text{el}}$ is assumed. Therefore, the projection tensor $\mathbb{P}$ can be neglected since σ_{11} is the only nonzero term of the stress tensor $\hat{\boldsymbol{\sigma}}$. Since the relation between the strain components at a uniaxial load is known (cf. Equation (3.48)) and by using the formulation of the stiffness tensor $\mathbb{C}$ for isotropic materials based on the Young's modulus E and the Poisson's ratio ν the resulting damage driving forces can be simplified to

$$Y = \frac{1}{2}\hat{\boldsymbol{\sigma}} : \boldsymbol{\varepsilon} = \frac{1}{2}\boldsymbol{\varepsilon} : \mathbb{C} : \boldsymbol{\varepsilon} = \frac{1}{2}E\varepsilon_{11}^2. \tag{3.84}$$

For the sake of clarity the index of the strain and stress will be dropped from now on. At damage initiation a specific initial damage driving force Y_0 need to be exceeded for damage evolution. For a uniaxial load case this point can be expressed as:

$$Y_0 = \frac{1}{2}\boldsymbol{\sigma}_0\boldsymbol{\varepsilon}_0 = \frac{1}{2}E\varepsilon_0^2. \tag{3.85}$$

By solving Equation (3.79) to the strain ε and substituting the failure ε_{f} by Equation (3.80) the damage driving force from Equation (3.84) can be expressed as follows

$$Y = \frac{1}{2}E\varepsilon^2 = Y_0 \frac{(g_{\text{d}} + Y_0)^2}{((1-d)\, g_{\text{d}} + Y_0)^2}. \tag{3.86}$$

In the same manner the exponential damage evolution law can be used to define the damage driving force. To find an adequate solution a new relation between

ε and ε_0 is introduced. By assuming that ε is a multiple of ε_0 a ratio between Y and Y_0 can be derived

$$\varepsilon = r_y \varepsilon_0 \Rightarrow r_y = \sqrt{\frac{Y}{Y_0}}. \tag{3.87}$$

Now by substituting the strain ε in Equation (3.82) by using the equation above, the exponential damage evolution based on damage driving force Y yields

$$\begin{aligned}
1 - d_{\mathrm{exp}} &= \frac{\varepsilon_0}{\varepsilon} \exp\left(-\frac{\sigma_0}{g_{\mathrm{d}}} (\varepsilon - \varepsilon_0)\right) \\
\Leftrightarrow 1 - d_{\mathrm{exp}} &= \frac{1}{r_y} \exp\left(-\frac{\sigma_0}{g_{\mathrm{d}}} \left(r_y \varepsilon_0 - \varepsilon_0\right)\right) \\
\Leftrightarrow Y &= \frac{\sqrt{Y_0 Y}}{1 - d_{\mathrm{exp}}} \exp\left(-\frac{1}{g_{\mathrm{d}}} \left(\sqrt{Y_0 Y} - Y_0\right)\right).
\end{aligned} \tag{3.88}$$

It is obvious that this equation has no closed solution and need to be solved iteratively. Using the assumed relation between ε and ε_0 also the damage evolution for a constant stress can be derived

$$d_{\mathrm{const}} = 1 - \frac{\varepsilon_0}{\varepsilon} = 1 - \sqrt{\frac{Y_0}{Y}}. \tag{3.89}$$

Each damage evolution law can be solved to the damage variable d. This allows to calculate a closed solution of d for a given damage driving force Y. An example of each damage law using the same energy g_{d} and the same initial driving force Y_0 is visualized in Figure 3.16. Even though the same g_{d} value is used, the hardening of each damage law is different. For all laws the rate of the damage growth is dependent on the value of the initial damage driving force Y_0. Additionally, the hardening rate of the linear and the exponential damage law is highly affected by g_{d}. For very high values of g_{d}, the damage evolution for a constant stress represents a limit case for the linear and exponential stress softening case. Although the damage evolution law of a linear stress softening is very simple and easy to implement, the transition at $d = 1$ leads to a vertex and is therefore not differentiable at this point. Therefore, the exponential damage evolution law is used to determine the matrix damage behavior. In combination with the damage surface Φ_{d} from Equation (3.75) the history term

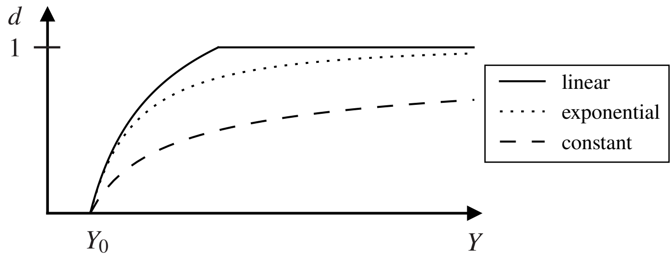

Figure 3.16: Examples of different damage evolution law based on the same energy g_d and the same initial driving force Y_0

Y_D is then defined by Equation (3.88) and the damage variable for tension and compression results to

$$\begin{aligned}
0 = \Phi_\mathrm{d}^{\pm} = Y^{\pm} - Y_\mathrm{D}^{\pm} = Y^{\pm} - \frac{\sqrt{Y_0^{\pm} Y^{\pm}}}{1 - d_\mathrm{exp}^{\pm}} \exp\left(-\frac{1}{g_\mathrm{d}^{\pm}}\left(\sqrt{Y_0^{\pm} Y^{\pm}} - Y_0^{\pm}\right)\right) \\
\Leftrightarrow d_\mathrm{exp}^{\pm} = 1 - \sqrt{\frac{Y_0^{\pm}}{Y^{\pm}}} \exp\left(-\frac{1}{g_\mathrm{d}^{\pm}}\left(\sqrt{Y_0^{\pm} Y^{\pm}} - Y_0^{\pm}\right)\right).
\end{aligned} \tag{3.90}$$

As the initial damage driving force Y_0 is dependent on the strain at failure initiation, this strain value should be known to capture the damage evolution correctly. This is crucial as the material point deformation can change and lead to a different location of the stress on the damage surface. To determine the initial damage driving force Y_0, a specific procedure is introduced in Appendix A.1.1.2.

3.3.2.5 Viscous Regularization

Damage models create a softening behavior of the stress due to stiffness degradation. Such conditions show severe convergence difficulties for an implicit solver, such as Abaqus/Standard. To overcome these difficulties, a viscous regularization scheme is used. This approach is as the name says a time dependent approach. Here the DUVAUT-LIONS regularization model [169] is used

$$\dot{d}_{\mathrm{v}} = \frac{1}{\mu_{\mathrm{d}}} \left(d - d_{\mathrm{v}} \right), \tag{3.91}$$

where μ_{d} denotes a viscosity coefficient representing the relaxation time of the damage evolution and d_{v} is the regularized damage variable. Since $d - d_{\mathrm{v}} \geq 0$ and by using the backward Euler scheme, the damage variable at $t + \Delta t$ results to

$$d_{\mathrm{v}\,t+\Delta t} = d_{\mathrm{v}\,t} + \Delta d_{\mathrm{v}}, \tag{3.92}$$

where Δd_{v} can be obtained from Equation (3.91) by discretization of $\dot{d}_{\mathrm{v}}$ as follows

$$\frac{\Delta d_{\mathrm{v}}}{\Delta t} = \frac{1}{\mu_{\mathrm{d}}} \left(d_{t+\Delta t} - d_{\mathrm{v}\,t+\Delta t} \right). \tag{3.93}$$

If Δd_{v} is substituted in Equation (3.92) and solved to $d_{\mathrm{v}\,t+\Delta t}$ the regularized damage variable results to

$$d_{\mathrm{v}\,t+\Delta t} = \frac{\Delta t}{\Delta t + \mu_{\mathrm{d}}} d_{t+\Delta t} + \frac{\mu_{\mathrm{d}}}{\Delta t + \mu_{\mathrm{d}}} d_{\mathrm{v}\,t}. \tag{3.94}$$

Two limiting cases can be observed:

- For $\mu_{\mathrm{d}} \rightarrow 0$ the regularized damage variable $d_{\mathrm{v}\,t+\Delta t}$ results to $d_{t+\Delta t}$. This solution correspond to a rate-independent formulation of the damage variable.
- For $\mu_{\mathrm{d}} \rightarrow \infty$ the regularized damage variable $d_{\mathrm{v}\,t+\Delta t}$ results to $d_{\mathrm{v}\,t}$. In this case no damage evolution is present.

It should be noted that the value of μ_{d} needs to be small compared to the time increment Δt. Otherwise, the results will be falsified due to very slow damage evolution. To determine a proper ratio between convergence of the simulation and accuracy of the results either a study with varying μ_{d} values need to be performed or the ratio between the dissipated energy due to viscous regularization and the damage energy for the whole part should not exceed e.g., a value of 0.1. With the definition of the viscous damage variables, the updated stress can be returned to the solver. As for the matrix plasticity the consistent tangent operator is also required to achieve rapid convergence. The full derivation of the tangent operator can be found in Appendix A.1.1.2.

3.4 Constitutive Fiber Model

At the micro scale both constituents, matrix and fiber, require a suitable constitutive model. While glass fibers are considered to be isotropic and the constitutive law requires only two parameters to model the stiffness, this is not the case for anisotropic fibers such as carbon fibers. Such fibers are considered to be a transversely isotropic material. Therefore, five independent material parameters are needed to describe the material stiffness. According to Vogler [99] the tensorial definition of a transversely isotropic material reads

$$\begin{aligned}\mathbb{C}^{\mathrm{TI}} = \lambda^{\mathrm{TI}} \boldsymbol{I} \otimes \boldsymbol{I} + 2\mu_{\mathrm{T}}^{\mathrm{TI}} \mathbb{I}^{\mathrm{s}} + \alpha^{\mathrm{TI}} \left(\boldsymbol{A} \otimes \boldsymbol{I} + \boldsymbol{I} \otimes \boldsymbol{A}\right) \\ + 2\left(\mu_{\mathrm{L}}^{\mathrm{TI}} - \mu_{\mathrm{T}}^{\mathrm{TI}}\right) \mathbb{I}^{\mathrm{A}} + \beta^{\mathrm{TI}} \boldsymbol{A} \otimes \boldsymbol{A},\end{aligned} \tag{3.95}$$

where $\boldsymbol{A}$ and $\mathbb{I}^{\mathrm{A}}$ are defined as

$$\boldsymbol{A} = \boldsymbol{a} \otimes \boldsymbol{a} \tag{3.96}$$

$$I^{\mathrm{A}}_{ijkl} = \frac{1}{2}\left(\delta_{ik} a_j a_l + \delta_{il} a_j a_k + \delta_{jl} a_i a_k + \delta_{jk} a_i a_l\right) \tag{3.97}$$

and λ^{TI}, α^{TI}, μ_L^{TI}, μ_T^{TI} and β^{TI} are the five invariant material coefficients of $\mathbb{C}^{\mathrm{TI}}$. The vector $\boldsymbol{a}$ denotes the axis normal to the plane of isotropy, which coincides with the fiber direction in case of both carbon fibers and UD fiber reinforced composites. Here the direction of the axis is considered to be along the x-axis direction and is therefore set to

$$\boldsymbol{a} = \begin{pmatrix} 1 & 0 & 0 \end{pmatrix}^{\top}. \tag{3.98}$$

Since material parameters are measured in engineering coefficients, such as Young's moduli E_1^{f} and E_2^{f}, the Poisson's ratio ν_{12}^{f} and the shear moduli G_{12}^{f} and G_{23}^{f}, a conversion of the invariant coefficients to the engineering ones is needed. Using the defined orientation of the normal axis $\boldsymbol{a}$ the invariant coefficients result to

$$\begin{aligned}
&\mu_{\mathrm{L}}^{\mathrm{TI}} = G_{12}^{\mathrm{f}}, \quad \lambda^{\mathrm{TI}} = \frac{1}{D^{\mathrm{f}}}\left(E_2^{\mathrm{f}}\left(\nu_{23}^{\mathrm{f}} + \nu_{12}^{\mathrm{f}}\nu_{21}^{\mathrm{f}}\right)\right),\\
&\mu_{\mathrm{T}}^{\mathrm{TI}} = G_{23}^{\mathrm{f}}, \quad \alpha^{\mathrm{TI}} = \frac{1}{D^{\mathrm{f}}}\left(E_2^{\mathrm{f}}\left(\nu_{12}^{\mathrm{f}}\nu_{23}^{\mathrm{f}} + \nu_{12}^{\mathrm{f}}\right)\right) - \lambda^{\mathrm{TI}},\\
&\beta^{\mathrm{TI}} = \frac{1}{D^{\mathrm{f}}}\left(E_1^{\mathrm{f}}\left(1 - \nu_{23}^{\mathrm{f}}\nu_{32}^{\mathrm{f}}\right) + E_2^{\mathrm{f}}\left(1 - \nu_{12}^{\mathrm{f}}\left(\nu_{21}^{\mathrm{f}} + 2\left(1 + \nu_{23}^{\mathrm{f}}\right)\right)\right)\right)\\
&\qquad - 4G_{12}^{\mathrm{f}}
\end{aligned} \tag{3.99}$$

with

$$D^{\mathrm{f}} = 1 - \nu_{23}^{\mathrm{f}}\nu_{32}^{\mathrm{f}} - 2\nu_{12}^{\mathrm{f}}\nu_{21}^{\mathrm{f}} - 2\nu_{23}^{\mathrm{f}}\nu_{21}^{\mathrm{f}}\nu_{12}^{\mathrm{f}}. \tag{3.100}$$

For clarity reasons the denotation 'f' is dropped in the following sections. The presented model covers the elastic transversely isotropic material behavior, which is extended by the nonlinear material behavior in fiber direction [23]. As the fiber has a very high stiffness, compared to the polymer matrix, it is assumed that applied stress states would only lead to failure in fiber direction. All other damage processes take place within the matrix or interface between fiber and matrix itself. Therefore, the failure initiation is triggered only by exceeding the material strength in fiber direction. An isotropic damage evolution is considered in order to avoid any spurious results in other material directions. Due to reasons mentioned in Section 3.2, especially for the fiber material the strain needs to be defined in the material axes coordinate system.

3.4.1 Nonlinear Material Behavior

Material behavior of carbon fibers is generally modeled linear elastic. However, experimental tests on single carbon fibers have shown that nonlinear behavior in fiber direction can be observed [21–23, 81]. According to various studies the axial misorientation of the crystallites in a carbon fiber are responsible to the nonHookean material behavior. This leads to the phenomenon that the Young's modulus in fiber direction increases for tension loads and decreases for compression loads [21]. The change of the modulus is dependent on the current strain in fiber direction ε_{11}. Such material behavior has been observed for Toray T300 carbon fibers with a modulus of about 222 GPa, but also for carbon fibers with a very high modulus, such as Toray M50J, of about 475 GPa [23] (cf. Figure 3.17). Neglecting such material behavior would lead to an underestimation of the actual stress in fiber direction. For example, for a Toray T300 carbon fiber, the increase of the modulus per 1 % strain is about 55 GPa. This lead to stress of 2.77 GPa at 1 % strain. On the other hand if a constant modulus is used, this leads to a stress of 2.22 GPa at 1 % strain, which is 20 % lower than the real stress. According to experimental results of Kant et al. [23], they suggest a universal constant relation between the static modulus $E_1^{\mathrm{f,init}}$ and the resulting modulus, independent of the PAN based carbon fiber type, if strain in fiber direction is applied. This relation is given by

$$E_1 = E_1^{\mathrm{f,init}} + \left(29.4 E_1^{\mathrm{f,init}} - 1010\,\mathrm{GPa}\right)\varepsilon_{11}. \tag{3.101}$$

If the static modulus of the fiber is known then the slope of the modulus is also defined. For a different fiber type using the slope of the modulus over strain (cf. Figure 3.17), the strain dependent modulus can also be expressed by

$$E_1 = E_1^{\mathrm{f,init}} + \frac{\Delta E}{\Delta \varepsilon}\varepsilon_{11} = E_1^{\mathrm{f,init}} + m_{\mathrm{f}}\varepsilon_{11} \tag{3.102}$$

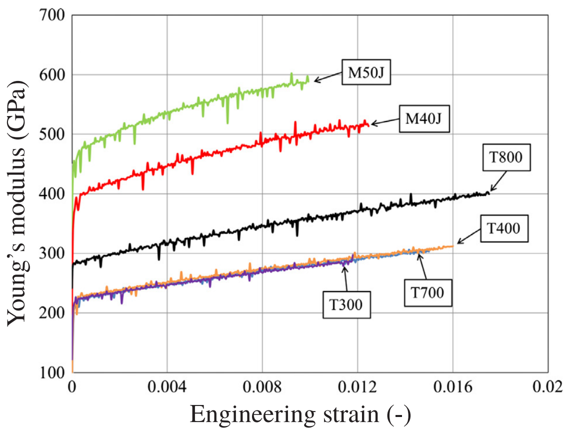

Figure 3.17: Experimental results of the stiffness of different carbon fibers over strain [23]

where $E_1^{\mathrm{f,init}}$ is the static modulus of the fiber and m_{f} is the slope of the modulus over strain. The resulting stress over strain for uniaxial tensile and compressive load cases is given exemplary in Figure 3.18. Using this formulation of the modulus requires some attention to ensure symmetry of the stiffness tensor. The new definition of the modulus also affects the Poisson's ratio ν_{12}. Due to symmetry of the stiffness tensor, the relation between E_1 and E_2 is given by

$$\frac{\nu_{12}}{E_1} = \frac{\nu_{21}}{E_2}. \tag{3.103}$$

Assuming that the later quotient is constant leads to a new definition of the Poisson's ratio ν_{12}

$$\nu_{12} = \frac{\nu_{12}^{\mathrm{f,init}}}{E_1^{\mathrm{f,init}}} E_1 \tag{3.104}$$

where $\nu_{12}^{\mathrm{f,init}}$ is the static Poisson's ratio of the carbon fiber.

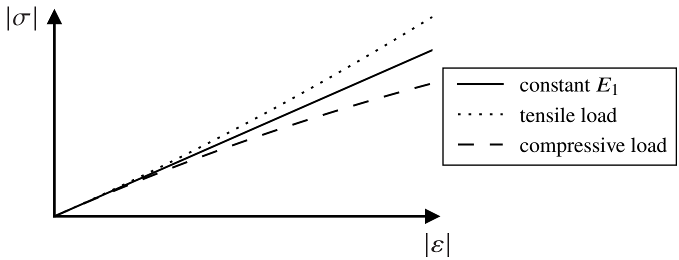

Figure 3.18: Nonlinear material behavior of a carbon fiber if tensile or compressive load is applied

3.4.2 Damage Initiation and Evolution

3.4.2.1 Failure Criteria

In addition to the material stiffness of the carbon fiber, the strength is needed to determine the point of damage initiation. Although the tensile strength in fiber direction can be measured, the strength in other directions, such as tensile and compressive strength transverse to the fiber direction or longitudinal and transverse shear strength, is in general not available. There are some publications which deal with tensile and compressive strength (X_T and X_C) of single carbon fibers in fiber direction [62, 63]. In comparison, it is shown that Toray T800S fibers have a compressive to tensile strength ratio of $X_C/X_T \approx 0.5$, while Toray T300 fibers have a ratio of $X_C/X_T \approx 1$. Since the stiffness of the fiber is much higher than the surrounding matrix, it is assumed that in case of transverse or shear loads the failure would occur within the matrix or the interface between both. Due to lack of experimental data regarding further strength values of the fiber and the significance of the strength in fiber direction for the composite material, only the failure initiation in fiber direction is evaluated. Here a maximum stress criterion is used for tension and compression

$$f_t = \frac{\hat{\sigma}_{11}}{X_T} \qquad \text{and} \qquad f_c = \frac{|\hat{\sigma}_{11}|}{X_C}, \tag{3.105}$$

where X_T and X_C are the strength in tensile and compressive direction respectively.

3.4.2.2 Damage Hardening Law and Damage Evolution

Based on the failure criteria, the stress in fiber direction needs to exceed the strength to initialize damage evolution. The propagation of the damage affects the material stiffness. Here the degradation of the stiffness is similar to the matrix material and is considered to be isotropic.

$$\boldsymbol{\sigma} = (1 - d)\,\mathbb{C}^{\mathrm{TI}} : \hat{\boldsymbol{\varepsilon}}_{\mathrm{el}} \tag{3.106}$$

According to explanations in Section 3.3.2, there are several approaches to define the damage hardening law. As for the matrix material, the exponential damage evolution law is used (cf. Equation (3.90)). Furthermore, also two damage variables $d^{\pm}$ are used to distinguish between positive and negative damage. Due to the effect of the negative damage variable on the resulting stress in case of tension the update of the positive damage variable is defined by Equation (3.68). Here the damage driving force Y is defined as

$$Y^{\pm} = \frac{1}{2}\hat{\sigma}_{11}\varepsilon_{11}, \tag{3.107}$$

where the distinction between the positive and the negative damage driving force is determined by the sign of the stress $\hat{\sigma}_{11}$. This includes that only the stress in fiber direction is responsible for further damage evolution. To determine the initial damage driving force $Y_0^{\pm}$ the corresponding scaling factor is needed. By using the definition of the failure initiation criterion (cf. Equation (3.105)) and by applying the scaling factor to the trial stress, the scaling factor results in an inverse definition of the failure criterion

$$f_{\mathrm{t,c}} = \frac{\lambda_0^{\pm}|\hat{\sigma}_{11}|}{X_{\mathrm{T,C}}} \overset{!}{=} 1 \Leftrightarrow \lambda_0^{\pm} = \frac{X_{\mathrm{T,C}}}{|\hat{\sigma}_{11}|}. \tag{3.108}$$

This definition lead to an initial damage driving force $Y_0^{\pm}$ based on the current acting damage driving force

$$Y_0^{\pm} = \lambda_0^{\pm 2} Y^{\pm}. \tag{3.109}$$

To prevent convergence issues during stress softening, the same viscous regularization scheme as for the matrix material is used to determine the viscous damage variable $d_{\mathrm{v}}^{\pm}$ (cf. Equation (3.94)). Since no plastic behavior occurs, only the elastic energy $g_{0\,\mathrm{el}}^{\pm}$ defines the energy $g_0^{\pm}$ prior to failure initiation. The resulting energy $g_{\mathrm{d}}^{\pm}$ is defined according to the matrix model, given in Equation (A.53). Using $Y^{\pm}$, $Y_0^{\pm}$ and $g_{\mathrm{d}}^{\pm}$ the damage evolution law according to Equation (3.90) is defined and the resulting stress $\boldsymbol{\sigma}$ can be returned to the solver. In addition, the consistent tangent operator which is needed for a rapid convergence is derived in Appendix A.1.2.1. It is also returned to the solver.

3.5 Constitutive Model for Composites

The combination of the material behavior of fiber and matrix leads to the material behavior of the composite material. In this section the nonlinear material behavior resulting from the matrix and the fiber are combined in a macroscopic constitutive model. Especially for composite materials the definition of the material axes is crucial. As discussed in Section 3.2 the nonlinear strain measure with the non-orthogonal material frame is applied here. The macroscopic material behavior in fiber direction is dominated by the nonlinear behavior of the fiber. Therefore, the same approach as for the fiber material is utilized here, but with adapted FVC-dependent material parameters. Besides elastic behavior, plasticity within the matrix takes place. A plasticity model by Thomson et al. [101] is used here. One advantage of this model is that it can be directly combined with the failure criteria developed by Puck [139]. The developed damage model distinguishes between different failure modes and considers the cracking direction caused by inter fiber failure. To cover the material behavior in conjunction with draping effects, the model is extended in order to consider not only the fiber orientation, but also varying fiber volume content and fiber waviness. As the elastic material parameters and the material strength values depend on the FVC, they are defined as a function of the FVC. In order to consider the material behavior due to waviness, an amplitude to wavelength dependent material response is developed. It utilizes the developed model for nonundulated laminates by assuming piecewise unidirectional behavior of the undulated region.

3.5.1 Nonlinear Material Behavior

3.5.1.1 Nonlinear Behavior in Fiber Direction

Since composite materials are considered to be transversely isotropic, only five material parameters, as for the carbon fiber material model, are needed to define the material stiffness. The inverse of an orthotropic composite material compliance $\boldsymbol{S}$ leads to the corresponding material stiffness $\boldsymbol{C}$

$$\boldsymbol{C} = \boldsymbol{S}^{-1} = \begin{pmatrix} \frac{1}{E_1} & -\frac{\nu_{21}}{E_2} & -\frac{\nu_{31}}{E_3} & 0 & 0 & 0 \\ -\frac{\nu_{12}}{E_1} & \frac{1}{E_2} & -\frac{\nu_{32}}{E_3} & 0 & 0 & 0 \\ -\frac{\nu_{13}}{E_1} & -\frac{\nu_{23}}{E_2} & \frac{1}{E_3} & 0 & 0 & 0 \\ 0 & 0 & 0 & \frac{1}{G_{12}} & 0 & 0 \\ 0 & 0 & 0 & 0 & \frac{1}{G_{13}} & 0 \\ 0 & 0 & 0 & 0 & 0 & \frac{1}{G_{23}} \end{pmatrix}^{-1} . \tag{3.110}$$

In case of transverse isotropy the following equality of the material parameters $E_3 = E_2$, $\nu_{13} = \nu_{12}$, $\nu_{31} = \nu_{21}$, $\nu_{32} = \nu_{23}$ and $G_{13} = G_{12}$ is given. For the full definition of the material stiffness see Appendix A.1.3.1. However, as discussed in Section 3.4.1, by using carbon fibers the material response in fiber direction is nonlinear due to axial misorientation of the crystallites within the fiber. In such case modulus in fiber direction E_1 of CFRP is one of the sources for nonlinear behavior. In addition, the nonlinear behavior is superimposed with intrinsic fabric undulations. These also lead to an initially reduced stiffness in fiber direction. According to experimental measurements performed by Wilhelmsson et al. [170], the mean angle of the intrinsic undulation ranges between 1.3° to 3.1°. Using the mean undulation angle of 3.1° would lead up to 5 GPa stiffness decrease in fiber direction. However, the intrinsic undulations have a smaller impact on the resulting modulus E_1 compared to the impact of the carbon fiber itself. By analyzing the experimental results of the modulus change ${}^{\mathrm{d}E_1}/_{\mathrm{d}\varepsilon_{11}}$ (cf. Figure 2.9), the increase or decrease of the modulus E_1 due to carbon fiber ranges between 1.04 TPa to 1.3 TPa [47].

For a given constant FVC, the resulting modulus E_1 can be determined by utilizing Equation (3.102) and replacing $E_1^{\mathrm{f,init}}$ and m_{f} by FVC-dependent ones. As for the fiber material to ensure symmetry of the stiffness matrix, the Poisson's ratio ν_{12} needs to be adjusted corresponding to Equation (3.104). A more general approach, which uses the FVC to determine modulus E_1 and Poisson's ratio ν_{12}, will be presented in Section 3.5.5.1.

3.5.1.2 Action Plane based Plasticity

As observed from experimental results, the matrix material shows a viscoplastic material behavior (cf. Section 2.4.1), which affects the material behavior of the composite. Several approaches are available to model plasticity of composites [96–101]. As for the matrix material the yielding of the composite is dependent on the applied hydrostatic pressure [171–174], which controls the initial yield stress of the composite. While the yield surface of the matrix is defined along the hydrostatic axis, this is not mandatory for a transversely isotropic material due to the reinforcing fiber. As discussed previously the failure of the matrix material can also be derived by using the yield surface, while the yield stresses in tension and compression are replaced by the corresponding strength of the material (cf. Section 3.3.2). If now a failure envelope for matrix dominant failure in composites is found, a transfer of the relation between the yield and failure surface of the matrix can be made. Since in fiber direction the fiber itself is responsible for failure of the composite, all transverse loads will lead to matrix dominant failure. According to Mohr [175] the fracture of brittle materials, such as composites, is determined by the stresses on the action plane. For transversely isotropic materials one can use the fiber direction as the rotation axis and rotate the stress to evaluate different action plane stresses

$$\boldsymbol{\sigma}_{\mathrm{ap}} = \boldsymbol{R}_{\mathrm{ap}}{}^{\top}\boldsymbol{\sigma}\boldsymbol{R}_{\mathrm{ap}} = \begin{pmatrix} \sigma_{11} & \tau_{\mathrm{n1}} & \tau_{\mathrm{t1}} \\ \tau_{\mathrm{n1}} & \sigma_{\mathrm{n}} & \tau_{\mathrm{nt}} \\ \tau_{\mathrm{t1}} & \tau_{\mathrm{nt}} & \sigma_{\mathrm{t}} \end{pmatrix}, \tag{3.111}$$

where $\boldsymbol{R}_{\mathrm{ap}}$ is the rotation matrix and is defined as

$$\boldsymbol{R}_{\mathrm{ap}} = \begin{pmatrix} 1 & 0 & 0 \\ 0 & \cos\theta_{\mathrm{ap}} & -\sin\theta_{\mathrm{ap}} \\ 0 & \sin\theta_{\mathrm{ap}} & \cos\theta_{\mathrm{ap}} \end{pmatrix} \tag{3.112}$$

and θ_{ap} is the action plane angle. Generally this angle is not known and need to be determined. Such approach, to use action plane stress dependent failure, has been addressed in several publications [139, 176, 177]. Puck [139] has provided a formulation of the matrix dominant inter-fiber failure for composite materials by using action plane dependent stresses. This formulation allows to determine the fracture plane θ_{fp}, which results from the maximum value of the failure index given at each action plane angle θ. A more detailed discussion to determine the fracture plane θ_{fp} is presented in the next section. This failure criterion is based on the action plane stresses σ_{n}, τ_{n1} and τ_{nt} (cf. Figure 3.19). These stress components result by rotating the stress tensor along the fiber direction by the angle θ_{fp}. A visualization of the resulting stresses on the fracture plane is given in Figure 3.19. If the failure surface is used

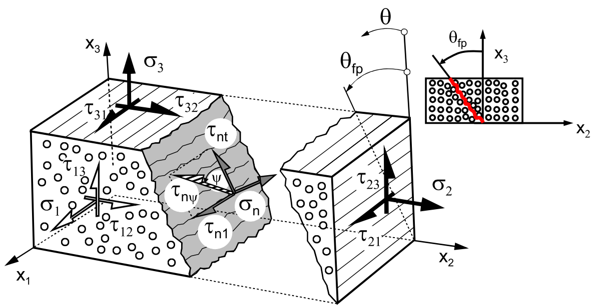

Figure 3.19: Resulting fracture plane stresses σ_{n}, τ_{n1} and τ_{nt} at fracture plane angle θ_{fp} [9]

as the yield surface for composites, the nonlinear material behavior due to plasticity can be modeled. Such approach is used by Thomson et al. [101]. While Puck's surface is similar to the parabolic shaped one used for the matrix (cf. Figures 3.11 and 3.20a), Thomson et al. [101] used a simple Drucker-Prager-type yield surface for the plasticity (cf. Figure 3.20b). The usage of such a yield surface results from the facts, that a linear correlation between the σ_n stress and the yield onset at different hydrostatic stresses has been experimentally observed [173], which is satisfied by the Drucker-Prager-type yield surface. Such yield surface can be expressed by the equivalent stress $\bar{\sigma}_{ap}$ and the hardening law τ_y as follows

$$\Phi_{ap} = \underbrace{\alpha_{ap}\sigma_n + \sqrt{\tau_{n1}^2 + e_{ap}\tau_{nt}^2}}_{\bar{\sigma}_{ap}} - \tau_y = 0, \tag{3.113}$$

where α_{ap} defines the slope along the σ_n axis, e_{ap} defines the ellipticity of the surface in the (τ_{n1}, τ_{nt})-plane and τ_y defines the isotropic hardening function. Originally the hardening function is extended to a strain rate dependency. However, as the experimental tests are all performed under quasi-static loads, a rate independent hardening function is used here. The flow potential g_{ap} is used to define the plastic flow rule

$$g_{ap} = \beta_{ap}\sigma_n + \sqrt{\tau_{n1}^2 + f_{ap}\tau_{nt}^2}, \tag{3.114}$$

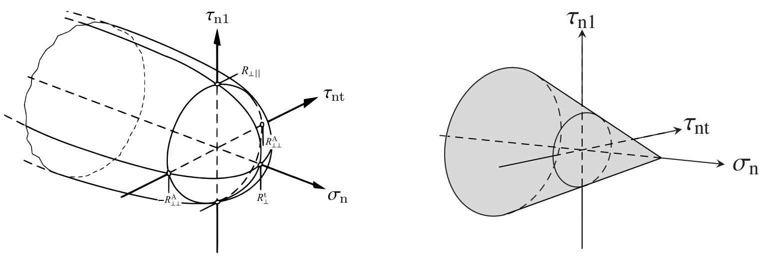

(a) (b)

Figure 3.20: Fracture surface according to Puck (visualized by Knops [9]) in the (σ_n, τ_{n1}, τ_{nt})-space (a) and Drucker-Prager-type yield surface used by Thomson et al. [101] (b)

where β_{ap} corresponds to the dilatancy coefficient in a DRUCKER-PRAGER model and f_{ap} defines the elliptical shear flow interaction in the $(\tau_{\text{n1}}, \tau_{\text{nt}})$-plane. It can be noticed that such flow potential leads to a nonassociative flow rule definition. The associative flow rule is recovered if $\beta_{\text{ap}} = \alpha_{\text{ap}}$ and $f_{\text{ap}} = e_{\text{ap}}$ is used. By determining the derivative of the flow potential g_{ap} to the action plane stress tensor $\boldsymbol{\sigma}_{\text{ap}}$ the flow rule is given by

$$\Delta\boldsymbol{\varepsilon}_{\text{pl,ap}} = \Delta\lambda_{\text{ap}} \frac{\partial g_{\text{ap}}}{\partial \boldsymbol{\sigma}_{\text{ap}}} = \Delta\lambda_{\text{ap}} \begin{pmatrix} 0 & \frac{\tau_{\text{n1}}}{2\sqrt{\tau_{\text{n1}}^2 + f_{\text{ap}}\tau_{\text{nt}}^2}} & 0 \\ \frac{\tau_{\text{n1}}}{2\sqrt{\tau_{\text{n1}}^2 + f_{\text{ap}}\tau_{\text{nt}}^2}} & \beta_{\text{ap}} & \frac{f_{\text{ap}}\tau_{\text{nt}}}{2\sqrt{\tau_{\text{n1}}^2 + f_{\text{ap}}\tau_{\text{nt}}^2}} \\ 0 & \frac{f_{\text{ap}}\tau_{\text{nt}}}{2\sqrt{\tau_{\text{n1}}^2 + f_{\text{ap}}\tau_{\text{nt}}^2}} & 0 \end{pmatrix}, \tag{3.115}$$

where $\Delta\lambda_{\text{ap}}$ is the action plane dependent plastic multiplier for composite materials. Similar to the matrix plasticity the KUHN-TUCKER conditions must be also fulfilled here. It is obvious that for such plasticity model no plastic strain in fiber direction or perpendicular to the $(1, n)$-plane occur. In order to determine the plastic strain increment based on the yield surface, the isotropic hardening function τ_{y} is utilized. Generally τ_{y} defines the plastic behavior of a material under a uniaxial stress load (e.g., shear stress load due to torsion). Here the material response between strain and stress can be directly correlated to each other. However, for a more general load case a complex strain state needs to be reduced to an equivalent scalar plastic strain $\bar{\varepsilon}_{\text{pl,ap}}$. Noticing that the plastic strain increment is based on the stress at the end of the time increment and by using the work conjugacy due to plasticity, the equivalent plastic strain $\Delta\bar{\varepsilon}_{\text{pl,ap}}$ can be obtained

$$\begin{aligned} \int_t^{t+\Delta t} \boldsymbol{\sigma}_{\text{ap}} \mathrm{d}\boldsymbol{\varepsilon}_{\text{pl,ap}} &= \int_t^{t+\Delta t} \bar{\sigma}_{\text{ap}} \mathrm{d}\bar{\varepsilon}_{\text{pl,ap}} \\ \Leftrightarrow \frac{1}{2}\left(\boldsymbol{\sigma}_{\text{ap}}\big|_{t+\Delta t} + \boldsymbol{\sigma}_{\text{ap}}\big|_{t}\right) : \Delta\boldsymbol{\varepsilon}_{\text{pl,ap}} &= \frac{1}{2}\left(\bar{\sigma}_{\text{ap}}\big|_{t+\Delta t} + \bar{\sigma}_{\text{ap}}\big|_{t}\right) \Delta\bar{\varepsilon}_{\text{pl,ap}} \\ \Leftrightarrow \Delta\bar{\varepsilon}_{\text{pl,ap}} &= \frac{\left(\boldsymbol{\sigma}_{\text{ap}}\big|_{t+\Delta t} + \boldsymbol{\sigma}_{\text{ap}}\big|_{t}\right) : \Delta\boldsymbol{\varepsilon}_{\text{pl,ap}}}{\bar{\sigma}_{\text{ap}}\big|_{t+\Delta t} + \bar{\sigma}_{\text{ap}}\big|_{t}}. \end{aligned} \tag{3.116}$$

Utilizing the definition of the equivalent plastic strain $\bar{\varepsilon}_{\text{pl,ap}}$, a correlation between the isotropic hardening function τ_{y} and the acting plastic strain $\boldsymbol{\varepsilon}_{\text{pl,ap}}$ can be defined. The definition of the isotropic hardening function τ_{y} is adapted to experimental results in conjunction with the equivalent plastic strain $\bar{\varepsilon}_{\text{pl,ap}}$. Following the hardening function of the matrix (cf. Equation (3.51)), a similar function can be defined for the composite

$$\tau_{\text{y}} = m_{\text{t,c}} A_{\text{t,c}} \left(\left(\frac{\tau_{\text{y}}^{\text{init}}}{A_{\text{t,c}}} \right)^{\frac{1}{n_{\text{t,c}}}} + \bar{\varepsilon}_{\text{pl,ap}} \right)^{n_{\text{t,c}}} + \left(1 - m_{\text{t,c}}\right) \left(\tau_{\text{s}} + \left(\tau_{\text{y}}^{\text{init}} - \tau_{\text{s}} \right) e^{-\frac{\bar{\varepsilon}_{\text{pl,ap}} \tau_{\text{s}}}{H_{0\text{t,c}}}} \right), \tag{3.117}$$

where $\tau_{\text{y}}^{\text{init}}$ denotes the yield onset. In contrast to the matrix hardening function no difference between plasticity evolution under tension and compression loads is assumed. For example, its definition can be obtained from an in-plane shear load case. In such case the fracture angle results to $\theta_{\text{fp}} = 0°$ where the only nonzero component is τ_{n1}, which is equivalent to σ_{12}, and the equivalent plastic strain $\bar{\varepsilon}_{\text{pl,ap}}$ yields $\gamma_{\text{pl}_{12}}$. Furthermore, to determine the parameters α_{ap} and e_{ap} the yield onset at different stress loads is needed. For example, such stress cases can be generated by off-axis tension or compression tests. The remaining parameters β_{ap} and f_{ap} are determined from a least square fit using also off-axis coupon tests.

To solve the action plane based yield surface and thus obtain the plastic strain a return mapping algorithm is used (see Appendix A.1.3.2). With the derived equations, the return mapping algorithm can be performed to determine the plastic corrector $\Delta\lambda_{\text{ap}}$ for a given action plane stress state. Afterwards plastic strain increment $\Delta\boldsymbol{\varepsilon}_{\text{pl,ap}}$ and action plane stress $\boldsymbol{\sigma}_{\text{ap}}$ need to be rotated back to the initial coordinate system. This allows to store the plastic strain $\boldsymbol{\varepsilon}_{\text{pl}}$ in a reference coordinate system, since the fracture plane angle can change during load propagation. The resulting stress $\tilde{\boldsymbol{\sigma}}$ defined in the reference coordinate system is then used to check whether failure initiation occurred or not. In case the applied trial stress $\hat{\boldsymbol{\sigma}}$ does not exceed the yield surface Φ_{ap} the stress after plasticity is set to the trial stress $\tilde{\boldsymbol{\sigma}} = \hat{\boldsymbol{\sigma}}$.

3.5.2 Failure Initiation

Compared to isotropic materials, composites have a different and complex failure behavior. For example, only two strength values (tensile and compressive strength) are required to determine failure initiation of isotropic materials (cf. Section 3.3.2). On the other hand transversely isotropic composites require the following strength values: tensile and compressive strength in fiber (X_T and X_C) and transverse direction (Y_T and Y_C) and additionally the in-plane shear strength S_{12} as also the out-of-plane shear strength S_{23}. By using these parameters a maximum stress criterion for each in-plane loading direction could be used. However, based on experimental results a strong interaction between the components of the stress tensor, which lead to inter-fiber failure (IFF) or fiber failure (FF), is observed. There are several failure initiation criteria available to predict composite failure (e.g., [73, 93–95]). This circumstance led to a competition of different failure initiation and damage evolution approaches to evaluate their capabilities and differences [107, 178–180]. As a result the failure criterion according to Puck [139] is able to predict experimental results for complex stress states by using only experimental results of unidirectional tests as input data. The main difference to most other approaches is the fact that Puck utilizes action plane dependent fracture for IFF, while other approaches predict failure independent of the actual fracture plane. The LaRC failure criteria [73] are also based on Mohr's idea, that failure of brittle materials is driven by the action plane. In this work, the failure criteria of Puck are used as the plasticity model relies on the action plane predicted from Puck's criteria. For example, compression test results on coupons with fiber angles between 45° and 90° showed fracture angles in a range of 40.1° to 59.1° [53]. Using Puck's failure criterion allows to determine such fracture angles for complex three-dimensional stress loads. As shown in Figure 3.20a the fracture surface is defined in the $(\sigma_n, \tau_{n1}, \tau_{nt})$-space. Failure is initiated if the fracture surface is exceeded for a given stress state. Within the surface the ratio between the length of the actual stress vector and the length of a fracture stress vector, which has the same direction but leading to the fracture, is called stress exposure f_{IFF}. This ratio can be considered as a failure index. It increases linearly with the applied stress and is a direct measure for the risk of fracture [93]. Along the normal direction σ_n, the surface can be distinguished into a positive and a negative part. This leads to the definition of the Puck IFF criterion [139]

$$f_{IFF} = \begin{cases} \sqrt{\left(\left(\frac{1}{Y_T} - \frac{p^t_\Psi}{S_\Psi}\right)\sigma_n\right)^2 + \left(\frac{\tau_{nt}}{S^{ap}_{23}}\right)^2 + \left(\frac{\tau_{n1}}{S_{12}}\right)^2} + \frac{p^t_\Psi}{S_\Psi}\sigma_n, & \sigma_n \geq 0 \\ \sqrt{\left(\frac{p^c_\Psi}{S_\Psi}\sigma_n\right)^2 + \left(\frac{\tau_{nt}}{S^{ap}_{23}}\right)^2 + \left(\frac{\tau_{n1}}{S_{12}}\right)^2} + \frac{p^c_\Psi}{S_\Psi}\sigma_n, & \sigma_n < 0 \end{cases} \tag{3.118}$$

where the expression

$$\frac{p_{\Psi}^{\mathrm{t,c}}}{S_{\Psi}} = \frac{p_{\mathrm{nt}}^{\mathrm{t,c}}}{S_{23}^{\mathrm{ap}}} \cos^2 \Psi + \frac{p_{\mathrm{n1}}^{\mathrm{t,c}}}{S_{12}} \sin^2 \Psi \tag{3.119}$$

denotes the ratio between the slope (so called inclination parameter) of the fracture surface $p_{\Psi}^{\mathrm{t,c}}$ at $\sigma_{\mathrm{n}} = 0$ and the term S_{Ψ}, which depends on the angle Ψ (cf. Figure 3.19) and defines a strength value between S_{12} and S_{23}^{ap}. The superscript of the inclination parameter $p^{\mathrm{t,c}}$ denotes two possible cases: tension (t) and compression (c). The strength S_{23}^{ap} does not represent the actual shear strength in the (2,3)-plane. Instead, it defines the resistance of the action plane against τ_{nt} shear stress. This strength can be determined from the transverse compressive strength Y_{C} and the inclination parameter $p_{\mathrm{nt}}^{\mathrm{c}}$ at $\sigma_{\mathrm{n}} = \tau_{\mathrm{n1}} = 0$

$$S_{23}^{\mathrm{ap}} = \frac{Y_{\mathrm{C}}}{2\left(1 + p_{\mathrm{nt}}^{\mathrm{c}}\right)}. \tag{3.120}$$

It is obvious that in case of $\sigma_{\mathrm{n}} = 0$ the failure criterion is reduced to a simple quadratic formulation of the failure envelope in the $(\tau_{\mathrm{n1}}, \tau_{\mathrm{nt}})$-plane. Further, in case of $\sigma_{\mathrm{n}} = 0$ and $\Psi = 0°$ only shear stress τ_{nt} is present and the failure criterion is reduced to a maximum stress criterion (this is also valid in case of $\Psi = 90°$). For $\sigma_{\mathrm{n}} > 0$ and $\tau_{\mathrm{n1}} = \tau_{\mathrm{nt}} = 0$ failure occurs if the normal stress reaches the transverse tensile strength $\sigma_{\mathrm{n}} = Y_{\mathrm{T}}$. While the material strengths required for the failure criterion can be determined from simple uniaxial load cases, the corresponding inclination parameters need experimental results with combined stress loads. For example, $p_{\mathrm{nt}}^{\mathrm{c}}$ can be determined by the knowledge of the fracture angle θ_{fp}. However, the resulting fracture angle is quite difficult to determine considering the fact that the material behavior is brittle. As these parameters are quite challenging to determine, a simplification can be made by assuming $p_{\mathrm{nt}}^{\mathrm{c}} = p_{\mathrm{nt}}^{\mathrm{t}} = p_{\mathrm{nt}}$. Further, a lower bound of the inclination parameter p_{nt} is then defined as follows [9]

$$p_{\mathrm{nt}} \leq \frac{\sqrt{(r+4)^2 + 2\left(r^2 - 4\right)(r+2)} - (r+4)}{2\,(r+2)}, \quad \text{with} \quad r = \frac{Y_{\mathrm{C}}}{Y_{\mathrm{T}}}. \tag{3.121}$$

Using off-axis compressive tests the inclination parameter $p_{\mathrm{n1}}^{\mathrm{c}}$ can be determined [53]. The same procedure can be performed to determine $p_{\mathrm{n1}}^{\mathrm{t}}$ using off-axis tensile tests. If $p^{\mathrm{t}} \neq p^{\mathrm{c}}$ then a kink of the fracture plane at the transition between positive and negative σ_n stress is created. As suggested by BLEIER [18] the inclination parameters p^{t}_{n1} and p^{c}_{n1} (and also p^{t}_{nt} and p^{c}_{nt}) can be equated, as their sensitivity for different values is small. A general recommendation and a more in-depth discussion of the choice of the inclination parameters is given in [9].

In addition to the challenge of determining the material strengths and inclination parameters, the fracture angle has to be also determined by performing a fracture angle search. As previously described, failure is determined by the stresses on the fracture plane. However, this plane is not clearly defined. By rotating the stress using the angle θ, a corresponding curve of the stress exposure f_{IFF} over the angle is achieved. In general, it is suggested to analyze θ in a range of $-90°$ to $90°$. Afterwards the fracture plane is determined by the overall maximum stress exposure f_{IFF}. However, this condition requires a lot of additional computational time. An optimized fracture angle search algorithm has been addressed by WIEGAND et al. [181] and SCHIRMAIER et al. [182]. According to SCHIRMAIER et al. there are up to three possible maxima of the stress exposure f_{IFF} over action plane angle θ_{ap}. Using material data for the AS4/3501-6 unidirectional prepreg material (cf. Table 3.1) and by choosing the corresponding inclination parameters to $p^{t,c}_{nt} = 0.25$ and $p^{t,c}_{n1} = 0.35$, three different stress states are evaluated (cf. Table 3.2). Using the definition of f_{IFF} (cf. Equation (3.118)) a curve for each stress state can be generated (cf. Figure 3.21). It can be seen that the number of stress exposure peaks over action plane angle θ_{ap} varies between 1 and 3. Therefore, it is necessary to know which angle corresponds to the overall maximum stress exposure. To find the overall maximum stress exposure within a precision of 1°, the optimized fracture angle search algorithm by SCHIRMAIER requires up to 36 supporting points instead of 180.

Failure in fiber direction has been determined by several approaches [73, 93–95, 176]. As for the IFF criterion, failure occurs if a failure index exceeds

Table 3.1: Material data for AS4/3501-6 unidirectional prepreg [68]

	Y_T /MPa	Y_C /MPa	S_{12} /MPa
AS4/3501-6	48	200	79

Table 3.2: Three different stress states resulting in different number of maxima for the stress exposure f_{IFF} over action plane angle θ_{ap}

	σ_{22} /MPa	σ_{33} /MPa	σ_{12} /MPa	σ_{13} /MPa	σ_{23} /MPa
stress state 1	34	0	22	46	0
stress state 2	34	-87	22	46	0
stress state 3	34	-87	22	46	25

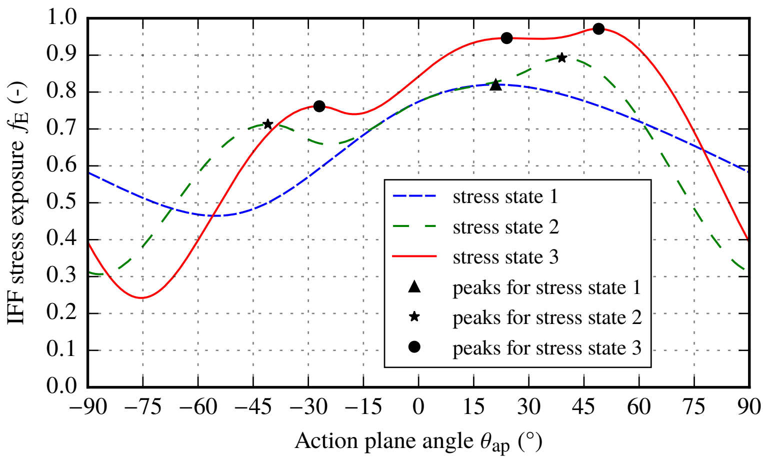

Figure 3.21: Inter-fiber stress exposure f_{IFF} over action plane angle θ_{ap} for three different stress states with up to three maxima

the value of one $f_1 > 1$. While CUNTZE [95] uses a simple maximum stress criterion to determine failure initiation in tensile and compression, others suggest extending such criteria to consider interaction between σ_{11} stress and other stress components. For example, HASHIN's fiber failure criterion [94, 176] is given by

$$\begin{cases} f_{\mathrm{FF}}^{+} = \frac{\sigma_{11}}{X_{\mathrm{T}}} + \frac{\sigma_{12}^2+\sigma_{13}^2}{S_{12}}, & \sigma_{11} \geq 0 \\ f_{\mathrm{FF}}^{-} = \frac{|\sigma_{11}|}{X_{\mathrm{C}}}, & \sigma_{11} < 0 \end{cases} \tag{3.122}$$

which considers the effect of the shear stresses σ_{12} and σ_{13} only in the tensile case. On the other hand the LaRC05 criterion [73] uses a simple maximum stress criterion for fiber tensile failure and considers fiber kinking and splitting as the main source for failure in compression. Here additional knowledge of the initial misalignment angle and a kink band search (comparable to Puck's fracture plane search) are necessary. While Puck used initially also a maximum stress criterion, it was later extended by considering the Poisson's effect due to σ_{22} and σ_{33} loads. However, it was found that in case of plane stress the difference between a maximum stress criterion and its extension to consider σ_{22} and σ_{33} stresses is small. Therefore, for simplicity reasons fiber failure is considered here by a maximum stress criterion

$$\begin{cases} f_{\mathrm{FF}}^{+} = \frac{\hat{\sigma}_{11}}{X_{\mathrm{T}}}, & \hat{\sigma}_{11} \geq 0 \\ f_{\mathrm{FF}}^{-} = \frac{|\hat{\sigma}_{11}|}{X_{\mathrm{C}}}, & \hat{\sigma}_{11} < 0 \end{cases} \tag{3.123}$$

where the trial stress $\hat{\sigma}_{11}$ is used to determine failure initiation for a given strain state.

One further aspect needs to be addressed. The load in fiber direction has an impact on the value of f_{IFF} [183]. If the failure envelope for a combined σ_{22}-σ_{12} stress state is plotted, the σ_{11} stress has no effect on the shape. However, experimental results showed that an interaction between σ_{11} and σ_{12} can be observed [74]. The increase of f_{FF}^{+} or f_{FF}^{-} can be directly incorporated into the updated definition of f_{IFF}. To the initial calculated value of f_{IFF} (here $f_{\mathrm{IFF}}^{\mathrm{init}}$), a weakening parameter is applied which increases the stress exposure in dependence on the value of f_{FF}. The relationship is expressed as follows [183]

$$f_{\mathrm{IFF}} = f_{\mathrm{IFF}}^{\mathrm{init}} / \eta_{\mathrm{w1}} \quad \text{with} \quad \eta_{\mathrm{w1}} = c\left(a\sqrt{c^2\left(a^2-s^2\right)+1}+s\right) / (ca)^2+1 \tag{3.124}$$

where

$$c = f_{\mathrm{IFF}}^{\mathrm{init}} / f_{\mathrm{FF}} \quad \text{and} \quad a = 1-s / \sqrt{1-m^2}. \tag{3.125}$$

The choice of f_{FF} depends on the sign of σ_{11}. This formulation of f_{IFF} affects the shape of the inter-fiber failure envelope with increasing f_{FF} value. The parameter s defines the onset from which the stress in fiber direction has an influence on the failure curve. Further, the parameter m defines the rate at which the failure envelope changes from the onset to the maximum σ_{11} value. Both parameters range is limited to $s = [0, 1]$ and $m = [0, 1]$.

3.5.3 Action Plane based Damage Evolution

Generally continuous fiber reinforced plastics are subjected to in-plane loads. However, in areas with holes or bearings three-dimensional loads occur. While in-plane loads tend to fail at an angle of $\theta_{ap} = 0°$ for transverse tensile and moderate compression loads, only in case of high compression stress σ_{22} stress values the fracture angle will result in a range of 0° to 60°. To consider the direction of the occurring damage at failure initiation, an action plane dependent damage model is derived. Similar attempts have been made by several authors [135, 184–188]. The Gibbs free energy for an orthotropic material is given by

$$\begin{aligned}
\Gamma = \frac{1}{2}\Bigg(&\frac{1}{E_1}\left(\frac{\langle\sigma_{11}^2\rangle}{1-d_1^+} + \frac{\langle-\sigma_{11}^2\rangle}{1-d_1^-}\right) + \frac{\sigma_{22}^2}{(1-d_{m2})\,E_2} + \frac{\sigma_{33}^2}{(1-d_{m3})\,E_3} \\
&+\frac{\sigma_{12}^2}{(1-d_{12})\,G_{12}} + \frac{\sigma_{13}^2}{(1-d_{13})\,G_{13}} + \frac{\sigma_{23}^2}{(1-d_{23})\,G_{23}} \\
&-\frac{\nu_{12}\sigma_{11}\sigma_{22}}{E_1} - \frac{\nu_{13}\sigma_{11}\sigma_{33}}{E_1} - \frac{\nu_{21}\sigma_{22}\sigma_{11}}{E_2} - \frac{\nu_{31}\sigma_{33}\sigma_{11}}{E_3} \\
&-\frac{\nu_{23}\sigma_{22}\sigma_{33}}{(1-d_{m23})\,E_2} - \frac{\nu_{32}\sigma_{33}\sigma_{22}}{(1-d_{m23})\,E_3}\Bigg),
\end{aligned} \tag{3.126}$$

with

$$\begin{aligned}
d_{m2} &= \frac{1}{\sigma_n}\left(\langle\sigma_n\rangle d_2^+ + \langle-\sigma_n\rangle d_2^-\right) \\
d_{m3} &= \frac{1}{\sigma_n}\left(\langle\sigma_n\rangle d_3^+ + \langle-\sigma_n\rangle d_3^-\right) \\
d_{m23} &= \max\{d_{m2}, d_{m3}\}
\end{aligned} \tag{3.127}$$

where $\langle\cdot\rangle$ is the Macaulay bracket operator, which is defined as

$$\langle x\rangle = \frac{x+|x|}{2}, \quad x \in \mathbb{R} \tag{3.128}$$

and allows to distinguish between positive and negative damage evolution. This differentiation is only applied to the damage in fiber and transverse direction. This condition is legitimate since according to numerical studies there is no sensitivity of the damaged shear modulus on the sign of the corresponding shear stress [189]. The derivative of Γ to $\boldsymbol{\sigma}$ leads to the definition of the elastic strain $\boldsymbol{\varepsilon}_{\mathrm{el}}$, while the second derivative yields the damaged material compliance matrix $\boldsymbol{S}_{\mathrm{D}}$. The inverse of the damaged compliance matrix defines the damaged material stiffness matrix $\boldsymbol{C}_{\mathrm{D}}$. Although the damage variables are only on the main diagonal of the compliance matrix, they cause an interaction between each stiffness component (cf. Equation (A.77)). While for transversely isotropic materials the number of material parameters can be reduced to five (cf. Section 3.5.1.1), the number of damage variables cannot be further reduced to achieve direction-dependent damage evolution. To ensure thermodynamic consistent damage evolution, the rate of the energy dissipation during damage propagation must satisfy the condition

$$Y_1^{\pm} \dot{d}_1^{\pm} + Y_2^{\pm} \dot{d}_2^{\pm} + Y_3^{\pm} \dot{d}_3^{\pm} + Y_{12} \dot{d}_{12} + Y_{13} \dot{d}_{13} + Y_{23} \dot{d}_{23} \geq 0 \tag{3.129}$$

where d_i correspond to the direction-dependent damage variables and Y denotes the corresponding thermodynamic damage driving force. The derivatives of Γ to each damage variable yield the corresponding damage driving forces Y_i. Since all derivatives result in the same structure

$$Y = \frac{\partial \Gamma}{\partial d} = \frac{1}{2} \frac{\sigma^2}{(1-d)^2 E} \tag{3.130}$$

and always lead to positive values of Y, the rate of energy dissipation will be positive if damage variables d are nondecreasing functions. This condition can be satisfied by updating damage variables during a time step as follows

$$d = \max\left\{d^{t+\Delta t}, d^t\right\}. \tag{3.131}$$

Further, as for the matrix and fiber constitutive models (cf. Section 3.3.2.1 and 3.4.2.2) damage evolution in compression affects also the resulting stress in tension and yields the following formulation

$$d_i^+ = \max\left\{d_i^+, d_i^-\right\}, \quad m \in \{1, 2, 3\}. \tag{3.132}$$

To consider direction-dependency within the damage evolution law, it needs to be a function of a direction-dependent scalar. Therefore, the failure index itself

($f_{\mathrm{FF}}^{\pm}$ or f_{IFF}) comes handy since it is based on the fracture direction. Based on the presented damage evolution laws in Section 3.3.2.4 the exponential one is used here. This damage evolution law is based on an equivalent strain. However, for the composite it is useful to define this damage evolution law in terms of the failure criteria itself. The benefit from such definition is that the failure criteria already considers complex stress states. To convert the exponential damage evolution law from a strain based one into a failure index one, a uniaxial tensile load case of a linear elastic material in 1D space is used as an example. The uniaxial load case represents the simplest load case and is captured by the failure criterion, which is also capable to consider complex stress states. Furthermore, nonlinearity prior to failure initiation can be neglected in this example as the stress at failure initiation is used. While the fiber failure index $f_{\mathrm{FF}}^{\pm}$ is a maximum stress criterion per se, for a uniaxial tensile load the IFF criterion f_{IFF} is also reduced to a maximum stress criterion. At failure initiation the criterion yields one and leads to the first equation which is needed to convert the damage evolution law

$$f_i \overset{!}{=} 1 = \frac{\sigma_0}{X} \Leftrightarrow \sigma_0 = X \tag{3.133}$$

where $i \in \{\mathrm{FF}, \mathrm{IFF}\}$, σ_0 is the stress at failure initiation and X correspond to the material strength. In a more general case the failure index can be expressed in terms of strains (ε and ε_0) and σ_0 by noticing that the stress can be expressed as $\hat{\sigma} = C\varepsilon = {}^{\sigma_0}/_{\varepsilon_0}\varepsilon$. In conjunction with Equation (3.133) the relation between f_i and strain leads to the second equation for the conversion of the damage evolution law

$$f_i = \frac{\hat{\sigma}}{X} = \frac{\sigma_0 \varepsilon}{\varepsilon_0 X} = \frac{\cancel{X}\varepsilon}{\varepsilon_0 \cancel{X}} \Leftrightarrow \frac{1}{f_i} = \frac{\varepsilon_0}{\varepsilon}. \tag{3.134}$$

If this equation is now plugged into the definition of d_{exp} (see Equation (3.82)) and by noticing that $2g_0 = \sigma_0\varepsilon_0$, the definition of the exponential damage evolution law based on the failure index is obtained

$$\begin{aligned} d_{\mathrm{exp}} &= 1 - \frac{\varepsilon_0}{\varepsilon} \exp\left(-\frac{\sigma_0}{g_{\mathrm{d}}}(\varepsilon - \varepsilon_0)\right) = 1 - \frac{\varepsilon_0}{\varepsilon} \exp\left(-\frac{\sigma_0\varepsilon_0}{g_{\mathrm{d}}}\left(\frac{\varepsilon}{\varepsilon_0} - 1\right)\right) \\ \Leftrightarrow d_{\mathrm{exp}} &= 1 - \frac{1}{f_i} \exp\left(-\frac{\sigma_0\varepsilon_0}{g_{\mathrm{d}}}(f_i - 1)\right) = 1 - \frac{1}{f_i} \exp\left(-\frac{2g_0}{g_{\mathrm{d}}}(f_i - 1)\right). \end{aligned} \tag{3.135}$$

The ratio of g_0 to g_d leads to two limit cases:

- For $g_\mathrm{d} \to \infty$ the exponential function yields one and the damage law results to a constant stress softening one.
- For $g_\mathrm{d} \to 0$ the exponential function yields zero, which leads to a drastic drop of the stress to zero at failure initiation since $d = 1$.

The different damage variables can now be defined by using the derived damage evolution law. For damage variables which are direction-dependent, such as $d_1^\pm$, $d_2^\pm$ and $d_3^\pm$, a case switch need to be defined. For example, using the stress in fiber direction, the components of the damage evolution law for fiber damage can be defined as follows

$$f_1 = \frac{1}{\sigma_{11}}\left(\langle\sigma_{11}\rangle f_\mathrm{FF}^+ + \langle-\sigma_{11}\rangle f_\mathrm{FF}^-\right), \quad g_\mathrm{d} = \frac{1}{\sigma_{11}}\left(\langle\sigma_{11}\rangle g_\mathrm{d}^+ + \langle-\sigma_{11}\rangle g_\mathrm{d}^-\right) \tag{3.136}$$

and

$$g_0 = \frac{1}{2\sigma_{11}}\left(\langle\sigma_{11}\rangle X_\mathrm{T}\varepsilon_0 + \langle-\sigma_{11}\rangle X_\mathrm{C}\varepsilon_0\right) \tag{3.137}$$

where ε_0 defines the strain in fiber direction at failure initiation. This strain can be obtained by solving to ε_{11} using the relationship between σ_{11} and ε_{11} for a uniaxial load at failure. Since the result depends on the modulus E_1, and E_1 depends on the strain ε_{11}, the relationship yields a quadratic polynomial. While fiber damage is defined by the fiber direction, damage evolution in transverse direction is based on the fracture angle θ_fp determined by Puck's failure criterion. Using the normal direction to the fracture plane, which coincide with σ_n, leads to the direction-dependent definition of the damage variable d_n

$$d_\mathrm{n}^\pm = 1 - \frac{1}{f_\mathrm{IFF}}\exp\left(-r_\mathrm{g}\left(f_\mathrm{IFF} - 1\right)\right) \tag{3.138}$$

where r_g defines the ratio of $2g_0$ to g_d. Based on the sign of σ_n the direction of the damage evolution is given ($\sigma_\mathrm{n} \geq 0$ leads to positive damage on the action plane d_n^+ and vice versa). Since d_n is dependent on the fracture angle θ_fp, it has also a direct effect on the definition of d_2 and d_3. For example, fracture angle $\theta_\mathrm{fp} = 0°$ leads to $d_2 = d_\mathrm{n}$ and $d_3 = 0$, while $\theta_\mathrm{fp} = 90°$ leads $d_3 = d_\mathrm{n}$ and $d_2 = 0$ (cf. Figure 3.22a and 3.22b). However, it is not sufficient to use a simple rotation of d_n to obtain d_2 and d_3 for an angle in the range of 0° to 90°, which is shown in the following. Since θ_fp defines the direction of

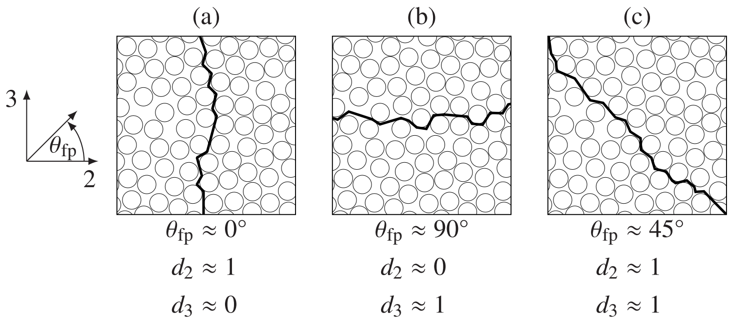

Figure 3.22: Three fracture plane results for $\theta_{fp} = \{0°, 45°, 90°\}$ leading to direction-dependent values of d_2 and d_3 by considering the projected crack area

the occurring crack (cf. Figure 3.22) and d_n is the only nonzero value of the damage tensor, the rotated tensor gives the definition of d_2 and d_3

$$d_2 = \cos^2\left(\theta_{fp}\right) d_n \quad \text{and} \quad d_3 = \sin^2\left(\theta_{fp}\right) d_n. \tag{3.139}$$

In case of $\theta_{fp} = 45°$ and a present crack through the whole ply ($d_n = 1$), the damage values result to the same value $d_2 = d_3 = 0.5$, which indicates that a remaining load capacity is available for loads in 2 or 3 direction. However, this is not the case, since the projected area due to the crack in both directions is equal to the cross section of the evaluated area of the ply (cf. Figure 3.22c). This condition leads to a necessary redefinition of the damage variables d_2 and d_3. Using the projected area of the crack in each direction, a case-dependent definition of d_2 and d_3 yields

$$\begin{aligned} d_2 &= \begin{cases} d_n, & 0° \leq \left|\theta_{fp}\right| \leq 45° \\ \cot^2\left(\theta_{fp}\right) d_n, & 45° \leq \left|\theta_{fp}\right| \leq 90° \end{cases} \\ d_3 &= \begin{cases} \tan^2\left(\theta_{fp}\right) d_n, & 0° \leq \left|\theta_{fp}\right| \leq 45° \\ d_n, & 45° \leq \left|\theta_{fp}\right| \leq 90°. \end{cases} \end{aligned} \tag{3.140}$$

Based on a numerical study using a 0°/90°/0° laminate with one discrete crack through the 90° ply, the resulting reduction of the E_2 and E_3 moduli at varying fracture angle θ_{fp} corresponds to the proposed approach to determine d_2 and d_3

[189]. Furthermore, the same behavior is observed for the corresponding shear damage variables d_{12} and d_{13}. Also, according to this study the remaining out-of-plane shear damage variable d_{23} seems to be not sensitive to transverse cracks and is assumed to remain zero during damage propagation. It should be noted, that the definition of the damage variables d_2 and d_3, according to Equation (3.140), yield from a quadratic region of interest (cf. Figure 3.22). However, other shapes of the region of interest would shift the transition angle (here $\theta_{\mathrm{fp}} = 45°$), which denotes the onset where the damage variable d_2 and d_3 start to change. The definition of in-plane shear damage variables d_{12} and d_{13} is coupled to d_2 and d_3. Regarding the resulting definition of these, there are several approaches available [73, 135, 136, 190]. While some damage models postulate the equality of d_2 and d_{12} during damage propagation, others uses an individual definition of these damage variables. Here the damage variables d_{12} and d_{13} are proposed to be functions of the fracture angle θ_{fp} and the stress expose f_{IFF}. The exact definition of these is discussed in the next section. It should be further noted that due damage evolution severe convergence issues can occur. To overcome such difficulties, a viscous regularization as for the matrix and fiber material model is used. Since anisotropic damage evolution is used, the regularized damage variables are defined by separate viscosity coefficients

$$d_{i,\mathrm{v}_{t+\Delta t}} = \frac{\Delta t}{\Delta t + \mu_{\mathrm{d},i}} d_{i\,t+\Delta t} + \frac{\mu_{\mathrm{d},i}}{\Delta t + \mu_{\mathrm{d},i}} d_{i,\mathrm{v}_t} \tag{3.141}$$

where $i \in \{1, 2, 3, 12, 13\}$.

3.5.4 Damage Variables Interaction

After the material strengths are exceeded, the first cracks appear which influence the material stiffnesses. While damage variable d_1 is not influenced by matrix cracking [191, 192], an interaction between the damage variables d_2 and d_{12} (or d_{n} and $d_{\mathrm{n}1}$ respectively) has been observed by numerical analysis and experimental tests [193–195]. Although transverse and shear modulus are both reduced due to occurring matrix cracks, according to experimental results this degradation is proportional and linear from low to high crack density [194]. Using the ratio of damaged moduli E_2 and G_{12} to the initial undamaged ones

E_2^{init} and G_{12}^{init} defined by $E_2/E_2^{\text{init}} = 1 - d_2$ and $G_{12}/G_{12}^{\text{init}} = 1 - d_{12}$, this relation can be expressed by

$$1 - d_{12} = m\,(1 - d_2) + b \tag{3.142}$$

where m denotes the proportional factor for d_2 to d_{12} and b is the ratio of $G_{12}/G_{12}^{\text{init}}$ at $d_2 = 1$. A visualization of this equation is given in Figure 3.23. Since transverse cracks affect the transverse modulus E_2 more than the in-plane shear modulus G_{12}, d_2 need to be greater than or equal to d_{12}. This limits the range of possible values for $m \in [0, 1]$ and since $b = 1 - m$ also of b. However, this is a simplified formulation due to the fact that in case of $d_2 = 1$ the shear damage variable yields a constant value $d_{12} = 1 - b$. This would imply that for $b \neq 0$, the resulting shear damage variable $d_{12} > 1 - b$ will lead to values greater than one of the transverse damage variable, which is obviously not feasible. To evaluate the bounds of possible solutions for the interaction between d_2 and d_{12} the constant stress softening damage evolution law is used as the upper bound. Using Equation (3.135) at fracture angle $\theta_{\text{fp}} = 0°$, the upper bound of the in-plane shear damage variable d_{12} is defined as

$$d_{12} = 1 - \frac{1}{f_{\text{IFF}}}. \tag{3.143}$$

The transverse damage variable d_2 is then obtained from Equations (3.138) and (3.140)

$$d_2 = 1 - \frac{1}{f_{\text{IFF}}} \exp\left(-r_{\text{g}}\,(f_{\text{IFF}} - 1)\right) \tag{3.144}$$

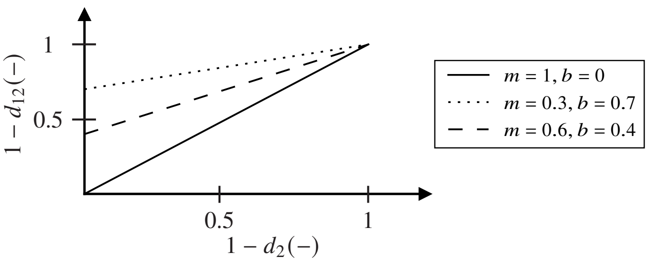

Figure 3.23: Interaction between the damage variables d_2 and d_{12} for different values of m and b

where r_g is the only parameter which allows to define the bounds of d_2 in a valid range. As discussed in Section 3.5.3 the parameter r_g can be in a range between zero and infinity. In case of $r_g = 0$ the damage variables would be equal $d_2 = d_{12}$ and for all values $r_g > 0$ the condition $d_2 > d_{12}$ is satisfied. If this relation is extended to fracture plane dependency, the general definition of d_{12} and d_{13} is obtained

$$
\begin{aligned}
d_{12} &= \begin{cases} 1 - \frac{1}{f_{\text{IFF}}}, & 0^\circ \leq \left|\theta_{\text{fp}}\right| \leq 45^\circ \\ \cot^2\left(\theta_{\text{fp}}\right)\left(1 - \frac{1}{f_{\text{IFF}}}\right), & 45^\circ \leq \left|\theta_{\text{fp}}\right| \leq 90^\circ \end{cases} \\
d_{13} &= \begin{cases} \tan^2\left(\theta_{\text{fp}}\right)\left(1 - \frac{1}{f_{\text{IFF}}}\right), & 0^\circ \leq \left|\theta_{\text{fp}}\right| \leq 45^\circ \\ 1 - \frac{1}{f_{\text{IFF}}}, & 45^\circ \leq \left|\theta_{\text{fp}}\right| \leq 90^\circ. \end{cases}
\end{aligned}
\tag{3.145}
$$

It should be noted that for all other damage evolution law definitions of d_{12} and d_{13} the corresponding bounds for r_g in Equation (3.138) need to be adjusted that the condition $d_2 \geq d_{12}$ is always satisfied.

3.5.5 Effect of the Fiber Volume Content on Nonundulated Composites

The so far presented model is valid for a composite material with nonundulated fibers. During forming process the fabric undergoes large deformation which can lead to thickness or local areal weight deviations. This condition affects the local FVC and therefore the composite material stiffness and strength. In contrast to stiffness and strength, hardening due to plasticity seems to be not affected by the FVC within the evaluated range (cf. Section 2.5.1). In the following subsections the previously presented model is extended by considering FVC-dependent stiffness and strength. Furthermore, the interaction of damage variables and their dependency on the FVC is derived.

3.5.5.1 Material Stiffness at Different Fiber Volume Contents

The initial stiffness of a unidirectional ply with straight fibers can be determined from rules of mixture. The resulting material stiffness must be between upper and lower bounds, which are in the simplest way defined by the Voigt and Reuss bounds. Since the carbon fiber is a transversely isotropic material, five different rules of mixtures are needed to define material stiffness for a given FVC. While there are several analytical homogenization methods (e.g., Mori-Tanaka method, self-consistent scheme, Interaction direct derivative approach) or semi-empirical methods (e.g., Chamis, Förster, Puck, Halpin-Tsai) available to determine the effective material properties of composites, the validity of the results and the complexity of each approach varies. Since the used unidirectional non-crimp fabric alone contains four different constituents (carbon fibers, glas fiber fixation, PES sewing thread and binder) in conjunction with the matrix, the ideal homogenization method would have to consider each constituent as a separate phase. For glass/epoxy composites a comparison of different approaches has been performed by Heidari-Rarani et al. [19]. According to experimental results Halpin-Tsai equations and Chamis model provide a very good agreement for the transverse modulus E_2 and the in-plane shear modulus G_{12}. In general, the Halpin-Tsai equations [84, 85] provide sufficient flexibility regarding the homogenization result, while remaining within the physical possible bounds. These equations are a simplified version of Hill's generalized self-consistent model [86]. The homogenized material stiffness can be expressed according to Halpin-Tsai equations as follows

$$\frac{\bar{p}}{p_\mathrm{m}} = \frac{1 + \zeta\eta\varphi}{1 - \eta\varphi} \tag{3.146}$$

with

$$\eta = \frac{p_\mathrm{f}/p_\mathrm{m} - 1}{p_\mathrm{f}/p_\mathrm{m} + \zeta}, \tag{3.147}$$

where φ is the FVC, $\bar{p}$ is the homogenized composite material modulus, p_f the corresponding fiber modulus, p_m the corresponding matrix modulus and ζ is a measure of reinforcement geometry which depends on loading conditions. The parameter ζ is defined within the range $\zeta \in [0, \infty]$, with the two possible bounds:

- For $\zeta \rightarrow 0$ the series-connected model of material moduli is obtained (aka Reuss bound).
- For $\zeta \rightarrow \infty$ a linear distribution of the material modulus over the FVC can be achieved (aka Voigt bound).

By varying the parameter ζ a wide range of resulting material stiffness can be obtained. For example, for $\zeta = 2$ the resulting material stiffness for $p_\mathrm{f} = 7p_\mathrm{m}$ is given in Figure 3.24.

In fiber direction the parallel-connected model of fiber and matrix stiffness is a suitable approach to approximate the homogenized material stiffness E_1 (and therefore also ν_{12}) This leads the following definition of E_1 and ν_{12}

$$E_1 = (1 - \varphi)\, E_\mathrm{m} + \varphi E_1^\mathrm{f} \tag{3.148}$$

$$\nu_{12} = (1 - \varphi)\, \nu_\mathrm{m} + \varphi \nu_{12}^\mathrm{f}, \tag{3.149}$$

where E_m is the Young's modulus of the matrix, E_1^f is the modulus of the fiber in fiber direction, ν_m is the Poisson's ratio of the matrix and ν_{12}^f is the Poisson's ratio in the (1,2)-plane. Since the carbon fiber shows a nonlinear behavior during loading (cf. Section 3.4.1) the modulus E_1^f in Equation (3.148) represents the static modulus $E_1^\mathrm{f,init}$. To consider nonlinear behavior of the composite in fiber direction for a given FVC, the slope of the modulus over strain m_f needs to be added to the definition of E_1. By replacing E_1^f in

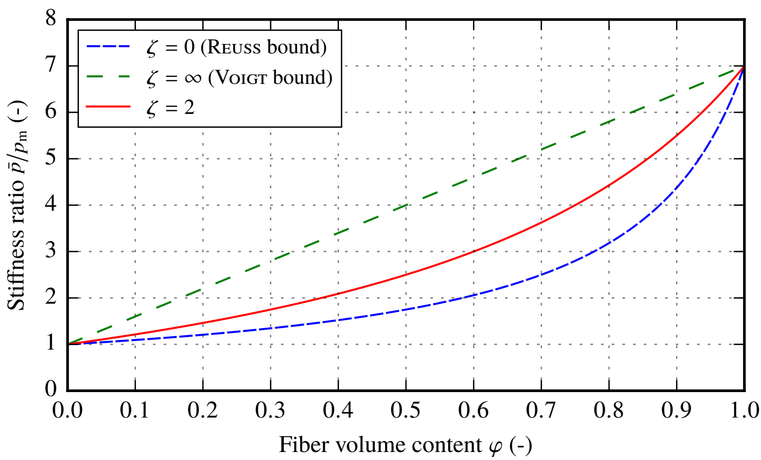

Figure 3.24: Visualization of the Halpin-Tsai equation for three different values of ζ

Equation (3.148) with (3.102) and by noticing that the slope m_{f} is zero for $\varphi = 0$, the stiffness E_1 yields

$$E_1 = (1-\varphi)\, E_{\mathrm{m}} + \varphi \left(E_1^{\mathrm{f,init}} + m_{\mathrm{f}} \varepsilon_{11} \right). \tag{3.150}$$

This condition also affects the definition of ν_{12}. Using Equation (3.104) and replacing the static values $E_1^{\mathrm{f,init}}$ and $\nu_{12}^{\mathrm{f,init}}$ in conjunction with Equations (3.148) to (3.150) the Poisson's ratio ν_{12} yields

$$\nu_{12} = \frac{(1-\varphi)\, \nu_{\mathrm{m}} + \varphi \nu_{12}^{\mathrm{f,init}}}{(1-\varphi)\, E_{\mathrm{m}} + \varphi E_1^{\mathrm{f,init}}} \left((1-\varphi)\, E_{\mathrm{m}} + \varphi \left(E_1^{\mathrm{f,init}} + m_{\mathrm{f}} \varepsilon_{11} \right) \right). \tag{3.151}$$

The remaining composite material stiffnesses E_2, G_{12} and G_{23} are obtained by using Halpin-Tsai equations (cf. Equation (3.146))

$$E_2 = E_{\mathrm{m}} \frac{1 + \eta_{E_2} \zeta_{E_2} \varphi}{1 - \eta_{E_2} \varphi} \quad \text{with} \quad \eta_{E_2} = \frac{E_2^{\mathrm{f}}/E_{\mathrm{m}} - 1}{E_2^{\mathrm{f}}/E_{\mathrm{m}} + \zeta_{E_2}} \tag{3.152}$$

and

$$G_i = G_{\mathrm{m}} \frac{1 + \eta_{G_i} \zeta_{G_i} \varphi}{1 - \eta_{G_i} \varphi} \quad \text{with} \quad \eta_{G_i} = \frac{G_i^{\mathrm{f}}/G_{\mathrm{m}} - 1}{G_i^{\mathrm{f}}/G_{\mathrm{m}} + \zeta_{G_i}} \tag{3.153}$$

where $i \in \{12, 23\}$, E_2^{f} is the modulus of the fiber in transverse direction and G_i is the shear modulus of the fiber in the corresponding plane. The parameters ζ_{E_2} and ζ_{G_i} for $i \in \{12, 23\}$ can be obtained from experimental results.

3.5.5.2 Material Strength at Different Fiber Volume Contents

Modelling failure initiation in composites with varying FVC is one of the main challenges if draping effects are considered. For a given FVC a set of experimental tests can provide a failure envelope to predict failure initiation. On the other hand for varying FVC an analytical solution of each strength component is handy to avoid large number of experimental test. However, there is no uniformly accepted approach available to determine each FVC-dependent strength. This results from a variety of possible combinations of different fabric and resin types. Even for a constant composite part thickness, during deformation of the fabric the areal weight can change and lead to local increase or decrease of the FVC. A homogeneous FVC distribution is generally aimed for. However, with increasing part complexity such aim requires a lot of effort to be achieved.

In general fiber and matrix strength is size dependent. Therefore, the strength of fiber or matrix is described well by a WEIBULL distribution using the characteristic length and the WEIBULL modulus. However, even if the strength distribution of the fiber and matrix is available, the used fabric within the composite material smears this dependency to other fabric specific properties such as intrinsic fiber misalignment. This condition makes an analytical definition of the strength even more challenging. A widely applied approach for tensile strength in fiber direction is derived from an assumption of an average stress distribution. This results in a simple definition of the stress in fiber direction

$$\sigma_{11} = (1 - \varphi)\, \sigma_{\mathrm{m}} + \varphi \sigma_{\mathrm{f}}, \tag{3.154}$$

where σ_{m} and σ_{f} denote the stress of matrix and fiber. The FVC combines the stress of each constituent to the resulting composite stress. Based on the stress in fiber direction and under an assumption of straight fibers, linear elastic behavior of fiber and matrix up to failure and brittle failure of the fiber, the tensile strength of the composite is can be derived from the equation above as

$$X_{\mathrm{T}} = (1 - \varphi)\, \sigma_{\mathrm{m}} \left(\varepsilon_{\mathrm{ft,max}}\right) + \varphi X_{\mathrm{T}}^{\mathrm{f}} \tag{3.155}$$

where the matrix stress σ_{m} is evaluated at fiber failure strain $\varepsilon_{\mathrm{ft,max}}$ and $X_{\mathrm{T}}^{\mathrm{f}}$ is the fiber tensile strength. This equation can be rewritten to

$$X_{\mathrm{T}} = X_{\mathrm{T}}^{\mathrm{f}} \left((1 - \varphi)\, {}^{E_{\mathrm{m}}}\!/_{E_1^{\mathrm{f}}} + \varphi\right) \tag{3.156}$$

and depends only on fiber tensile strength $X_{\mathrm{T}}^{\mathrm{f}}$, matrix modulus E_{m} and E_1^{f} modulus of the fiber. Since the fiber modulus E_1^{f} is dependent on strain in fiber direction ε_{11}, tensile strength in fiber direction can then be expressed in terms of fiber failure strain $\varepsilon_{11,\mathrm{max}}^{\mathrm{f}}$

$$X_{\mathrm{T}} = X_{\mathrm{T}}^{\mathrm{f}} \left((1 - \varphi)\, \frac{E_{\mathrm{m}}}{E_1^{\mathrm{f,init}} + m_{\mathrm{f}} \varepsilon_{11,\mathrm{max}}^{\mathrm{f}}} + \varphi\right). \tag{3.157}$$

Such formulation provides sufficient accurate predictions of the FVC-dependent fiber tensile strength.

While FVC-dependent tensile strength is based on average distribution, compressive strength is more complex. One of the most cited and earliest work on compressive failure is published by Rosen [91]. He suggested that compressive fiber failure is triggered by microbuckling of the fibers. Two possible modes are introduced: in-phase buckling (shear mode, Figure 3.25a) and out-of-phase bucking (extension mode, Figure 3.25b). Using such approach and under assumption of linear elastic behavior of an isotropic fiber and matrix, the composite FVC-dependent compressive strength is given by

$$X_{\mathrm{C}} = \min \left\{ 2\varphi \sqrt{\frac{\varphi E_{\mathrm{m}} E_{\mathrm{f}}}{3\,(1-\varphi)}}, \frac{G_{\mathrm{m}}}{1-\varphi} \right\} \tag{3.158}$$

where E_{m} and G_{m} are the Young's and shear modulus of the matrix, while E_{f} is the isotropic fiber modulus. Here the first term correspond to the solution of the extension mode and the second one to the shear mode. However, an evaluation and comparison of compressive strength prediction models has been performed by Naik et al. [25] where Rosen's model overestimate the compressive strength in the range of 30 % to 70 % FVC by about 200 %. This circumstance led to the model by Lager and June [196] where the shear modulus (or Young's modulus respectively) of the matrix is multiplied by an influence coefficient k_{c}, which must be fitted to experimental results

$$X_{\mathrm{C}} = \min \left\{ 2\varphi \sqrt{\frac{\varphi k_{\mathrm{c}} E_{\mathrm{m}} E_{\mathrm{f}}}{3\,(1-\varphi)}}, \frac{k_{\mathrm{c}} G_{\mathrm{m}}}{1-\varphi} \right\}. \tag{3.159}$$

While this model fits to experimental results, it is still a semi-empirical formulation of the compressive strength. On the other hand, several model based

(a) shear mode (b) extension mode

Figure 3.25: Two possible microbuckling failure modes according to Rosen: shear mode (a) and extension mode (b)

on fiber kinking were developed (e.g., BUDIANSKY model). Such models have also been compared by NAIK et al. [25] and led to a better agreement between analytical models and experimental results. For all kinking models additional information such as fiber misalignment or other geometrical (or strength parameters) are needed. A simplified yet physically feasible model is the BUDIANSKY kinking model. It unifies the ROSEN model and the ARGON kinking criteria [197] for an elastic and ideal plastic composite to the following expression:

$$X_{\mathrm{C}} = \frac{G_{\mathrm{m}}}{(1-\varphi)\left(1+\bar{\phi}/\gamma_{\mathrm{y}}\right)} \tag{3.160}$$

where $\bar{\phi}$ is the fiber misalignment angle and γ_{y} is the yield strain of the composite under longitudinal shear. While $\bar{\phi}$ is considered to be a material property and can be measured from high detailed micrograph images [37], the yield strain is an assumed value based on an elastic-perfectly plastic model. By comparing the available experimental results [170, 198] for different fabric types, the average fiber misalignment angle is in the range of $1°$ to $4°$, while the maximum angle can be up to $8°$ for woven fabrics. In this work the BUDIANSKY model is used, since it requires only one additional parameter $\bar{\phi}/\gamma_{\mathrm{y}}$ to predict physical feasible material behavior over the evaluated range of FVC.

For the remaining material strengths, such as transverse tensile and compressive strength or in-plane shear strength, several analytical models are available [20, 88–90]. These models predict the strength at different fiber volume contents, but they lack of validation by experimental results. A general evaluation of each model is given in Appendix A.1.3.4. As shown and discussed in Section 2.5.1.3 the transverse tensile strength seems to be constant within the evaluated FVC range. On the other hand, the in-plane shear strength shows a slight and the transverse compressive strength significant increase towards high fiber volume contents. This leads to a discrepancy to select one specific analytical model for all strength values. To predict transverse tensile and in-plane shear strength, KAW model [90] seems to be handy, as it provides similar results as the experiments and only requires one additional parameter. For carbon fibers HUANG's model [20] requires the knowledge of transverse tensile strength of the fiber $Y_{\mathrm{T}}^{\mathrm{f}}$, which is currently not possible to be determined experimentally. Therefore, such model provides no benefit to others as the resulting strength is dependent on this parameter. Since energy release rate G_{Ic} is determined from coupon tests, which comes with a high scatter, the geometry of the coupon itself highly affects the obtained values. Therefore, the prediction of BARBERO's energy release rate model [89] would be highly affected by this material parameter. Furthermore, the knowledge of local ply thickness is another parameter, which is not easily available after the manufacturing process. BARBERO's void volume content empirical model at $\varphi_\mathrm{V} = 0\,\%$ (which is equal to CHAMIS model [88]) seems to be suitable to predict transverse compressive strength of the composite at different fiber volume contents, while requiring only one additional parameter. However, the required increase of strength per FVC percent is too small for this model if the prediction is compared to experimental results (cf. Figure 2.12d). In conclusion, it can be summarized that all evaluated analytical models cannot satisfy the required prediction accuracy with a low number of additional parameters. For the experimentally observed results a simple linear correlation seems to be well suited to predict the material strength at a specific FVC. Since the transverse tensile strength Y_T seems to be constant within the evaluated FVC range, a constant strength value over the whole range is used. However, the transverse compressive strength Y_C and the in-plane shear strength S_{12} are defined via a linear function based on the strength at $\varphi = 50\,\%$. The analytical formulation is defined as follows

$$\begin{aligned} Y_\mathrm{C} &= \frac{\partial Y_\mathrm{C}}{\partial \varphi}(\varphi - 0.5) + Y_\mathrm{C}|_{\varphi=0.5} \quad \text{and} \\ S_{12} &= \frac{\partial S_{12}}{\partial \varphi}(\varphi - 0.5) + S_{12}|_{\varphi=0.5} \end{aligned} \tag{3.161}$$

where $\frac{\partial Y_\mathrm{C}}{\partial \varphi}$ and $\frac{\partial S_{12}}{\partial \varphi}$ define the slope of the strength over FVC.

3.5.5.3 Failure initiation at Different Fiber Volume Contents

Using the predicted strength values for a given FVC, the defined failure initiation criteria in Section 3.5.2 can be extended. FVC-dependent failure in fiber direction can be derived by using Equation (3.123), where the material strengths are replaced with the predictions of Equations (3.157) and (3.160). While failure in fiber direction is dependent only on the strength in loading direction, by using PUCK's IFF criteria the Y_T, Y_C and S_{12} strength parameters are connected. For a plane stress load ($\sigma_{33} = \sigma_{13} = \sigma_{23} = 0$) the failure envelope can be given in the $(\sigma_{22}, \sigma_{12})$-plane. Here three different failure modes can be observed: mode A, B and C (cf. Figure 3.26). For plane transverse loads $\sigma_{22} \geq 0$ the fracture plane yields $\theta_{fp} = 0°$ and therefore the fracture plane stress components are given by $\sigma_n = \sigma_{22}$ and $\tau_{n1} = \sigma_{12}$. The first mode A defines the region for plane transverse loads $\sigma_{22} \geq 0$. The failure envelope results from Equation (3.118) by considering that $\tau_{nt} = 0$ since $\theta_{fp} = 0°$. For stress loads $\sigma_{22} < 0$ the fracture angle remains zero until $|\sigma_{22}|/Y_C$ does not exceed a certain threshold. Until this point the mode B can be defined. If the threshold at $|\sigma_{22}|/Y_C$ is exceeded, fracture occurs on a different plane $\theta_{fp} \neq 0°$. Since the strength parameters Y_T, Y_C and S_{12} are functions of the FVC, they need to be redefined in the definition of Puck's failure criteria (see Equation (3.118)). For increasing FVC the fracture surface expands, and it shrinks for decreasing ones. Depending on the sensitivity of each strength parameter the failure surface can be unequally expanded or shrunken. Additionally, to each strength value the inclination parameters p_{n1} and p_{nt} need to be defined as functions of the FVC. The lower bound of p_{nt} (cf. Equation (3.121)) is already dependent on the transverse strength value Y_T and Y_C, which are defined for varying fiber volume contents. Therefore, only the inclination parameter p_{n1} needs to be defined as a function of the FVC. Here a linear approach similar to the transverse compressive strength is used

$$p_{n1} = \frac{\partial p_{n1}}{\partial \varphi} (\varphi - 0.5) + p_{n1}|_{\varphi=0.5}. \tag{3.162}$$

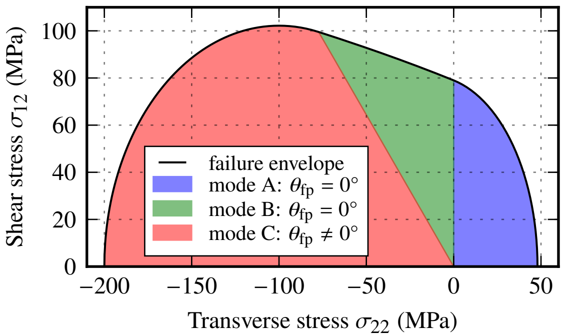

Figure 3.26: Plane IFF failure envelope according to Puck with three possible failure modes A,B and C

A visualization of the failure envelope in the $(\sigma_{22}, \sigma_{12})$-plane is given in Figure 3.27.

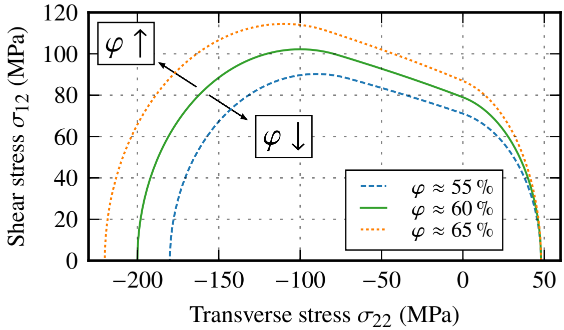

Figure 3.27: Effect of the fiber volume content on the plane IFF failure envelope

3.5.5.4 Damage Evolution at Different Fiber Volume Contents

As shown in Section 3.5.3 damage evolution depends on the failure initiation (f_{FF} or f_{IFF}) and the energy g_{d}. In the case of FVC change the corresponding material strength will change, which has an effect on failure initiation. On the other hand the effect on the energy g_{d} is unknown due to lack of experimental results. It is assumed that in the evaluated FVC range g_{d} remains constant. This assumption can lead to an oversimplification of the resulting damage propagation and needs to be considered in subsequent work. In the case of constant g_{d}, increasing FVC will generate a more abrupt stiffness reduction (which correlates to the reduction of the stress) since σ_0 and thus g_0 in Equation (3.135) increases. If FVC is reduced damage evolution will start earlier, but with retarded progression.

The interaction of damage variables as discussed in Section 3.5.4 needs to be also considered for varying FVC. However, due to lack of experimental data a direct deduction of the effect of the FVC on damage variables interaction cannot be derived. Using a simplified isotropic damage evolution, Fuhr [27] was able to evaluate the degradation of the axial modulus of angle-ply laminates for different fiber volume contents. As a result damage propagation is not affected, but a dependency of the maximum achievable damage variable in conjunction with varying FVC is observed. To evaluate the dependency of damage variables on FVC, an extension of the work of Deuschle [189] using numerical studies with varying number of cracks in a 90° ply of a 0°/90°/0° laminate can be utilized. Such approach will be performed in the following section to evaluate the sensitivity of the parameter r_g from Equation (3.144) against FVC.

3.5.6 Effect of Undulations on the Material Response of Composites

A further major draping effect, which results after forming, is undulation of the rovings. This local direction change of the fiber orientation reduces the local laminate stiffness significantly. Since undulation has such an impact not only on the stiffness but also especially on the strength in fiber direction, there are several publications available. For example, analytical functions to determine the effective elastic parameters of laminates with waviness have been found [118, 199]. Further, the impact of the FVC on the effective elastic parameters has been evaluated using micro-scale models [123]. The model presented here utilizes the analytical approach to determine effective elastic material properties. To determine nonlinear behavior or failure several approaches can be found in [30, 32, 33, 38, 200]. In general, a ply-wise evaluation of the maximum misalignment angle due to waviness is used to predict the failure of the laminate. Previous publications focus on undulation in thickness direction and its effect on the whole laminate. However, for the used fabric in-plane undulation is more likely. In a recent experimental analysis of laminates with imposed waviness an analytical approach to determine the resulting tensile and compression strength in fiber direction has been proposed by the author in [47]. In contrast to other publications, a new developed model that considers in-plane undulations is presented. The model considers a continuous change of the waviness during loading. Additionally, the FVC is considered to determine the effective elastic properties as also the failure strength values. The new model is presented in the following.

3.5.6.1 Effective Elastic Material Parameters

Using simulation methods, undulations can be approximated by assigning different fiber angles to two neighbor elements [27]. This approach depends on the wavelength of the undulation, since the element size must be lower than the half wavelength. Using fine meshes, quite accurate results for stiffness can be achieved, since each slice of the wave is modeled by a separate fiber orientation. For large parts or very local waviness a homogenization of the waviness is more suitable to save computation time. Therefore, the effective elastic material parameters of regions with an imposed waviness are determined. To do so for every applied deformation in the (x, y, z)-space, the corresponding strain $\boldsymbol{\varepsilon}_{\mathrm{x}}$ must lead to the effective stress $\boldsymbol{\sigma}_{\mathrm{x}}$ which considers waviness by utilizing homogenized material properties. To determine these effective material properties, the local transversely isotropic material properties in the $(1, 2, 3)$-space, can be integrated over the wavelength λ. This assumption yield from an infinitesimal slice Δx, where the fiber direction is constant (cf. Figure 3.28). The fiber position along λ is given by

$$y = A \sin \frac{2\pi x}{\lambda} \tag{3.163}$$

where A is the amplitude of the curved fiber. To determine the angle θ of the fiber, which correspond to the fiber direction at position x, the derivative of y to x can be utilized

$$\tan \theta = \frac{\mathrm{d}y}{\mathrm{d}x} = \frac{2\pi A}{\lambda} \cos \frac{2\pi x}{\lambda}. \tag{3.164}$$

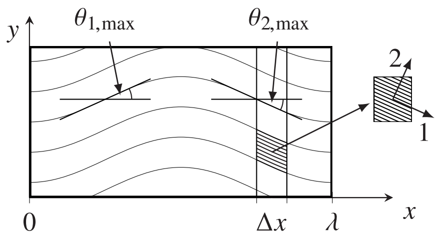

Figure 3.28: Ideal fiber waviness over a full wavelength λ in the (x, y)-plane with corresponding maximal fiber misalignment angles $\theta_{1,\max}$ and $\theta_{2,\max}$

The maximal misalignment angles $\theta_{1,\max}$ and $\theta_{2,\max}$ (cf. Figure 3.28) are located at the turning points of the wave and are defined by amplitude and wavelength

$$\theta_{1,\max} = \theta_{2,\max} = \arctan \frac{2\pi A}{\lambda}. \tag{3.165}$$

The relationship between global strain $\boldsymbol{\varepsilon}_{\mathrm{x}}$ and the resulting global stress $\boldsymbol{\sigma}_{\mathrm{x}}$ for an infinitesimal slice Δx can be obtained by using the effective compliance matrix $\bar{\boldsymbol{S}}$. The relationship between $\boldsymbol{\varepsilon}_{\mathrm{x}}$ and $\boldsymbol{\sigma}_{\mathrm{x}}$ is given by

$$\boldsymbol{\varepsilon}_{\mathrm{x}} = \boldsymbol{R}_{\mathrm{w}}{}^{\top}\boldsymbol{\varepsilon}_1 = \boldsymbol{R}_{\mathrm{w}}{}^{\top}\boldsymbol{S}\boldsymbol{\sigma}_1 = \underbrace{\boldsymbol{R}_{\mathrm{w}}{}^{\top}\boldsymbol{S}\boldsymbol{R}_{\mathrm{w}}}_{\bar{\boldsymbol{S}}}\,\boldsymbol{\sigma}_{\mathrm{x}} \tag{3.166}$$

with $\boldsymbol{R}_{\mathrm{w}}$

$$\boldsymbol{R}_{\mathrm{w}} = \begin{pmatrix} \cos^2\theta & \sin^2\theta & 0 & 2\sin\cos\theta & 0 & 0 \\ \sin^2\theta & \cos^2\theta & 0 & -2\sin\cos\theta & 0 & 0 \\ 0 & 0 & 1 & 0 & 0 & 0 \\ -\sin\cos\theta & \sin\cos\theta & 0 & \cos^2\theta - \sin^2\theta & 0 & 0 \\ 0 & 0 & 0 & 0 & \cos\theta & \sin\theta \\ 0 & 0 & 0 & 0 & -\sin\theta & \cos\theta \end{pmatrix}, \tag{3.167}$$

where $\boldsymbol{S}$ is the material compliance of a transversely isotropic material and θ is the misalignment angle. It should be noted that the compliance $\boldsymbol{S}$, the strain $\boldsymbol{\varepsilon}_{\mathrm{x}}$ and stress $\boldsymbol{\sigma}_{\mathrm{x}}$ in the equation above are written in Nye notation. Each component of the homogenized compliance matrix $\bar{\boldsymbol{S}}$ can now be obtained by integrating over the path defined by the wave [38, 118]

$$\bar{\boldsymbol{S}} = \frac{1}{\lambda}\int_0^{\lambda} \boldsymbol{S}\mathrm{d}x. \tag{3.168}$$

For example, the component $\bar{S}_{\mathrm{xx}}$ of the effective compliance matrix yields

$$\bar{S}_{\mathrm{xx}} = \frac{1}{\lambda}\int_0^{\lambda} \hat{S}_{11}\cos^4\theta + \left(2\hat{S}_{12} + \hat{S}_{44}\right)\sin^2\theta\cos^2\theta + \hat{S}_{22}\sin^4\theta\mathrm{d}x \tag{3.169}$$

where $\hat{S}_{ij}$ are components of the transversely isotropic material compliance matrix (cf. Equation (3.110)). All other components $\bar{S}_{ij}$ of the effective material compliance are given in [201]. To integrate these components first some preparations are needed. From trigonometric relationship following conversions can be made

$$\cos^2\theta = \frac{1}{1+\tan^2\theta} \quad \text{and} \quad \sin^2\theta = \frac{\tan^2\theta}{1+\tan^2\theta}. \tag{3.170}$$

By using Equation (3.164) the expression $\tan^2\theta$ can be substituted by

$$\tan^2\theta = \left(\frac{2\pi A}{\lambda}u\right)^2 \text{ with } u = \cos\frac{2\pi x}{\lambda}. \tag{3.171}$$

The derivative of u yields

$$\frac{\mathrm{d}u}{\mathrm{d}x} = -\frac{2\pi}{\lambda}\sin\frac{2\pi x}{\lambda} = \begin{cases} -\frac{2\pi}{\lambda}\sqrt{1-u^2}, & 0 \le x \le \lambda/2 \\ \frac{2\pi}{\lambda}\sqrt{1-u^2}, & \lambda/2 \le x \le \lambda. \end{cases} \tag{3.172}$$

For example, if the integral of $\cos^4\theta$ is formed by using the previous substitutions, the following result can be obtained

$$\Upsilon_1 = \frac{1}{\lambda}\int_0^\lambda \cos^4\theta \mathrm{d}x = \frac{1}{\pi}\int_{-1}^{1} \frac{\mathrm{d}u}{\left(1+(2\pi A/\lambda u)^2\right)^2\sqrt{1-u^2}} = \frac{1+\frac{1}{2}(2\pi A/\lambda)^2}{\left(1+(2\pi A/\lambda)^2\right)^{3/2}}. \tag{3.173}$$

In the same manner the remaining sin or cos components can be determined and are given in Appendix A.1.3.5. If the results of all integrands are plugged into $\bar{\boldsymbol{S}}$, the homogenized material parameters can be obtained by applying uniaxial stress loads. For example, the inverse of $\bar{S}_{\mathrm{xx}}$ leads to the effective modulus in x-direction. For a composite with induced waviness the material is no longer transversely isotropic but rather orthotropic. All effective material parameters are given in Appendix A.1.3.5. It is obvious that material parameters are only dependent on the ratio of the amplitude A to the wavelength λ and in case of $A = 0$ the transversely isotropic material parameters are recovered.

3.5.6.2 Deformation of a Waviness

In the initial configuration, amplitude and wavelength are known. During deformation these two values can change and must be determined prior to calculation of the effective material parameters. For a given vector $\boldsymbol{\lambda}^{\mathrm{init}}$, which initially corresponds to the x-direction (cf. Figure 3.29a), the length of the deformed vector $\boldsymbol{\lambda}$ corresponds to the updated wavelength

$$\lambda = \|\boldsymbol{\lambda}\| = \|\boldsymbol{F}\boldsymbol{\lambda}^{\text{init}}\| \tag{3.174}$$

where $\boldsymbol{F}$ is the deformation gradient.

Additionally, if the amplitude is defined by the vector $\boldsymbol{A}^{\text{init}}$, after deformation the corresponding amplitude A results from the shortest distance between $\boldsymbol{\lambda}$ and $\boldsymbol{A}$

$$A = \frac{\|\boldsymbol{\lambda} \times \boldsymbol{A}\|}{\lambda} \tag{3.175}$$

with

$$\boldsymbol{A} = \boldsymbol{F}\boldsymbol{A}^{\text{init}}. \tag{3.176}$$

The ratio A/λ of the updated amplitude and wavelength are utilized to determine the effective elastic properties of the composite. It should be noted that due to deformation the initial maximum misalignment angles $\theta_{1,\max}^{\text{init}}$ and $\theta_{2,\max}^{\text{init}}$ can change and be different to each other (cf. Figure 3.29).

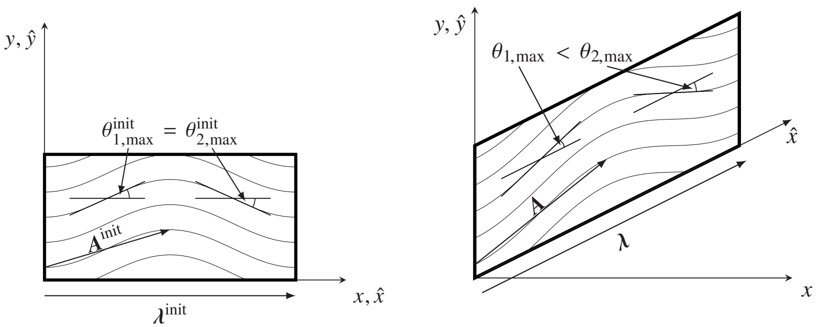

(a) Initial waviness

(b) Deformed waviness

Figure 3.29: Deformation of a representative area with waviness and the corresponding deformed vectors $\boldsymbol{\lambda}$ and $\boldsymbol{A}$ with the resulting maximal misalignment angles $\theta_{1,\max}$ and $\theta_{2,\max}$

3.5.6.3 Homogenized Stress Response of a Waviness

As described before, a waviness can be approximated by two opposing fiber direction angles. Previous publications have used the maximum misalignment angle to calculate off-axis stress states, which lead to the effective stress response of a waviness [32, 118, 200]. However, these approaches use only one angle instead of two angles. As shown in Figure 3.29b, due to deformation of the wave a difference between the maximum misalignment angles can occur. Therefore, an approach which considers both angles is presented here. The process to determine the homogenized stress response due to waviness is visualized in Figure 3.30 and explained in the following.

Initially the amplitude to wavelength ratio A/λ and the applied strain $\boldsymbol{\varepsilon}_{\mathrm{x}}$ are known (cf. Figure 3.30a). Based on the initial ratio A/λ an updated ratio is calculated as described above. The strain $\boldsymbol{\varepsilon}_{\mathrm{x}}$ is derived using the same procedure as for areas with straight fibers. It should be noted that the strain also considers the deformation of the initial material axes. To consider both maximum misalignment angles, first the effective trial stress $\hat{\boldsymbol{\sigma}}_{\mathrm{x}}$ of the waviness

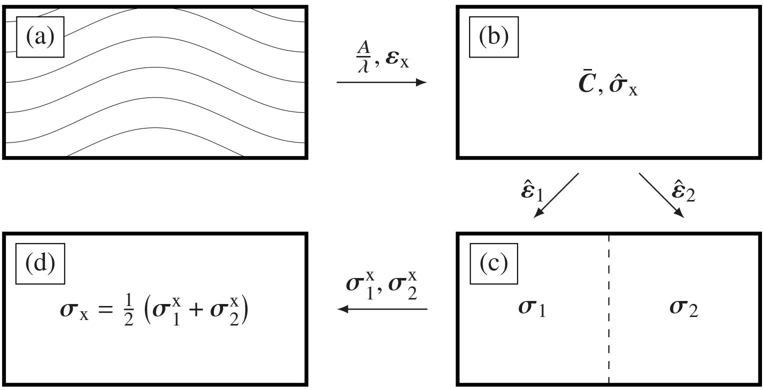

Figure 3.30: Homogenization steps of a waviness to determine the effective stress response: (a) initial model providing effective strain $\boldsymbol{\varepsilon}_{\mathrm{x}}$ and amplitude to wavelength ratio A/λ; (b) homogenized elastic trial stress $\hat{\boldsymbol{\sigma}}_{\mathrm{x}}$ providing local trial strain $\hat{\boldsymbol{\varepsilon}}_1$ and $\hat{\boldsymbol{\varepsilon}}_2$; (c) local stress $\boldsymbol{\sigma}_1$ and $\boldsymbol{\sigma}_2$ of a waviness providing the transformed effective stress $\boldsymbol{\sigma}_1^{\mathrm{x}}$ and $\boldsymbol{\sigma}_2^{\mathrm{x}}$; (d) homogenized stress of a waviness $\boldsymbol{\sigma}_{\mathrm{x}}$

is determined (cf. Figure 3.30b). This trial stress can be obtained from the applied strain $\boldsymbol{\varepsilon}_{\mathrm{x}}$ and the effective material stiffness $\bar{\boldsymbol{C}}$. The effective material stiffness $\bar{\boldsymbol{C}}$ defines an orthotropic material behavior (cf. Equation (3.110)) and is based on effective material parameters. As described in Section 3.5.6.1, each effective material parameter is a function of the amplitude to wavelength ratio A/λ and the local material properties of a transversely isotropic material. Additionally, the local material properties take the FVC into account, which enable the FVC-dependent waviness modeling. The definition of each effective material parameter is given in Appendix A.1.3.5.

To consider both waviness angles, an imaginary cut of the volume into two equal volumes is performed (cf. Figure 3.30c). Based on the effective trial stress, the local trial strain $\hat{\boldsymbol{\varepsilon}}_1$ and $\hat{\boldsymbol{\varepsilon}}_2$ for each volume can be obtained. The local trial strain is the product of the local trial stress $\hat{\boldsymbol{\sigma}}_i$ ($i \in 1, 2$) and the undamaged compliance matrix $\boldsymbol{S}$ (cf. Equation 3.110). However, at first the local trial stress needs to be obtained from the effective trial stress. By transforming the effective trial stress to the local direction, the required local trial stress can be determined. The corresponding local directions are defined by the maximum misalignment angles $\theta_{1,\max}$ and $\theta_{2,\max}$ (cf. Figure 3.29b). The waviness is initially present in the (x,y)-plane and it is assumed that due to deformation it remains in the $(\hat{x},\hat{y})$-plane. Using Equation (3.165) the initial misalignment vectors $\boldsymbol{x}_1^{\mathrm{init}}$ and $\boldsymbol{x}_2^{\mathrm{init}}$ are given in the (x,y)-plane by

$$\boldsymbol{x}_1^{\mathrm{init}} = \begin{pmatrix} 1 & \frac{2\pi A}{\lambda} & 0 \end{pmatrix}^{\top} \quad \text{and} \quad \boldsymbol{x}_2^{\mathrm{init}} = \begin{pmatrix} 1 & -\frac{2\pi A}{\lambda} & 0 \end{pmatrix}^{\top} \tag{3.177}$$

while the perpendicular vectors $\boldsymbol{y}_1^{\mathrm{init}}$ and $\boldsymbol{y}_2^{\mathrm{init}}$ yield

$$\boldsymbol{y}_1^{\mathrm{init}} = \begin{pmatrix} -\frac{2\pi A}{\lambda} & 1 & 0 \end{pmatrix}^{\top} \quad \text{and} \quad \boldsymbol{y}_2^{\mathrm{init}} = \begin{pmatrix} \frac{2\pi A}{\lambda} & 1 & 0 \end{pmatrix}^{\top}. \tag{3.178}$$

These vectors define the local maximum misalignment, which correlates with the local material direction. By applying a deformation, the direction of the vectors can change. As a result the deformed vectors ($\boldsymbol{x}_1$, $\boldsymbol{x}_2$, $\boldsymbol{y}_1$ and $\boldsymbol{y}_2$) may be no longer perpendicular to each other and have additional stretching. These vectors can be used to form transformation matrices $\boldsymbol{R}_{1,\max}$ and $\boldsymbol{R}_{2,\max}$. The transformation matrices define the change of the reference system from the $(\hat{\boldsymbol{x}}, \hat{\boldsymbol{y}}, \hat{\boldsymbol{z}})$-space to the $(\boldsymbol{x}_i, \boldsymbol{y}_i, \boldsymbol{z}_i)$-space. However, the deformed vectors ($\hat{\boldsymbol{x}}, \hat{\boldsymbol{y}}, \hat{\boldsymbol{z}}$ and $\boldsymbol{x}_i, \boldsymbol{y}_i, \boldsymbol{z}_i$) must be normalized beforehand. It should be noted that the through thickness direction is equal for both local sections $\hat{\boldsymbol{z}} = \boldsymbol{z}_1 = \boldsymbol{z}_2$. To calculate the components of the transformation matrices $\boldsymbol{R}_{1,\max}$ and $\boldsymbol{R}_{2,\max}$, Equation (3.22) can be used. Since the stress is given in vector notation, the transformation matrices are rewritten to 6×6 transformation matrices $\boldsymbol{T}_i$ ($i \in 1, 2$). By applying the transformation matrices to the trial stress $\hat{\boldsymbol{\sigma}}_{\mathrm{x}}$ and by using the undamaged compliance matrix $\boldsymbol{S}$, the local trial strains $\hat{\boldsymbol{\varepsilon}}_1$ and $\hat{\boldsymbol{\varepsilon}}_2$ are obtained.

Next step is to calculate the local stress response $\boldsymbol{\sigma}_1$ and $\boldsymbol{\sigma}_2$ (cf. Figure 3.30c). Using the trial strain $\hat{\boldsymbol{\varepsilon}}_1$ and $\hat{\boldsymbol{\varepsilon}}_2$ and the developed material model for straight fibers, the local stress response is obtained. The model for straight fibers covers the local nonlinear behavior and failure mechanisms, such as plasticity or fiber and inter-fiber failure. Additionally, the FVC defines the local strength values and is used within the failure criteria. This approach allows to model waviness and simultaneously consider FVC and nonlinear material behavior of the composite. The local stress needs to be transformed back to the $(\hat{\boldsymbol{x}}, \hat{\boldsymbol{y}}, \hat{\boldsymbol{z}})$-space to define the effective stress response of the waviness. Using the inverse of transformation matrices $\boldsymbol{R}_{i,\max}^{-1}$ allows to form the 6×6 back transformation matrices $\tilde{\boldsymbol{T}}_i$. The transformed effective stress $\boldsymbol{\sigma}_1^{\mathrm{x}}$ and $\boldsymbol{\sigma}_2^{\mathrm{x}}$ are obtained by applying $\tilde{\boldsymbol{T}}_1$ and $\tilde{\boldsymbol{T}}_2$ to the corresponding local stress $\boldsymbol{\sigma}_1$ and $\boldsymbol{\sigma}_2$.

Finally the homogenized stress response of the waviness $\boldsymbol{\sigma}_{\mathrm{x}}$ can be determined. Since the two imaginary volumes are equal in size, the volumetric homogenization leads to simple mean values of the stress components $\boldsymbol{\sigma}_1^{\mathrm{x}}$ and $\boldsymbol{\sigma}_2^{\mathrm{x}}$ as the results for $\boldsymbol{\sigma}_{\mathrm{x}}$ (see Figure 3.30d). In general, the whole calculation process can be defined as

$$\boldsymbol{\sigma}_{\mathrm{x}} = {}^1\!/\!{}_2 \left(\boldsymbol{\sigma}_1^{\mathrm{x}} + \boldsymbol{\sigma}_2^{\mathrm{x}} \right) \tag{3.179}$$

with

$$\begin{aligned} \boldsymbol{\sigma}_1^{\mathrm{x}} &= \tilde{\boldsymbol{T}}_1 \boldsymbol{C}_{\mathrm{D}}^{(1)} \hat{\boldsymbol{\varepsilon}}_1^{\mathrm{el}} = \tilde{\boldsymbol{T}}_1 \boldsymbol{C}_{\mathrm{D}}^{(1)} \boldsymbol{S} \hat{\boldsymbol{\sigma}}_1 = \tilde{\boldsymbol{T}}_1 \boldsymbol{C}_{\mathrm{D}}^{(1)} \boldsymbol{S} \boldsymbol{T}_1 \hat{\boldsymbol{\sigma}}_{\mathrm{x}} = \tilde{\boldsymbol{T}}_1 \boldsymbol{C}_{\mathrm{D}}^{(1)} \boldsymbol{S} \boldsymbol{T}_1 \bar{\boldsymbol{C}} \boldsymbol{\varepsilon}_{\mathrm{x}} \\ \boldsymbol{\sigma}_2^{\mathrm{x}} &= \tilde{\boldsymbol{T}}_2 \boldsymbol{C}_{\mathrm{D}}^{(2)} \hat{\boldsymbol{\varepsilon}}_2^{\mathrm{el}} = \tilde{\boldsymbol{T}}_2 \boldsymbol{C}_{\mathrm{D}}^{(2)} \boldsymbol{S} \hat{\boldsymbol{\sigma}}_2 = \tilde{\boldsymbol{T}}_2 \boldsymbol{C}_{\mathrm{D}}^{(2)} \boldsymbol{S} \boldsymbol{T}_2 \hat{\boldsymbol{\sigma}}_{\mathrm{x}} = \tilde{\boldsymbol{T}}_2 \boldsymbol{C}_{\mathrm{D}}^{(2)} \boldsymbol{S} \boldsymbol{T}_2 \bar{\boldsymbol{C}} \boldsymbol{\varepsilon}_{\mathrm{x}} \end{aligned} \tag{3.180}$$

where the damaged stiffness matrix $\boldsymbol{C}_{\mathrm{D}}^{(i)}$ considers damage evolution and $\hat{\boldsymbol{\varepsilon}}_i^{\mathrm{el}}$ results from the plasticity model. For a rapid convergence of the constitutive model, which considers waviness, the consistent tangent operator is needed and is derived in Appendix A.1.3.6.

3.5.7 Summarizing Flowcharts of the Constitutive Model

The constitutive model for regions with a waviness and for regions with straight fibers performs several calculation steps. A flowchart for the whole constitutive model which considers draping effects, with two misalignment angles to define waviness and varying FVC is given in Figure 3.31. Additionally, the flowchart for the transversely isotropic material considering material nonlinearities, failure initiation and damage propagation, which is used by the waviness constitutive model, is given in Figure 3.32.

Compared to previously published models the developed model can process information of draping effects. These very important input draping information allows continuous composites to be modeled more realistically. In general, the usage of deformed material axes is crucial, as experimental results show a significant change. Further, the combination of the provided strain measure with material nonlinearity (such as carbon fiber-specific nonlinearity, action plane plasticity and direction dependent damage evolution) is implemented here for the first time. Especially the intense evaluation of the available FVC-dependent experimental data leads to the conclusion that for IFF the provided linear functions of FVC-dependent material parameters are sufficient. Finally, the continuous change of the waviness for both maximum misalignment angles based on the deformation of the material is considered.

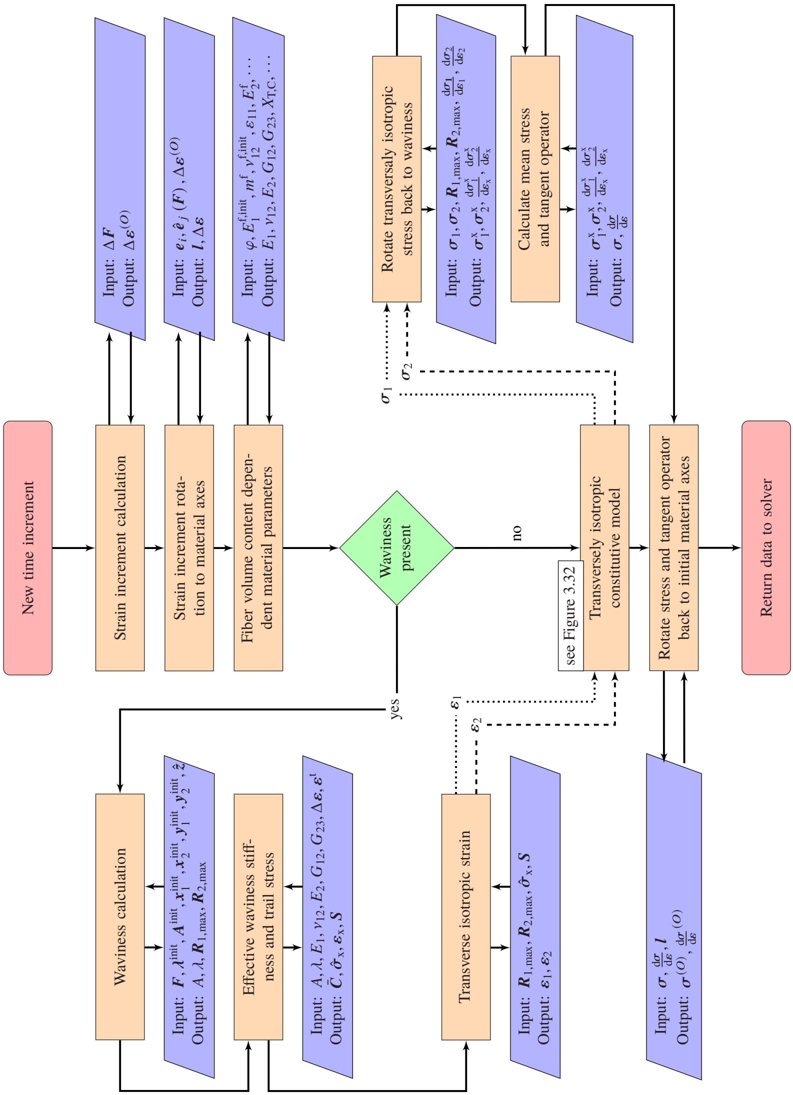

Figure 3.31: Flowchart of the composite constitutive model considering FVC and waviness by using the developed constitutive model for transversely isotropic materials

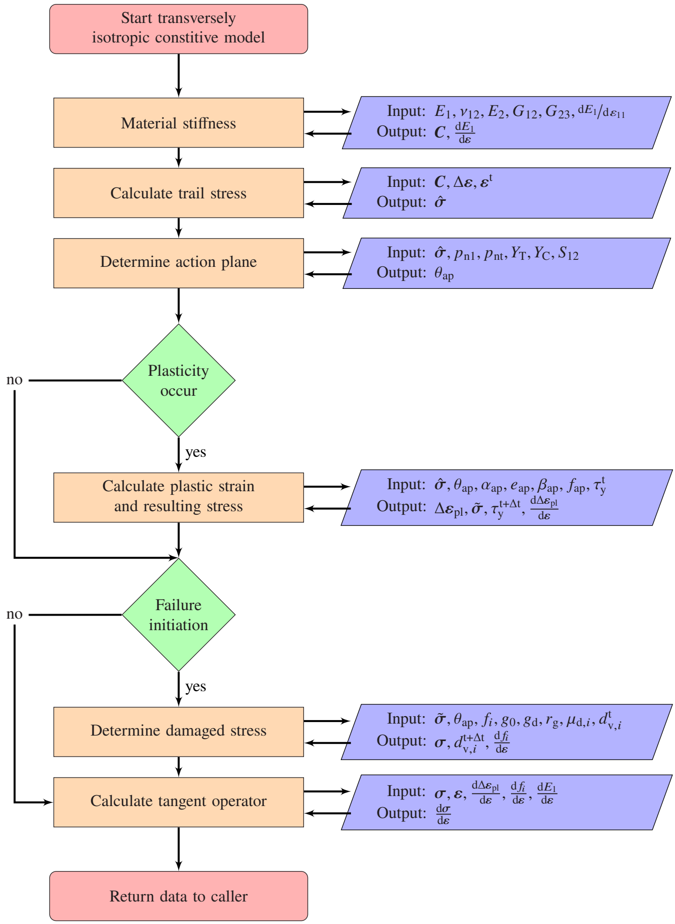

Figure 3.32: Flowchart of the constitutive model for transversely isotropic materials considering nonlinear material behavior, failure initiation and damage propagation

4 Virtual Process Chain for Composites considering Draping Effects

4.1 Literature Review

The holistic view of the manufacturing process provides a major advantage regarding reliable structure simulation results. To do so, the outcome of each manufacturing step must be known. To consider draping effects two possible ways are available: experimental measurement and simulation of the draping process. There are several approaches to experimentally analyze the deformed fabric after the draping step [27, 202–206]. However, in general, such methods demand high effort, while providing only the fiber orientation as a homogenized result. The actual deformation of the fabric is not available. Additionally, the inner plies are in general not evaluated at all. On the other hand, the actual deformation of the fabric for all plies can be obtained by using draping simulation methods. There are several approaches available to model the draping process [2, 59, 207–211]. Especially the model developed by Schirmaier [2, 3] provides reliable results for the UD-NCF material, which is used in the present work [4].

Since the deformation of the fabric during the forming process has the most impact on the resulting draping effects, the draping simulation is best suited to obtain the necessary data for the structural simulation. By transferring the simulation results of one manufacturing step to the next, one follows the realistic manufacturing process of composite parts. Such virtual process chains are under ongoing research and have been applied in several composite development processes [1, 27, 75–77, 212]. In general, the meshes of the different simulation steps are not equal and the resulting data need to be mapped. There are several mapping algorithms available, which allow transferring scalars, vectors, and tensorial data [213, 214]. It is one thing to develop a constitutive model which considers draping effects, but the results of such a model are strongly dependent on the input data. Such data can be influenced by the mapping step, but also by the previous simulation results, which serve as input for the mapping process. As the input data is obtained from draping simulations, these have to be validated based on experimental results. By using macroscopic draping models, a homogenization step of the fabric is already performed. Especially in the case of UD-NCF materials, which consist of several components, such macroscopic models have some limitations regarding occurring gaps within the fabric or other comparable deformations of the fabric. However, these limitations do not outweigh the enormous advantage over a conventional design of fiber composite components. In a conventional design process the fiber orientation is provided, either by a kinematic draping algorithm or by a simple projection of the initial fiber orientation of the fabric to the composite part. Such approaches do not consider the actual material behavior of the fabric and can lead to erroneous results. Additionally, draping simulations provide information about the local deformation which may cause a change of the FVC or may induce fiber waviness.

If the influence of the manufacturing process is taken into account for structural simulation, a much better prediction of the resulting stiffness and strength can be achieved [1, 27, 215]. However, to provide the necessary information to the structural simulation model, the used FEA-software can have some limitations. First, it must be possible to use a user-defined material model. Second, it must be possible to provide the mapping data to this model. Third, it must be possible to save the read-in data permanently in order not to unnecessarily extend the runtime of the simulation. By using the FEA-software Abaqus it is possible to implement user-defined material models and compare different approaches to import the mapped data [216]. However, the mapping methods used have spent most of the simulation time reading the data. Therefore, a new method must be found to reduce this bottleneck. Since the fiber orientation, the fiber volume content and fiber waviness are to be taken into account in the structural simulation, these data must be obtained from the draping simulation. To do so, new methods must be developed to process macroscopic draping simulation results.

4.2 Evaluation and Processing Draping Simulation Results

4.2.1 Obtaining the Fiber Orientation

The material properties of transversely isotropic materials are defined corresponding to the fiber orientation. Therefore, it is a major aspect to predict the local fiber orientation to obtain reliable simulation results. The fiber orientation is primarily defined by the used fabric and its orientation within the reference coordinate system of the composite part. During the draping process, due to the deformation of the fabric, the fiber orientation may change. There are several possibilities to approximate fiber orientation. One of them is the projection of the initial fiber orientation of the fabric on to the composite part. Here the quality of the projection is highly dependent on the geometry itself. For example, the prediction quality of the fiber orientation for plane components with almost no height gradients will be quite high. However, with increasing part complexity, especially in double curved areas, the fabric will be more subjected to shear deformation modes which result in a reorientation of the initial fiber direction that cannot be captured by a pure projection. Another possibility is to obtain the fiber orientation results from kinematic draping algorithms. Such a method uses a mathematical approach that considers the geometry of the components and assumes a dominant shear mode, being either pure shear (for woven fabrics) or simple shear (for UD fiber reinforcements). However, the quality of the results is highly dependent on the choice of the starting point [217]. Further, the results are more accurate if woven fabrics are used and if the occurring shear deformation does not get close to the critical shearing angle. On the other hand, such methods are less accurate for UD-NCF materials since the fabric can undergo different deformation modes such as stretching or compression of the sewing. Therefore, draping simulation methods are more suitable. Such models allow considering the actual material behavior of the fabric. With increasing computational power, the required time to obtain results is manageable. Another major advantage of FE-based draping simulation models, besides the fiber orientation itself, is the capability to predict local draping effects such as varying FVC or fiber waviness.

The fiber orientation resulting from draping simulation models depends on the used mesh. For example, shell elements are quite useful to determine the in-plane deformation [2, 207, 208]. However, in such a case the material behavior of the fabric through the thickness cannot be determined. Therefore, the 2D modeling approach limits a more accurate prediction of the fabric volume change during deformation but provides a reliable prediction of the fiber orientation. Initially, the fiber orientation within the fabric is defined and its change is tracked during deformation. To do so the deformation gradient $\boldsymbol{F}$ is utilized. For any initial fiber orientation $\boldsymbol{f}_1^{\text{init}}$ the deformed fiber orientation $\boldsymbol{f}_1$ is given by

$$\boldsymbol{f}_1 = \boldsymbol{F}\boldsymbol{f}_1^{\text{init}}. \tag{4.1}$$

For example, if the initial fiber orientation corresponds to the $\boldsymbol{x}$-axis, after the deformation the fiber orientation corresponds to the first column of the deformation gradient. In general, material axes are expressed as unit vectors, therefore, the fiber orientation also needs to be normalized. The usage of the deformation gradient to determine the actual fiber orientation is crucial as shown in Section 3.2.

4.2.2 Methods to Determine Fiber Volume Content

The FVC has a major impact on the resulting mechanical properties of composites. As shown previously the FVC for UD-NCF can be determined by the knowledge of the fabric areal weight and the ply thickness (cf. Equation (2.2)). During deformation of the fabric, the initial area weight of the fabric can change [50]. By defining the cavity height of the tool, the laminate thickness is set. Knowing this information, the resulting FVC can be predicted. The shell element-based draping simulation models provide the capability to predict the change of the areal weight of the fabric. As this material property consists of two parameters, the reference area, and the fabric areal weight, only the area change can be determined from the draping simulation. The weight of the fabric is assumed to be constant for each element. By utilizing the in-plane deformation gradient $\boldsymbol{F}$ (third row and column of the deformation gradient are neglected), the resulting area can be determined as follows

$$A_{\text{f}} = \det(\boldsymbol{F})A_{\text{f}}^{\text{init}} = (F_{11}F_{22} - F_{12}F_{21})\,A_{\text{f}}^{\text{init}} \tag{4.2}$$

where $A_{\text{f}}^{\text{init}}$ is the reference area and F_{ij} are the components of the deformation gradient. To determine the FVC, Equation (2.2) is utilized. By extending the definition of the areal weight m_w to its parameters, fabric weight m_0, and reference area A_f, and by utilizing the equation above, a new definition of the FVC is derived

$$\varphi = \frac{m_0}{A_\mathrm{f}} \frac{n_\mathrm{L}}{\rho_\mathrm{f} t_\mathrm{L}} = \frac{m_0}{\det(\boldsymbol{F}) A_\mathrm{f}^\mathrm{init}} \frac{n_\mathrm{L}}{\rho_\mathrm{f} t_\mathrm{L}} = \frac{\varphi_0}{\det(\boldsymbol{F})} \tag{4.3}$$

where φ_0 is the initial FVC for a specific areal weight of the fabric and a specific laminate thickness. It is obvious that in the case of reduced reference area ($\det(\boldsymbol{F}) < 1$), the fiber volume increases and is reduced the other way around. In any case such approach has been experimentally evaluated and shows a very good correlation with the prediction of the draping simulation models [50]. However, by assuming a certain laminate thickness, the compactability of the fabric, which is a common material behavior, is not taken into account. As the fabric can undergo a thickness change and each single ply can undergo different thickness change, this material behavior also needs to be considered providing more accurate predictions of the FVC [55, 56].

4.2.3 Deduction of Occurring Fiber Waviness

As shown by experimental results, fiber waviness has an impact on stiffness and strength. Therefore, it is crucial to provide such information to the structural simulation. In contrast to the fiber orientation and the FVC, the local occurring fiber waviness is more challenging to determine. As waviness represents a local variation of the fiber orientation, the resulting amplitude and wavelength ratio must be determined. It is easier to express the waviness in terms of piecewise changes of the fiber orientation. In such a case, a fine FE-mesh must be used to avoid any loss of manufacturing process information. To consider this piecewise fiber orientation change in the structural simulation, the mesh needs to be also fine. This condition leads to long simulation runtime, which is in general counterproductive in terms of an efficient design process. A simplified approach expressing waviness in terms of two adjacent complementary vectors has been already used [27]. Such an approach is highly mesh-size-dependent. For example, by choosing a mesh size of 5 mm, a wavelength of 10 mm can be expressed by two neighboring elements. Additionally, such an approach neglects the fact that the used macroscopic draping simulation model represents a homogenized material behavior of the fabric. Therefore, it cannot be guaranteed that each homogenized element also reflects a state without any present waviness.

Since waviness occurs in areas where the rovings are compressed, the resulting strain in fiber direction ε_{11} is evaluated. By assuming an initially straight roving, a negative strain in fiber direction leads to an undulation. To determine the resulting amplitude and wavelength the following approach is used

$$\frac{A}{\lambda} = \begin{cases} f\left(s_\lambda, \varepsilon_{11}\right), & \varepsilon_{11} < 0 \\ 0, & \varepsilon_{11} \geq 0 \end{cases} \tag{4.4}$$

where the function $f\left(s_\lambda, \varepsilon_{11}\right)$ returns the amplitude to wavelength ratio based on the initial arc length s_λ and the acting strain in fiber direction ε_{11}. To define such a function, it is assumed that in the case of a straight roving ($A = 0$) and no applied strain in fiber direction ($\varepsilon_{11} = 0$), the wavelength λ corresponds to the initial arc length s_λ. For an initially straight roving, the initial arc length defines the length of the observed roving that forms a waviness when compression occurs. As the A/λ ratio is a dimensionless quantity, the choice of the initial arc length is arbitrary. If the roving is compressed, a waviness is formed, leading to a reduction of the wavelength, while the arc length remains the same. To determine the wavelength, the strain in fiber direction is utilized

$$\lambda = \left(1 + \varepsilon_{11}\right) \lambda^{\text{init}} \tag{4.5}$$

where λ^{init} correspond to the initial wavelength. As the wavelength and the arc length are known, only the corresponding amplitude A needs to be determined. By using Equation (2.14) the inverse of the elliptic integral of the second kind need to be solved to obtain the amplitude. However, an analytical solution of the inverse is not known. Therefore, an iterative method is used (e.g., Newton-Raphson method). A visualization of the resulting amplitude to wavelength ratio A/λ as a function of the acting fiber direction stain is given in Figure 4.1. It is obvious that even small strain values lead to an immediate increase of the A/λ ratio. Such an approach can be used as a simple estimation of the occurring waviness. However, by using macroscopic draping simulation models, the material behavior of the fabric in fiber direction needs to be modeled more accurately. This means that the material behavior itself is actually influenced by the occurring waviness, leading to nonlinear behavior of the modulus in

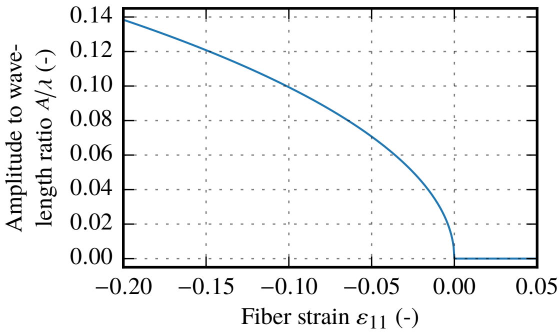

Figure 4.1: Resulting amplitude to wavelength ratio A/λ vs fiber direction strain ε_{11} using draping simulation results

fiber direction and an additional in-plane bending of the roving. Therefore, this condition has to be kept in mind while using the described method above.

4.3 Gathering Data from Draping Simulation

The deformed fabric provides the input data for the structural simulation. Since the meshes of the draping and structural simulations differ, a mapping step that transfers data from one mesh to another is needed. To do so, the draping simulation data containing information about fiber orientation, the FVC, and the fiber waviness need to be extracted. The VTK file format [218] is used to export the data to a neutral format, which can be read by a mapping tool. The file format provides sufficient flexibility to export different elements (e.g., shell or solid elements) or data types (e.g., scalars, vectors, or tensors). Following the VTK definitions, the nodes, and their connectivity to form a mesh are needed. After the mesh is defined, the data obtained from the draping simulation is assigned to each element. In general, a laminate contains multiple plies and the data need to be mapped ply-wise. The VTK file format allows you to export the laminate to a single file, but the affiliation of individual elements to a particular ply is lost. Therefore, each ply is written as a separate file.

As the draping simulation is performed using the Abaqus/Explicit solver, the resulting data can be obtained using the Python API. In the first step, the nodes and their connectivity are obtained to define a mesh. To gather all necessary data for the structural simulation, the deformation gradient is obtained for each element. As described in Section 4.2 the fiber orientation and the FVC are directly determined using the deformation gradient. The amplitude to wavelength ratio results from the fiber strain, which can also be obtained directly from the deformation gradient. Using the draping simulation model developed by Schirmaier [2], the strain in fiber direction can be determined by

$$\varepsilon_{11} = \frac{\|\boldsymbol{f}_1\|}{\|\boldsymbol{f}_1^{\mathrm{init}}\|} = \frac{\|\boldsymbol{F}\boldsymbol{f}_1^{\mathrm{init}}\|}{\|\boldsymbol{f}_1^{\mathrm{init}}\|}. \tag{4.6}$$

Here only the initial fiber orientation vector $\boldsymbol{f}_1^{\mathrm{init}}$ is needed as an additional parameter. Using the fiber strain and the resulting wavelength, the amplitude to wavelength ratio can be determined for each element (see Section 4.2.3). The resulting ply-wise data is then written to separate VTK files.

4.4 Mapping and Import Data to Structural Simulation

4.4.1 Mapping Process

To perform the mapping step the mapping library Maplib [214] is used. The mapping library needs the source and target mesh as input in VTK file format. To define the search radius between the two meshes, as well as the desired mapping algorithm, an additional configuration file needs to be provided. The mapping algorithms use the defined search radius (the tangential and normal radius for shell, or sphere radius for solid elements) starting from the target mesh to look up the data in the source mesh. Here the `shapefct` algorithm is used as it considers the shape function of the different FE-based elements. The processed data contains only vectors (fiber orientation) and scalars (FVC and amplitude to wavelength ratio).

As the mapping step requires a VTK file of the structural simulation model mesh, a preprocessing Python script is developed to extract the mesh of a model. Ideally, the orientation of the reference coordinate system is equal for draping simulation as well as for structural simulation. However, in some cases, the geometry needs to be translated or rotated to position both meshes to each other. Since the draping simulation results are available ply-wise, the structural simulation mesh also needs to be extracted for each ply. An example of the mapped results is given in Figure 4.2. The fiber direction of the draping simulation is shown with gray arrows, while the mapped vectors are shown in red (cf. Figure 4.2a). An occurring shear strain leads to a local increase of the FVC, which is visualized by the red colored path (cf. Figure 4.2b). Here the underlying mesh corresponds to the draping simulation mesh and the top one is the structural simulation mesh.

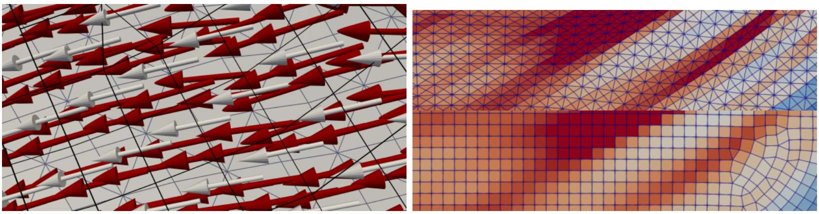

(a) Mapped fiber orientation: red arrows show the draping simulation mesh and gray arrows are the mapped vectors to the structural simulation mesh.

(b) Mapped fiber volume content: top mesh shows the draping simulation mesh and the bottom mesh corresponds to the structural simulation mesh.

Figure 4.2: Mapped draping effects information from draping simulation to structural simulation

4.4.2 Methods to Import Mapped Data in Abaqus

The processed and mapped data need to be imported in order to use this information in the structural simulation. By using Abaqus there are several possibilities to do so. The fiber orientation can be directly assigned to each element and the corresponding strain at the integration point will be directly transformed into the corresponding coordinate system. However, if a directly assigned fiber orientation is used the global deformation gradient $\boldsymbol{F}$ is not provided to the user subroutine. Instead, the deformation gradient is expressed in terms of the corotational element frame. As shown in Section 3.2, a material axis frame is used which follows the material-specific directions. Additionally, the scalar information of FVC and amplitude to wavelength ratio for each element cannot be assigned and processed by the user subroutine. One possible workaround is to use a read-in step at the beginning of the analysis. This approach however will result in unnecessary time consumption [216].

A further possibility exists in Abaqus to provide the local fiber orientation, the FVC and fiber waviness. By using the keyword "`*Initial Conditions, type=SOLUTION`", an averaged value for the whole element can be written directly into the `STATEV` array of the user subroutine. This allows the processing of the provided draping effects information directly at each integration point. While the FVC and the amplitude to wavelength ratio are scalars and can be directly assigned, the fiber direction needs some attention. The deformation of each element is evaluated in the global coordinate system. To consider the local fiber orientation at least two material axes (e.g., fiber and transverse direction) need to be provided to the subroutine in order to consider consistent stacking direction. Ideally, the fiber orientation vector after the mapping step is perpendicular to the normal stacking direction of the element. However, this is not the case as the meshes can deviate especially in double curved corner regions. Therefore, the fiber direction vector is projected onto the element surface defined by the stacking direction of the laminate. Special care needs to be taken by defining the normal direction $\boldsymbol{v}_\mathrm{n}$ of the element surface. After the stacking direction of the mesh is defined, which has an impact on the order of the element connectivity, the vector $\boldsymbol{v}_\mathrm{n}$ is derived by using the first three nodes of the element to form a plane. To obtain the projected fiber orientation $\boldsymbol{f}_1^\mathrm{proj}$ only the mapped fiber orientation $\boldsymbol{f}_1$ and the normal direction $\boldsymbol{v}_\mathrm{n}$ are needed (cf. Figure 4.3). The projected fiber orientation is given by

$$\boldsymbol{f}_1^\mathrm{proj} = \boldsymbol{f}_1 - (\boldsymbol{f}_1 \cdot \boldsymbol{v}_\mathrm{n})\, \boldsymbol{v}_\mathrm{n}. \tag{4.7}$$

Afterwards, the resulting vector needs to be normalized in order to obtain a unit material axis direction. Together with the transverse direction $\boldsymbol{f}_2$, which can be obtained from the cross product of the normal direction and the projected fiber direction, the material axes can be passed to the keyword definition. It should be noted that the deformed fabric can have nonorthogonal material axes. However, for the structural simulation the initial state is defined after consolidation by an orthogonal coordinate system defined primarily by $\boldsymbol{f}_1$ and $\boldsymbol{f}_2$.

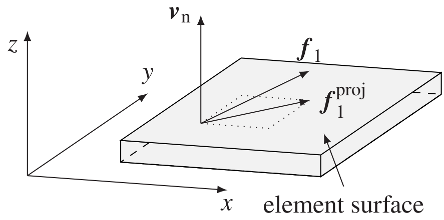

Figure 4.3: Fiber orientation projection from draping simulation results ($\boldsymbol{f}_1$) onto the element surface of a structural mesh ($\boldsymbol{f}_1^{\text{proj}}$), which is necessary in case of differently oriented draping and structural mesh, e.g. at double curved corner regions

A simple fiber projection approach, which does not consider draping simulation results, will be introduced in the following, in order to compare it later with the approach that considers draping information. An unsuitable engineering approach for such fiber projection would simply assign a global direction as fiber orientation, since it can lead to nonphysical results in curved areas. A better projection approach uses a plane that cuts each element and defines the projected fiber direction. To determine the fiber direction resulting from the cutting plane, the cross product of the normal vectors of the cutting plane and the element surface needs to be calculated. For example, if the normal direction of the cutting plane is $\boldsymbol{v}_{\text{n}}^{\text{cp}} = (0, 1, 0)^\top$ and the element normal corresponds to $\boldsymbol{v}_{\text{n}} = (0, 0, 1)^\top$, the projected fiber direction yields $\boldsymbol{f}_1^{\text{proj}} = (1, 0, 0)^\top$ (c.f. Figure 4.4). A special case can occur in which both normal vectors are equal,

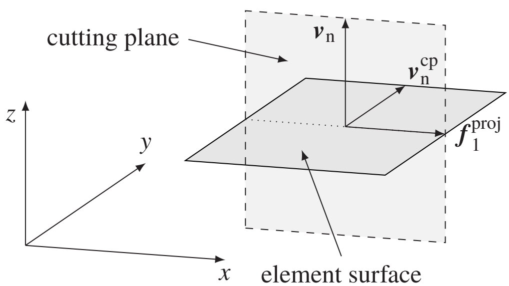

Figure 4.4: Fiber orientation projection onto the element surface based on cutting plane method

which leads to a null vector as a projection. In such a case, the global direction of the fiber orientation can be assigned directly. In addition to the fiber orientation, the fiber volume content and the fiber waviness can be set directly to a constant value, and a comparison of the different approaches becomes possible. Thus, an evaluation of the impact of each draping effect on the mechanical properties and failure behavior can be made.

5 Application and Validation of Constitutive Models

5.1 Draping Effects on Microscopic Scale

Fiber reinforced composites consist of two main components: fiber and matrix. However, the used fabric material contains additional sewing and glass rovings as carrier material. While the additional components are mainly responsible for the formability during the draping process, the fiber and matrix are still the main factors which have an impact on the material properties of the composite. It is known that the matrix and fiber-matrix interface failure are the main trigger for inter-fiber failure and filaments breakage are responsible for failure in fiber direction. While at the end the structure mechanical behavior of composite parts should be predicted, the results are highly dependent on the provided material data. Large scale experimental campaigns are costly and often not always necessary. In order to analyze the impact of the fiber and matrix on the mechanical behavior of unidirectional and also of undulated composites, micro-mechanical models can be used. Especially if the origin of the resulting FVC-dependent elasticity parameters and material strength should be analyzed, micro-scale models are very useful. Here a more profound understanding of the impact of each constituent or the associated fiber distribution and shape on the failure and damage evolution can be obtained. In perspective of occurring draping effects, the knowledge of material parameters which affect the inter-fiber failure and therefore the corresponding failure envelope are to be evaluated. The experimentally observed FVC-dependent material behavior can be analyzed in detail. Finally, by achieving reliable results or trends out of micro-scale models, tests which are not possible to be performed experimentally (or only with a very high effort) can be conducted numerically. In conclusion using micro-scale models the required amount of information can be quickly generated and reduces the necessary experimental work and coupon samples manufacturing effort. Furthermore, the occurring uncertainties, regarding the material parameters in macroscopic models, can be evaluated and constrained.

5.1.1 Generating Micro Models

In general microstructures are complex and the numerical geometrical approximation must satisfy the reality. To do so there are several approaches available. For example, one could use microscopic images or computed tomography scans as input for the numerical model. However, while such approaches represent the reality, data acquisition for such model is time-consuming and costly. Another possibility is to create a representative volume element (RVE). In such case the RVE represent a cutout of the actual material which is representative for the whole material. To reflect the composite material behavior, periodic boundary conditions are applied to the outer surfaces of the RVE. In the past, regularly arranged or cylindrical models were used. As an example such models can be a hexagonal arranged RVE or a model with a single round fiber embedded in a cylindrical matrix. In any case these models represent a strong periodic microstructure. Such approach is in generally used to determine the material stiffness and in some terms the resulting material strength values. However, due to such strong periodicity these models do not reflect reality. As the regular RVE represents a small cutout of the material, any failure within this RVE would also indicate an immediate failure of the whole material, which is obviously not the case. After failure initiation, crack propagation through the material causes a sequential degradation of the material. Nowadays the modeling techniques has been further developed, which considers statistical distribution of the filaments. Such statistical representative volume element (SRVE) considers several dozen filaments and contrary to RVEs the filament diameter and the distance between adjacent filaments varies. It has been shown, that using SRVE the failure behavior of composites can be modeled quite well [219–221].

5.1.1.1 Fiber Distribution

One of the main challenges creating SRVE models lies in the collision free distribution of the filaments, while achieving high fiber volume contents in a manageable time effort. There are two kinds of approaches to create such models: manual placing of filaments and automatic positioning. In order to analyze several representations of SRVE only the fully automated methods are useful. An advanced method to create representative volume elements with random distribution of the filaments was introduced by Melro [222]. This method allows creating models with a very high FVC (up to $\varphi \approx 65\,\%$) in a short amount of time. Here the filaments are assumed to be round as the collision detection is easy to implement. As shown in Section 2.4.2 using microscopic images, the cross section of the filaments can be elliptical. This shape can occur in case of a slightly tilted microsection sample, cutting the filaments under a certain angle, or naturally by the filaments itself. Nevertheless, by using a model generator which only can process round filament shapes, the minor radii of the ellipse is used as the lower bound.

In order to create a microstructure several input parameters, such as mean filament diameter, its variance as also the dimensions of the final geometry and the required FVC, are needed. To create a microstructure the algorithm performs three steps (cf. Figure 5.1). First the filaments are placed randomly and collision-free (hard-core model). If the required FVC is not achieved, new space is needed in order to be able to put new filaments into the structure. Therefore, the next two steps are used to move the filaments to allow the addition of new filaments. During the second step, each filament is moved to the next neighbor according to a special neighbor selection technique (stirring step). Finally, the filaments at the edges of the evaluation region are moved towards the center (moving outskirts step). Now the algorithm starts over and further filaments can be added. In total, this algorithm creates a highly dynamic movement of each filament, which allows creating multiple microstructures in a short amount of time. It should be noted that an exact FVC cannot be set, since each added filament has its own cross section which can lead to larger values as requested. However, the impact of this condition reduces with increasing

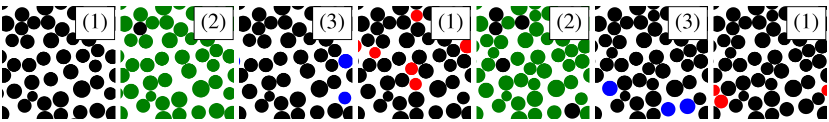

Figure 5.1: Three steps of the fiber distribution algorithm: (1) hard-core model, (2) stirring the fibers and (3) fibers in the outskirts (added or moved fibers are colored in each step)

SRVE size. As observed in microsection samples, for most of the filaments the distance between the filaments is very small (cf. Figure 2.8). Therefore, this geometrical condition needs to be reflected by the generated micro structure. For all generated models the minimum distance between fibers is set to zero. However, due to the nature of the fiber positioning algorithm the possibility of a direct contact of two filaments is quasi nonexistent and a very short distance is rather likely.

5.1.1.2 Model Generation

After the required FVC is reached, the position of each filament and its diameter are written to a separate file. In conjunction with the dimensions of the SRVE, the model can be generated in Abaqus using a Python preprocessing script. Here the fiber distribution is recreated on a plane surface and the meshing process is performed. In the next step the 2D elements are extruded to create a volume. If a unidirectional and nonundulated material is analyzed only one element row in fiber direction is needed. After assigning the material properties of fiber and matrix to specific element sets, the desired load cases need to be assigned. In order to achieve characteristic material behavior, strong periodic boundary conditions are needed [223, 224]. Therefore, each node on the outer face, edge and corner needs to be restrained to induce the specific periodic material behavior. By enforcing these boundary conditions, the SRVE can be subjected to an average strain or stress. This allows to create iso-stress, iso-strain or combined load cases to determine the homogenized material properties. For a better understanding of the required periodic equations, a visualization of the embedded periodic cell is given in Figure 5.2. Here each face, edge and corner has a counterpart. For example, the face 1 and its counterpart 2 are connected due to periodicity of the cell (cf. Figure 5.2a). To define the corresponding boundary conditions, different deformations (or loads) can be analyzed. By analyzing each face, edge and corner pair there are three face equations, 18 edge equations and 28 corner equation in total. However, while all face equations are needed, only nine edge and seven corner equations are required to enforce fully periodic boundary conditions. In previous publications only partial equations have been used

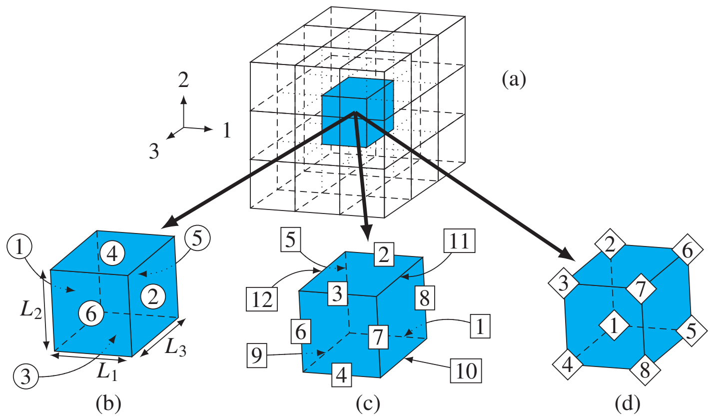

Figure 5.2: Embedded periodic representative volume element (a) and the extracted element with the corresponding labels of the (b) faces, (c) edges and (d) corners

to model microstructures [223, 224]. The used equations for the faces are summarized to

$$u_i^{②} - u_i^{①} - L_1\hat{\varepsilon}_{i1} = 0, \quad u_i^{④} - u_i^{③} - L_2\hat{\varepsilon}_{i2} = 0, \quad u_i^{⑥} - u_i^{⑤} - L_3\hat{\varepsilon}_{i3} = 0 \quad (5.1)$$

where u_i defines the displacement, the index i defines the direction ($i \in \{1,2,3\}$), L_i is the corresponding length of the cell and $\hat{\varepsilon}_{ij}$ is the applied average strain to a reference node. The corresponding edge and corner equations are given in Equations (5.2) and (5.3).

$$\begin{aligned}
&u_i^{\boxed{3}} - u_i^{\boxed{1}} - L_2\hat{\varepsilon}_{i2} - L_3\hat{\varepsilon}_{i3} = 0 \qquad && u_i^{\boxed{8}} - u_i^{\boxed{5}} - L_1\hat{\varepsilon}_{i1} = 0 \\
&u_i^{\boxed{2}} - u_i^{\boxed{1}} - L_2\hat{\varepsilon}_{i2} = 0 && u_i^{\boxed{10}} - u_i^{\boxed{9}} - L_1\hat{\varepsilon}_{i1} = 0 \\
&u_i^{\boxed{4}} - u_i^{\boxed{1}} - L_3\hat{\varepsilon}_{i3} = 0 && u_i^{\boxed{11}} - u_i^{\boxed{9}} - L_1\hat{\varepsilon}_{i1} - L_2\hat{\varepsilon}_{i2} = 0 \\
&u_i^{\boxed{6}} - u_i^{\boxed{5}} - L_3\hat{\varepsilon}_{i3} = 0 && u_i^{\boxed{12}} - u_i^{\boxed{9}} - L_2\hat{\varepsilon}_{i2} = 0 \\
&u_i^{\boxed{7}} - u_i^{\boxed{5}} - L_1\hat{\varepsilon}_{i1} - L_3\hat{\varepsilon}_{i3} = 0 &&
\end{aligned} \qquad (5.2)$$

$$
\begin{aligned}
&u_i^{\langle 2\rangle} - u_i^{\langle 1\rangle} - L_2\hat{\varepsilon}_{i2} = 0 && u_i^{\langle 6\rangle} - u_i^{\langle 1\rangle} - L_1\hat{\varepsilon}_{i1} - L_2\hat{\varepsilon}_{i2} = 0 \\
&u_i^{\langle 3\rangle} - u_i^{\langle 1\rangle} - L_2\hat{\varepsilon}_{i2} - L_3\hat{\varepsilon}_{i3} = 0 && u_i^{\langle 7\rangle} - u_i^{\langle 1\rangle} - L_1\hat{\varepsilon}_{i1} - L_2\hat{\varepsilon}_{i2} - L_3\hat{\varepsilon}_{i3} = 0 \\
&u_i^{\langle 4\rangle} - u_i^{\langle 1\rangle} - L_3\hat{\varepsilon}_{i3} = 0 && u_i^{\langle 8\rangle} - u_i^{\langle 1\rangle} - L_1\hat{\varepsilon}_{i1} - L_3\hat{\varepsilon}_{i3} = 0. \\
&u_i^{\langle 5\rangle} - u_i^{\langle 1\rangle} - L_1\hat{\varepsilon}_{i1} = 0 &&
\end{aligned}
\tag{5.3}
$$

The equations above constrain the movement of each reference point and allow the application of average loads to the cell. To impose these equations Abaqus provides the keyword `*Equation`, where each node set for faces, edges and corners can be defined connected to the reference points by the boundary equations above. As mentioned in Section 3.2 the material axes directions are crucial to obtain physically consistent results. Therefore, the material axes directions are applied to the fiber and also to the matrix. The Abaqus keyword "`*Initial Conditions, type=SOLUTION`" allows to provide the information of the local material axes of each element to the matrix and fiber user subroutines.

Representative volume elements can also be used to analyze undulated material behavior. To create undulated microstructures additional steps are needed. The geometry generation process for undulated microstructures is shown in Figure 5.3. The dimensions of an undulated structure are larger than those of a nonundulated microstructure. The meshed plane surface is extruded sufficiently deep (cf. Figure 5.3a and 5.3b). To find the sufficient depth of the undulated SRVE model, it is recommended to perform a mesh study and compare the results of E_x with the analytical solution. Now that the solid elements are created, the position of all nodes needs to be modified to create a waviness. For each node the corresponding offset is calculated and a sinusoidal shape of the microstructure is created. To reduce the model creation time, an offset can be directly applied to all nodes on the same plane. The remaining model creation steps are identical to the nonundulated SRVE models.

5.1.1.3 Evaluation of Stiffness and Strength Values

To evaluate each elasticity material parameter an iso-stress load is applied and by utilizing the material compliance matrix $\boldsymbol{S}$ each parameter can be calculated. Since nonlinear material behavior can occur due to material axes rotation,

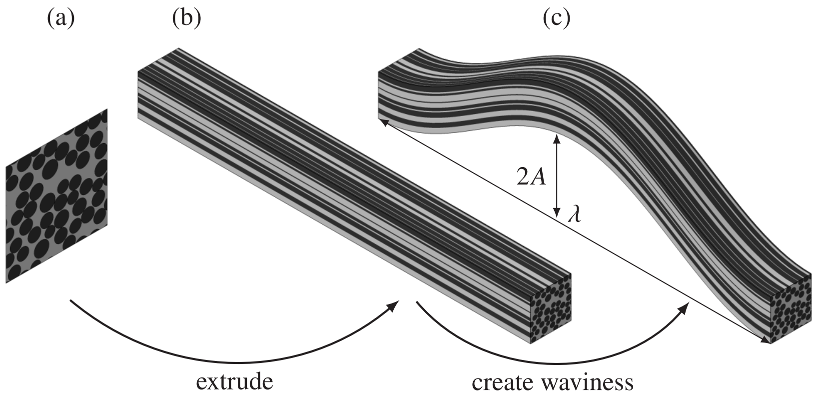

Figure 5.3: Model generation workflow for micro-scale models with waviness: (a) plane 2D fiber distribution, (b) extruded model and (c) imposed waviness

plasticity or occurring damage, only very small deformations are applied to obtain initial linear elastic material parameters. To obtain the material strength, the corresponding load needs to be vastly increased to trigger complete failure of the microstructure. Depending on the load case and the material response of fiber and matrix, different failure behavior can be achieved. For example, a shear load can lead to a continuous hardening of the stress-strain curve, without any sudden drop of the stress at failure initiation. On the other hand, transverse tension can show a sudden drop of the stress at failure of the microstructure. However, in both cases the maximum value of the analyzed iso-stress load case is used as the resulting homogenized material strength for the corresponding load direction. For combined loads (e.g., transverse tension and shear) the maximum stress can occur at different time points. Therefore, to determine the failure stresses of combined loads, for each time point the norm of the stress vector is determined. The maximum value is then determined, and the corresponding stress values are taken as the final failure points of the combined load.

The obtained results from micro-scale simulations need to be processed in order to obtain homogenized values. To analyze the resulting material stiffness and strength, the occurring local strains and stresses need to be integrated over the whole model

$$\hat{\boldsymbol{\varepsilon}} = \int \boldsymbol{\varepsilon} \mathrm{d}V = \frac{1}{V}\sum_{i=1}^{N} \boldsymbol{\varepsilon}_i V_i \quad \text{and} \quad \hat{\boldsymbol{\sigma}} = \int \boldsymbol{\sigma} \mathrm{d}V = \frac{1}{V}\sum_{i=1}^{N} \boldsymbol{\sigma}_i V_i \tag{5.4}$$

where N is the number of elements and V is the total volume. However, depending on the analyzed model the strain and stress need to be evaluated in a suitable coordinate system. For example, undulations create an orthotropic material behavior [30, 118], but locally the material is still transversely isotropic (see Section 3.5.6). Therefore, the material response in terms of strain and stress is evaluated within the global coordinate system. Now that the homogenized values are available, the corresponding material parameters can be determined.

5.1.1.4 Material Parameters for Fiber and Matrix Constitutive Models

The used material models require a number of parameters which can be partly determined from experiments. The experimental test results of the matrix can be used to define the elastic as well as the rate dependent plastic behavior. Furthermore, some material properties of the fiber, such as stiffness and strength in fiber direction, can be obtained from experimental results or literature. However, some model-dependent parameters for both constituents are not available and must be chosen wisely. For example, the material energy release rate G_f has a major impact in the damage evolution. For both constituents this material parameter is different for tension and compression loads (G_f^+ and G_f^-). During damage propagation through the micro-structure these energy release rates interact with each other, as they can trigger different stress states and therefore different failure modes. Furthermore, SRVE are subject to scatter due to the geometrical factors, which lead to different results for the same energy release rates. These conditions make it difficult to perform a parameter fitting analysis, rather than by choosing the required material parameters wisely. Additionally, the material properties of the fiber, besides the one in fiber direction, are quite challenging or currently not possible to determine and can be obtained via reverse engineering from composite coupon tests.

In detail, the material parameters of matrix and fiber are determined as follows. The initial linear elastic material behavior of the matrix (E_m and ν_m) can be directly obtained from experimental results. The material parameters for the plastic behavior are obtained by using a nonlinear optimization algorithm of the Python package SciPy called `differential_evolution`. The resulting material parameters of the matrix are summarized in Tables A.3 to A.6. For the used carbon fiber the manufacturer provides only the stiffness and tensile strength in fiber direction. However, by using the obtained experimental unidirectional coupon results and by variation of the unknown material properties (such as E_2^{f}, G_{12}^{f} or ν_{23}^{f}) within the numerical microstructure simulation, a suitable material parameter data set can be identified. The used carbon fibers have similar mechanical properties (e.g., E_1^{f} and $X_{\mathrm{T}}^{\mathrm{f}}$) as the Toray T300 carbon fiber. Therefore, a tensile/compressive strength ratio of $X_{\mathrm{C}}/X_{\mathrm{T}} \approx 1$ is used [63]. As the used material model for the fiber requires only the strength in fiber direction besides the elastic properties, all material parameters can be fully defined. The summarized data set of the required fiber material properties is given in Table A.7.

5.1.2 Stiffness and Strength of Nonundulated Models

When it comes to a more profound understanding of material behavior of composites, micro-scale models are the key. However, many parameters can influence the outcome results. Especially if microstructures with a random fiber distribution are used, the results are subjected to natural scatter. In order to obtain reliable results first the parameters with the most impact have to be analyzed. Besides the statistical distribution of the filament position and the corresponding diameter of each filament, the size of the microstructure is crucial. In previous publications [143, 225] it could be shown that by choosing a sufficient microstructure size the results converge. This factor has not only an impact on the material stiffness (compared to regular microstructures) but also on the resulting homogenized material strength. Here the SRVE size of $15R \times 15R$, where R is the mean filament radius, is used. This size turned out to be sufficient if the number of micro-scale models at the same FVC is large enough. Therefore, a total number of ten different microstructures at each FVC has been evaluated. The number of filaments varies between 33 to 35 at $\varphi \approx 45\,\%$ and 50 to 53 at $\varphi \approx 65\,\%$. In the following subsections the impact of each constituent on the material behavior of the composite is analyzed. Especially the impact on the elastic parameters of the composite and the resulting failure envelope is evaluated. The effect of the FVC itself is also evaluated. As observed from experimental results (cf. Figure 2.11), the nonlinear behavior of the composite due to plasticity of the matrix is not affected by the FVC. By varying the plasticity parameters of the matrix, it assumed that only the stress-strain curve of the composite would be affected. Furthermore, the carbon fiber specific nonlinearity will have a major impact on the stiffness in fiber direction and little to none in other loading directions. Therefore, the nonlinear behavior due to plasticity of the matrix and nonlinear behavior of the carbon fiber are not evaluated.

5.1.2.1 Impact of the Constituents on the Linear Elastic Parameters

By using micro-scale models the resulting homogenized stiffness must correlate with the experimental results of coupons. The directly obtained material properties of fiber and matrix are determined by the method as described in Section 5.1.1.4. Other material properties are generally determined via reverse engineering using micro-scale models or analytical solutions. Using the material parameters for the constituents (Tables A.3 and A.7) a variation of each parameter is performed to determine the impact on the resulting composite stiffness or Poisson's ratio. Further the increase of the stiffness in fiber direction ${}^{\mathrm{d}E_1}/{}_{\mathrm{d}\varepsilon_{11}}$ is set to zero, as only the initial linear elastic material properties are evaluated. To avoid any impact of the material nonlinearity, such as plasticity or damage, the applied loads are very small. The loads create iso-stress states, which allow to determine the elastic material response more easily. To ensure the comparability of the variation, each individual parameter is reduced or increased by 10 % while all other parameters remain the same. General the material properties of the composite are effected by any change of the material parameters of the constituents. However, some changes are very small (e.g., the variation of the transverse modulus E_2^{f} leads to a change of the Poisson's ratio ν_{23} lower than 1 %). In order to show only the most significant impact, only the parameters which change the resulting material property by at least 1 % are presented. All parameters are evaluated for a FVC of $\varphi \approx 60\,\%$. The results are shown in Figure 5.4.

In fiber direction the material stiffness E_1 is well described by a parallel-connected model. The change of the fiber stiffness E_1^{f} leads to a direct change of 10 % since the matrix has a much smaller stiffness. All other parameter

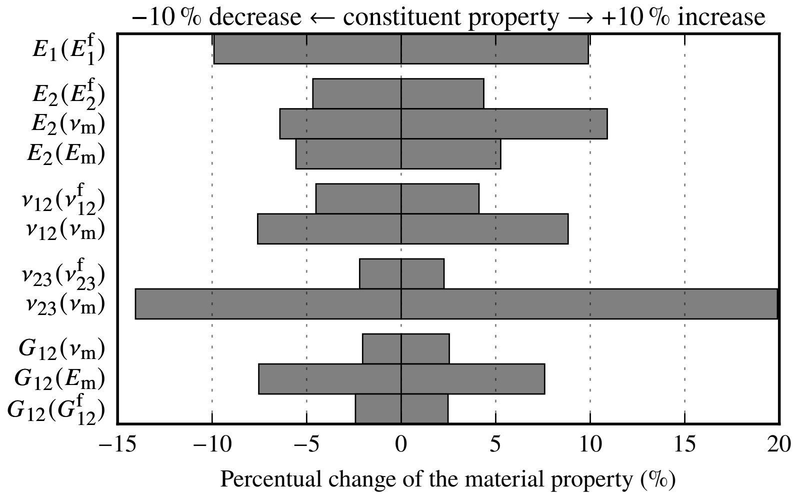

Figure 5.4: The most significant impact on the linear elastic material properties of the composite by varying the material properties of the constituents by 10 %

variations, such as the Young's modulus of the matrix E_m, lead to a change of E_1 lower than 1 %. By analyzing the impact on transverse stiffness E_2 several observations can be made. The variation of the transverse stiffness of the fiber E_2^f has the lowest impact on the resulting modulus. This can be explained by the usage of the lower bound of the transverse stiffness, which is defined by a series-connected model. Here the increase of E_2 is highly affected by the FVC. At $\varphi \approx 60\,\%$ the impact of E_2^f is still small compared to the impact of the matrix itself. However, at large FVC the material properties of the fiber will predominate and therefore have the most impact on the transverse stiffness. The change of E_2^f leads to almost the same percentage increase or decrease of E_2. On the other hand, the Poisson's ratio of the matrix ν_m leads to different observations. If ν_m is increased by 10 % the transverse modulus is disproportionate increased by over 10 %. In case of a reduction, it has a more severe impact as the Young's modulus of the matrix E_m. The reason for both observations lies in the Poisson effect itself. If ν_m is increased by 10 % it tends towards $\nu_m \rightarrow 0.5$, which induces incompressibility of the matrix and leads to a stress increase within the fiber. The matrix stiffness E_m has a similar impact on E_2 as E_2^f regardless of the percentage increase or decrease.

If the Poisson's ratios ν_{12} and ν_{23} are analyzed, they show a similarity. The variation of the fiber material properties has a smaller impact than the matrix Poisson's ratio. As ν_{12} can also be defined by parallel-connected model, which leads to a linear distribution over the FVC, and the matrix Poisson's ratio is more than two times larger than ν_{12}^f, its variation causes also a greater change. The Poisson's ratio in the transverse isotropic plane ν_{23} changes most significantly, if the Poisson's ratio of the matrix is varied by 10 %.

Finally, the results of the shear modulus G_{12} are evaluated. Compared to the transverse modulus E_2, the impact of the fiber shear modulus G_{12}^f is small on the outcome. Although the shear modulus of the fiber G_{12}^f is about 23 times larger than the shear modulus of the matrix G_m, according to the series-connected model a significant increase of the composite stiffness G_{12} is achieved for FVC above 70 %. The matrix shows an impact on the shear modulus G_{12} by varying E_m and ν_m. In detail, the Young's modulus of the matrix has a higher impact than the Poissons's ratio of the matrix on the resulting composite shear modulus G_{12}. This condition can be the result of the material deformation under shear loads. While transverse loads cause a volume change, which is affected by the Poisson's ratio of the matrix, shear loads lead to a more pronounced shape deformation while the volume remains almost constant.

In summary, for the evaluated FVC the impact of the uncertainty of the unknown material parameters of the fiber is relatively small (except for the stiffness in fiber direction) compared to the impact of the material properties of the matrix. Therefore, the accuracy of the matrix material properties is crucial to obtain reliable results. Generally to obtain more accurate fiber material properties, test results of coupons with a very high FVC have to be considered. Here the fiber material properties are predominant compared to the matrix and by remodeling the corresponding coupon tests the fiber material parameters can be defined more precisely. If deviations between the experimentally obtained composite material properties and the micromechanical models occur, the primary reason could result from inaccurate matrix properties rather than unknown fiber material properties.

Using statistical representative volume elements allow to analyze the occurring material properties scatter. In order to compare the statistical scatter of SRVEs ten different microstructures at five different fiber volume contents have been created. Each fiber distribution is evaluated to obtain all material properties to define the linear elastic behavior of a unidirectional composite material. The results are given in Figure 5.5. Due to transversely isotropic material behavior, the corresponding material property has been added to the same plot (e.g., E_2 and E_3). In several publications the regular RVE with hexagonal fiber configuration is used to determine the actual material stiffness. Therefore, the hexagonal array distribution is added as a comparison. As expected the material parameters E_1, ${}^{\mathrm{d}E_1}/_{\mathrm{d}\varepsilon_{11}}$ and ν_{12} are well described by a parallel-connected model. In this case the increase or decrease of each specific parameter can be defined by a linear function. However, in terms of scatter the numerical results of the Poisson's ratio ν_{12} (or ν_{13}) are more affected (cf. Figure 5.5e) compared to the stiffness in fiber direction. The hexagonal array results correspond very well with the statistical distribution ones. By comparing the results of E_2 and G_{12} a more nonlinear behavior over the FVC can be observed. It should be noted that the shear modulus G_{23} can be directly deducted from E_2 and ν_{23} (see Equation (2.1)) and shows therefore also a nonlinear increase for higher fiber volume contents. One remarkable observation is that the hexagonal array for E_2, G_{12} and ν_{23} show a more pronounced serial-connected model behavior. This is especially observed for the shear modulus G_{12} where the difference between the results of the SRVE and regular RVE increase over the FVC. At $\varphi \approx 65\,\%$ the difference is about $30\,\%$, although same material parameters are used. The generally higher shear modulus of SRVEs are the result of the distance between filaments, compared to a regular hexagonal array distribution. In areas with close filaments the shear stiffness of the fiber is more dominant as in other areas. In total these areas contribute to the higher shear modulus G_{12}. As a result the usage of regular RVE seems to be inappropriate to determine shear properties of composites. By comparing the scatter of each cluster the results for most parameters are in a range of $2\,\%$, only the in-plane shear modulus G_{12} show a scatter in a range of $3\,\%$ to $5\,\%$. The corresponding experimental results show a good to very good agreement with numerical ones. The trends over the FVC are clearly given. Only a larger deviation in the slope ${}^{\mathrm{d}E_1}/_{\mathrm{d}\varepsilon_{11}}$ can be observed. This difference results from the fact, that the material properties of the fiber are determined from single filament tests. However, the experimental results at the given fiber volume contents are obtained from coupon tests. Here the used fabric contains an intrinsic waviness as it is not pretensioned impregnated. In this case the results are not directly comparable with single filament tests, where each filament is preloaded. To

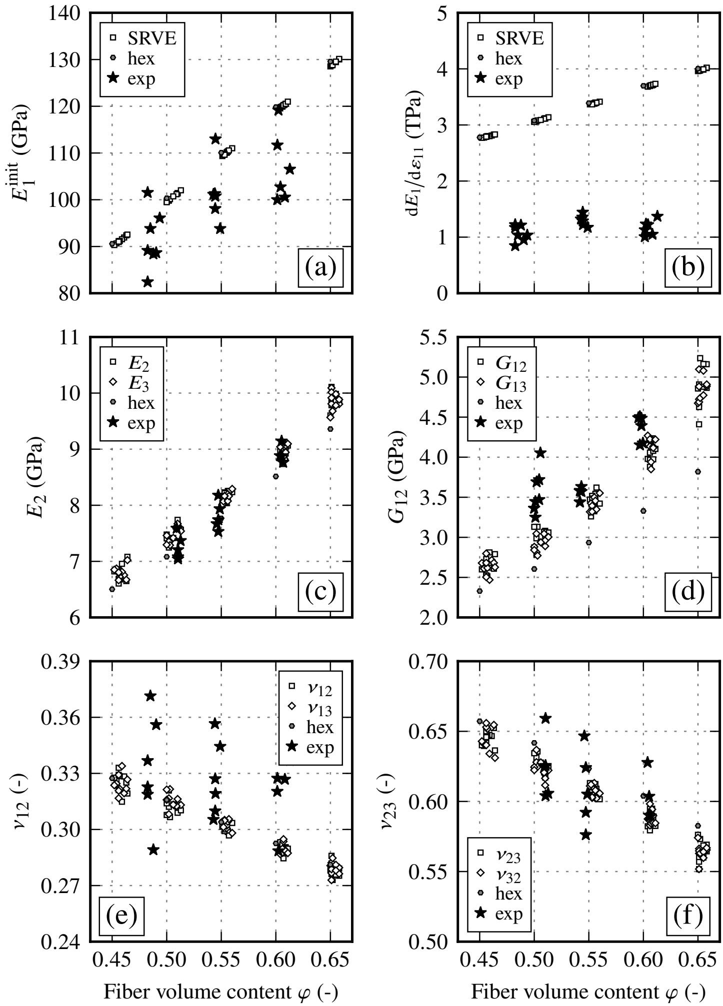

Figure 5.5: Resulting material properties from experiments (exp), RVE with hexagonal fiber arrangement (hex) and SRVE with statistic fiber arrangement at different FVC: (a) static modulus and (b) slope of the modulus in fiber direction, (c) transverse modulus, (d) in-plane shear modulus, (e) in-plane and (f) through-thickness Poisson's ratio

model the intrinsic waviness of the fabric, either the fiber stiffness $E_1^{\mathrm{f,init}}$ and the increase of fiber stiffness m_{f} should be reduced, or models with waviness of the filaments should be used. Nevertheless, it is obvious that the micro model with the determined material parameters of the matrix and fiber can sufficiently reflect the observed material behavior from coupon tests.

5.1.2.2 Failure Envelopes at Different Fiber Volume Contents

Due to combination of fiber and matrix, the resulting homogenized stress also results from the stresses of each constituent. The proportion of each constituent depends on the corresponding fiber volume fraction. Since the fibers have a much higher stiffness than the matrix, most of the deformation occurs within the matrix to achieve stress equilibrium. For example, a unidirectional iso-stress load case leads to zero stress in all other directions. However, in a heterogeneous material these homogenized zero stress components can only be achieved if the stresses of each constituent counterbalance each other. If a tensile load is applied in the transverse direction of a composite, a negative strain is applied in fiber direction due to Poisson's effect. Since the fiber has a much higher stiffness than the matrix, the acting strain results in a compressive stress within the fiber. On the other hand tensile stresses occur in the matrix, which together with the compressive stress of the fiber will produce a zero stress.

Generally the tensile strength of the matrix is higher than the resulting transverse tensile strength of the composite. This condition can yield from a weak bond or interface between fiber and matrix, but also from a triaxial stress state within the matrix. In both cases a stress concentration at the edge of each filament occurs, which leads to initial microscopic failure. There are several numerical studies available which utilize representative volume elements to determine the uniaxial strengths of the composite or its failure envelopes [219, 220, 226]. It could be shown that the interface between fiber and matrix plays a significant role on the failure under transverse tension loads. However, if an in-plane shear or transverse compression load is applied, the failure of the matrix itself is more important. Especially Melro [143] analyzed the resulting failure envelopes using SRVE models and compared the results to the analytical ones. While the results in the transverse tension region (cf. Figure 3.26 Puck's mode A) correlate very well with the used failure envelope, greater deviations occur under transverse compressive loads. Especially the increase of the failure resistance due to combined transverse compressive and in-plane shear stress (cf. Figure 3.26 transition from mode B to C) is not observed. As for such loads the matrix failure is more significant than the fiber-matrix interface failure, it is assumed that the experimentally determined matrix tensile and compressive strengths used as material properties are to be questioned (cf. Section 2.4.1). Especially on micro-scale the size effect of the matrix is crucial and tends to result in higher tensile and compressive strengths. Nevertheless, using the obtained matrix plasticity parameters and the provided material properties of fiber and matrix (see Appendix A.5), the failure envelope at different fiber volume contents can be obtained. Using the previously generated microstructures, 21 different load cases are evaluated. All load combinations are performed in the $(\sigma_{22}, \sigma_{12})$-plane ranging from pure tension to pure compression in transverse direction while the amount of shear is varied. The load cases are summarized as following, a total of ten load cases each for transverse tension or compression and an additional pure shear load case. In order to analyze the impact of the FVC on the failure envelope, a FVC range from 45 % to 65 % is modeled. The results are given in Figure 5.6. All failure points create a specific distribution in the $(\sigma_{22}, \sigma_{12})$-plane. To constrain these, the Puck-failure criterion is used, with strength values determined by

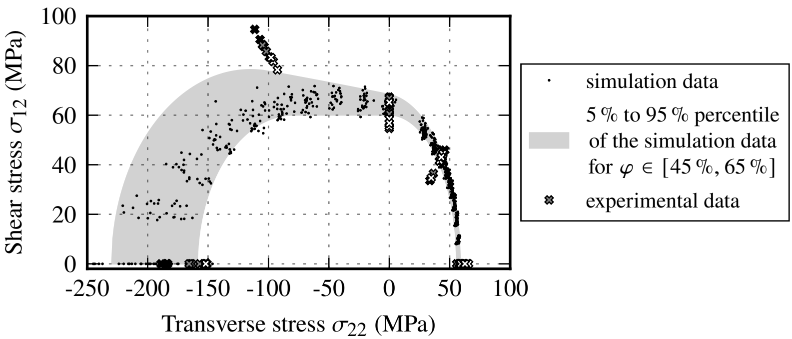

Figure 5.6: Failure envelope resulting from micro-scale model simulations at different FVC compared to selected experimental results at different FVC $\varphi \in [48\,\%, 60\,\%]$

the 5 % and 95 % percentiles at the corresponding load cases. The inclination parameters $p^{t}_{n1} = p^{c}_{n1} = p_{n1}$ are adjusted so that the resulting scatter band well encloses the failure points. The lower bound of the band shows that p_{n1} is equal to zero. However, the upper bound show in some extent a pronounced slope. The corresponding inclination parameter results $p^{t}_{n1} = p^{c}_{n1} = 0.1$, which is still much smaller than generally observed in experimentally results [53, 227]. Such observation has been also made by Melro [143]. The reason for the deviation, especially in the failure mode B range, is not conclusively clarified. One possible reason is the used material strength values of the matrix. Another possible explanation is the occurring damage evolution and propagation. An in-depth discussion can be found in Appendix A.2. In addition to the numerical results, selected experimental data is added in Figure 5.6. Here the numerical results correlate quite well with the experimental transverse tensile loads. The small scatter for experimental transverse tensile and in-plane shear strength over the evaluated FVC range is supported by micro-scale models (cf. Figures 2.12 and 2.13). The increase of the transverse compressive strength over the FVC is also present. However, the scatter band of numerical results overestimate the resulting transverse compressive strength values. Additionally, the band is highly affected by the choice of the matrix strength values or damage parameters. An in-depth study with different matrix strength values and their impact on the results failure envelopes is given in Appendix A.2. In general, the matrix strength values affect not only the uniaxial tensile, compressive or in-plane shear strength values, but also the inclination parameters of the failure envelope. Nevertheless, using micro-scale models for nonundulated areas in composite parts can be used to predict a more conservative failure envelope range at different fiber volume contents.

In conclusion the evaluated models showed that the linear elastic material parameters and the strength values of the composite are highly affected by the matrix properties. As for the FVC variation the SRVE results show a very good source to predict linear elastic properties of the composite. To be able to predict the FVC strength values, only the transverse tension loads can be covered reliably. At this point the usage of micro-scale models for transverse compressive loads show some limitations. From the observed numerical results it is recommended to use the numerically obtained transverse strength values Y_T and Y_C in conjunction with the in-plane shear S_{12}. However, to be able to predict the failure envelope of the composite for combined compression and shear, the inclination parameter p_{n1} should be taken from experimental tests or literature.

5.1.3 Stiffness and Strength of Undulated Models

Compared to areas of laminates with straight fibers, undulated areas have a major impact on the mechanical behavior. Micro-scale models can be used to model waviness and evaluate its dependence on the grade of waviness or FVC. In contrast to homogenized macroscopic models a clear distinction of the failure mechanisms can be made. Additionally, no previous assumptions regarding homogenized material properties of the composite need to be made. In the following micro-scale models are used to evaluate the prediction capability of analytical methods in comparison with numerical results. Furthermore, the failure initiation and damage propagation is analyzed and compared to experimental results. Finally, the FVC is varied to evaluate the resulting strength values.

5.1.3.1 Linear elastic in-plane properties

The effective elastic material properties of composites with wavy areas are dependent on the local nonundulated material properties. Additionally, the impact of the FVC in conjunction with waviness is generally not considered. In order to evaluate different amplitude to wavelength ratios $^{A}/_{\lambda}$, while varying the FVC, previously generated micro-scale models have been used. As shown in Figure 5.5 different microstructures tend to create a certain material parameter scatter. Therefore, using all micro-scale models the resulting transverse isotropy is evaluated for each microstructure. The fiber distribution with the lowest overall orthotropy grade for E_2 vs. E_3, ν_{12} vs. ν_{13} and G_{12} vs. G_{13} is selected to perform further analyses. According to a previously performed numerical study, the wavelength is set to $\lambda = 512\,\mu\text{m}$ [228]. By varying the $^{A}/_{\lambda}$-ratio the amplitude can be specifically adjusted. Since the in-plane global material properties (E_x, E_y, ν_{xy} and G_{xy}) are highly affected by undulations, only these are evaluated for different $^{A}/_{\lambda}$-ratios and fiber volume contents. The numerical results for all micro-scale models are given in Figure 5.7. Using the analytical solutions for each material property the correspondent range can be calculated (gray areas in Figure 5.7). The used equations are given in

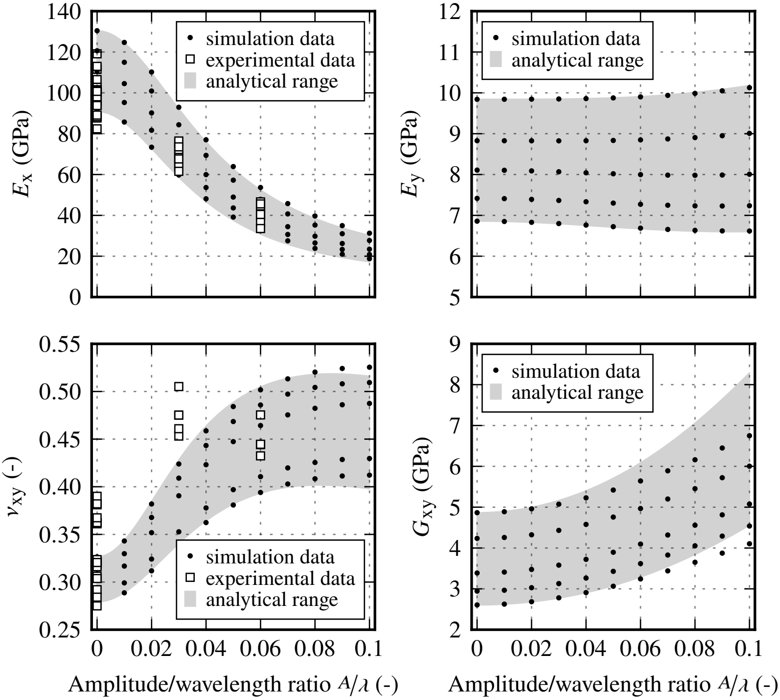

Figure 5.7: Resulting elasticity material properties of composites with imposed waviness for varying fiber volume contents $\varphi = [45\,\%, 65\,\%]$ (experimental results performed at ILK [47])

Appendix A.1.3.5. Besides the amplitude to wavelength ratio each analytical equation requires the in-plane composite material properties as input. As these parameters vary with the corresponding FVC, the numerical results of the micro-scale models at $A/\lambda = 0$ have been used to determine the bounds of the range for the analytical solution. The analytical results are in a very good agreement with the numerical ones. Major deviations occur for the in-plane shear modulus G_{xy} for a FVC $\varphi = 65\,\%$. It can be observed that the deviation increases with increasing A/λ-ratio. One possible explanation is that the analytical result oversimplifies the actual material behavior, due to shape deformation and fiber reorientation. In addition to the numerical and analytical results, the available experimental results have been added to Figure 5.7. At $A/\lambda = 0$ the experimental results are equivalent to the ones in Figure 5.5. Here the largest deviations occur for coupons with a lower FVC for both E_{x} and ν_{xy} (which are equal to E_1 and ν_{12} at $A/\lambda = 0$). Comparing the experimental results for the stiffness E_{x} with the numerical and analytical ones, a very good agreement can be observed. However, the Poisson's ratio ν_{xy} shows a larger deviation. Following the numerical and analytical results, the Poisson's ratio increases with the amplitude to wavelength ratio. Here the experimental results show a A/λ-ratio independent increase, compared to nonundulated coupon samples. Although the transverse modulus E_{y} is affected by the FVC, the A/λ-ratio has almost no effect on the resulting value. This condition results from the fact that with increasing A/λ-ratio, the impact of the initial modulus E_2 is reduced, while at the same time the in-plane shear modulus G_{12} contributes a greater impact on the resulting transverse modulus E_{y}. Here both parameters counterbalance each other with increasing A/λ-ratio.

5.1.3.2 Failure Initiation and Damage Propagation

Contrary to the in-plane failure damage behavior, a waviness leads to a damage evolution along the fiber direction. As experimentally observed (cf. Figure 2.25), besides the initial failure at the coupon edges, further damage occurs at the turning points of the waves. The micro-scale models cannot capture the edge failure due to periodic boundary conditions. By applying a tension load to a micro-scale model the failure initiation and damage evolution can be analyzed. The failure initiation at the turning points and its progression towards the fiber direction can be reproduced (cf. Figure 5.8). The percentage of the damaged matrix volume d_{V} is evaluated at different steps. Due to occurring damage within the matrix, the local stiffness is reduced. This leads to a more pronounced deformation of the matrix. As a consequence the distance between filaments changes. Additionally, the filaments are reoriented and lead to a further damage propagation within the matrix. On the other hand, the failure initiation in the filaments itself is triggered much later, compared to the matrix. This is obviously due to the high strength of the fibers. Furthermore, the failure initiation in the fibers is not homogeneous. Due to the curvature of the filaments, the tension load creates a bending moment on the fibers. Therefore, a tension and a compression load is triggered within the fiber. The tensile

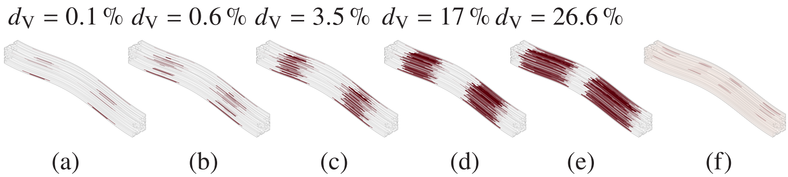

Figure 5.8: Damage evolution in a micro-scale model under a tensile load in fiber direction with an amplitude to wavelength ratio $A/\lambda = 0.03$: matrix damage evolution (a)-(e) and fiber damage at max stress (f)

stress dominates and reaches the tensile strength of the filaments, which leads to the initial failure. The location of the initial fiber failure corresponds to areas close to the largest curvature of the fibers (cf. Figure 5.8f). Overall initial fiber failure leads to a sudden decrease of the load capability of the area with an imposed waviness. As observed in experimental results the pronounced deformation of the coupon samples, even with multiple perpendicular cracks, comes to a sudden stop as the load cannot be carried by the fibers alone.

Using the developed fiber and matrix material models, the experimental tests on undulated samples have been remodeled. Here both compression and tensile tests are evaluated. To evaluate the impact of the microstructure, three different fiber distributions have been created for each configuration. The FVC has been set to $\varphi = 55\,\%$. The amplitude to wavelength ratios correspond to the approximate ones from experimental tests $A/\lambda = \{0.03, 0.06\}$. Obtained results are given in Figure 5.9. Based on different microstructures all the stress-strain curves follow the same path. By comparing the stiffness of the numerical and experimental results a good correlation can be observed. The main differences arise in the resulting strength. For $A/\lambda = 0.03$ the maximum stress values are all in a small scatter range. Compared to the experimental results, the predicted numerical strength values are higher. The numerical stress-strain curves for tensile loads show similarities for both A/λ-ratios. In both cases a pronounced change of the stress-strain path can be observed, for $A/\lambda = 0.03$ at about 400 MPa and for $A/\lambda = 0.06$ at about 160 MPa. At this point the matrix damage has progressed from one side of the microstructure to the other side. The same observation could be made from the experimental results, where the cracks along the fiber direction become visible (cf. Figure 2.25d and 2.25e). As in experimental results, further damage progression follows

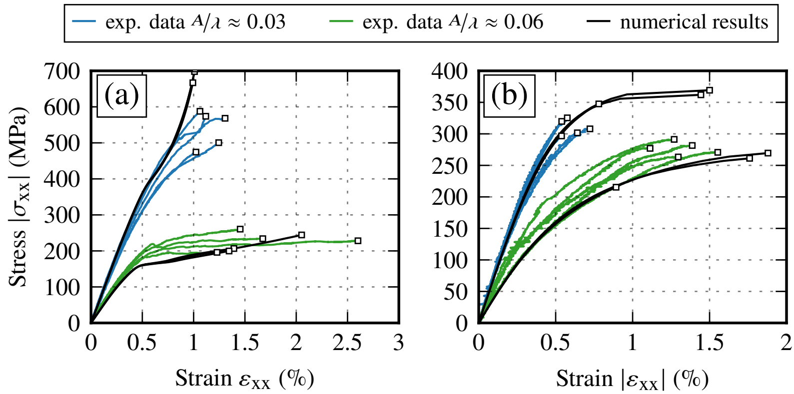

Figure 5.9: Comparison of numerical results of micro-scale models and experimental results for tensile loads (a) and compressive loads (b)

the fiber direction. This condition allows that the fibers are further stretched, which affects the tangential stiffness. In general the described damage evolution above (cf. Figure 5.8) applies to the evaluated numerical models. After first damage initiation in the filaments, tensile load cannot be further increased. On the other hand no fiber damage is triggered in compressive loads. In fact the damage within the matrix is not only present in the area of the turning point of the wave (as for tensile loads), but rather over the whole model. Therefore, the maximum stress yields from the matrix damage and the fiber reorientation alone. The experimentally observed fiber kinking (cf. Figure 2.25f) could not be reproduced.

5.1.3.3 Impact of the Fiber Volume Content on the Strength

The experimental results for specific A/λ-ratios, coincide with a specific FVC [47, 50]. Using micro-scale models an in-depth analysis of the FVC-dependent strength can be performed. To do so, two different amplitude to wavelength ratios $A/\lambda = \{0.05, 0.1\}$ and three fiber volume contents $\varphi = \{50\,\%, 55\,\%, 60\,\%\}$ have been analyzed. To consider the loading direction, tension and compressive load cases has been evaluated. The results are given in Figure 5.10. The

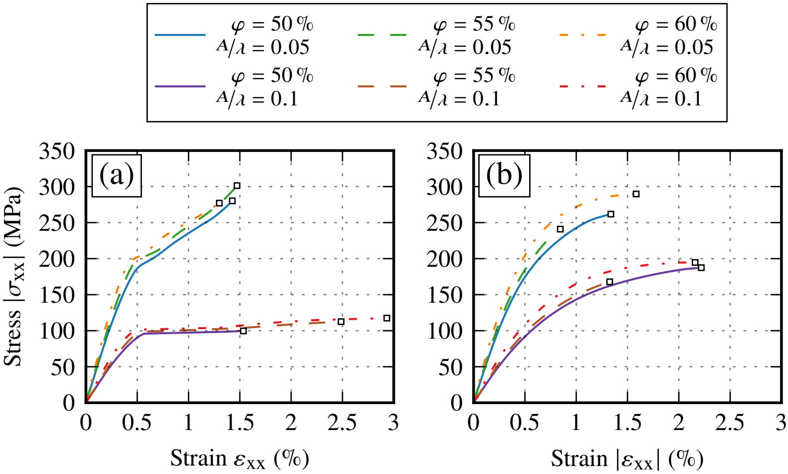

Figure 5.10: Numerical results of micro-scale models for different amplitude to wavelength ratios and varying fiber volume contents for tension (a) and compression (b) loads

obvious stiffness differences yield from the FVC. The failure and damage mechanisms are comparable to the ones already observed. However, the resulting strength values seem to be not affected by the FVC. This behavior is especially obvious for the tension loads. Although a 5 % FVC difference between each curve is set, the reached stress values are very close to each other. This behavior is similar to transverse tensile loads with superimposed in-plane shear, where the failure range is barely affected by the FVC (cf. Figures 2.14 and 5.6). On the other hand, the results for compression loads seem to be more diffuse and contradictory. Especially the results for φ = 55 % show much lower strength values. However, this behavior can also yield from the used fiber distribution. This assumption seems to be reasonable since for the same FVC, the same microstructure is used and only the A/λ-ratio is changed. The resulting strength values for both ratios are smaller in comparison to the two other fiber volume contents. At this point it seems that the FVC in undulated areas affects only the stiffness. A similar observation is made by analyzing analytical predictions of the strength at different amplitude to wavelength ratios [47].

5.2 Draping Effects on Macroscopic Scale

The understanding of the mechanical behavior of composites is crucial to obtain reliable results to design composite parts. The use of macroscopic material models for the design of components is widespread. However, the necessary material properties are in generally obtained at a specific configuration which can vary due to manufacturing. Without any further experimental results or draping effect information, the predictability of the mechanical behavior comes with some uncertainties. With increasing part complexity different mechanical characteristics are present.

In order to capture the relevant material behavior on component level, basic material parameters need to be provided to the macroscopic material model. Additionally, model specific parameters are required. The presented micro-scale models can be used as a virtual material characterization toolbox for a variety of different load cases. Another possibility is to use simple unidirectional coupon tests for a basic material characterization and different laminate layups for the material model validation. In Section 5.2.1 the deduction of the required material and model parameters are presented. Using the developed macroscopic material models, the experimental coupon tests are remodeled. In Section 5.2.2 the fiber rotation, the nonlinear behavior and failure is validated based on off-axis and angle-ply coupon tests. Finally, the experimentally analyzed fiber waviness is modeled. The numerical results are given in Section 5.2.2. Once all results are validated on coupon level, several numerical studies are performed on an automotive composite part (see Section 5.2.3). Here the impact of the draping effects on component level are evaluated and conclusions are drawn.

5.2.1 Determination of Macroscopic Model Parameters

In order to model the elastic material behavior, the developed material model requires several basic parameters. Using elasticity parameters of fiber and matrix only the Halpin-Tsai parameters such as ζ_{E_2}, $\zeta_{G_{12}}$ and $\zeta_{G_{23}}$ need to be defined. To do so the different material stiffness values from experiments or micro-scale models are used to calibrate the Halpin-Tsai parameters. The decision whether experimental results or micro-scale models should be used depends on the available material data of the constituents. If the material properties of fiber and matrix are known, the Halpin-Tsai parameters can be defined using coupon tests. On the other hand, if the material properties of the fiber are not known, it is suitable to use micro-scale models to determine the fiber properties. This is the case for the used fiber. Based on the results from the micromodels and by utilizing experimental results of the coupon test, the Halpin-Tsai parameters are determined. After these parameters are defined, the elastic behavior of the composite is given over the whole FVC range. The obtained elasticity parameters are summarized in Table A.8. Besides linear elastic behavior the main cause of nonlinear material behavior is plasticity. The used plasticity material model requires five parameters ($\tau_{\mathrm{y}}, \alpha_{\mathrm{ap}}, e_{\mathrm{ap}}, \beta_{\mathrm{ap}}$ and f_{ap}) for a single FVC. In order to obtain these parameters only the experiments with nonlinear behavior due to plasticity can be used. As the plasticity model considers the acting action plane, first the Puck failure envelope parameters need to be determined. Since the inclination parameters in the (1,n1)-plane $p^{\mathrm{t}}_{\mathrm{n1}}$ and $p^{\mathrm{c}}_{\mathrm{n1}}$ are set to be equal and the inclination parameters $p^{\mathrm{t}}_{\mathrm{nt}}$ and $p^{\mathrm{c}}_{\mathrm{nt}}$ are a function of the $Y_{\mathrm{T}}/Y_{\mathrm{C}}$-ratio, only the in-plane strength values and the inclination parameter p_{n1} need to be defined. The strength values and the inclination parameter are also functions of the FVC. Here the experimental results of different off-axis, compression UD90° and in-plane shear coupon tests can be utilized. The resulting Puck failure envelope is given in Figure 5.11. As discussed in Section 2.5.1 some failure stress values are to be questioned. For

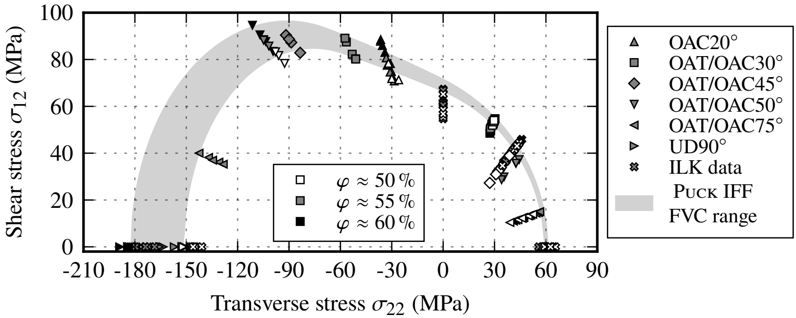

Figure 5.11: Failure envelope for in-plane loads at different fiber volume contents based on experimental results at different off-axis angles (20° to 90°)

example, the scatter for positive σ_{22} value is very high, indicating that the FVC dependency is much larger. However, as observed from micro mechanical models and in conjunction with the experimental results from ILK, this scatter can yield from a premature failure near the end tabs. Furthermore, the in-plane shear strength obtained from double V-notch rail shear coupon tests is smaller compared to the predicted failure envelope. The experimental results are highly affected by the notch of the samples and therefore tend also to fail prematurely.

Using the defined Puck failure envelope parameters, each action plane for a corresponding stress state can be defined. This is important to define the plasticity material parameters. By analyzing the performed coupon tests, an action plane angle $\theta_{\mathrm{ap}} \approx 0°$ could be observed for all off-axis tension tests (mode A) and several compression tests (mode B). In this case the acting stresses are limited to σ_{n} and τ_{n1}, while τ_{nt} equals to zero. This condition allows to determine the yield onset τ_{y} and the slope α_{ap} along the σ_{n} axis. First the yield onset is determined. Generally this parameter can be obtained from in-plane shear tests. In such case σ_{n} is equal to zero. However, the yield onset must be suitable for all other load cases. Here additional off-axis tension and compression tests have been used to determine the yield onset. Such load cases create support points in the (σ_{n},τ_{n1})-plane. These points allow to define the slope α_{ap} of the cone. The evolution of τ_{y} depends on the equivalent plastic strain $\bar{\varepsilon}_{\mathrm{pl,ap}}$. Using the stress-strain of the double V-notch rail shear test, the plastic strain can be extracted (see Figure 2.11). The experimentally obtained plasticity stress-strain curve is fitted to the used hardening function (cf. Equation (3.117)). Since the equivalent plastic strain for an action plane angle $\theta_{\mathrm{ap}} = 0°$ has a dependency on the dilatancy coefficient β_{ap}, an in-depth analysis is performed to determine the impact of this parameter. By comparing the results of the off-axis and angle-ply models, it could be shown that the best results are obtained if β_{ap} is set to zero. The other plasticity parameters, such as e_{ap} and f_{ap}, are mainly important if θ_{ap} is not zero. Especially the UD90° compression tests have the highest action plane angle within the evaluated test plan. Here only the parameter e_{ap} shows a significant sensitivity on the results, while f_{ap} is more important for large deformations of angle-ply compression tests. The used plasticity parameters, the corresponding in-plane strength values and inclination parameter are given in Tables A.9 and A.10. Since the strength of the composite is FVC-dependent, the corresponding dependency is added to Table A.10. It should be noted that the tensile strength in fiber direction is solely defined by the matrix and fiber strength. However, the compressive strength is defined by Equation (3.160) and therefore by the parameter $\bar{\phi}/\gamma_{\mathrm{y}}$ and the shear modulus of the matrix alone. Such formulation allows to define the strength values with a certain safety within the evaluated FVC range.

5.2.1.1 Damage Variables Interaction

As shown in Section 3.5.4 the parameter r_{g} can be used to define the interaction between the normal direction damage variable d_{n} and the shear damage variables d_{12} and d_{13}. As discussed in Section 3.5.3 this parameter can range between zero and infinity. However, it is unclear whether this parameter is affected by the FVC or not and how the damage variables interaction can be defined. Using a specific laminate layup with a $(0°/90°/0°)$ configuration, the interaction of the damage variables can be experimentally analyzed [194, 195, 229, 230]. The middle 90° ply is generally thick enough to visually observe the occurring cracks or to trigger sudden force drops for each new occurring crack. Each crack is formed if the transverse tensile strength of the inner ply is exceeded. While the transverse tensile strength is obviously not FVC-dependent, the in-plane shear strength shows a slight increase over the FVC [47]. Since experimental results with varying FVC and the specified laminate layup are not available, numerical studies can be used instead. The same procedure as for the experimental tests from literature is used: for each occurring crack the global stiffness drop can be recorded. As the cracks are formed due to IFF, these cracks can also be explicitly modeled. Such behavior can be achieved by adjusting the mesh of the middle ply. The mesh of this ply contains equidistant slit cracks represented by neighbor elements, which does not share the same nodes in the crack plane (cf. Figure 5.12). Since the cracks are already present, the resulting effective stiffness of the inner ply can be determined. The previously introduced methods for microscopic models can be used to model a representative area of the laminate. As the laminate is a representative portion of the evaluated area, periodic boundary conditions need to be applied. To do so, the Equations (5.1) to (5.3) can be utilized. However, only a portion of these equations is used since only the plane periodicity needs to be achieved. Using numerical models the number of cracks and the FVC can be varied. To determine the effective stiffness, the effective stress in load direction of the inner ply is obtained and in conjunction with the overall displacement of the

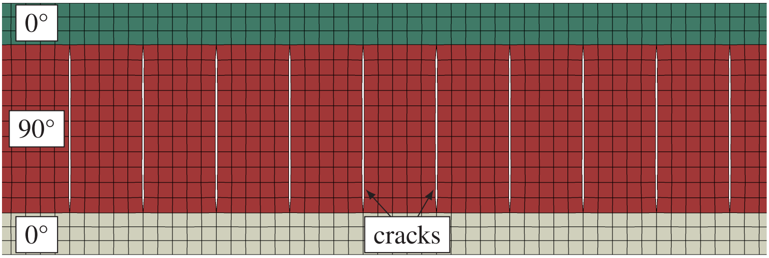

Figure 5.12: Side view of a model with a (0°/90°/0°) laminate and imposed cracks in the middle ply

laminate, the effective strain is also obtained. Since the strain is determined from displacements, which represent a linearized strain measure, only very small displacements represent accurate results. To evaluate the evolution of the damage variables d_2 and d_{12} and draw conclusions regarding their interaction, two different load cases are analyzed: transverse tension and in-plane shear. It should be noted that the linearized strain for transverse tension results from only one displacement component, while the shear strain corresponds to the shear angle. For each FVC the initial undamaged transverse modulus E_2 as well as the shear modulus G_{12} are known. Since only small loads are applied, the nonlinear material behavior due to fiber rotation or plasticity is not present. The actual damage variable for each load case is obtained from the ratio of the initial modulus and the one with cracks (e.g., $d = 1 - {}^{E_2}/_{E_2^{\mathrm{init}}}$). With increasing number of cracks, the crack density δ_{c} of the middle ply is increased. The crack density defines the number of cracks per unit length. It is obvious that with increasing crack density the damage variable values are also increased. To evaluate the interaction between d_2 and d_{12}, the thickness of both 0° plies has been set to $t_{\mathrm{L}} = 0.2875\,\mathrm{mm}$. The thickness of the middle ply is 14 times thicker. For each crack density the effective moduli are obtained. For both load cases the crack density is the connecting parameter, which can be used to draw a graph (cf. Figure 5.13). Using the numerical results the interaction between the two damage variables can be analyzed. Using the definition of the damage variables d_2 and d_{12} from Equations (3.143) and (3.144), the interaction parameter for this study yields $r_{\mathrm{g}} = 0.175$. This value is used for all further simulations. The numerical results show that the FVC has no effect on

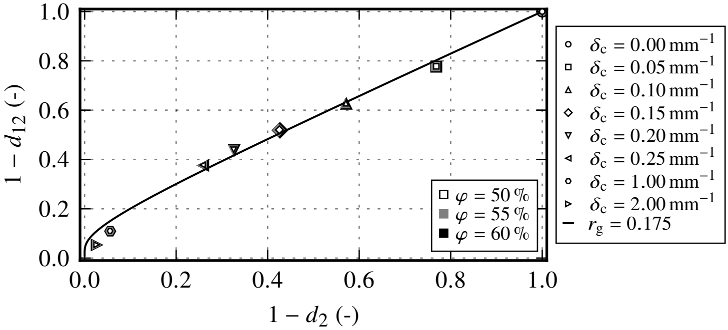

Figure 5.13: Interaction of damage variables d_2 and d_{12} with the fitted energy ratio parameter r_g for varying fiber volume contents and different crack densities δ_c

r_g. This condition reduces the number of variables to model FVC-dependent failure significantly.

5.2.2 Coupon Tests

To validate the developed macroscopic material model experimental coupon tests are remodeled. Due to complex material behavior different load cases trigger specific material responses. The major factors such as fiber direction, FVC and fiber waviness allow to activate these triggers. As the experimental results showed, several factors lead to nonlinear behavior. First, the experimental results of fiber rotation caused by deformation is compared with numerical results. Next, the stress-strain curves from numerical and experimental results are compared. Here unidirectional laminates and angle-ply laminates are analyzed. While these results cover the material response triggered by the fiber direction and its deformation, the next step is to additionally investigate the FVC. Finally, the macroscopic material response for an imposed waviness is compared with experimental results.

5.2.2.1 Material Axes Rotation

The general material behavior is driven by the fiber direction of the laminate. As shown from experimental results, for all cases where the load is applied not in fiber direction or transverse to the fiber direction, the material axes are forced to rotate. The developed material model captures this behavior. However, the impact of the fiber rotation on the stress-strain response is not clear. Using the developed model three combinations are possible: no material axes rotation, considering only the rotation of the fiber direction (orthogonal coordinate system) and rotation of all material axes (nonorthogonal coordinate system). By analyzing the experimental results the off-axis and angle-ply laminates with $\theta = 45°$ lead to severe fiber rotation. Therefore, an off-axis compression (OAC) and an angle-ply tension load case are evaluated regarding the resulting impact on the stress-strain curve. Here only the different cases of fiber rotation with enabled plasticity are evaluated. Besides the global material response (ε_{xx} and σ_{xx}), which both define the response along the x-axis, also the local nonzero stress components (σ_{11}, σ_{22} and σ_{12}) are evaluated. In the local material frame the stress σ_{11} defines the load in fiber direction. On the other hand, the local stress σ_{22} represent the load transverse to the fiber direction. The local shear stress σ_{12} defines the shear response in the (1,2)-plane. The fiber rotation angle and the angle between material axes for the OAC45° load case is given in Figure 5.14 and for the ±45° laminate in Figure 5.15. The numerical stress results for both load cases are given in Figures 5.16 and 5.17. The numerical results show a fiber rotation of about $\Delta\theta = 1.5°$ at $\varepsilon_{xx} \approx 8\,\%$ for the OAC45° load case. This value is reached for two strain measures: rotation of the fiber direction and rotation of all material axes. As expected the fiber direction angle without rotation remains zero. Furthermore, the angle between material axes changes only if all material axes are rotated. In other cases an orthogonal coordinate system is preserved ($\theta_{12} = 90°$). The angle-ply ±45° laminate shows a more pronounced fiber rotation compared to the OAC45° load case. The fiber rotation reaches a value of about $\Delta\theta = -4.5°$. While the model using only the rotation of the fiber direction shows a linear trend with increasing strain, the model using the rotation of all material axes has a nonlinear increase of the fiber rotation angle. The remaining observations are similar to the OAC45° load case.

By comparing the different approaches for the OAC45° load a distinct deviation for the stress values can be observed. While no fiber rotation and fiber

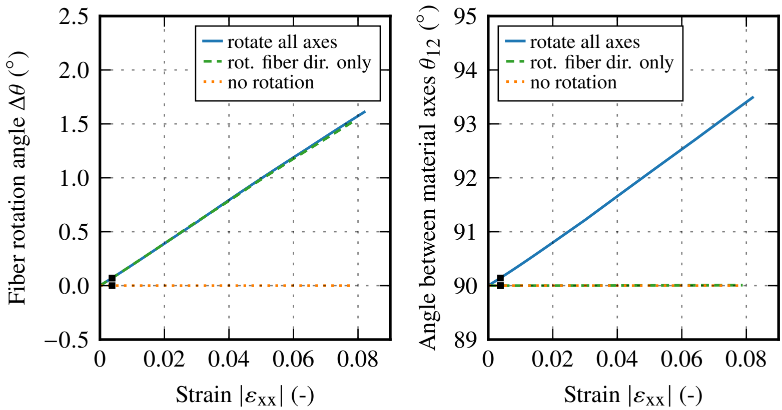

Figure 5.14: Resulting fiber rotation and the angle between material axes for different strain measures for an off-axis compression (OAC45°) model (plasticity onset denoted by square markers)

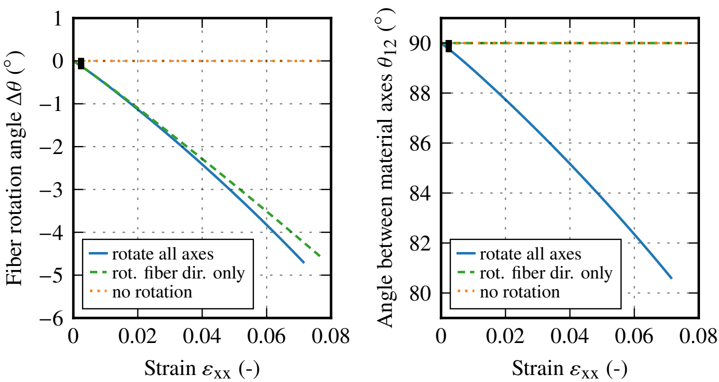

Figure 5.15: Resulting fiber rotation and the angle between material axes for different strain measures an angle-ply ±45° model under tensile load (plasticity onset denoted by square markers)

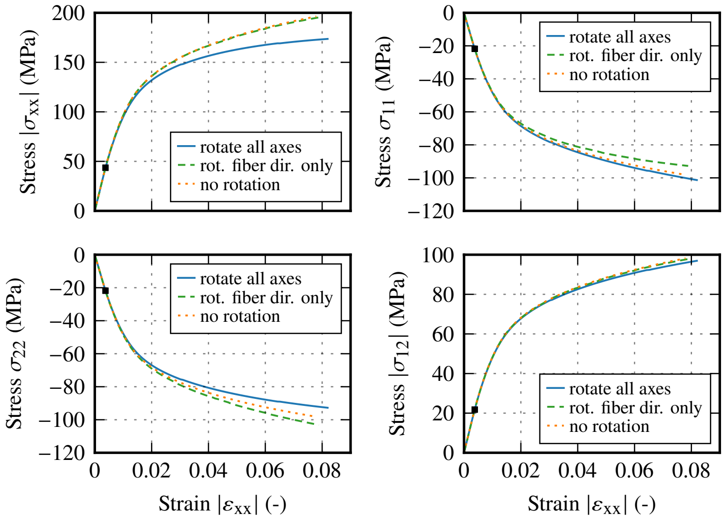

Figure 5.16: Resulting stress response (global stress σ_{xx} along x-axis and local nonzero stress σ_{ij}) for different strain measures for an off-axis compression (OAC45°) model (plasticity onset denoted by square markers)

rotation only lead to nearly equal σ_{xx} stress results, the rotation of all material axes reduces the stress response significantly. By comparing other stress components in case of fiber rotation only, the stress in fiber direction σ_{11} is reduced and the transverse stress σ_{22} is increased. This behavior can be explained due to increase of the actual fiber angle, towards the material response of a UD90° laminate, with increasing compression load. On the other hand, the shear stress σ_{12} seems to be independent of the actual fiber rotation case. The added square marker to the stress-strain curve indicates the plasticity onset. It is obvious that this onset does not correspond to the point where the stress responses start to deviate. It seems to be rather the case that the associated deformation causes the differences between the individual results.

On the other hand, the stress response of an angle-ply ±45° laminate shows more pronounced stress components differences (cf. Figure 5.17). Although the applied deformation of about $\varepsilon_{xx} \approx 8\,\%$ is similar for both models, the

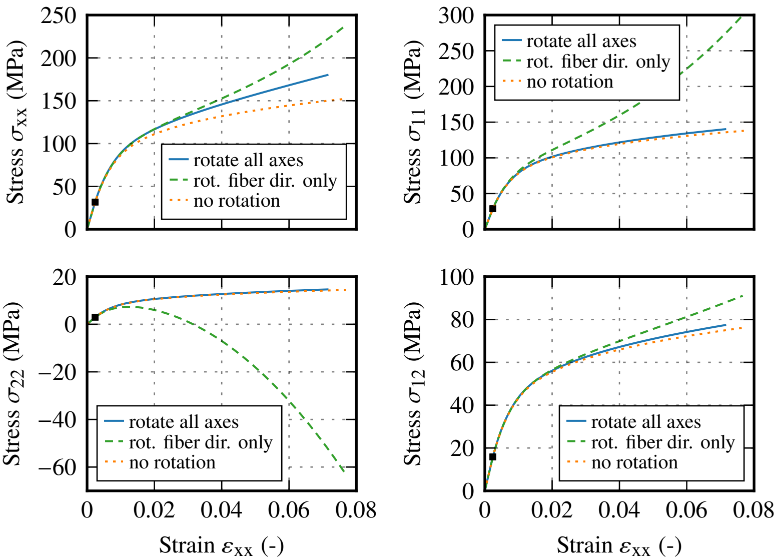

Figure 5.17: Resulting stress response for different strain measures for an angle-ply ±45° model under tensile load (plasticity onset denoted by square markers)

fiber rotation for the angle-ply laminate is absolute about three times larger (cf. Figure 5.14 and 5.17). By comparing the stress response of the fiber rotation only, a unique attribute can be observed. The initial positive transverse stress σ_{22} changes the sign with increasing deformation. Similar observations have been already published [11]. The reason for such behavior is the corresponding material axis frame. For the fiber rotation model the material axes remain orthogonal ($\theta_{12} = 90°$). The tension load leads to a continuous change towards smaller angles in each ply. Initially σ_{11} and σ_{22} are both positive values for a ±45° laminate. If the maximum fiber rotation angle $\Delta\theta \approx 4.5°$ is used, the laminate layup changes from ±45° to ±40.5°. In such case the initial transverse stress σ_{22} is no longer positive. On the other hand, the two other strain measures lead to positive σ_{22} stress values. The reason for this is that the model without fiber rotation does not affect the laminate layup. Likewise, the model where all material axes are rotated leads to the deformation of the transverse material axis, which leads to a tensile stress. If only the fiber rotation is considered and the material frame remains orthogonal, a change in the failure mode can be observed. The initially active failure mode A changes to mode B and C. Overall each stress component for the fiber rotation only case leads to a large deviation to both other presented methods. As mentioned in Chapters 2 and 3 the occurrence of transverse and perpendicular cracks indicates that the σ_{22} stress remains positive. Since the fiber direction angle is reduced, the dominance of the fiber is more pronounced and leads to an increase of the global stress response. Evaluating the stress response due to no fiber rotation or by rotating all material axes shows almost no difference for the local stress components. However, the global stress response shows a dependency on the used fiber rotation method. Similar to the off-axis results the plasticity onset, denoted by square markers (see Figure 5.17), does not correspond to the onset of the stress deviation between the three cases. From the observed numerical results it can be concluded that by considering only the fiber rotation a severe discrepancy can occur. Therefore, in conjunction with experimental results it is obvious that the rotation of all material axes needs to be taken into account to model the material behavior of composites correctly.

In order to compare the material model predictions of the fiber rotation angle $\Delta\theta$ and the corresponding angle between material axes θ_{12} with experimental results, all evaluated experiments with an FVC of $\varphi \approx 54\,\%$ have been remodeled. From each numerical result both angles have been obtained using the deformation gradient. The comparison of the results for the off-axis tests are given in Figures 5.18 and 5.19, while the results for angle-ply laminates are given in Figures 5.20 and 5.21. By comparing the numerical off-axis results with the experimental ones, an overall good to very good correlation can be observed. Especially all tensile loads are in a very good agreement. On the other hand, the deviation for compressive loads can be observed for off-axis compression tests with $\theta \in [45°, 50°, 75°]$. By evaluating the acting failure mode for these angles, a transition from failure mode B (fracture angle $\theta_{\mathrm{fp}} = 0°$) to failure mode C (fracture angle $\theta_{\mathrm{fp}} \neq 0°$) can be observed. All evaluated load cases with a stress state leading to failure mode C show a deviation (cf. Figure 5.18 OAC45°, OAC50° and OAC75°). This observation is present for the fiber rotation angle and the angle between material axes. In all these cases the numerical prediction lead to smaller fiber rotation angles and angle between material axes as the experimental results. Therefore, the numerical results underestimate the material behavior. An in-depth analysis of

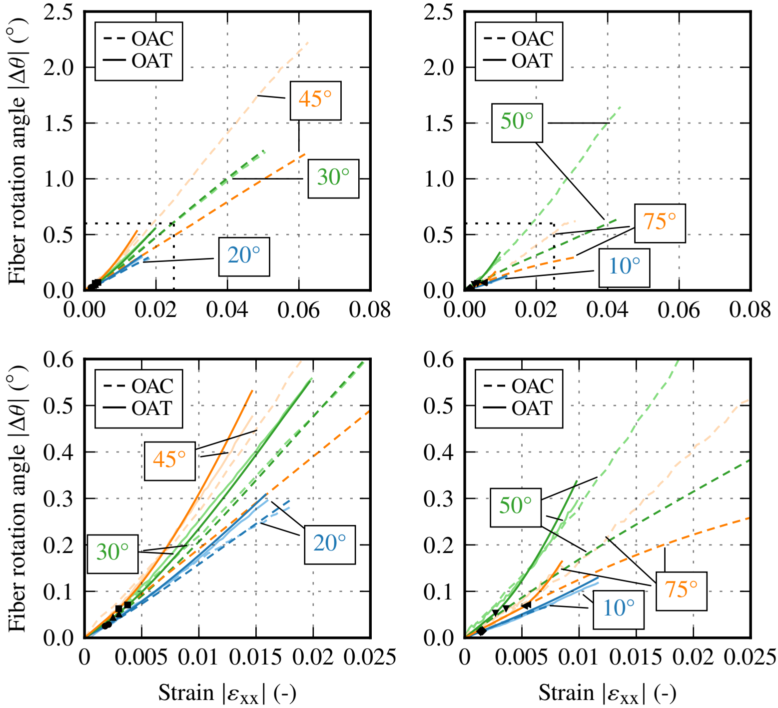

Figure 5.18: Comparison of the fiber rotation angle from numerical (dark color) and experimental (light color) off-axis tension (OAT) and off-axis compression (OAC) tests (off-axis angles are annotated and plasticity onset is denoted by markers)

the material behavior for fracture angles $\theta_{fp} \neq 0°$ is needed to determine the source of the deviation.

The numerical results for the fiber rotation of angle-ply laminates show a better agreement with experimental observations as for off-axis tests (cf. Figure 5.20). The only two laminates which show slight deviation to the experimental results are the ±40° tension and the ±50° compression test cases. Using the developed model, fiber rotation for a ±45° laminate is captured very well up to $|\Delta\theta| \approx 5°$.

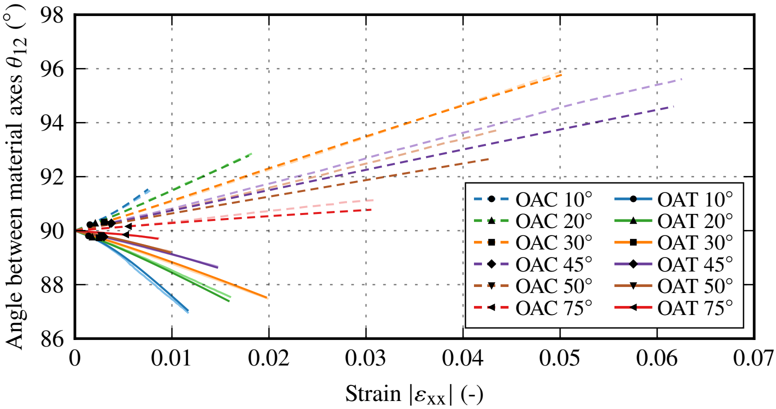

Figure 5.19: Comparison of the angle between material axes from numerical and experimental off-axis tension (OAT) and off-axis compression (OAC) tests (plasticity onset denoted by markers)

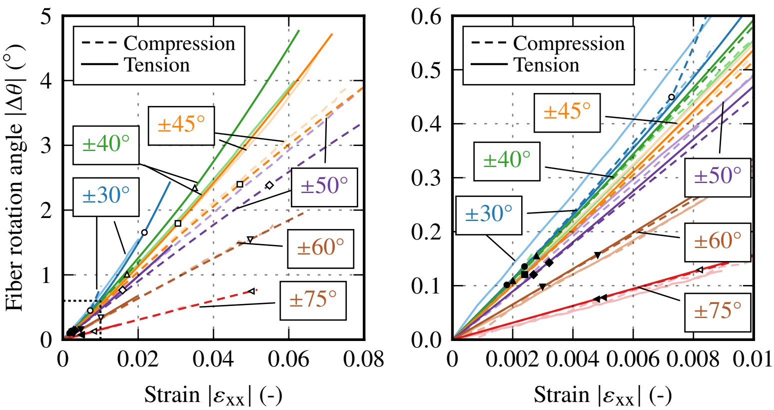

Figure 5.20: Comparison of the fiber rotation angle from numerical and experimental angle-ply tests (angle-ply angles are annotated, plasticity onset denoted by black markers, and inter-fiber failure onset is denoted by white markers)

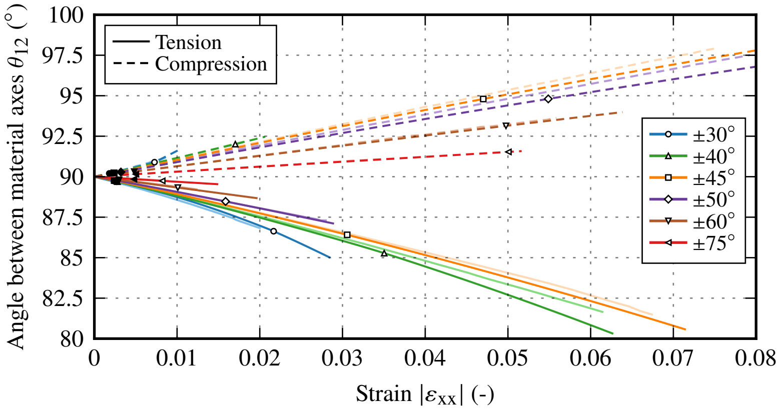

Figure 5.21: Comparison of the angle between material axes from numerical and experimental angle-ply tests (plasticity onset denoted by black markers and inter-fiber failure onset is denoted by white markers)

The angle between the material axes also shows a good correlation up to an angle change of 10°. As angle-ply laminates do not fail if first cracks occur, the point of inter-fiber failure initiation can be specified. In the case of ±30° compression tests, the IFF onset lead to a kink and an increase of the fiber rotation angle. Overall the developed model provides reliable results regarding fiber direction change for large deformations.

5.2.2.2 Stress-Strain Curves for Unidirectional and Angle-Ply Laminates

Besides the fiber rotation the general comparison of the stress-strain curves is also performed. The experimental results of off-axis and angle-ply tests at a FVC of $\varphi \approx 54\,\%$ are compared with numerical results. The corresponding stress-strain curves are given in Figures 5.22 and 5.23. By comparing the off-axis results a very good correlation between experimental and numerical results is given. The overall nonlinear behavior due to plasticity is well captured. Although the initial stiffness at the same angle is equal for tensile and compressive loads, the plasticity model can clearly create a distinct difference during hardening. Regarding the final failure several observations can be made.

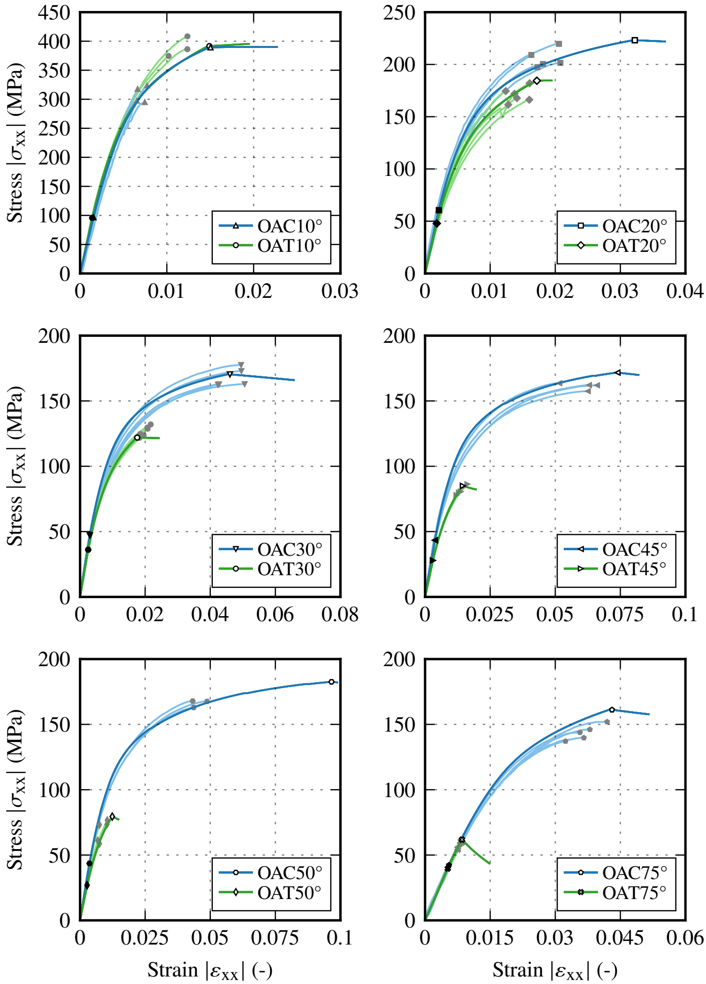

Figure 5.22: Comparison of numerical stress-strain curves of off-axis models (dark color) with experimental results (light color) from off-axis compression (OAC, dashed curves) and off-axis tension (OAT, continuous curves) (Maximum stress from experiments is denoted by gray markers, numerical plasticity onset denoted by black markers and numerical inter-fiber failure onset is denoted by white markers)

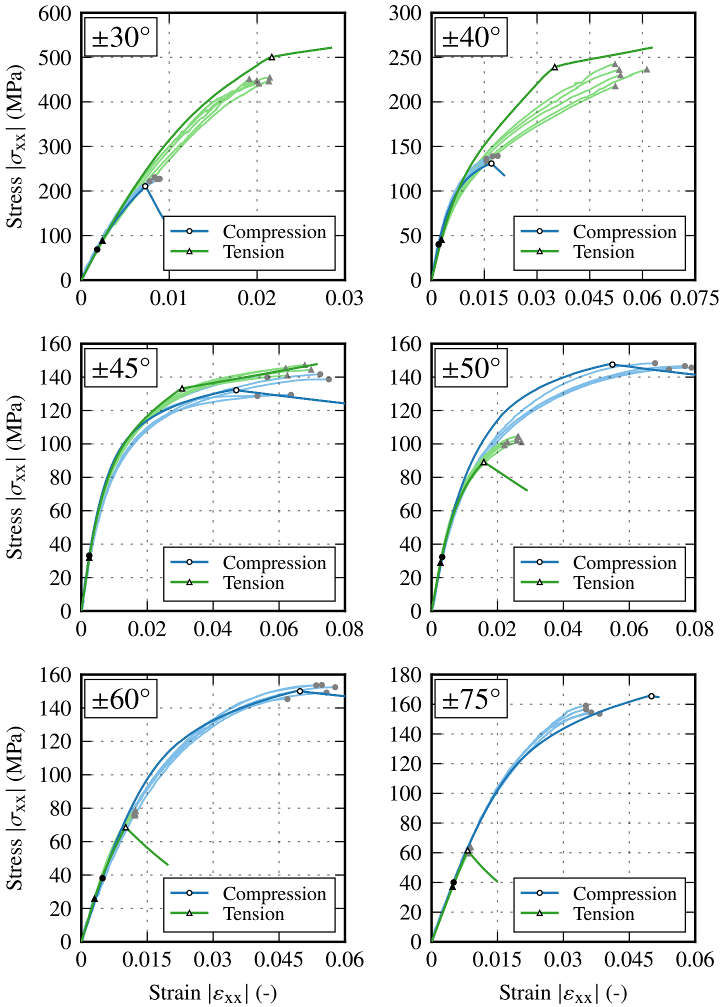

Figure 5.23: Comparison of numerical stress-strain curves of angle-ply models (dark color) with experimental results (light color) from angle-ply compression and tension (Maximum stress from experiments is denoted by gray markers, numerical plasticity onset denoted by black markers and numerical inter-fiber failure onset is denoted by white markers)

As discussed in Section 2.5.1 the off-axis compression tests at 10° and 20° lead to premature failure due to buckling. Therefore, the final failure stress values do not represent the actual material failure behavior. The numerical failure stress values for both compression tests are the result of the used failure envelope, which lead to higher failure stress values. Although previously observed deviation of the fiber rotation for OAC45° and OAC75° models is present, the achieved strain prior to IFF show a good agreement with experimental results. A major failure strain difference for OAC50° result can be observed. Here the required stress to trigger IFF is reached only at very high strain. However, the stress level is similar to the experimental results.

The stress states of angle-ply laminates are quite different to off-axis stress states. Due to opposed fiber direction, the only nonzero global stress components are σ_{xx} and σ_{xy}. For the same fiber direction angle the local stress components of an angle-ply laminate and an off-axis load case are totally different. This leads to stress states which create differences in the stress-strain curve results. For example, the nonlinear behavior due to plasticity shows a good correlation for angle-ply laminates with an angle of 45° and greater. However, due to dominance of the fiber direction stress σ_{11} for the ±30° laminate, which has no effect on the hardening evolution, slight deviation occur for the tensile load. The stress-strain curve of the tensile load for the ±40° laminate show an obvious difference between experimental and numerical results. By performing a sensitivity analysis of the plasticity material parameters to achieve a better correlation between the results, only the β_{ap} show a pronounced sensitivity. This parameter corresponds to the dilatancy coefficient and has been set to zero to achieve a better agreement between numerical and experimental results. However, the effect of dilatancy especially for the ±40° laminate seem to be more relevant as for other laminate layups. On the other hand, the failure stress at IFF correspond to the failure stress range of ±40° laminates. Therefore, it is assumed that the dilatency is laminate layup specific and need to be considered by the plasticity model. By comparing the tension load cases for ±50° and ±60° laminates, the numerical results predict an early IFF followed by a pronounced degradation. It is assumed that the experimentally observed strength of these laminate is higher due to in-situ effects. Contrary to unidirectional laminates, the transverse tensile strength of each ply of and angle-ply laminate can be higher due to in-situ effects. Such behavior is primarily determined by the thickness of the ply and the fiber direction of the neighbor plies. By comparing the compression load cases the reached failure stress values are in a very good agreement for all angle-ply laminates. Overall, the developed material model shows a great capability to predict the nonlinear behavior for different stress states and the corresponding failure stress values. Further aspects such as in-situ strength, effect of the dilatancy or the fiber direction stress on the plasticity model need to be further evaluated and developed. Nevertheless, the developed material model provides already reliable results for a constant FVC and provides a solid basis to consider further impact due to draping.

5.2.2.3 Fiber Volume Contents on Coupon Level

The impact of the fiber orientation and the accompanying fiber rotation on the mechanical behavior could be reliably reproduced. However, the previously presented results are obtained for a specific FVC. The developed model is able to process the draping information in terms of FVC. Using the performed experimental results, two different FVC are utilized to compare the numerical predictions. One of these tests is carried out in fiber direction at different fiber volume contents [47]. Although the tensile and compressive strength in fiber direction are determined by the analytical functions for different fiber volume contents, the stress-strain curves show nonlinear material behavior. As discussed in Section 3.4.1, the stiffness in fiber direction is determined by the nonlinear material behavior of the carbon fiber. A comparison of the stress-strain curves in the fiber direction for different fiber volume contents is given in Figure 5.24. For both loading directions, the nonlinear material behavior can be observed. The results show a very good agreement between the experimental and numerical stress-strain curves under a tensile loading. On the other hand, the experimental results of the compression tests show significantly higher stiffnesses than the numerical results. On closer examination, it is noticeable that the differences between the numerical and experimental results differ by a constant multiple for both FVC values. The experimental results achieve approximately 20 % higher stiffnesses. As already shown in literature, the static stiffness is independent of the loading direction [21]. However, a special experimental device is needed for this purpose. For this reason, it is suspected that the acquisition of strain in the (1,2)-plane provides too small values due to strain restraint. To investigate this circumstance further, the strain should be recorded from two sides of the coupon sample. If a strain difference in the fiber direction occurs in the same test, a reliable stiffness determination from compression tests is not possible. In this case using the E_1 stiffness

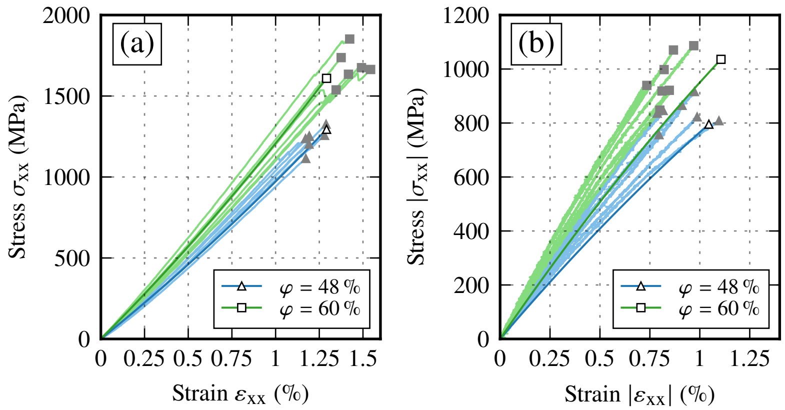

Figure 5.24: Comparison of the stress-strain curves of (a) tensile and (b) compressive tests in fiber direction at different fiber volume contents

from tensile tests would be a more reliable source. Nevertheless, the nonlinear material behavior in compression tests is well represented by the developed material model.

For selected off-axis tests, the FVC is varied to further investigate the influence on matrix-dominant load cases (cf. Figure 2.18). Compared to the FVC-dependent results in fiber direction, the matrix dominant off-axis tests are characterized by a pronounced nonlinear material behavior. The resulting failure stress values are the result of the FVC dependent Puck failure criterion. In addition to the dependence of the stiffness and strength values on the FVC, the material parameters for plasticity are also dependent on it. As observed experimentally (see Figure 2.11), the hardening curves are independent of the evaluated FVC range. In other words for $\sigma_n = 0$ the material plasticity response does not change with variation of the FVC. For stresses $\sigma_n \neq 0$ and increasing FVC, the sensitivity of the plasticity model towards σ_n stress decreases. Conversely, this means that the load direction-dependence on the plastic material behavior becomes smaller and the parameter α_{ap} evolves towards zero. On the other hand, with increasing FVC the parameter e_{ap} needs to be also increased to capture the material plasticity. For the parameters β_{ap} and f_{ap} no conclusive statement can be made regarding their dependence on the FVC. For this purpose, tests must be carried out on angle-ply laminates with different fiber volume contents. The comparison of the stress-strain curves of the experimental and numerical results at different fiber volume contents, off-axis angles and load directions is given in Figure 5.25. Overall a very good agreement between experimental and numerical results can be achieved by the developed material model at different FVC values.

5.2.2.4 Waviness on Coupon Level

Besides the impact of fiber orientation and FVC, a local fiber waviness is another aspect that significantly influences the mechanical properties of FRP materials. The developed material model processes the amplitude to wavelength ratio to determine the corresponding effective stiffness and the local fiber orientation in each section of the wave. Using the developed material model for unidirectional straight composites, the experimental tests are remodeled. The comparison of numerical and experimental results is given in Figure 5.26. A comparison of the resulting numerical and experimental results shows that both the stress-strain curves and the strengths exhibit significant deviations. First, the lack of pronounced nonlinear behavior can be observed. Although in each half of the wave nonlinear behavior due to plasticity is predicted, the global stress seems to be not affected at all. It is assumed that the back transformation of the local stress into the global coordinate system leads to a diminishing effect. Furthermore, the numerical failure stress values overestimate the experimental ones. Since the occurring discrepancy occurs for both tensile and compression tests, its cause must lie in the failure initiation. As mentioned above the local stress response leads to a very pronounced nonlinear material behavior. Since the global deformation increases, the global strain leads to even higher local plastic strain. However, the occurring stress state does not trigger the failure initiation as the local plasticity is severely pronounced. For testing purposes the plasticity model is suspended to specifically trigger the local failure initiation. In general, the plasticity should be always considered when waviness is modeled. As previously shown, the material behavior is highly affected by plasticity (cf. Figure 5.22). When comparing the stress-strain curves without plasticity, a much better agreement of the obtained strength values can be observed. The obtained strength values are the result of a combination of the local IFF and the corresponding damage evolution. This observation is supported by the numerical micro-scale models and experimen-

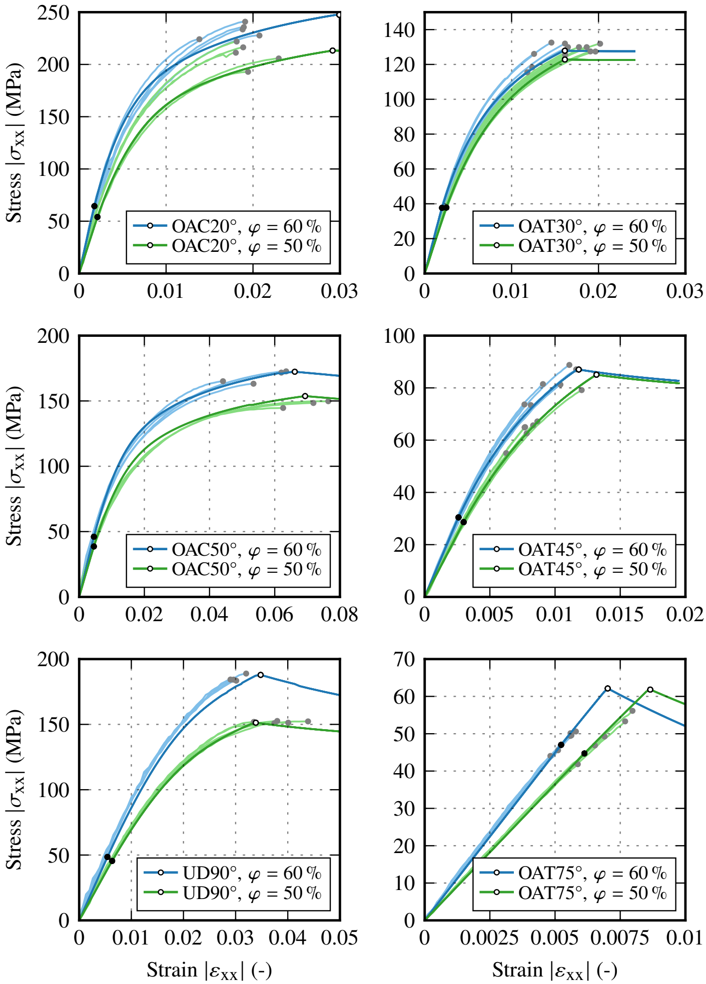

Figure 5.25: Comparison of numerical and experimental results on off-axis compression (OAC, left), transverse compression (UD90°, left) and off-axis tension (OAT, right) at different fiber volume contents (Maximum stress from experiments is denoted by gray markers, numerical plasticity onset denoted by black markers and numerical inter-fiber failure onset is denoted by white markers)

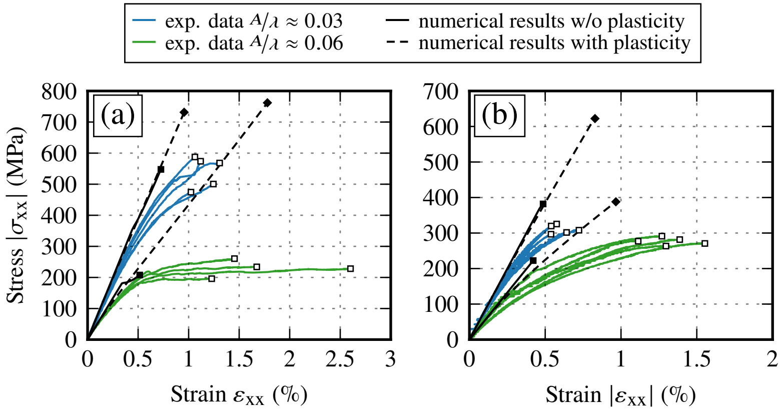

Figure 5.26: Comparison of experimental and numerical stress-strain curves for (a) tension and (b) compression tests for coupons with two different amplitude to wavelength ratios (experimental failure stress is denoted by white markers and the numerical ones by black markers)

tal results. However, this improvement regarding the failure stress range leads to an oversimplification of the actual nonlinear material behavior on component level. Therefore, caution is advised as the deformation of the material could be much higher (cf. Figure 5.26b). Generally by neglecting the plastic material behavior, the deformation of the material prior to failure is predicted too small. In this case, a premature failure initiation would not consider the load-bearing capacity of the material. As a consequence, if a material model is used without any plasticity model, the failure on a component level can represent a lower limit of the total load-bearing capacity. To consider the more accurate strength due to waviness, a case dependent distinction on component is made. The plasticity is enabled for all elements, except those with a present waviness. However, from the obtained numerical results a further development of the material model is needed, to achieve a better agreement between numerical and experimental results.

5.2.3 Numerical Prediction of the Mechanical Behaviour at Part Level

The previous results are validated on simple coupons. The obvious impact at coupon level is now to be verified at component level. For this purpose, a component from the automotive sector is used as a numerical example. Since different laminate configurations can be used in a real component, several draping simulations with different laminate configurations have been performed. Using the developed material model, the impact of draping effects is modeled. Finally, the impact of draping effects on the component failure and performance is evaluated.

5.2.3.1 Acquisition and Processing of Experimental Results from Draping Tests

The quality of numerical results rely upon validated input data. For the validity of the numerically predicted draping effects after forming, the resulting deformation is first investigated on a reference component. As already shown, the experimentally determined coupon tests can be very well reproduced. The input data required such as fiber orientation, FVC or fiber waviness are directly specified. During component manufacture, these parameters are set by the forming process. If the forming process is robust and the quality of the used fabric is ensured, a detailed full-field measurement of the deformed preform can be performed. In previous publications [27, 204, 205], the homogenized fiber orientation could be successfully measured. The results are captured optically or by means of eddy current measurement. However, these methods are not suitable to determine the deformation of the fabric itself, as they only record the homogeneously distributed fiber orientation.

In-depth investigations are therefore carried out at the Institute of Lightweight Engineering and Polymer Technology (ILK) of TU Dresden on the here used fabric [206, 231]. A new approach is adopted to determine the deformation of the fabric. The initially flat undeformed fabric is imprinted with a dot grid and afterwards deformed (see Figure 5.27). After forming, the position of the individual points can be determined over the entire surface using the GOM Argus system. This is done by taking images from different viewing angles, with specially placed reference markers serving as orientation aids. Since the

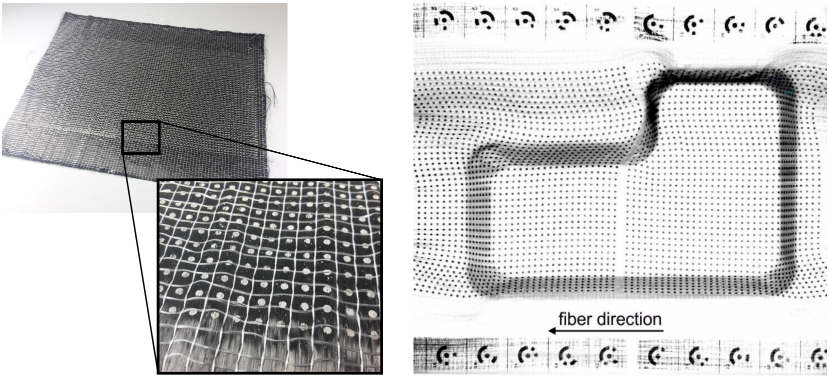

Figure 5.27: Imprinted dots on the preform (left) and the detected grid dots on a deformed fabric with the associated reference markers (right) [57, 206]

position of the reference markers is known, the coordinate of each point can be determined by means of triangulation. Thus, the deformed surface of the components can be captured relatively quickly and efficiently. If the initial spacing of the imprinted point grid is specified and a corresponding coordinate system is defined, the displacement of each point can be quantified. To determine the resulting fiber orientation, the individual points must be connected along the initial fiber orientation. However, compared to other optical methods, this measurement method can also detect the deformation of a ply inside a stack. The inner points have to be detected differently. For this purpose, the points are printed with a silver-containing ink [206]. Due to the high material density of the dots, the deformed dots can be easily detected using projection radiography. Here, the fabric is radiated in a computer tomograph and the printed dots can be made visible. For more details on the data acquisition of the grid points see Kunze et al [206]. If a deformed mesh is formed from the individual points, the deformation gradient $\boldsymbol{F}$ can be determined directly. Using this central factor all required data such as fiber direction, FVC or fiber waviness are directly obtained.

To determine a mesh from the initial grid of points, Delaunay triangulation is used. This method creates a mesh using triangular elements. An already implemented method of the Delaunay triangulation can be used from the Python package SciPy. Once a mesh is created, the deformation gradient is calculated using the element shape function for triangular elements based on the initial and deformed coordinates of each node of an element. In order to validate the draping simulation results, a direct comparison of the numerical and experimental results can be made. However, some preparations are required first. Since the original coordinate system from the draping simulation does not correspond to the coordinate system of the experimental one, these must first be transferred into each other. A manual positioning of both geometries to each other can be very difficult, since several support points have to be calibrated at the same time. Therefore, an automated method is implemented that determines both the required translation and the rotation of the coordinate system of the experimental measurement with respect to the coordinate system of the draping simulation. For this purpose, reference nodes are defined in advance as support points for the automated positioning. Once the two geometries are aligned, both meshes (draping simulation and deformed preform) can be mapped to a uniform mesh. To transfer the data to a unified mesh, the mapping process according to Section 4.4.1 is used. This method ensures the possibility that the results can be compared directly.

The L-shaped geometry with different draft angles is used to validate the results from the draping simulation (see Figure 5.28). Since the validity of numerical draping results has been investigated and validated for simple plane forming tests [50], the focus here is on inner preform layers of an eight-layer

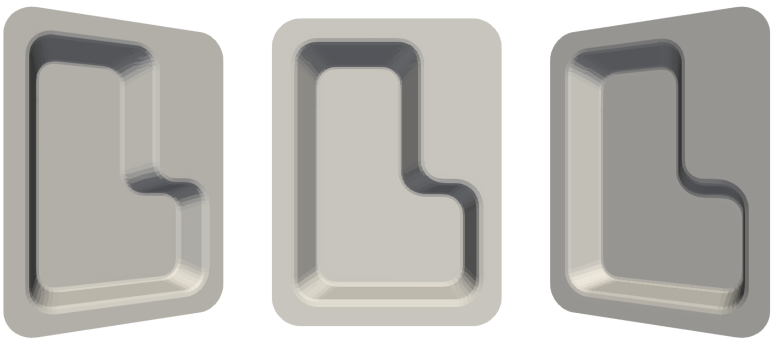

Figure 5.28: Selected L-shaped geometry for draping simulation validation

unidirectional stack. The dot pattern is applied in such a way that they are located exactly between the fourth and fifth preform layers. The forming of the stack is subject to scatter, therefore a total of three preforms are evaluated. Due to manufacturing reasons, the dot pattern is printed in two adjacent areas. After forming, the coordinates of the individual points are determined and as previously described a mesh is generated. The model of the draping simulation is simulated according to the real test setup. Eight layers are modeled taking the friction between the individual layers and the mold into account. The numerical strain results are used from the fourth layer for the comparison with experimental results. Based on the used strain measure in the draping simulation [2], the individual strain components ε_1 and ε_2 as well as the perpendicular transverse strain $\varepsilon_\perp$ are determined (cf. Figure 5.29). The shear strain γ_{12} can be measured as the shear angle between the fiber direction and the second material axis. In addition to the strains, further information can be extracted from the measurements. This includes the fiber orientation $\boldsymbol{f}_1$ as well as the area change $^A/_{A_0}$, which is an indicator of the occurring FVC (see Figure 5.29). As mentioned in Section 4.2.3, the potential fiber waviness along a roving can be determined from the strain in the fiber direction. In order to be able to compare the numerical and experimental results directly, a uniform L-shape geometry is meshed and the results from the draping simulation and the experimental measurement are mapped onto it (see Figure 5.30). This uniform geometry is smaller than the dimensions of the draping simulation and larger than the measured area. Therefore, after mapping the experimental results to the unit geometry, areas will appear where no information is available. The mapped experimental results of the three samples for the evaluated quantities

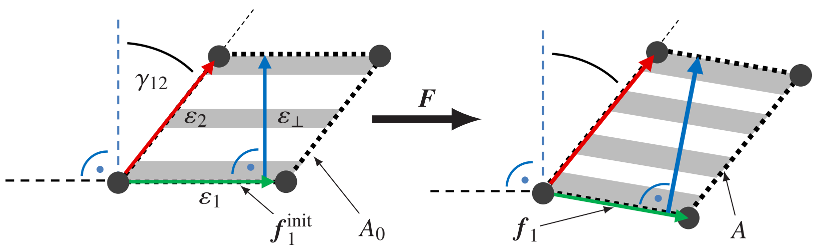

Figure 5.29: Strain measure in the draping simulation and the resulting fiber orientation, as well as the associated change in area of the element

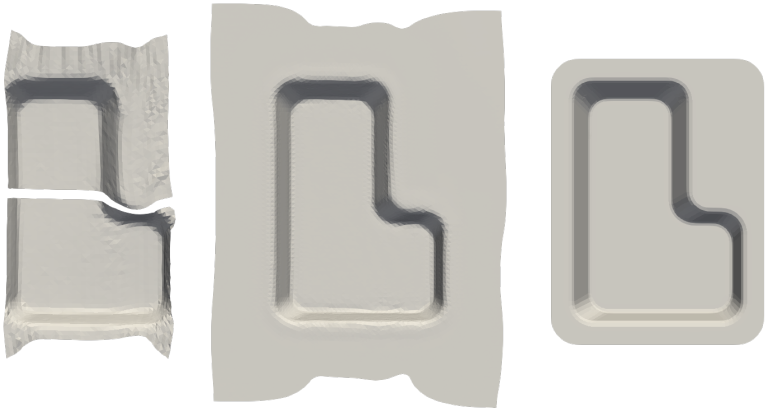

(a) (b) (c)

Figure 5.30: Deformed fabric layer from experimental forming (a), draping simulation (b) and the uniform geometry for the mapping process (c)

is shown in Figure 5.31. If a general comparison of the different quantities is made for the entire test series (vertical comparison), a very good agreement is shown. This means that the test procedure is reproducible and thus the test results are reliable. In order to be able to perform a comparison of the fiber orientation, the local fiber orientation is compared with the direction along the 1-axis which represent the ideal fiber direction (see coordinate system bottom left in Figure 5.31). For this purpose, the vector in the 1-direction is projected into each element and the difference in degrees θ is calculated. There are several areas where deviation angle is almost zero. Thus, in these regions, the preform is barely reoriented. In contrast, a strong reorientation of the fiber direction occurs in all corners (inside or outside) of the geometry. Due to the difference in running length of neighboring rovings, a rotation of the initial fiber direction occur. In addition to the fiber orientation, the local area change has been considered. By assuming a constant thickness of the cavity, an area change has a direct effect on the local area weight of the fabric, and therefore the FVC is affected. To evaluate the area change the ratio A/A_0 of the local area A to its initial area A_0 is calculated. From the experimental results the area ratio ranges from $A/A_0 = 0.8$ to 1.1. If the ratio is $A/A_0 < 1$, the area weight increases and thus the FVC also increases. This condition works in

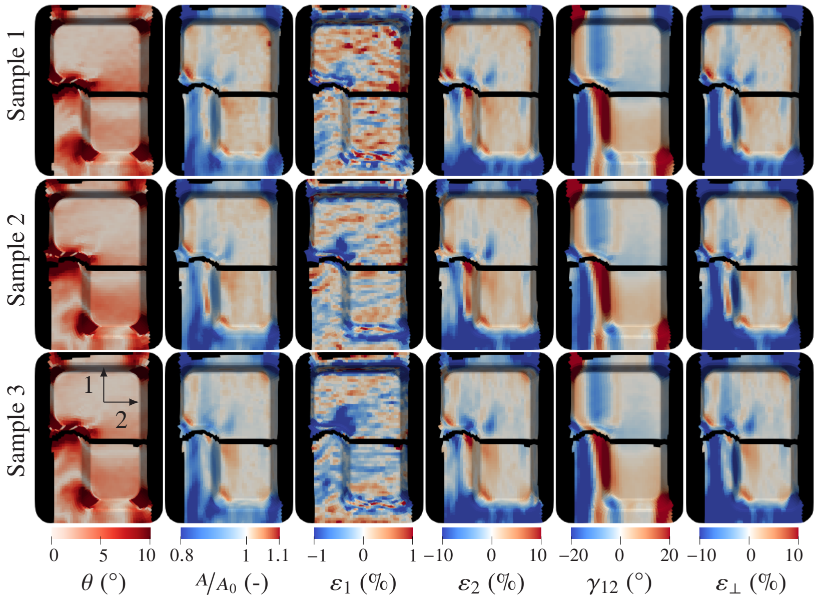

Figure 5.31: Comparison of test results of three different preforms (Sample 1,2 and 3): deviation from an ideal angle θ, area ratio change A/A_0, strain in fiber direction ε_1, strain along the second material axis ε_2, shear angle γ_{12} and strain perpendicular to the fiber direction $\varepsilon_\perp$ (in black areas there is no information)

both directions, which shows the pronounced effect on the FVC. In the entire bottom area, moderate to minimal area changes in the whole area are present. The most significant changes are in the corners of the component. As with the fiber orientation, an increase in the area weight occurs here due to the material accumulation. The distribution of strain in the fiber direction ε_1 is very diffuse. It seems as if compressed areas alternate with stretched areas in a wave-like manner. In particular, a high degree of compression is evident in the center of the geometry near the inner corner. In this region, a locally clearly visible waviness is found in experimental tests, which supports the assumption of negative strain in fiber direction as an indicator for a waviness setting in. In all other areas, there is no visually perceptible waviness. The distribution of the strain along the second material axis ε_2 and the strain perpendicular to the fiber direction $\varepsilon_\perp$ show clear similarities. Here, only a small strain occurs over a large area in the entire bottom region. However, a clear difference can be seen in the lower left flank. The strain ε_2 is nearly zero, whereas the vertical strain $\varepsilon_\perp$ is clearly negative. This can only be explained by occurring shear in this region. Indeed, a higher shear angle γ_{12} is evident here over the entire flank. Since the shear angle is initially zero, a change can be observed in all areas where a material flow occur. This explains why there is hardly any effect of the deformation on the investigated quantities in the entire bottom area and even more clearly in double-curved areas.

A comparison of the numerical results with the experimental ones is given in Figure 5.32. The occurring rotation of the fiber direction is reproduced very well by the simulation. As in the experiment, the largest angular changes θ occur in areas with strong reorientation of the fiber. This shows that the predicted fiber orientation from the draping simulation is reliable. As another relevant parameter, the area change A/A_0 shows a widely good agreement between experiment and simulation. The homogeneous distribution in the

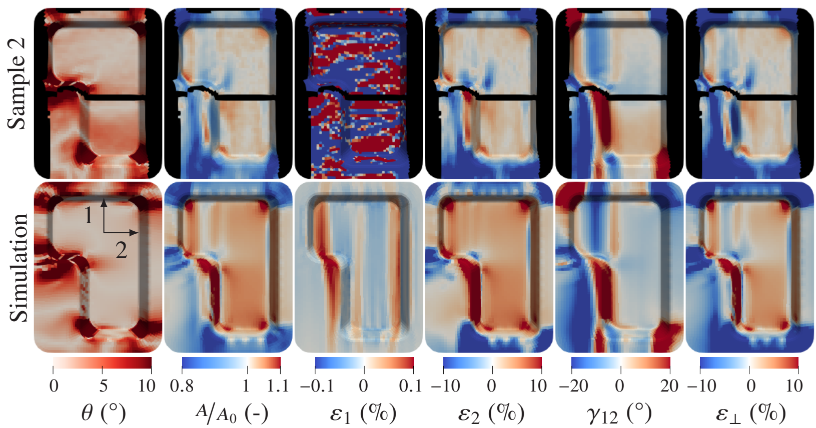

Figure 5.32: Comparison of experimental and numerical results: angle deviation θ, area ratio change A/A_0, strain in fiber direction ε_1, strain along the second material axis ε_2, shear angle γ_{12} and strain perpendicular to the fiber direction $\varepsilon_\perp$ (in black areas there is no information)

bottom area is reflected in the experiment. The difference between experiment and simulation here is at most 2 %. Likewise, the effect of the inner corner, where waviness is formed, is reflected in both results. The only noteworthy difference occurs in the lower left flank. Here, the simulation shows a decrease of the area, whereas an increase can be observed in the experiment. Since further deviations occur in this flank, they will be discussed in the following. As observed in the experiment, a significant shearing γ_{12} occurs in this region. This observation is reliably reproduced in the simulation. In general, the resulting shear is in a very good agreement. Shearing is also accompanied by the resulting fiber orientation and clearly shows the reliability of the numerical results for both quantities. Besides the shear in this flank, a very large area spread of the strain along the second material axis ε_2 is evident. Likewise, a significant perpendicular strain $\varepsilon_\perp$ to the fiber direction occurs. Since both quantities are coupled by the resulting shear (for further details see [50]), the discrepancy between experiment and simulation is suspected to be the result of a too small numerical transverse stiffness E_2. This stiffness is determined based on experimental tensile tests on plane fabrics at different off-axis angles [50]. Therefore, in further detailed investigations, the impact of the determined transverse stiffness should be analyzed. By evaluating the further distribution of ε_2 and $\varepsilon_\perp$ in the draping simulation, it is found that the perpendicular strain $\varepsilon_\perp$ shows similar results as in the experiment. The largely homogeneous distribution of $\varepsilon_\perp$ in the bottom region and the occurring disruption of the strain distribution by the inside corner are very well reproduced. Likewise, to the left of the critical flank, a similar strain distribution in the form of a vertical strip with positive strain $\varepsilon_\perp > 0$ is evident. This circumstantial evidence suggests that only the transverse stiffness would need to be increased to achieve lower ε_2 strains in the lower left flank. The strain distribution in the fiber direction ε_1 shows a clear difference between the experiment and the simulation. The numerical result shows that the run length difference is clearly reflected in the fiber strain. Here, the strain changes from the positive to the negative range. However, the calculated strain is much smaller than the one occurring in the experiment. Here the stiffness in the fiber direction E_1 is suspected to be the cause of the significant differences. The used material stiffness seems to be also to high as the resulting strains are very small. In the constitutive law used for UD-NFC, the stiffness in the fiber direction is assumed to be a constant which will be in general not the case. Since the material behavior of the fabric is very complex, further investigations should analyze whether this assumption is legitimate. Likewise, it should be evaluated in detail whether a lower stiffness E_1 will lead to similar results as in the experiment.

From a structural mechanics point of view, the prediction accuracy of the draping simulation for the fiber orientation and the resulting FVC is very high. Only the occurring waviness is not yet reproduced with sufficient accuracy. Nevertheless, it becomes apparent that the use of the results from the draping simulation provides a solid basis of input data for a more reliable structural-mechanical analysis of FRP components.

5.2.3.2 Draping Simulation and Mapping of Draping Results

Based on the reliability of the draping simulation results to predict the most significant draping effects, the firewall of a car will be analyzed in the following as a numerical example. The goal is to evaluate the impact of draping effects on the mechanical component behavior. Following the process chain, a rectangular blank of the used semi-finished product need to be draped to obtain the final shape of the component. The draping model consists of an upper and a lower tool (see Figure 5.33). The stack of individual layers of the subsequent laminate is located between the tools. The material model used and the material parameters of the individual layers are taken from the forming of the L-shaped geometry. When selecting the dimensions of the stack, special

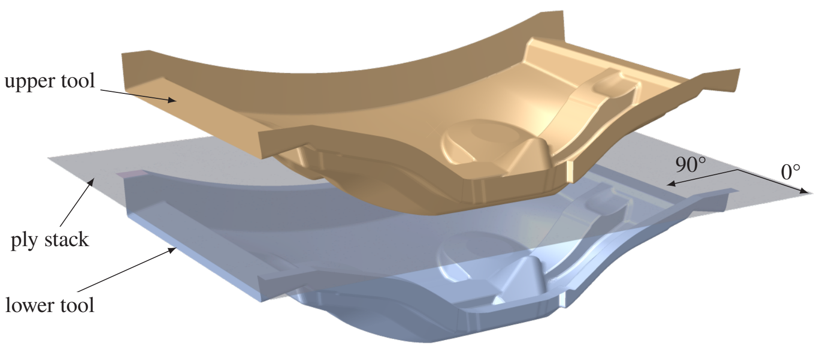

Figure 5.33: Draping simulation setup of the final firewall geometry

care must be taken to ensure that the subsequent component geometry is completely covered. Since the geometry has many multiple curvatures, the initial edge length of the stack is determined from the path along the geometry. This simplification showed that especially due to the flow of the semi-finished product, the corners of the later component are not covered. Therefore, iteratively the dimension of the stack is adjusted until complete coverage is achieved. An exemplary representation of the forming process is given in Figure 5.34.

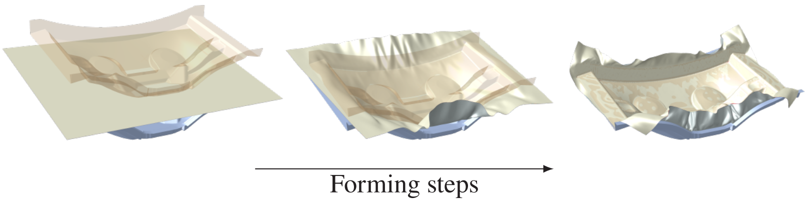

Figure 5.34: Forming steps of the semi-finished product to the final component geometry

The formed preform does not yet have any recesses for the later geometry and still shows an overhang of the semi-finished product. However, the resulting deformation defines the distribution of the draping effects in the stack. According to the virtual process chain, this distribution is mapped from the draping simulation mesh to the structure mechanical mesh. Here, the procedure corresponds to the methods described in Chapter 4. A comparison of the distribution of the draping effects determined in the draping simulation and the mapped data on the structural-mechanical mesh is given in Figure 5.35. A direct comparison shows that due to the different meshing of both models, a certain smoothing of the local extreme values occurs. Nevertheless, a satisfactory mapping result can be seen in general.

5.2.3.3 Distribution of Draping Effects for Different Laminate Layups

Since the deformation behavior during the forming process is dominated by the laminate layup, a total of four different laminate layups are investigated. Each stack consists of a total of four individual layers arranged symmetrically with respect to the center plane. Each ply has a thickness of $t_L = 0.3$ mm.

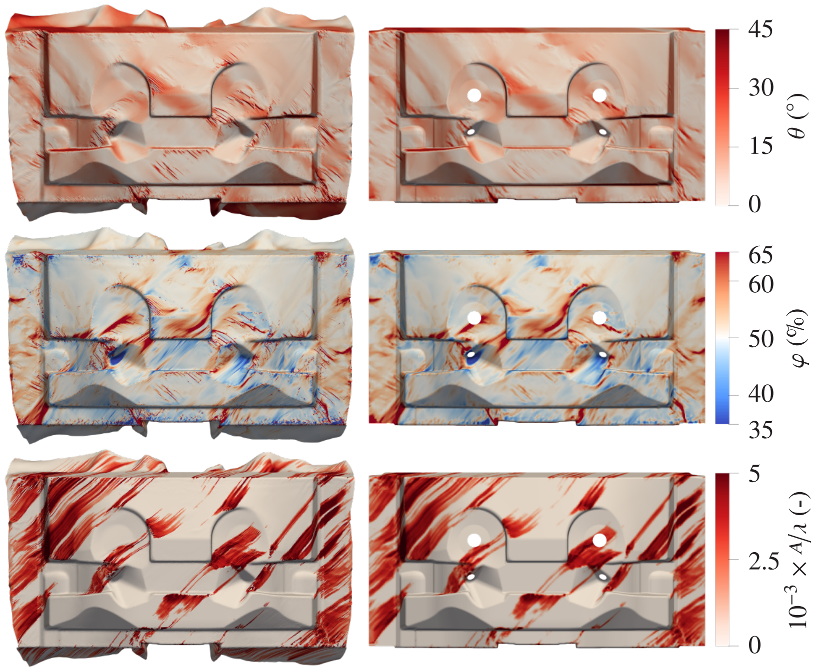

Figure 5.35: Transfer of information on fiber orientation (top), fiber volume content (middle) and fiber waviness (bottom) from the draping simulation (left) to the structure simulation (right)

The order of the single layers is defined such that the first layer is in direct contact with the upper tool and is layered in the direction of the lower tool. The evaluated laminate layups are (0°_4), (90°_4), $(0^\circ, 90^\circ)|_s$ and $(45^\circ/-45^\circ)|_s$. Due to the symmetry of the geometry along the 0° axis, the results differ only for a $(45^\circ/-45^\circ)|_s$ laminate structure on the left and right sides of the component geometry. Therefore, in the following, the results are discussed using the ±45° laminate setup. All other results are given in Appendix A.4.

The distribution of the fiber orientation strongly determines the mechanical component behavior. By specifying the fiber orientation within the semi-finished product, its deviation from the initial state can be determined after forming. The resulting distribution of fiber orientation deviation for a ±45° laminate structure is given in Figure 5.36. Due to the same orientation of the second and third layers of the laminate, only a minimal difference occurs between these two layers. This observation holds true for all investigated laminate layups with equally aligned and adjacent plies (see Figures A.6 to A.8). The difference in running length in adjacent areas leads to shearing of the material, which in turn leads to reorientation of the fiber direction. With such a complex geometry, a deviation from the ideal fiber orientation must always be expected. A simplified projection of the fiber direction is not sufficient for a reliable prognosis.

In addition to the fiber orientation, the distribution of the FVC is very heterogeneous (cf. Figure 5.37). No generally valid relationship in the change of FVC can be derived from the distribution. Thus, the local deformation of the semi-finished product is the sole factor for the resulting distribution. For plies with the same orientation, the difference in FVC between the plies is very small. This circumstance can be observed for all other laminate layups as well

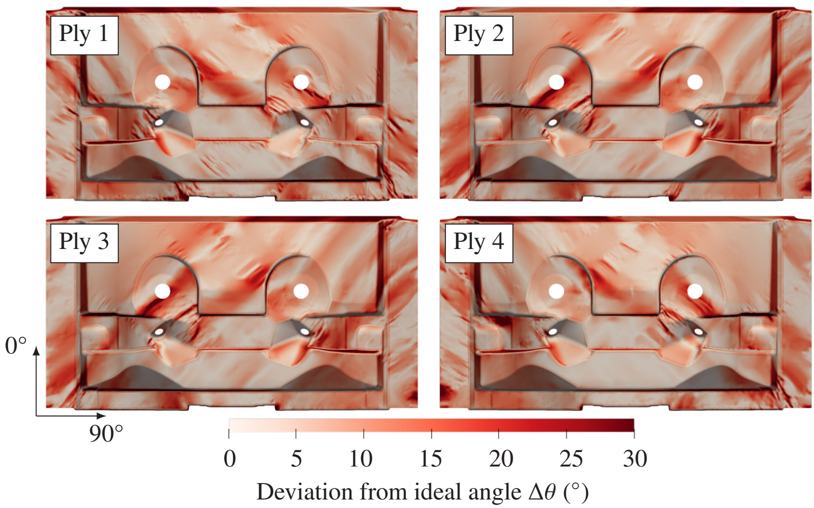

Figure 5.36: Deviation from the initial fiber direction angle for each ply of the $(45°/-45°)|_S$ angle-ply laminate

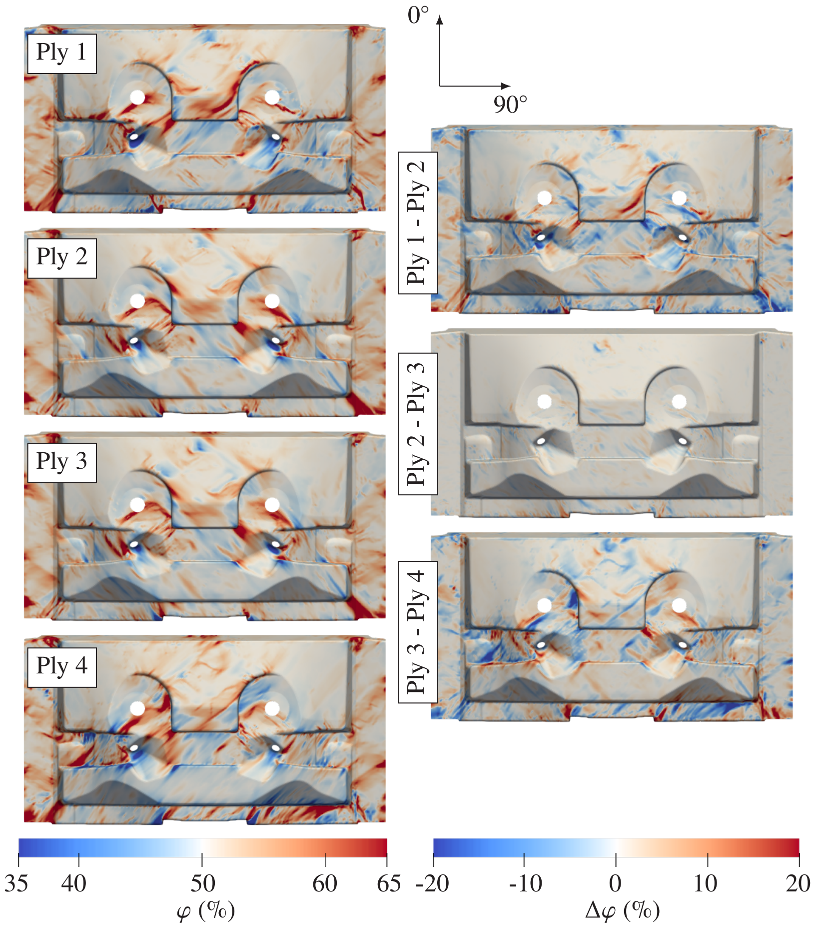

Figure 5.37: Distribution of the fiber volume content and the difference between adjacent layers for a $(45°/-45°)|_s$ angle-ply laminate

(see Figures A.9 to A.11). Depending on the load case the gradual change of the FVC in the different areas of the component can lead to local stress concentrations.

When evaluating the predicted fiber waviness, the underlying fiber orientation can be identified (compare Figure 5.38). The nearly equal distribution for equidirectional neighboring plies observed for fiber orientation and FVC, can only be observed here in a rudimentary way. As the order of the plies has an impact on the deformation of the individual plies, the fiber orientation itself, the FVC and fiber waviness are also affected. Since the individual plies adhere to each other as a result of friction, their relative displacement with respect to each other is the dominant factor for the resulting fiber waviness. In some cases, a local compression of the fiber may be present in one ply, while a stretching of the fiber is present at the same location in the adjacent ply with the same fiber orientation (cf. Figure A.12 differences in waviness distribution between Ply 2 and 3).

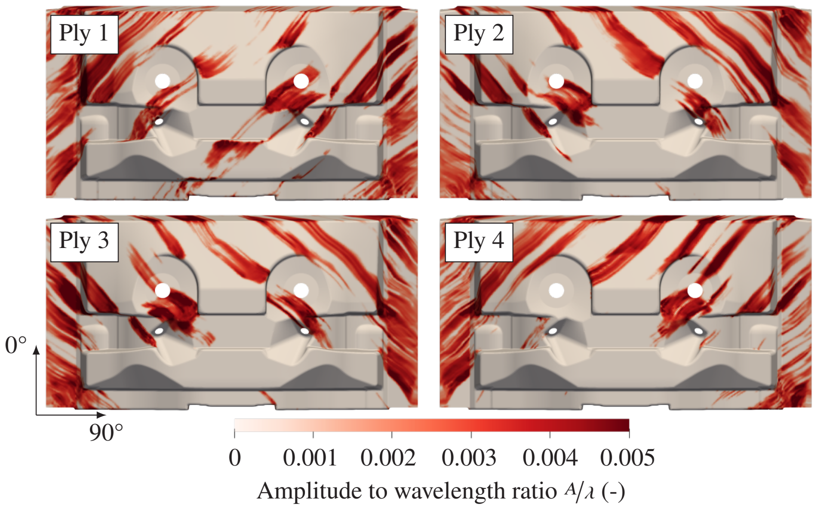

Figure 5.38: Areas with a predicted waviness for a $(45°/-45°)|_s$ angle-ply laminate

5.2.3.4 Mechanical Behavior of the Component

The impact of draping effects on the structure mechanical behavior observed at the coupon level can be analyzed at the component level. In contrast to coupon tests, which produce largely uniform stress states, stress jumps and stress concentrations inevitably occur in complex component geometries. On the other hand, the geometry of the component itself can cause additional stiffening, which reduces the influence of draping effects. However, this circumstance depends on the associated load case. The firewall used here is primarily intended to separate the passenger compartment from the engine compartment. Beams are attached to the firewall and absorb the energy in the event of a crash. Accordingly, a bending load case can be isolated as the main load. In principle, the load is applied over as much of the surface of the component as possible in order to avoid unnecessary stress concentrations. Here, a direct load application to the center of the firewall is selected as load case (see Figure 5.39). To fix the firewall, the degrees of freedom of movement of the lateral flanks are restricted. Since a force-controlled simulation would not find a solution in case of a sudden force drop and thus abort the simulation, a displacement load is imposed instead. The resulting distribution of the displacement in load direction for a ±45° laminate is given in Figure 5.39. The imposed displacement leads to indentation of the component. At the same time, the firewall bulges against the direction of loading, which indicates buckling in the blue areas (compare displacements in Figure 5.39). This condition results due to the relatively thin laminate (t_L = 1.2 mm). Nevertheless, the failure distribution can be evaluated

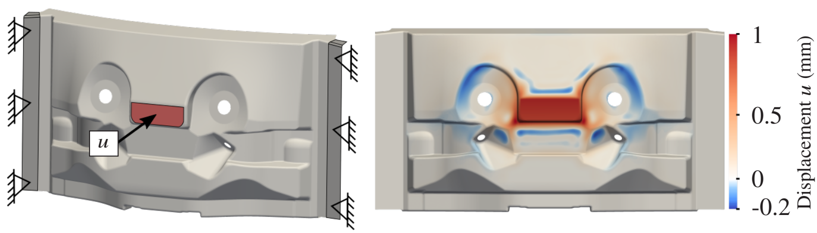

Figure 5.39: Imposed load case on the firewall with the associated boundary conditions (left) and the resulting distribution of displacements for a ±45° laminate in load direction (right)

for fiber failure as well as for inter-fiber failure based on the proposed failure criteria.

In order to analyze the impact of draping effects on the structure mechanical component behavior, two different types of simulations are carried out. On one hand, all draping effects are neglected, and on the other hand, all draping effects are taken into account. When neglecting the draping effects, the initial fiber orientation of the fabric is only projected, a constant FVC is used and no waviness is assigned. For the visualization of the differences, the element-wise difference of the failure criterion between both cases is created ($\Delta f_{\mathrm{IFF}} = f_{\mathrm{IFF}}^{\mathrm{w/o}} - f_{\mathrm{IFF}}^{\mathrm{w/}}$). Since both inter-fiber failure and fiber failure are possible, a comparison is formed for both failure criteria (see Figures 5.40 and 5.41). For fiber failure, the sign of the σ_{11} stress determines whether tension or compression failure is induced. Since positive as well as negative σ_{11} stresses are present in the component, but never both at the same time in one element, the maximum of the tensile fiber failure and the compressive fiber failure criterion is presented for easier comparison.

When evaluating the inter-fiber failure criterion, it is noticeable that the IFF distribution is very similar for both simulation models. This is also true for all other laminate layups investigated (see Figures A.15, A.17 and A.19). Due to the imposed load case, there are areas in which hardly any differences exist between the two models. In particular, the edge areas of the component are barely loaded and therefore do not show any significant use to capacity. Nevertheless, the inhomogeneous distribution of the individual draping effects is also clearly visible here. The areas with the largest values of f_{IFF} are found near the force initiation. The difference in the inter-fiber failure criterion Δf_{IFF} shows that locally very significant differences exist between the two approaches (cf. Figure 5.42). In particular, laminate structures with different fiber orientations such as $(45°/-45°)|_{\mathrm{s}}$ and $(0°/90°)|_{\mathrm{s}}$ show local jumps of the inter-fiber failure criterion in many regions of the component. Accordingly, only isolated local differences occur for equidirectional laminates for the imposed load case (see Figures A.15 and A.17). The characteristics shown for inter-fiber failure also appear for fiber failure (see Figures 5.41, A.16, A.18, and A.20). For both failure criteria, the position of the maxima shifts depending on the model. This has the consequence that the damage initiation and the propagation would differ. For example, the model without draping effects predicts a higher value for the inter-fiber failure on the left side below the large

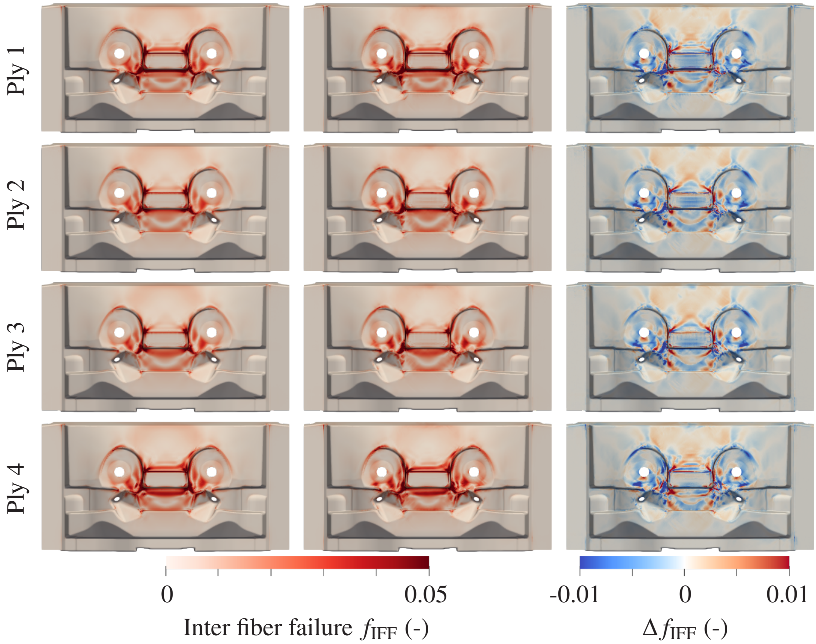

Figure 5.40: Distribution of inter-fiber failure if the draping effects are neglected (left) or considered (middle) and the corresponding difference of the inter-fiber failure criterion for a $(45° / -45°)|_{\mathrm{s}}$ angle-ply laminate

hole (cf. Figure 5.42 black rectangle). In contrast, the model with draping effects hardly shows any capacity utilization at this point, which in turn means that when draping effects are taken into account, stress concentrations can be significantly mitigated.

As a further point, the compliance of the models can be analyzed. Normally, the geometric stiffness plays a much greater role than the variation of the draping characteristics. For all laminate layups investigated, the resulting force and displacement at the load application point is recorded. The ratio of the displacement and the force u/F results in the compliance and is evaluated at each displacement point. For the laminate layups (0°_4), (90°_4) and $(0°, 90°)|_{\mathrm{s}}$, no difference between the models with draping effects and without arises

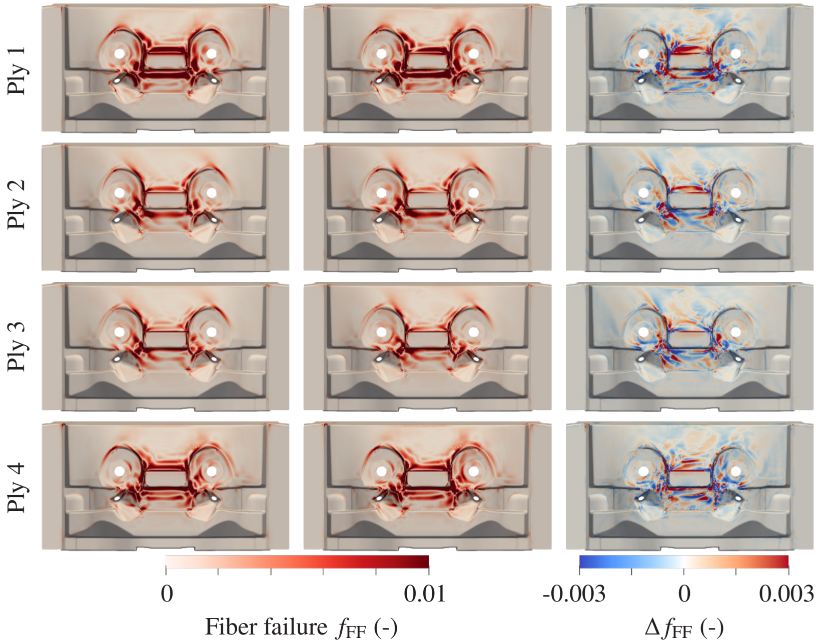

Figure 5.41: Distribution of fiber failure if the draping effects are neglected (left) or considered (middle) and the corresponding difference of the inter-fiber failure criterion for a $(45°/-45°)|_s$ angle-ply laminate

here. On the other hand, the model with a $(45°/-45°)|_s$ laminate, which initially shows hardly any difference in the force-displacement curve, shows a significant difference between the two models as the displacement increases (see Figure 5.44 left). If the draping effects are taken into account, a higher force is achieved than in the model without draping effects. Conversely, this means that the compliance decreases when the draping effects are taken into account. In the direct comparison it becomes clear that the compliance differs up to 10 % between the two models (see Figure 5.44 right). Thus, draping effects extend the geometric factor to the local material behavior, demonstrating the importance of considering draping effects to correctly capture the mechanical component behavior.

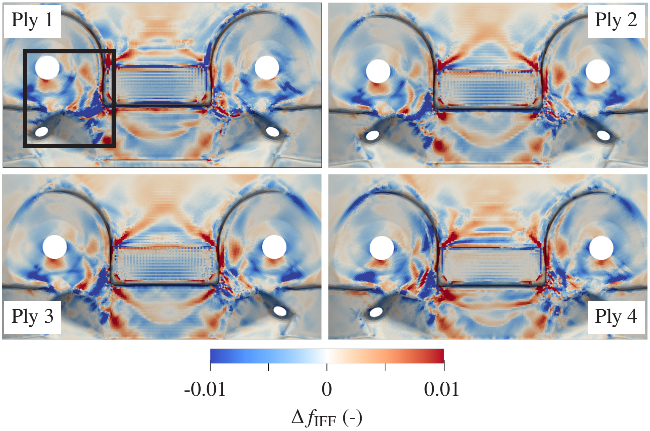

Figure 5.42: Difference of the inter-fiber failure criterion $\Delta f_{\mathrm{IFF}} = f_{\mathrm{IFF}}^{\mathrm{w/o}} - f_{\mathrm{IFF}}^{\mathrm{w/}}$ for a $(45°/{-45°})|_{\mathrm{s}}$ angle-ply laminate between the results without draping effects and with draping effects (blue areas show underestimated IFF and red areas show overestimated IFF)

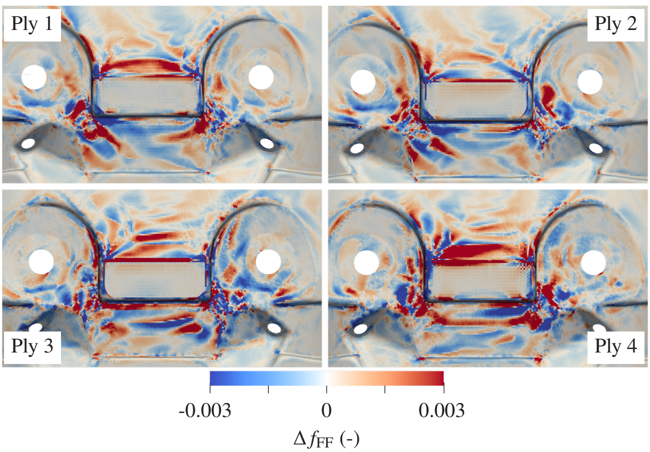

Figure 5.43: Difference of the fiber failure criterion $\Delta f_{\mathrm{FF}} = f_{\mathrm{FF}}^{\mathrm{w/o}} - f_{\mathrm{FF}}^{\mathrm{w/}}$ for a $(45°/{-45°})|_{\mathrm{s}}$ angle-ply laminate between the results without draping effect and with draping effect (blue areas show underestimated FF and red areas show overestimated FF)

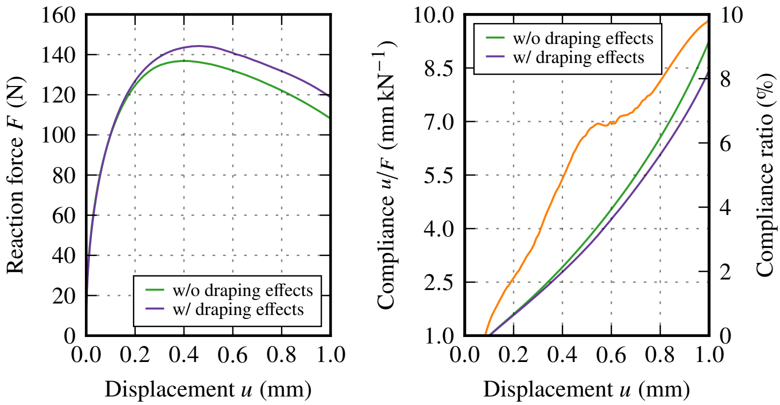

Figure 5.44: Resulting force-displacement curves for a $(45°/-45°)|_S$ angle-ply laminate (left) and the corresponding compliance with the percentual difference (right) between the models with and without draping effects

5.3 Conclusions on Material Modelling and Draping Effects

New insights have been gained through an intensive analysis of the mechanical material behavior when draping effects occur. In terms of a virtual material testing the usage of micro-scale models show promising results. Especially, the failure and damage analysis can be adapted to different matrix and fiber types. The microscopic models are capable to model undulated and nonundulated regions reliably. Special care needs to be taken when the material properties of the constituents are not known. The matrix has a significant impact on the elastic as well as resulting strength values of the composite. From the modeling prospective, the choice of the strain measure for fiber and matrix is crucial. The continuous change of the material axes leads to other failure modes, which might not be predicted correctly, if simplistic strain measures are used.

Based on the observations from experiments and micro-scale models the requirements for the macroscopic material model are identified. The advantage of the developed macroscopic model is that all analyzed draping effects can be modeled simultaneously. The information from the draping simulation regarding draping effects are passed to each mesh element. This allows to model draping effects on component level without any further assumptions. As the fiber orientation is a key factor for FRPs, the developed model covers the continuous material axes rotation. This aspect has been for the first time evaluated experimentally and validated numerically. Regarding the nonlinear behavior of the composite, several mechanisms are identified. The nonlinear behavior of carbon fiber in the fiber direction is important because the stiffness changes significantly during loading. This condition leads to different interpretation of the obtained stress-strain curves and the resulting strength values. In general, the nonlinear behavior due to plasticity for nonundulated areas can be reliably reproduced. As an important side note, no FVC-dependent plastic behavior is observed.

When FVC is taken into account, the stiffness and strength values must be adjusted immediately. The developed macroscopic model utilizes available analytical approaches to predict the stiffness. Based on experimental tests and microscale model observations, FVC-dependent strength values can now be defined not only for FF but also for IFF. Especially, the transverse compressive strength shows a distinct dependency on the FVC. By comparing the experimental results with numerical predictions, the accurate prediction of the strength is key to exploitation of the lightweight potential. Otherwise, material reserves are not activated or oversimplified. Using numerical results, no FVC-dependent interaction between different IFF damage variables is observed. Therefore, the material behavior during damage evolution is defined using only one parameter.

In addition to fiber direction and FVC, the significant stiffness and strength loss due to waviness is critical. The developed model utilizes available analytical approaches to predict the stiffness for wavy areas. However, the quality of the prediction depends to a large extent on the exact knowledge about the waviness grade. Based on the results of micro-scale models and analytical models developed to determine the strength of a waviness in fiber direction, no significant FVC-dependent behavior is observed. The reason that the strength is independent of the FVC is due to the failure mode and the resulting local stress state. When the load is applied in the direction of waviness, an inter fiber fracture occurs. The sensitivity due to FVC-dependency of the strengths determining the inter fiber fracture is very low at this stress state.

6 Recommendations for Material Characterization to Virtually Evaluate Composite Parts with Draping Effects

The following recommendations can be deduced for the design of fiber reinforced composite components with complex geometries, for which the impact of draping effects is relevant to the performance. In the first step, the material properties are required. Ideally, the tests should be carried out for at least two different FVC. It is useful to evaluate the limits of the expected FVC range (e.g., $\varphi = 50\,\%$ and $\varphi = 60\,\%$). The experimental plan should cover both the linear elastic and the strength parameters. The material parameters in fiber direction can be determined from UD0° samples tested under a tensile and compressive load. Thus, the strengths in fiber direction X_T and X_C are determined. In addition, the material parameters E_1^init, ${}^{\mathrm{d}E_1}/_{\mathrm{d}\varepsilon_{11}}$ and ν_{12} are determined by the tests as well. These parameters are all affected by the FVC. To use the analytical approaches presented in Section 3.5.5.1, the material properties of the matrix and the fiber are required. Since these characteristic properties are usually not available, literature data or manufacturer's data for the matrix can be used. The required fiber properties (such as $E_1^\mathrm{f,init}$ etc.) can be determined via reverse engineering from composite coupon tests.

For the material properties transverse to the fiber direction, tensile and compression tests should be performed on UD90° laminates. This will allow further parameters such as E_2, ν_{23}, Y_T and Y_C to be determined. For the strengths, a linear or constant value, over the considered FVC range, seems to be sufficient. In order to model the dependence on FVC, the mechanical properties of the fiber are also necessary. For the elastic material parameters transverse to the fiber direction, there are two possibilities to parameterize the analytical equations. On the one hand, the stiffness of the matrix E_m and the literature parameters of the fiber E_2^f [18, 69, 70] can be used to determine the

Halpin-Tsai parameter ζ_{E_2} from the experimental results of the two different FVC. On the other hand, it is possible using micro-scale models and reverse engineering to identify the fiber parameters. The same methods can be used to determine the major through-thickness Poisson's ratio ν_{23} (or corresponding shear modulus G_{23}) and the specific Halpin-Tsai parameter $\zeta_{G_{23}}$. As shown in Section 5.1.2.1, for the parameters E_2 and ν_{23} the Poisson's ratio of the matrix ν_{m} plays a significant role. Therefore, caution should be applied when taking the material properties of the matrix from the literature or the manufacturer's specifications.

To determine the material shear properties, it is convenient to perform OAT45° and OAC45° coupon tests. This allows to determine the shear modulus G_{12} quite reliably. Similarly, the tests can be used to determine the IFF envelope. To determine the Halpin-Tsai parameter $\zeta_{G_{12}}$, it is suitable to use the material properties of the matrix in conjunction with the coupon test results or in conjunction with the micro-scale models. Since the shear modulus G_{12} is strongly dominated by the stiffness of the matrix, reliable manufacturer data or literature parameters should be used.

For the parameterization of the plasticity model, the IFF envelope must be determined first. If the results of the UD90° tension and compression tests, as well as the OAT45° and OAC45° tests are plotted in a $(\sigma_{22}, \sigma_{12})$-plane, only the shear strength S_{12} and the slope parameter p_{n1} are missing to define the IFF envelope. This can be done using an optimization algorithm that takes as input the Puck failure criterion and the individual measured stress values as input. In order to consider the impact of the FVC, the parameter optimization is performed for one FVC at a time. Subsequently, the parameters found can be described with a linear approach over the FVC range considered. Since the inter-fiber failure is influenced by the load in the fiber direction, the interaction factors m and s have to be defined. Choosing the parameters to be $m = s = 0$ leads to a conservative result, since the maximum interaction between f_{FF} and f_{IFF} is assumed here. Now all parameters for the fiber reinforced composite specifying failure initiation are determined. Based on the findings for the plasticity model, only parameters α_{ap}, e_{ap} and f_{ap} are relevant. The parameter β_{ap} can be set to zero. In addition to the plasticity model parameters, the hardening curve is needed. Based on the results of the OAT45° and OAC45° tests, as well as the UD90° compression tests, a suitable set of parameters can be found using an optimization algorithm. The remaining parameters of the energy release rate due to fiber failure G_d and interaction parameter r_g are material dependent values and can only be roughly determined. It is recommended to perform a sensitivity study to analyze the influence of these parameters on the damage behavior.

As shown in Section 5.2.2.1 the used strain measure has a crucial influence on the resulting stress of the fiber reinforced composite. Therefore, it is recommended to consider the rotation of all material axes when modeling fiber reinforced composites. If only the rotation of the fiber orientation is considered, a failure mechanism deviating from the experiment can be predicted. To determine the resulting tensile and compressive strengths for areas with waviness, the analytical approaches presented in Section 2.5.3 can be used. The material parameters required for this approach, such as the compressive strength in the fiber direction X_C and the parameters required for the calculation of the IFF criterion according to Puck Parameters are completely sufficient.

Based on the determined material parameters and the established material model requirements, it is possible to predict the component behavior considering draping effects. The described scope of experiments represents a minimum requirement. Compared to a material characterization that does not take any draping effects into account, the number of tests required is doubled due to the consideration of two different FVCs. However, all draping effects investigated (fiber orientation, FVC and fiber waviness) are covered by these tests. This justifies the additional effort for a more realistic analysis.

7 Conclusion and Outlook

7.1 Conclusion

The forming of UD-NCF semi-finished products results in local draping effects (fiber orientation, fiber volume content and fiber waviness), which influence the mechanical material behavior. The influence of the draping effects is investigated experimentally, and requirements for a macroscopic material model are derived. For this purpose, first the linear elastic material parameters and the nonlinear material properties are determined for different types of draping effects. Furthermore, the material strengths are obtained at different fiber volume contents (FVC). The FVC not only has an influence on the material stiffnesses and strengths in fiber direction, but also a decisive influence on the transverse compressive strength. It is found that for the range of FVC considered, linear relationships for different strength values proved to be sufficiently accurate in most cases. Thus, the experimental effort can be reduced to only two fiber volume contents to be investigated. However, plastic strain hardening is independent of FVC, which means that it only needs to be determined for one FVC. In addition, the nonlinear material behavior is recorded under different fiber angles and laminate structures. The consideration of the fiber direction and the accompanying rotation of the material axes is identified as an essential aspect. It is shown that, in addition to the rotation of the fiber direction, the angle between the fiber direction and the transverse material axis also changes with the load. Since the forming of semi-finished products can lead to local fiber waviness, different degrees of waviness are tested under tensile and compressive load. This draping effect is found to also have a significant influence on the mechanical properties. As with nonundulated laminates, the local fiber orientation also changes with the load applied.

Based on the experimental findings, a suitable strain measure for modeling fiber composites with draping effects is identified. Here, all material axes are transformed depending on the load. The resulting stress response has an influence on the failure initiation and failure mode. In addition to modeling the linear elastic material behavior, a fracture plane based plasticity model is implemented. This is directly linked to the fracture plane based failure criterion used. For the modeling of the FVC-dependent material behavior, different existing analytical approaches are adopted and new ones are developed. Since the influence of the FVC on the damage behavior requires a lot of experimental effort to evaluate different stress loads, numerical investigations are carried out. It is found that the FVC does not influence the interaction between the damage mechanisms. To account for the influence of fiber waviness, homogenized approaches specifically related to fiber waviness are implemented in the material model.

Numerical studies are performed at the microscale for a comprehensive analysis of the effective material behavior on macroscale. By varying the different material parameters of each constituent, the influence on the resulting composite material properties could be derived. It can be seen that the matrix has a dominant influence on the elastic material properties, as well as the resulting strengths of the composite. The experimentally observed influence of the FVC on the material strengths could be reproduced. Likewise, on the microscale, the material behavior in presence of fiber waviness is investigated. The basic phenomena, such as nonlinearity, failure initiation and propagation, and fracture, are in good agreement with experiments. In addition, it is shown by means of micro-scale models that the FVC does not affect the strength with increasing fiber waviness.

For the validation of the developed macroscopic material model, the experimental and numerical results are compared. The change in fiber orientation and the angle between the material axes could be reproduced very well. Likewise, the nonlinear material behavior could be validated for different fiber orientations and laminate layups. When comparing the results for fiber waviness, differences in the stress-strain curves appeared that need further attention. However, the stiffness due to waviness and in some terms the corresponding experimental strength could be reproduced. In addition to the validation of the developed material model, the information provided from the draping simulation regarding the occurring draping effects is compared with experimental forming tests. For local fiber orientation and FVC, a very good prediction quality of the draping simulation is found. For prediction of local fiber waviness, deviations still occur at the moment. With regard to the development of fiber composite components with complex geometries, a much more realistic design can now be achieved by utilizing the virtual process chain. In combination with the developed structural-mechanical material model under consideration of the addressed draping effects, a significant extension and improvement of the previous approach has been achieved.

7.2 Outlook

By taking into account the draping effects that occur, the material behavior of fiber composites can be predicted more accurately. However, when modeling the draping effects, other material-specific aspects have come to light that have not been taken into account so far. For example, a different degree of waviness may be present in each layer during forming, and such dissimilar adjacent layers may interact during loading. Since the influence of fiber waviness has a significant role on the local material properties, the material behavior should therefore be further investigated for different laminate structures (e.g., angle-ply laminates with waviness) and the material model should be extended and validated accordingly. Similarly, laminate thickness changes can occur that lead to a local nesting effect. In this case, a combination of a change in FVC and out-of-plane waviness occurs. Based on experimental tests, the influence of local nesting effects should therefore be investigated for different laminate structures. Another aspect is the modeling of the influence of FVC on further material properties. It is generally known that the thickness of the individual layers in a laminate can lead to higher strengths due to the in-situ effect. An investigation in connection with the FVC is still pending. Similarly, the influence of FVC on the experimentally determinable intralaminar energy release rates has not yet been explored. Furthermore, homogenized modeling of fiber waviness still poses challenges. In subsequent investigations, it would therefore be useful to develop new methods that capture the material behavior as a result of waviness more accurately.

A Appendix

A.1 Further Derivations for the Material Models

A.1.1 Matrix Material

A.1.1.1 Viscoplasticity Model

Plasticity Return Mapping Algorithm In this section the implementation of the viscoplastic model into a finite element user subroutine in ABAQUS is described. The implemented user material model must provide the stress $\boldsymbol{\sigma}$ and the consistent tangent modulus ${}^{\mathrm{d}\Delta\boldsymbol{\sigma}}/_{\mathrm{d}\Delta\boldsymbol{\varepsilon}}$ at the end of each increment to the solver. To determine these parameters the finite element solver provides at the beginning of each increment a strain increment $\Delta\boldsymbol{\varepsilon}$ which is utilized to compute the trial stress $\hat{\boldsymbol{\sigma}}$ at the end of the increment. If the trial stress leads to $\Phi_{\mathrm{pl}} \geq 0$ a return mapping algorithm must be performed. Generally this means that the current stress state exceeds the yield surface and must be mapped back to the surface. This condition is satisfied if a solution for the plastic multiplier $\Delta\lambda_{\mathrm{pl}}$ in Equation (3.58) is found. If no solution is found, the strain increment must be reduced to perform a new trial to find a solution. To obtain the resulting stress Equation (3.32) in conjunction with Equation (3.44) can be defined as

$$\boldsymbol{\sigma} = \mathbb{C} : \boldsymbol{\varepsilon}_{\mathrm{el}} = \hat{\boldsymbol{\sigma}} - \Delta\lambda_{\mathrm{pl}}\mathbb{C} : \frac{\partial g_{\mathrm{pl}}}{\partial \boldsymbol{\sigma}}. \tag{A.1}$$

This expression can be further separated into the deviatoric and the volumetric part by using Equations (3.34) and (3.35), which allows to formulate a simple relationship between the trial deviatoric and volumetric stresses and the resulting true stresses

$$\boldsymbol{\sigma}_{\mathrm{dev}} = \hat{\boldsymbol{\sigma}}_{\mathrm{dev}} - \frac{3G_{\mathrm{m}}\Delta\lambda_{\mathrm{pl}}}{g_{\mathrm{pl}}}\boldsymbol{\sigma}_{\mathrm{dev}} \Leftrightarrow \boldsymbol{\sigma}_{\mathrm{dev}} = \frac{g_{\mathrm{pl}}}{3G_{\mathrm{m}}\Delta\lambda_{\mathrm{pl}} + g_{\mathrm{pl}}}\hat{\boldsymbol{\sigma}}_{\mathrm{dev}} \tag{A.2}$$

$$-p = -\hat{p} + \frac{K_\mathrm{m}\alpha\Delta\lambda_\mathrm{pl}}{g_\mathrm{pl}}p \Leftrightarrow p = \frac{g_\mathrm{pl}}{K_\mathrm{m}\alpha\Delta\lambda_\mathrm{pl} + g_\mathrm{pl}}\hat{p}. \tag{A.3}$$

However, the flow potential g_pl is itself based on the resulting stress $\boldsymbol{\sigma}$ (cf. Eq. (3.43)). Therefore, if the definition of the resulting deviatoric and volumetric stress from Equations (A.2) and (A.3) is used and by recalling that $\sigma_\mathrm{vm} = \sqrt{3J_2} = \sqrt{3/2\boldsymbol{\sigma}_\mathrm{dev} : \boldsymbol{\sigma}_\mathrm{dev}}$ the flow potential results to

$$\begin{aligned} g_\mathrm{pl} &= \sqrt{\sigma_\mathrm{vm}^2 + \alpha p^2} \\ &= \sqrt{3/2\boldsymbol{\sigma}_\mathrm{dev} : \boldsymbol{\sigma}_\mathrm{dev} + \alpha p^2} \\ &= \sqrt{3/2\left(\frac{g_\mathrm{pl}}{3G_\mathrm{m}\Delta\lambda_\mathrm{pl} + g_\mathrm{pl}}\right)^2 \hat{\boldsymbol{\sigma}}_\mathrm{dev} : \hat{\boldsymbol{\sigma}}_\mathrm{dev} + \alpha\left(\frac{g_\mathrm{pl}}{K_\mathrm{m}\alpha\Delta\lambda_\mathrm{pl} + g_\mathrm{pl}}\hat{p}\right)^2} \\ &= \sqrt{\left(\frac{g_\mathrm{pl}}{3G_\mathrm{m}\Delta\lambda_\mathrm{pl} + g_\mathrm{pl}}\right)^2 \hat{\sigma}_\mathrm{vm}^2 + \alpha\left(\frac{g_\mathrm{pl}}{K_\mathrm{m}\alpha\Delta\lambda_\mathrm{pl} + g_\mathrm{pl}}\right)^2 \hat{p}^2}. \end{aligned} \tag{A.4}$$

If the equation above is solved to g_pl a quartic equation of the following type will result

$$g_\mathrm{pl}^4 + b g_\mathrm{pl}^3 + c g_\mathrm{pl}^2 + d g_\mathrm{pl} + e = 0 \tag{A.5}$$

where the parameters b, c, d, e are functions of the parameters $G_\mathrm{m}, K_\mathrm{m}, \Delta\lambda_\mathrm{pl}, \alpha, \hat{\sigma}_\mathrm{vm}$ and $\hat{p}$. Such type of equation can either be solved by Newton-Raphson scheme or directly by using the solution to such equation proposed by Lodovico Ferrari (first published 1545 in [232]). By observing Equation (3.43) it leads to the conclusion that g_pl must be greater zero, since all terms in this equation lead to positive values. However, by solving the quartic equation the roots can also result to complex conjugate nonreal roots. By analyzing each root of the quartic equation only one solution leads to a real and positive root in this case. At each time step all parameters of Equations (A.2) and (A.3) except $\Delta\lambda_\mathrm{pl}$ are known. To determine the plastic multiplier a further equation is needed. Using Equation (3.58) and solving for $\Delta\lambda_\mathrm{pl}$ the stress response at the end of the increment can be determined. Due to interdependence of $\Delta\lambda_\mathrm{pl}$ and the resulting stress $\boldsymbol{\sigma}$ results in a generally nonlinear function. Utilizing the Newton-Raphson scheme to solve such equation is an optimal choice. However, the derivative of the viscoplastic consistency condition R_pl to $\Delta\lambda_\mathrm{pl}$ is needed. First R_pl needs to be expressed in terms of parameters which are only dependent on $\Delta\lambda_\mathrm{pl}$ and the trial stresses.

To do so all necessary equations are also redefined and simplified to solve for $\Delta\lambda_{\mathrm{pl}}$. To simplify Equations (A.2) and (A.3) the factors to $\hat{\boldsymbol{\sigma}}_{\mathrm{dev}}$ and $\hat{p}$ are redefined to

$$\begin{aligned} \frac{g_{\mathrm{pl}}}{3G_{\mathrm{m}}\Delta\lambda_{\mathrm{pl}} + g_{\mathrm{pl}}} &= \frac{1}{1 + \frac{3G_{\mathrm{m}}\Delta\lambda_{\mathrm{pl}}}{g_{\mathrm{pl}}}} = \frac{1}{\zeta_{\mathrm{dev}}} \\ \frac{g_{\mathrm{pl}}}{K_{\mathrm{m}}\alpha\Delta\lambda_{\mathrm{pl}} + g_{\mathrm{pl}}} &= \frac{1}{1 + \frac{K_{\mathrm{m}}\alpha\Delta\lambda_{\mathrm{pl}}}{g_{\mathrm{pl}}}} = \frac{1}{\zeta_{\mathrm{vol}}}. \end{aligned} \tag{A.6}$$

Since R_{pl} depends on Φ_{pl} the solution of the yield stresses are required. In order to determine the yield stresses in tension and compression (cf. Eq. (3.51)) the equivalent plastic strain increment $\Delta\bar{\varepsilon}_{\mathrm{pl}}$ is also needed. Applying Equations (3.44), (A.2), (A.3) and (A.6) to Equation (3.54) result in an expression of equivalent plastic strain increment which is dependent on $\Delta\lambda_{\mathrm{pl}}$ as the only unknown parameter

$$\begin{aligned} \Delta\bar{\varepsilon}_{\mathrm{pl}} &= \sqrt{k\Delta\boldsymbol{\varepsilon}_{\mathrm{pl}} : \Delta\boldsymbol{\varepsilon}_{\mathrm{pl}}} \\ &= \frac{\Delta\lambda_{\mathrm{pl}}}{2g_{\mathrm{pl}}}\sqrt{k\left(\frac{6\hat{\sigma}_{\mathrm{vm}}^2}{\zeta_{\mathrm{dev}}^2} + \frac{4\alpha^2\hat{p}^2}{3\zeta_{\mathrm{vol}}^2}\right)}. \end{aligned} \tag{A.7}$$

For simplified reading the expression within the square root is substituted by

$$\eta = k\left(\frac{6\hat{\sigma}_{\mathrm{vm}}^2}{\zeta_{\mathrm{dev}}^2} + \frac{4\alpha^2\hat{p}^2}{3\zeta_{\mathrm{vol}}^2}\right). \tag{A.8}$$

Now the derivative of the viscoplastic consistency condition (cf. Eq. (3.58)) to $\Delta\lambda_{\mathrm{pl}}$ can be determined

$$\begin{aligned} \frac{\partial R_{\mathrm{pl}}}{\partial\Delta\lambda_{\mathrm{pl}}} &= \frac{\partial}{\partial\Delta\lambda_{\mathrm{pl}}}\left(\left(\frac{\Delta\lambda_{\mathrm{pl}}\mu}{\Delta t}\right)^h - \frac{\Phi_{\mathrm{pl}}}{2\sigma_{\mathrm{t}}\sigma_{\mathrm{c}}}\right) \\ &= \frac{h}{\Delta\lambda_{\mathrm{pl}}}\left(\frac{\Delta\lambda_{\mathrm{pl}}\mu}{\Delta t}\right)^h - \frac{1}{2\sigma_{\mathrm{t}}\sigma_{\mathrm{c}}}\left(\frac{\partial\Phi_{\mathrm{pl}}}{\partial\Delta\lambda_{\mathrm{pl}}} - \Phi_{\mathrm{pl}}\left(\frac{1}{\sigma_{\mathrm{c}}}\frac{\partial\sigma_{\mathrm{c}}}{\partial\Delta\lambda_{\mathrm{pl}}} + \frac{1}{\sigma_{\mathrm{t}}}\frac{\partial\sigma_{\mathrm{t}}}{\partial\Delta\lambda_{\mathrm{pl}}}\right)\right). \end{aligned} \tag{A.9}$$

Considering Equations (A.2), (A.3) and (A.6) the derivative of the yield surface Φ_{pl} is expressed by

$$\begin{aligned}\frac{\partial \Phi_{\mathrm{pl}}}{\partial \Delta\lambda_{\mathrm{pl}}} &= \frac{\partial}{\partial \Delta\lambda_{\mathrm{pl}}}\left(6J_2 + 2I_1\left(\sigma_{\mathrm{c}} - \sigma_{\mathrm{t}}\right) - 2\sigma_{\mathrm{c}}\sigma_{\mathrm{t}}\right)\\ &= -\frac{12\hat{J}_2}{\zeta_{\mathrm{dev}}^3}\frac{\partial \zeta_{\mathrm{dev}}}{\partial \Delta\lambda_{\mathrm{pl}}} - 2\left(\sigma_{\mathrm{c}} - \sigma_{\mathrm{t}}\right)\frac{\hat{I}_1}{\zeta_{\mathrm{vol}}^2}\frac{\partial \zeta_{\mathrm{vol}}}{\partial \Delta\lambda_{\mathrm{pl}}}\\ &\quad + 2\left(\frac{\hat{I}_1}{\zeta_{\mathrm{vol}}} - \sigma_{\mathrm{t}}\right)\frac{\partial \sigma_{\mathrm{c}}}{\partial \Delta\lambda_{\mathrm{pl}}} - 2\left(\frac{\hat{I}_1}{\zeta_{\mathrm{vol}}} - \sigma_{\mathrm{c}}\right)\frac{\partial \sigma_{\mathrm{t}}}{\partial \Delta\lambda_{\mathrm{pl}}},\end{aligned} \tag{A.10}$$

where $\hat{J}_2$ and $\hat{I}_1$ correspond to the trial second invariant of the trial deviatoric stress tensor and the first invariant of the trial stress tensor. Since the hardening laws in tension and compression are dependent on the equivalent plastic strain increment and therefore on $\Delta\lambda_{\mathrm{pl}}$, the derivative is defined as

$$\begin{aligned}\frac{\partial \sigma_{\mathrm{c}}}{\partial \Delta\lambda_{\mathrm{pl}}} &= \frac{\partial \sigma_{\mathrm{c}}}{\partial \Delta\bar{\varepsilon}_{\mathrm{pl}}}\frac{\partial \Delta\bar{\varepsilon}_{\mathrm{pl}}}{\partial \Delta\lambda_{\mathrm{pl}}} = H_{\mathrm{c}}\frac{\partial \Delta\bar{\varepsilon}_{\mathrm{pl}}}{\partial \Delta\lambda_{\mathrm{pl}}}\\ \frac{\partial \sigma_{\mathrm{t}}}{\partial \Delta\lambda_{\mathrm{pl}}} &= \frac{\partial \sigma_{\mathrm{t}}}{\partial \Delta\bar{\varepsilon}_{\mathrm{pl}}}\frac{\partial \Delta\bar{\varepsilon}_{\mathrm{pl}}}{\partial \Delta\lambda_{\mathrm{pl}}} = H_{\mathrm{t}}\frac{\partial \Delta\bar{\varepsilon}_{\mathrm{pl}}}{\partial \Delta\lambda_{\mathrm{pl}}},\end{aligned} \tag{A.11}$$

where $H_{\mathrm{t,c}}$ are the hardening rates in tension and compression direction. Next the derivative of the equivalent plastic strain increment $\Delta\bar{\varepsilon}_{\mathrm{pl}}$ is determined. Since the nonassociative flow potential g_{pl} is used to determine $\Delta\bar{\varepsilon}_{\mathrm{pl}}$ (cf. Eq. (A.7)) and g_{pl} is based on the parameters ζ_{dev} and ζ_{vol} (while these themselves depend on g_{pl}), first the derivative of g_{pl} to $\Delta\lambda_{\mathrm{pl}}$ needs to be determined. By using Equation (A.6) the derivatives of ζ_{dev} and ζ_{vol} are defined as

$$\begin{aligned}\frac{\partial \zeta_{\mathrm{dev}}}{\partial \Delta\lambda_{\mathrm{pl}}} &= \frac{3G_{\mathrm{m}}}{g_{\mathrm{pl}}}\left(1 - \frac{\Delta\lambda_{\mathrm{pl}}}{g_{\mathrm{pl}}}\frac{\partial g_{\mathrm{pl}}}{\partial \Delta\lambda_{\mathrm{pl}}}\right)\\ \frac{\partial \zeta_{\mathrm{vol}}}{\partial \Delta\lambda_{\mathrm{pl}}} &= \frac{K_{\mathrm{m}}\alpha}{g_{\mathrm{pl}}}\left(1 - \frac{\Delta\lambda_{\mathrm{pl}}}{g_{\mathrm{pl}}}\frac{\partial g_{\mathrm{pl}}}{\partial \Delta\lambda_{\mathrm{pl}}}\right).\end{aligned} \tag{A.12}$$

With these equations and the definition of g_{pl} (cf. Eq. (A.4)) the derivative can be solved to

$$\begin{aligned}
\frac{\partial g_{\text{pl}}}{\partial \Delta\lambda_{\text{pl}}} &= \frac{\partial}{\partial \Delta\lambda_{\text{pl}}}\left(\sqrt{\frac{\hat{\sigma}_{\text{vm}}^2}{\zeta_{\text{dev}}^2} + \alpha\frac{\hat{p}^2}{\zeta_{\text{vol}}^2}}\right) \\
&= -\frac{1}{g_{\text{pl}}}\left(\underbrace{\frac{3G_{\text{m}}}{g_{\text{pl}}}\frac{\hat{\sigma}_{\text{vm}}^2}{\zeta_{\text{dev}}^3}}_{\kappa_{\text{dev}}} + \underbrace{\frac{K_{\text{m}}\alpha^2}{g_{\text{pl}}}\frac{\hat{p}^2}{\zeta_{\text{vol}}^3}}_{\kappa_{\text{vol}}}\right)\left(1 - \frac{\Delta\lambda_{\text{pl}}}{g_{\text{pl}}}\frac{\partial g_{\text{pl}}}{\partial \Delta\lambda_{\text{pl}}}\right) \qquad \text{(A.13)}\\
\Leftrightarrow \frac{\partial g_{\text{pl}}}{\partial \Delta\lambda_{\text{pl}}} &= \frac{(\kappa_{\text{dev}} + \kappa_{\text{vol}})\, g_{\text{pl}}}{(\kappa_{\text{dev}} + \kappa_{\text{vol}})\,\Delta\lambda_{\text{pl}} - g_{\text{pl}}^2}.
\end{aligned}$$

Finally, the derivative of the equivalent plastic strain is deduced from Equations (A.8), (A.12) and (A.13)

$$\frac{\partial \Delta\bar{\varepsilon}_{\text{pl}}}{\partial \Delta\lambda_{\text{pl}}} = \frac{\partial}{\partial \Delta\lambda_{\text{pl}}}\left(\frac{\Delta\lambda_{\text{pl}}}{2g_{\text{pl}}}\sqrt{\eta}\right) = \frac{1}{2g_{\text{pl}}}\left(\sqrt{\eta} - \frac{\Delta\lambda_{\text{pl}}}{g_{\text{pl}}}\sqrt{\eta}\frac{\partial g_{\text{pl}}}{\partial \Delta\lambda_{\text{pl}}} + \frac{1}{2}\frac{\Delta\lambda_{\text{pl}}}{g_{\text{pl}}\sqrt{\eta}}\frac{\partial \eta}{\partial \Delta\lambda_{\text{pl}}}\right) \qquad \text{(A.14)}$$

where $\frac{\partial \eta}{\partial \Delta\lambda_{\text{pl}}}$ is defined as

$$\begin{aligned}
\frac{\partial \eta}{\partial \Delta\lambda_{\text{pl}}} &= \frac{\partial}{\partial \Delta\lambda_{\text{pl}}}\left(k\left(\frac{6\hat{\sigma}_{\text{vm}}^2}{\zeta_{\text{dev}}^2} + \frac{4\alpha^2\hat{p}^2}{3\zeta_{\text{vol}}^2}\right)\right) \\
&= -k\left(12\kappa_{\text{dev}} + \frac{8}{3}\alpha\kappa_{\text{vol}}\right)\left(1 - \frac{\Delta\lambda_{\text{pl}}}{g_{\text{pl}}}\frac{\partial g_{\text{pl}}}{\partial \Delta\lambda_{\text{pl}}}\right).
\end{aligned} \qquad \text{(A.15)}$$

Special care needs to be taken for the boundaries of $\Delta\lambda_{\text{pl}}$. Since the plastic strain increment $\Delta\boldsymbol{\varepsilon}_{\text{pl}}$ is limited by the actual strain increment $\Delta\boldsymbol{\varepsilon}$, the upper bound of $\Delta\lambda_{\text{pl}}$ is near the value of the trial equivalent plastic strain increment. This trial value can be determined by replacing the plastic strain increment $\Delta\boldsymbol{\varepsilon}_{\text{pl}}$ in Equation (3.54) by the actual strain increment $\Delta\boldsymbol{\varepsilon}$. However, the lower bound of $\Delta\lambda_{\text{pl}}$ must be greater than zero in order to solve the Newton-Raphson, since the plastic corrector is the denominator in the first term of Equation (A.9). Within these bounds the quadratic convergence of the Newton's iterative method can be achieved.

Plasticity Consistent Tangent Operator To ensure rapid convergence of the equilibrium of the finite element solver a proper definition of the consistent tangent operator is required. In general by using a UMAT in the FE tool ABAQUS, the derivative of the strain increment to the resulting stress increment $\mathrm{d}\Delta\boldsymbol{\sigma}/\mathrm{d}\Delta\boldsymbol{\varepsilon}$ needs to be determined. However, since the resulting stress increment $\Delta\boldsymbol{\sigma}$ is dependent on the resulting stress $\boldsymbol{\sigma}$ and the stress itself is determined from trial stresses $\hat{\boldsymbol{\sigma}}$, which are based on the trial elastic strain $\hat{\boldsymbol{\varepsilon}}_{\mathrm{el}} = \boldsymbol{\varepsilon}_{\mathrm{el}} + \Delta\boldsymbol{\varepsilon}$, derivative can be rewritten to

$$\frac{\mathrm{d}\Delta\boldsymbol{\sigma}}{\mathrm{d}\Delta\boldsymbol{\varepsilon}} = \frac{\mathrm{d}\boldsymbol{\sigma}}{\mathrm{d}\hat{\boldsymbol{\varepsilon}}_{\mathrm{el}}}. \tag{A.16}$$

Using Equation (A.1) the stress can be expressed by a trial stress state and the plastic strain increment. The derivative to the trial elastic strain results to

$$\frac{\mathrm{d}\boldsymbol{\sigma}}{\mathrm{d}\hat{\boldsymbol{\varepsilon}}_{\mathrm{el}}} = \frac{\mathrm{d}\mathbb{C} : \left(\hat{\boldsymbol{\varepsilon}}_{\mathrm{el}} - \Delta\boldsymbol{\varepsilon}_{\mathrm{pl}}\right)}{\mathrm{d}\hat{\boldsymbol{\varepsilon}}_{\mathrm{el}}} = \mathbb{C} - \mathbb{C} : \frac{\mathrm{d}\Delta\boldsymbol{\varepsilon}_{\mathrm{pl}}}{\mathrm{d}\hat{\boldsymbol{\varepsilon}}_{\mathrm{el}}}. \tag{A.17}$$

It should be noted that the expression $\frac{\mathrm{d}\Delta\boldsymbol{\varepsilon}_{\mathrm{pl}}}{\mathrm{d}\hat{\boldsymbol{\varepsilon}}_{\mathrm{el}}}$ is a forth-order tensor. By the double dot product of $\mathbb{C}$ and $\frac{\mathrm{d}\Delta\boldsymbol{\varepsilon}_{\mathrm{pl}}}{\mathrm{d}\hat{\boldsymbol{\varepsilon}}_{\mathrm{el}}}$ a contraction to a new forth-order tensor is performed. Furthermore, it is obvious that in case of a pure elastic step only the stiffness tensor $\mathbb{C}$ remains as consistent tangent operator. Since the resulting plastic strain increment depends mainly on the plastic corrector $\Delta\lambda_{\mathrm{pl}}$, the trial deviatoric stress $\hat{\boldsymbol{\sigma}}_{\mathrm{dev}}$ and the trial hydrostatic pressure $\hat{p}$, the derivative of $\Delta\boldsymbol{\varepsilon}_{\mathrm{pl}}$ to $\hat{\boldsymbol{\varepsilon}}_{\mathrm{el}}$ will result in a following expression

$$\frac{\mathrm{d}\Delta\boldsymbol{\varepsilon}_{\mathrm{pl}}}{\mathrm{d}\hat{\boldsymbol{\varepsilon}}_{\mathrm{el}}} = \boldsymbol{\xi} \otimes \frac{\mathrm{d}\Delta\lambda_{\mathrm{pl}}}{\mathrm{d}\hat{\boldsymbol{\varepsilon}}_{\mathrm{el}}} + \chi \frac{\mathrm{d}\hat{\boldsymbol{\sigma}}_{\mathrm{dev}}}{\mathrm{d}\hat{\boldsymbol{\varepsilon}}_{\mathrm{el}}} + \boldsymbol{\psi} \otimes \frac{\mathrm{d}\hat{p}}{\mathrm{d}\hat{\boldsymbol{\varepsilon}}_{\mathrm{el}}} \tag{A.18}$$

where $\boldsymbol{\xi}$ and $\boldsymbol{\psi}$ are second-order tensors and χ is a scalar factor. However, to obtain these components several derivatives need to be determined. First direct solution of the plastic strain increment derivative using Eq. (3.44), (A.2), (A.3) and (A.6) results to

$$\begin{aligned}
\frac{\mathrm{d}\Delta\boldsymbol{\varepsilon}_{\mathrm{pl}}}{\mathrm{d}\hat{\boldsymbol{\varepsilon}}_{\mathrm{el}}} &= \frac{\mathrm{d}}{\mathrm{d}\hat{\boldsymbol{\varepsilon}}_{\mathrm{el}}} \left(\frac{\Delta\lambda_{\mathrm{pl}}}{2g_{\mathrm{pl}}} \left(\frac{3\hat{\boldsymbol{\sigma}}_{\mathrm{dev}}}{\zeta_{\mathrm{dev}}} - \frac{2\alpha\hat{p}}{3\zeta_{\mathrm{vol}}} \boldsymbol{I} \right) \right) \\
&= \frac{1}{\Delta\lambda_{\mathrm{pl}}} \Delta\boldsymbol{\varepsilon}_{\mathrm{pl}} \otimes \frac{\mathrm{d}\Delta\lambda_{\mathrm{pl}}}{\mathrm{d}\hat{\boldsymbol{\varepsilon}}_{\mathrm{el}}} - \frac{1}{g_{\mathrm{pl}}} \Delta\boldsymbol{\varepsilon}_{\mathrm{pl}} \otimes \frac{\mathrm{d}g_{\mathrm{pl}}}{\mathrm{d}\hat{\boldsymbol{\varepsilon}}_{\mathrm{el}}} + \frac{\Delta\lambda_{\mathrm{pl}}}{2g_{\mathrm{pl}}} \left[\frac{3}{\zeta_{\mathrm{dev}}} \left(\frac{\mathrm{d}\hat{\boldsymbol{\sigma}}_{\mathrm{dev}}}{\mathrm{d}\hat{\boldsymbol{\varepsilon}}_{\mathrm{el}}} \right.\right. \\
&\quad \left.\left. -\boldsymbol{\sigma}_{\mathrm{dev}} \otimes \frac{\mathrm{d}\zeta_{\mathrm{dev}}}{\mathrm{d}\hat{\boldsymbol{\varepsilon}}_{\mathrm{el}}} \right) - \frac{2\alpha}{3\zeta_{\mathrm{vol}}} \left(\boldsymbol{I} \otimes \frac{\mathrm{d}\hat{p}}{\mathrm{d}\hat{\boldsymbol{\varepsilon}}_{\mathrm{el}}} - p\boldsymbol{I} \otimes \frac{\mathrm{d}\zeta_{\mathrm{vol}}}{\mathrm{d}\hat{\boldsymbol{\varepsilon}}_{\mathrm{el}}} \right) \right].
\end{aligned} \tag{A.19}$$

Next the derivatives of ζ_{dev} and ζ_{vol} are needed to determine the derivative of g_{pl}.

$$\begin{aligned}\frac{\mathrm{d}\zeta_{\mathrm{dev}}}{\mathrm{d}\hat{\boldsymbol{\varepsilon}}_{\mathrm{el}}} &= \frac{3G_{\mathrm{m}}}{g_{\mathrm{pl}}}\left(\frac{\mathrm{d}\Delta\lambda_{\mathrm{pl}}}{\mathrm{d}\hat{\boldsymbol{\varepsilon}}_{\mathrm{el}}} - \frac{\Delta\lambda_{\mathrm{pl}}}{g_{\mathrm{pl}}}\frac{\mathrm{d}g_{\mathrm{pl}}}{\mathrm{d}\hat{\boldsymbol{\varepsilon}}_{\mathrm{el}}}\right)\\ \frac{\mathrm{d}\zeta_{\mathrm{vol}}}{\mathrm{d}\hat{\boldsymbol{\varepsilon}}_{\mathrm{el}}} &= \frac{K_{\mathrm{m}}\alpha}{g_{\mathrm{pl}}}\left(\frac{\mathrm{d}\Delta\lambda_{\mathrm{pl}}}{\mathrm{d}\hat{\boldsymbol{\varepsilon}}_{\mathrm{el}}} - \frac{\Delta\lambda_{\mathrm{pl}}}{g_{\mathrm{pl}}}\frac{\mathrm{d}g_{\mathrm{pl}}}{\mathrm{d}\hat{\boldsymbol{\varepsilon}}_{\mathrm{el}}}\right)\end{aligned} \tag{A.20}$$

Using Equations (A.13) and (A.20) and also the definition of κ_{dev} and κ_{vol} after some simplifications the derivative of g_{pl} is deduced to

$$\begin{aligned}\frac{\mathrm{d}g_{\mathrm{pl}}}{\mathrm{d}\hat{\boldsymbol{\varepsilon}}_{\mathrm{el}}} &= \frac{1}{g_{\mathrm{pl}}}\left(\frac{\sigma_{\mathrm{vm}}}{\zeta_{\mathrm{dev}}}\left(\frac{\mathrm{d}\hat{\sigma}_{\mathrm{vm}}}{\mathrm{d}\hat{\boldsymbol{\varepsilon}}_{\mathrm{el}}} - \sigma_{\mathrm{vm}}\frac{\mathrm{d}\zeta_{\mathrm{dev}}}{\mathrm{d}\hat{\boldsymbol{\varepsilon}}_{\mathrm{el}}}\right) + \frac{\alpha p}{\zeta_{\mathrm{vol}}}\left(\frac{\mathrm{d}\hat{p}}{\mathrm{d}\hat{\boldsymbol{\varepsilon}}_{\mathrm{el}}} - p\frac{\mathrm{d}\zeta_{\mathrm{vol}}}{\mathrm{d}\hat{\boldsymbol{\varepsilon}}_{\mathrm{el}}}\right)\right) \Leftrightarrow\\ &= \frac{\partial g_{\mathrm{pl}}}{\partial\Delta\lambda_{\mathrm{pl}}}\left(\frac{\mathrm{d}\Delta\lambda_{\mathrm{pl}}}{\mathrm{d}\hat{\boldsymbol{\varepsilon}}_{\mathrm{el}}} - \frac{1}{\kappa_{\mathrm{dev}} + \kappa_{\mathrm{vol}}}\left(\frac{\sigma_{\mathrm{vm}}}{\zeta_{\mathrm{dev}}}\frac{\mathrm{d}\hat{\sigma}_{\mathrm{vm}}}{\mathrm{d}\hat{\boldsymbol{\varepsilon}}_{\mathrm{el}}} + \frac{\alpha p}{\zeta_{\mathrm{vol}}}\frac{\mathrm{d}\hat{p}}{\mathrm{d}\hat{\boldsymbol{\varepsilon}}_{\mathrm{el}}}\right)\right).\end{aligned} \tag{A.21}$$

For further simplifications the deviatoric and the volumetric plastic strains ($\Delta\boldsymbol{\varepsilon}_{\mathrm{pl}_{\mathrm{dev}}}$ and $\Delta\boldsymbol{\varepsilon}_{\mathrm{pl}_{\mathrm{vol}}}$) by using Equation (3.44) are introduced

$$\Delta\boldsymbol{\varepsilon}_{\mathrm{pl}_{\mathrm{dev}}} = \frac{3\Delta\lambda_{\mathrm{pl}}}{2g_{\mathrm{pl}}}\boldsymbol{\sigma}_{\mathrm{dev}} \quad \text{and} \quad \Delta\boldsymbol{\varepsilon}_{\mathrm{pl}_{\mathrm{vol}}} = -\frac{\alpha p\Delta\lambda_{\mathrm{pl}}}{3g_{\mathrm{pl}}}\boldsymbol{I}. \tag{A.22}$$

Next the derivatives of g_{pl}, ζ_{dev} and ζ_{vol} are substituted into Equitation (A.19). By collecting the factors of the derivatives of $\hat{\boldsymbol{\sigma}}_{\mathrm{dev}}$, $\hat{p}$ and $\Delta\lambda_{\mathrm{pl}}$ and simplifying each factor using previously defined expressions, such as Equations (A.12) and (A.13), the parameters $\boldsymbol{\xi}$, $\boldsymbol{\psi}$ and χ from Equation (A.18) are defined as

$$\boldsymbol{\xi} = \left(\frac{1}{\Delta\lambda_{\mathrm{pl}}} - \frac{1}{g_{\mathrm{pl}}}\frac{\partial g_{\mathrm{pl}}}{\partial\Delta\lambda_{\mathrm{pl}}}\right)\Delta\boldsymbol{\varepsilon}_{\mathrm{pl}} - \frac{1}{\zeta_{\mathrm{dev}}}\frac{\partial\zeta_{\mathrm{dev}}}{\partial\Delta\lambda_{\mathrm{pl}}}\Delta\boldsymbol{\varepsilon}_{\mathrm{pl}_{\mathrm{dev}}} - \frac{1}{\zeta_{\mathrm{vol}}}\frac{\partial\zeta_{\mathrm{vol}}}{\partial\Delta\lambda_{\mathrm{pl}}}\Delta\boldsymbol{\varepsilon}_{\mathrm{pl}_{\mathrm{vol}}} \tag{A.23}$$

$$\begin{aligned}\boldsymbol{\psi} = \frac{\alpha p}{g_{\mathrm{pl}}\zeta_{\mathrm{vol}}\left(\kappa_{\mathrm{dev}} + \kappa_{\mathrm{vol}}\right)}\frac{\partial g_{\mathrm{pl}}}{\partial\Delta\lambda_{\mathrm{pl}}}&\left[\Delta\boldsymbol{\varepsilon}_{\mathrm{pl}} - \frac{\Delta\lambda_{\mathrm{pl}}}{g_{\mathrm{pl}}}\left(\frac{3G_{\mathrm{m}}}{\zeta_{\mathrm{dev}}}\Delta\boldsymbol{\varepsilon}_{\mathrm{pl}_{\mathrm{dev}}}\right.\right.\\ &\left.\left. + \frac{K_{\mathrm{m}}\alpha}{\zeta_{\mathrm{vol}}}\Delta\boldsymbol{\varepsilon}_{\mathrm{pl}_{\mathrm{vol}}}\right)\right] - \frac{\Delta\lambda_{\mathrm{pl}}\alpha}{3g_{\mathrm{pl}}\zeta_{\mathrm{vol}}}\boldsymbol{I}\end{aligned} \tag{A.24}$$

$$\chi = \frac{\Delta\lambda_{\mathrm{pl}}\sigma_{\mathrm{vm}}}{g_{\mathrm{pl}}^2\left(\kappa_{\mathrm{dev}} + \kappa_{\mathrm{vol}}\right)}\frac{\partial g_{\mathrm{pl}}}{\partial\Delta\lambda_{\mathrm{pl}}}\left(\frac{3}{2}\sigma_{\mathrm{vm}}\zeta_{\mathrm{dev}} - \frac{81}{8}\frac{G_{\mathrm{m}}\Delta\lambda_{\mathrm{pl}}}{g_{\mathrm{pl}}}\right) + \frac{3\Delta\lambda_{\mathrm{pl}}}{2g_{\mathrm{pl}}\zeta_{\mathrm{dev}}}. \tag{A.25}$$

While the solution of derivatives of $\hat{\boldsymbol{\sigma}}_{\mathrm{dev}}$ and $\hat{p}$ are trivial and results to

$$\frac{\mathrm{d}\hat{\boldsymbol{\sigma}}_{\mathrm{dev}}}{\mathrm{d}\hat{\boldsymbol{\varepsilon}}_{\mathrm{el}}} = 2G_{\mathrm{m}}\mathbb{I}_{\mathrm{dev}} \quad \text{and} \quad \frac{\mathrm{d}\hat{p}}{\mathrm{d}\hat{\boldsymbol{\varepsilon}}_{\mathrm{el}}} = -K_{\mathrm{m}}\boldsymbol{I}, \tag{A.26}$$

the derivative of the plastic corrector $\Delta\lambda_{\mathrm{pl}}$ in unknown and needs to be determined from the viscoplastic consistency condition (cf. Eq. (3.58)). Similar to the solution of the return mapping procedure to determine $\Delta\lambda_{\mathrm{pl}}$, the derivative of R_{pl} and the hardening laws (σ_{c} and σ_{t}) to the elastic trial stress results to

$$\begin{aligned}
\frac{\mathrm{d}R_{\mathrm{pl}}}{\mathrm{d}\hat{\boldsymbol{\varepsilon}}_{\mathrm{el}}} &= \frac{\mathrm{d}}{\mathrm{d}\hat{\boldsymbol{\varepsilon}}_{\mathrm{el}}}\left(\left(\frac{\Delta\lambda_{\mathrm{pl}}\mu}{\Delta t}\right)^{h} - \frac{\Phi_{\mathrm{pl}}}{2\sigma_{\mathrm{t}}\sigma_{\mathrm{c}}}\right) \\
&= \frac{h}{\Delta\lambda_{\mathrm{pl}}}\left(\frac{\Delta\lambda_{\mathrm{pl}}\mu}{\Delta t}\right)^{h}\frac{\mathrm{d}\Delta\lambda_{\mathrm{pl}}}{\mathrm{d}\hat{\boldsymbol{\varepsilon}}_{\mathrm{el}}} \\
&\quad - \frac{1}{2\sigma_{\mathrm{t}}\sigma_{\mathrm{c}}}\left(\frac{\mathrm{d}\Phi_{\mathrm{pl}}}{\mathrm{d}\hat{\boldsymbol{\varepsilon}}_{\mathrm{el}}} - \Phi_{\mathrm{pl}}\left(\frac{1}{\sigma_{\mathrm{c}}}\frac{\mathrm{d}\sigma_{\mathrm{c}}}{\mathrm{d}\hat{\boldsymbol{\varepsilon}}_{\mathrm{el}}} + \frac{1}{\sigma_{\mathrm{t}}}\frac{\mathrm{d}\sigma_{\mathrm{t}}}{\mathrm{d}\hat{\boldsymbol{\varepsilon}}_{\mathrm{el}}}\right)\right),
\end{aligned} \tag{A.27}$$

$$\frac{\mathrm{d}\sigma_{\mathrm{c}}}{\mathrm{d}\hat{\boldsymbol{\varepsilon}}_{\mathrm{el}}} = H_{\mathrm{c}}\frac{\mathrm{d}\Delta\bar{\varepsilon}_{\mathrm{pl}}}{\mathrm{d}\hat{\boldsymbol{\varepsilon}}_{\mathrm{el}}} \qquad \text{and} \qquad \frac{\mathrm{d}\sigma_{\mathrm{t}}}{\mathrm{d}\hat{\boldsymbol{\varepsilon}}_{\mathrm{el}}} = H_{\mathrm{t}}\frac{\mathrm{d}\Delta\bar{\varepsilon}_{\mathrm{pl}}}{\mathrm{d}\hat{\boldsymbol{\varepsilon}}_{\mathrm{el}}}. \tag{A.28}$$

However, the derivatives of Φ_{pl}, $\Delta\bar{\varepsilon}_{\mathrm{pl}}$ and η to the elastic strain differs from the derivatives to $\Delta\lambda_{\mathrm{pl}}$ due to the additional dependency on the strain. The results of these derivatives are expressed by

$$\begin{aligned}
\frac{\mathrm{d}\Phi_{\mathrm{pl}}}{\mathrm{d}\hat{\boldsymbol{\varepsilon}}_{\mathrm{el}}} &= \frac{\mathrm{d}}{\mathrm{d}\Delta\lambda_{\mathrm{pl}}}\left(6J_2 + 2I_1\left(\sigma_{\mathrm{c}} - \sigma_{\mathrm{t}}\right) - 2\sigma_{\mathrm{c}}\sigma_{\mathrm{t}}\right) \\
&= -\frac{12\hat{J}_2}{\zeta_{\mathrm{dev}}^3}\frac{\mathrm{d}\zeta_{\mathrm{dev}}}{\mathrm{d}\hat{\boldsymbol{\varepsilon}}_{\mathrm{el}}} - 2\left(\sigma_{\mathrm{c}} - \sigma_{\mathrm{t}}\right)\frac{\hat{I}_1}{\zeta_{\mathrm{vol}}^2}\frac{\mathrm{d}\zeta_{\mathrm{vol}}}{\mathrm{d}\hat{\boldsymbol{\varepsilon}}_{\mathrm{el}}} \\
&\quad + 2\left(\frac{\hat{I}_1}{\zeta_{\mathrm{vol}}} - \sigma_{\mathrm{t}}\right)\frac{\mathrm{d}\sigma_{\mathrm{c}}}{\mathrm{d}\hat{\boldsymbol{\varepsilon}}_{\mathrm{el}}} - 2\left(\frac{\hat{I}_1}{\zeta_{\mathrm{vol}}} - \sigma_{\mathrm{c}}\right)\frac{\mathrm{d}\sigma_{\mathrm{t}}}{\mathrm{d}\hat{\boldsymbol{\varepsilon}}_{\mathrm{el}}} \\
&\quad + \frac{6}{\zeta_{\mathrm{dev}}^2}\frac{\mathrm{d}\hat{J}_2}{\mathrm{d}\hat{\boldsymbol{\varepsilon}}_{\mathrm{el}}} + \frac{2\left(\sigma_{\mathrm{c}} - \sigma_{\mathrm{t}}\right)}{\zeta_{\mathrm{vol}}}\frac{\mathrm{d}\hat{I}_1}{\mathrm{d}\hat{\boldsymbol{\varepsilon}}_{\mathrm{el}}},
\end{aligned} \tag{A.29}$$

$$\begin{aligned}\frac{\mathrm{d}\Delta\bar{\varepsilon}_{\mathrm{pl}}}{\mathrm{d}\hat{\boldsymbol{\varepsilon}}_{\mathrm{el}}} &= \frac{\mathrm{d}}{\mathrm{d}\hat{\boldsymbol{\varepsilon}}_{\mathrm{el}}}\left(\frac{\Delta\lambda_{\mathrm{pl}}}{2g_{\mathrm{pl}}}\sqrt{\eta}\right) \\ &= \frac{1}{2g_{\mathrm{pl}}}\left(\sqrt{\eta}\frac{\mathrm{d}\Delta\lambda_{\mathrm{pl}}}{\mathrm{d}\hat{\boldsymbol{\varepsilon}}_{\mathrm{el}}} - \frac{\Delta\lambda_{\mathrm{pl}}}{g_{\mathrm{pl}}}\sqrt{\eta}\frac{\mathrm{d}g_{\mathrm{pl}}}{\mathrm{d}\hat{\boldsymbol{\varepsilon}}_{\mathrm{el}}} + \frac{1}{2}\frac{\Delta\lambda_{\mathrm{pl}}}{g_{\mathrm{pl}}\sqrt{\eta}}\frac{\mathrm{d}\eta}{\mathrm{d}\hat{\boldsymbol{\varepsilon}}_{\mathrm{el}}}\right),\end{aligned} \tag{A.30}$$

and

$$\begin{aligned}\frac{\mathrm{d}\eta}{\mathrm{d}\hat{\boldsymbol{\varepsilon}}_{\mathrm{el}}} &= \frac{\mathrm{d}}{\mathrm{d}\hat{\boldsymbol{\varepsilon}}_{\mathrm{el}}}\left(k\left(\frac{6\hat{\sigma}_{\mathrm{vm}}^2}{\zeta_{\mathrm{dev}}^2} + \frac{4\alpha^2\hat{p}^2}{3\zeta_{\mathrm{vol}}^2}\right)\right) \\ &= k\left[\left(12\kappa_{\mathrm{dev}} + \frac{8}{3}\alpha\kappa_{\mathrm{vol}}\right)\left(\frac{\Delta\lambda_{\mathrm{pl}}}{g_{\mathrm{pl}}}\frac{\mathrm{d}g_{\mathrm{pl}}}{\mathrm{d}\hat{\boldsymbol{\varepsilon}}_{\mathrm{el}}} - \frac{\mathrm{d}\Delta\lambda_{\mathrm{pl}}}{\mathrm{d}\hat{\boldsymbol{\varepsilon}}_{\mathrm{el}}}\right)\right. \\ &\qquad \left. + \frac{8}{3}\frac{\alpha^2\hat{p}}{\zeta_{\mathrm{vol}}^2}\frac{\mathrm{d}\hat{p}}{\mathrm{d}\hat{\boldsymbol{\varepsilon}}_{\mathrm{el}}} + \frac{12\hat{\sigma}_{\mathrm{vm}}}{\zeta_{\mathrm{dev}}^2}\frac{\mathrm{d}\hat{\sigma}_{\mathrm{vm}}}{\mathrm{d}\hat{\boldsymbol{\varepsilon}}_{\mathrm{el}}}\right].\end{aligned} \tag{A.31}$$

If now the results of Equations (A.20), (A.21) and (A.29) to (A.31) are substituted into Equation (A.27), the following expression is obtained

$$\begin{aligned} 0 &= \beta_{\Delta\lambda_{\mathrm{pl}}}\frac{\mathrm{d}\Delta\lambda_{\mathrm{pl}}}{\mathrm{d}\hat{\boldsymbol{\varepsilon}}_{\mathrm{el}}} + \beta_{\mathrm{p}}\frac{\mathrm{d}\hat{I}_1}{\mathrm{d}\hat{\boldsymbol{\varepsilon}}_{\mathrm{el}}} + \beta_{\mathrm{dev}}\frac{\mathrm{d}\hat{J}_2}{\mathrm{d}\hat{\boldsymbol{\varepsilon}}_{\mathrm{el}}} \\ \Leftrightarrow \quad \frac{\mathrm{d}\Delta\lambda_{\mathrm{pl}}}{\mathrm{d}\hat{\boldsymbol{\varepsilon}}_{\mathrm{el}}} &= -\frac{1}{\beta_{\Delta\lambda_{\mathrm{pl}}}}\left(\beta_{\mathrm{p}}\frac{\mathrm{d}\hat{I}_1}{\mathrm{d}\hat{\boldsymbol{\varepsilon}}_{\mathrm{el}}} + \beta_{\mathrm{dev}}\frac{\mathrm{d}\hat{J}_2}{\mathrm{d}\hat{\boldsymbol{\varepsilon}}_{\mathrm{el}}}\right)\end{aligned} \tag{A.32}$$

where $\beta_{\Delta\lambda_{\mathrm{pl}}}$, β_{p} and β_{dev} are scalar factors to each derivative. The full derivation of these factors is presented in the next section. Using the result of the derivative of $\Delta\lambda_{\mathrm{pl}}$ the consistent tangent operator of the viscoplastic matrix material behavior is fully defined.

Factors of the Vicoplastic Consistent Tangent Operator The derivative of the viscoplastic consistency condition R_{pl} to $\hat{\boldsymbol{\varepsilon}}_{\mathrm{el}}$ results to an expression based on the derivative of $\Delta\lambda_{\mathrm{pl}}$, $\hat{I}_1$ and $\hat{J}_2$ with the factors $\beta_{\Delta\lambda_{\mathrm{pl}}}$, β_{p} and β_{dev} respectively. To determine these factors first the derivatives of $\hat{p}$ and $\hat{\sigma}_{\mathrm{vm}}$ are needed. Since $p = -{}^1\!/\!{}_3 I_1$ and $\sigma_{\mathrm{vm}} = \sqrt{{}^3\!/\!{}_2 J_2}$ the derivatives result to

$$\frac{\mathrm{d}\hat{p}}{\mathrm{d}\hat{\boldsymbol{\varepsilon}}_{\mathrm{el}}} = -\frac{1}{3}\frac{\mathrm{d}\hat{I}_1}{\mathrm{d}\hat{\boldsymbol{\varepsilon}}_{\mathrm{el}}} \qquad \text{and} \qquad \frac{\mathrm{d}\hat{\sigma}_{\mathrm{vm}}}{\mathrm{d}\hat{\boldsymbol{\varepsilon}}_{\mathrm{el}}} = \frac{3}{2\hat{\sigma}_{\mathrm{vm}}}\frac{\mathrm{d}\hat{J}_2}{\mathrm{d}\hat{\boldsymbol{\varepsilon}}_{\mathrm{el}}}. \tag{A.33}$$

To simplify the expression of each factor the trial values are replaced where possible to true values (eg., $\hat{I}_1/\zeta_{\text{vol}} = I_1$). If the results of the derivatives of R_{pl} and Φ_{pl} are analyzed, it can be observed that the derivative of $\Delta\bar{\varepsilon}_{\text{pl}}$ separates the required factors $\beta_{\Delta\lambda_{\text{pl}}}$, β_{p} and β_{dev} to a fixed term Ω (this term is based on the hardening laws $\sigma_{\text{t,c}}$ itself, their hardening rates $H_{\text{t,c}}$ and the plastic yield surface Φ_{pl}) and a remaining term considering the derivatives of $\hat{J}_2$ and $\hat{I}_1$. Each factor has then the same form, which is given as:

$$\beta_i = \underbrace{(\cdots)}_{\Omega}\,\omega_i + \underbrace{\cdots}_{\text{remaining term}}, \qquad i \in \left\{\Delta\lambda_{\text{pl}}, \text{p}, \text{dev}\right\}. \tag{A.34}$$

The term Ω can be summarized to

$$\Omega = \left(1 + \frac{1}{2}\frac{\Phi_{\text{pl}}}{\sigma_{\text{t}}\sigma_{\text{c}}}\right)\left(\frac{H_{\text{c}}}{\sigma_{\text{c}}} + \frac{H_{\text{t}}}{\sigma_{\text{t}}}\right) - \frac{(H_{\text{c}} - H_{\text{t}})\,I_1}{\sigma_{\text{t}}\sigma_{\text{c}}}. \tag{A.35}$$

Since the derivative of $\Delta\bar{\varepsilon}_{\text{pl}}$ depends on the derivative g_{pl} a further simplification can be obtained for the remaining term of the factors β_{p} and β_{dev}. In both factors the following expression can be substituted:

$$\Xi = \left(\frac{1}{2}\frac{(\sigma_{\text{c}} - \sigma_{\text{t}})\,I_1 K_{\text{m}}\alpha}{\zeta_{\text{vol}}} + \frac{9G_{\text{m}}J_2}{\zeta_{\text{dev}}}\right)\frac{\Delta\lambda_{\text{pl}}}{(\kappa_{\text{dev}} + \kappa_{\text{vol}})\,g_{\text{pl}}^2}\frac{\partial g_{\text{pl}}}{\partial\Delta\lambda_{\text{pl}}}. \tag{A.36}$$

Finally, each factor is defined as

$$\beta_{\Delta\lambda_{\text{pl}}} = \Omega\omega_{\Delta\lambda_{\text{pl}}} + \frac{h}{\Delta\lambda_{\text{pl}}}\left(\frac{\Delta\lambda_{\text{pl}}\mu}{\Delta t}\right)^h + \frac{1}{\sigma_{\text{t}}\sigma_{\text{c}}}\left(\frac{I_1}{\zeta_{\text{vol}}}\frac{\partial\zeta_{\text{vol}}}{\partial\Delta\lambda_{\text{pl}}} + \frac{6J_2}{\zeta_{\text{dev}}}\frac{\partial\zeta_{\text{dev}}}{\partial\Delta\lambda_{\text{pl}}}\right) \tag{A.37}$$

$$\beta_{\text{p}} = \Omega\omega_{\text{p}} - \frac{\frac{2}{3}\Xi\alpha p + \sigma_{\text{c}} + \sigma_{\text{t}}}{\sigma_{\text{c}}\sigma_{\text{t}}\zeta_{\text{vol}}} \tag{A.38}$$

$$\beta_{\text{dev}} = \Omega\omega_{\text{dev}} + \frac{3\,(\Xi - 1)}{\sigma_{\text{c}}\sigma_{\text{t}}\zeta_{\text{dev}}^2} \tag{A.39}$$

where $\omega_{\Delta\lambda_{\text{pl}}}$, ω_{p} and ω_{dev} are defined as

$$\omega_{\Delta\lambda_{\text{pl}}} = \frac{\partial\Delta\bar{\varepsilon}_{\text{pl}}}{\partial\Delta\lambda_{\text{pl}}} \tag{A.40}$$

$$
\begin{aligned}
\omega_{\mathrm{p}} = & \left(\frac{k\Delta\lambda_{\mathrm{pl}}}{\sqrt{\eta}}\left(\frac{2}{9}\alpha\kappa_{\mathrm{vol}} + \kappa_{\mathrm{dev}}\right) - \frac{\sqrt{\eta}}{6}\right)\frac{\Delta\lambda_{\mathrm{pl}}\alpha p}{\left(\kappa_{\mathrm{dev}} + \kappa_{\mathrm{vol}}\right) g_{\mathrm{pl}}^2 \zeta_{\mathrm{vol}}}\frac{\partial g_{\mathrm{pl}}}{\partial\Delta\lambda_{\mathrm{pl}}} \\
& - \frac{2}{9}\frac{k\Delta\lambda_{\mathrm{pl}}\alpha^2 p}{\zeta_{\mathrm{vol}}\sqrt{\eta}g_{\mathrm{pl}}}
\end{aligned} \tag{A.41}
$$

$$
\begin{aligned}
\omega_{\mathrm{dev}} = & \left(\frac{3}{4}\sqrt{\eta} - \frac{k\Delta\lambda_{\mathrm{pl}}}{\sqrt{\eta}}\left(\alpha\kappa_{\mathrm{vol}} + \frac{9}{2}\kappa_{\mathrm{dev}}\right)\right)\frac{\Delta\lambda_{\mathrm{pl}}}{\left(\kappa_{\mathrm{dev}} + \kappa_{\mathrm{vol}}\right) g_{\mathrm{pl}}^2 \zeta_{\mathrm{dev}}^2}\frac{\partial g_{\mathrm{pl}}}{\partial\Delta\lambda_{\mathrm{pl}}} \\
& + \frac{9}{2}\frac{k\Delta\lambda_{\mathrm{pl}}}{\sqrt{\eta}g_{\mathrm{pl}}\zeta_{\mathrm{dev}}^2}.
\end{aligned} \tag{A.42}
$$

A.1.1.2 Damage Model

Procedure to Model Progressive Damage To determine the resulting stress after failure initiation several values need to determined in first place. For example, the definition of the initial damage driving force Y_0 in Equation (3.88) needs to be determined to a corresponding damage variable for a given damage driving force Y. Furthermore, plastic strain can occur, which affects the resulting elastic strain to determine the damage driving forces. In general after failure initiation $f_{\mathrm{M}} > 1$ and if plastic strain is present the resulting elastic strain would be underestimated. Therefore, a correction of the plastic strain increment needs to be performed. A linear distribution of the strain increment during a time increment is assumed. Here the stress at $f_{\mathrm{M}} = 1$ would result to

$$
\boldsymbol{\sigma}_0 = \boldsymbol{\sigma}_t + \lambda_0^{(\mathrm{init})}\Delta\boldsymbol{\sigma} = \boldsymbol{\sigma}_t + \lambda_0^{(\mathrm{init})}\mathbb{C} : \Delta\boldsymbol{\varepsilon}_{\mathrm{el}} \tag{A.43}
$$

where $\lambda_0^{(\mathrm{init})}$ is a scaling factor in range from 0 to 1. Since the material stiffness $\mathbb{C}$ is a constant parameter, this factor affects only the elastic strain increment and therefore the plastic strain increment. The resulting elastic and plastic strain increment at $f_{\mathrm{M}} = 1$ is then defined by

$$
\Delta\boldsymbol{\varepsilon}_{\mathrm{pl}_0} = \lambda_0^{(\mathrm{init})}\Delta\boldsymbol{\varepsilon}_{\mathrm{pl}} \qquad \text{and} \qquad \Delta\boldsymbol{\varepsilon}_{\mathrm{el}0} = \lambda_0^{(\mathrm{init})}\Delta\boldsymbol{\varepsilon}_{\mathrm{el}} \tag{A.44}
$$

To determine the scaling factor $\lambda_0^{(\mathrm{init})}$ the failure criterion f_{M} needs to be set to one and solved to $\lambda_0^{(\mathrm{init})}$. In such case the invariants ${J_2}^{(\mathrm{init})}$ and ${I_1}^{(\mathrm{init})}$ are dependent on the resulting stress $\boldsymbol{\sigma}_0$. Since the stress itself can be decomposed according to Equation (A.43) the failure criterion f_M results to

$$\begin{aligned}
1 \stackrel{!}{=} f_\mathrm{M} &= \frac{1}{2X_\mathrm{T}X_\mathrm{C}}\left(6{J_2}^{(\mathrm{init})} + 2\left(X_\mathrm{C} - X_\mathrm{T}\right){I_1}^{(\mathrm{init})}\right) \\
&= \frac{1}{2X_\mathrm{T}X_\mathrm{C}}\Big[3\left(\boldsymbol{\sigma}_{\mathrm{dev}t} + \lambda_0^{(\mathrm{init})}\Delta\boldsymbol{\sigma}_\mathrm{dev}\right) : \left(\boldsymbol{\sigma}_{\mathrm{dev}t} + \lambda_0^{(\mathrm{init})}\Delta\boldsymbol{\sigma}_\mathrm{dev}\right) \\
&\qquad\qquad + 2\left(X_\mathrm{C} - X_\mathrm{T}\right) tr(\boldsymbol{\sigma}_t + \lambda_0^{(\mathrm{init})}\Delta\boldsymbol{\sigma})\Big] \\
&= \frac{1}{2X_\mathrm{T}X_\mathrm{C}}\Big[6\left(\lambda_0^{(\mathrm{init})\,2}\Delta J_2 + \lambda_0^{(\mathrm{init})}\boldsymbol{\sigma}_{\mathrm{dev}t} : \Delta\boldsymbol{\sigma}_\mathrm{dev} + J_{2t}\right) \\
&\qquad\qquad + 2\left(X_\mathrm{C} - X_\mathrm{T}\right)\left(I_{1t} + \lambda_0^{(\mathrm{init})}\Delta I_1\right)\Big].
\end{aligned} \tag{A.45}$$

Due to exponent of the scaling factor a quadratic polynomial needs to be solved, which leads to two solutions. However, only one solution leads to values of $\lambda_0^{(\mathrm{init})}$ in a range of 0 to 1 and is defined as

$$\lambda_0^{(\mathrm{init})} = \frac{1}{6\Delta J_2}\left(\kappa_0 + \sqrt{\kappa_0^2 - 12\left(\left(X_\mathrm{C} - X_\mathrm{T}\right)I_{1t} - X_\mathrm{C}X_\mathrm{T} + 3J_{2t}\right)\Delta J_2}\right) \tag{A.46}$$

where κ_0 is defined as

$$\kappa_0 = \left(X_\mathrm{T} - X_\mathrm{C}\right)\Delta I_1 - 3\boldsymbol{\sigma}_{\mathrm{dev}t} : \Delta\boldsymbol{\sigma}_\mathrm{dev}. \tag{A.47}$$

Special care needs to be taken in case of pure hydrostatic pressure. Here the second invariant $J_2^{(\mathrm{init})}$ of the deviatoric stress tensor yields zero and therefore a simplified solution of $\lambda_0^{(\mathrm{init})}$ is obtained

$$\lambda_0^{(\mathrm{init})}\Big|_{J_2^{(\mathrm{init})}=0} = \frac{X_\mathrm{C}X_\mathrm{T}}{\left(X_\mathrm{C} - X_\mathrm{T}\right)\Delta I_1} - \frac{I_{1t}}{\Delta I_1}. \tag{A.48}$$

Using the obtained scaling factor the updated elastic stress $\Delta\boldsymbol{\varepsilon}_\mathrm{el}$ is determined from the current strain increment and the corrected plastic strain increment.

$$\Delta\boldsymbol{\varepsilon}_\mathrm{el} = \Delta\boldsymbol{\varepsilon} - \Delta\boldsymbol{\varepsilon}_{\mathrm{pl}_0}. \tag{A.49}$$

Now the updated trial stress $\hat{\boldsymbol{\sigma}}$ can be calculated and also the corresponding damage driving forces Y. It should be noted that the loading path can change during further damage propagation. This would have an effect on the initial damage driving force Y_0 and needs to be considered during damage evolution. While the initial scaling factor $\lambda_0^{(\mathrm{init})}$ is calculated once at damage initiation and is primarily needed to determine the values such as plastic strain at damage initiation, a further scaling factor λ_0 during damage propagation is needed to determine Y_0. The corresponding scaling factor can be determined in the same manner as the initial one. The only difference is that the scaling factor is directly applied to the trial stress $\hat{\boldsymbol{\sigma}}$ instead to the stress increment $\Delta\boldsymbol{\sigma}$. The scaling factor is then given as

$$\lambda_0 = \begin{cases} \frac{1}{6\hat{J}_2}\left((X_\mathrm{T} - X_\mathrm{C})\,\hat{I}_1 + \sqrt{12\hat{J}_2 X_\mathrm{C} X_\mathrm{T} + \left((X_\mathrm{C} - X_\mathrm{T})\,\hat{I}_1\right)^2}\right), & \hat{J}_2 \neq 0 \\ \frac{X_\mathrm{C} X_\mathrm{T}}{(X_\mathrm{C} - X_\mathrm{T})\hat{I}_1}, & \hat{J}_2 = 0 \end{cases} \tag{A.50}$$

To determine the actual damage variables, the energy term g_d needs to be first determined. As shown in Figure 3.15 the area under a loading path is defined as g and can be separated into an area prior to failure initiation and afterwards. Since plastic strain can occur the area prior to failure initiation can be defined as following

$$g_0^\pm = g_{0_\mathrm{el}}^\pm + g_{0_\mathrm{pl}}^\pm, \tag{A.51}$$

where the elastic and the plastic energy are defined as:

$$g_{0_\mathrm{el}}^\pm = \int_0^{\boldsymbol{\varepsilon}_{\mathrm{el}0}} \sigma_0^\pm \mathrm{d}\boldsymbol{\varepsilon}_\mathrm{el} \qquad \text{and} \qquad g_{0_\mathrm{pl}}^\pm = \int_0^{\boldsymbol{\varepsilon}_{\mathrm{pl}_0}} \sigma_0^\pm \mathrm{d}\boldsymbol{\varepsilon}_\mathrm{pl}. \tag{A.52}$$

The area after failure initiation g_d is then given as

$$g_\mathrm{d}^\pm = g^\pm - g_0^\pm = \frac{G_\mathrm{f}^\pm}{L_\mathrm{C}} - g_0^\pm, \tag{A.53}$$

where G_f is the material energy release rate under tensile or compressive load, while L_C is the characteristic length of the corresponding finite element. The value of $g_0^\pm$ is stored at damage initiation and is used for further damage evolution. Using the resulting initial damage driving forces $Y_0^\pm$ defined by $\boldsymbol{\sigma}_0^\pm$ and also the trial damage driving forces $Y^\pm$, the damage variables in tension and compression can be determined (cf. Equation (3.90)).

Damage Consistent Tangent Operator In combination with plastic strain the resulting stress after damage initiation is given by Equation (3.62). To distinguish between positive and negative damage evolution, the definition of $\mathbb{M}$ from Equation (3.69) is used. To determine the consistent tangent operator derivative of the stress to the strain is given by

$$\frac{\mathrm{d}\boldsymbol{\sigma}}{\mathrm{d}\hat{\boldsymbol{\varepsilon}}_{\mathrm{el}}} = \frac{\mathrm{d}\mathbb{C}_{\mathrm{D}} : \boldsymbol{\varepsilon}_{\mathrm{el}}}{\mathrm{d}\hat{\boldsymbol{\varepsilon}}_{\mathrm{el}}} = \frac{\mathrm{d}\mathbb{C}_{\mathrm{D}}}{\mathrm{d}\hat{\boldsymbol{\varepsilon}}_{\mathrm{el}}} : \boldsymbol{\varepsilon}_{\mathrm{el}} + \mathbb{C}_{\mathrm{D}} : \frac{\mathrm{d}\boldsymbol{\varepsilon}_{\mathrm{el}}}{\mathrm{d}\hat{\boldsymbol{\varepsilon}}_{\mathrm{el}}}. \tag{A.54}$$

While the later derivative accounts the change due to plasticity, the derivative of $\mathbb{C}_{\mathrm{D}}$ covers the damage evolution. The derivative of $\mathbb{C}_{\mathrm{D}}$ is a sixth-order tensor and is contracted to a forth-order tensor by $\boldsymbol{\varepsilon}_{\mathrm{el}}$. Using the results of the consistent tangent operator is case of plasticity (cf. Section A.1.1.1), the derivative of the elastic strain in conjunction with the initial scaling factor $\lambda_0^{(\mathrm{init})}$ results to

$$\frac{\mathrm{d}\boldsymbol{\varepsilon}_{\mathrm{el}}}{\mathrm{d}\hat{\boldsymbol{\varepsilon}}_{\mathrm{el}}} = \frac{\mathrm{d}\hat{\boldsymbol{\varepsilon}}_{\mathrm{el}} - \lambda_0^{(\mathrm{init})}\Delta\boldsymbol{\varepsilon}_{\mathrm{pl}}}{\mathrm{d}\hat{\boldsymbol{\varepsilon}}_{\mathrm{el}}} = \mathbb{I}^{\mathrm{s}} - \left(\frac{\mathrm{d}\lambda_0^{(\mathrm{init})}}{\mathrm{d}\hat{\boldsymbol{\varepsilon}}_{\mathrm{el}}} \otimes \Delta\boldsymbol{\varepsilon}_{\mathrm{pl}} + \lambda_0^{(\mathrm{init})}\frac{\mathrm{d}\Delta\boldsymbol{\varepsilon}_{\mathrm{pl}}}{\mathrm{d}\hat{\boldsymbol{\varepsilon}}_{\mathrm{el}}}\right). \tag{A.55}$$

Since the damaged material stiffness $\mathbb{C}_{\mathrm{D}}$ depends on the damage tensor $\mathbb{M}$, the derivative of $\mathbb{C}_{\mathrm{D}}$ results to

$$\frac{\mathrm{d}\mathbb{C}_{\mathrm{D}}}{\mathrm{d}\hat{\boldsymbol{\varepsilon}}_{\mathrm{el}}} = \frac{\mathrm{d}\mathbb{M}}{\mathrm{d}\hat{\boldsymbol{\varepsilon}}_{\mathrm{el}}} : \mathbb{C} = \frac{\mathrm{d}\mathbb{M}^{+}}{\mathrm{d}\hat{\boldsymbol{\varepsilon}}_{\mathrm{el}}} : \mathbb{P}^{+} : \mathbb{C} + \frac{\mathrm{d}\mathbb{M}^{-}}{\mathrm{d}\hat{\boldsymbol{\varepsilon}}_{\mathrm{el}}} : \mathbb{P}^{-} : \mathbb{C}. \tag{A.56}$$

The results of the derivatives of $\mathbb{M}^{+}$ and $\mathbb{M}^{-}$ differs only by the usage of $\mathbb{P}^{+}$ and $\mathbb{P}^{-}$ respectively. Using the definition of $\mathbb{M}$ from Equation (3.61) the derivative is expressed by

$$\frac{\mathrm{d}\mathbb{M}^{\pm}}{\mathrm{d}\hat{\boldsymbol{\varepsilon}}_{\mathrm{el}}} = -\frac{\mathrm{d}d_{\mathrm{v}}^{\pm}}{\mathrm{d}\hat{\boldsymbol{\varepsilon}}_{\mathrm{el}}} \otimes \mathbb{I}^{\mathrm{s}}. \tag{A.57}$$

The only factor in the formulation of the viscous damage variable $d_{\mathrm{v}}^{\pm}$ which depends on the trial strain $\hat{\boldsymbol{\varepsilon}}_{\mathrm{el}}$ is the true damage variable $d^{\pm}$. Therefore, the derivative of $d_{\mathrm{v}}^{\pm}$ results to

$$\frac{\mathrm{d}d_{\mathrm{v}}^{\pm}}{\mathrm{d}\hat{\boldsymbol{\varepsilon}}_{\mathrm{el}}} = \frac{\mathrm{d}d_{\mathrm{v}}^{\pm}}{\mathrm{d}d^{\pm}}\frac{\mathrm{d}d^{\pm}}{\mathrm{d}\hat{\boldsymbol{\varepsilon}}_{\mathrm{el}}} = \frac{\Delta t}{\Delta t + \mu_{\mathrm{d}}}\frac{\mathrm{d}d^{\pm}}{\mathrm{d}\hat{\boldsymbol{\varepsilon}}_{\mathrm{el}}}. \tag{A.58}$$

Since the damage variables $d^{\pm}$ are dependent on the initial and the trial damage driving forces ($Y_0^{\pm}$ and $Y^{\pm}$), using the chain rule the derivative can be summarized to

$$\frac{\mathrm{d}d^{\pm}}{\mathrm{d}\hat{\boldsymbol{\varepsilon}}_{\mathrm{el}}} = \frac{\mathrm{d}d^{\pm}}{\mathrm{d}Y^{\pm}}\frac{\mathrm{d}Y^{\pm}}{\mathrm{d}\hat{\boldsymbol{\varepsilon}}_{\mathrm{el}}} + \frac{\mathrm{d}d^{\pm}}{\mathrm{d}Y_0^{\pm}}\frac{\mathrm{d}Y_0^{\pm}}{\mathrm{d}\hat{\boldsymbol{\varepsilon}}_{\mathrm{el}}}. \tag{A.59}$$

By noticing that the initial damage driving force is connected via the scaling factor λ_0 to the trial damage driving force, the derivative of $Y_0^{\pm}$ is given by

$$\frac{\mathrm{d}Y_0^{\pm}}{\mathrm{d}\hat{\boldsymbol{\varepsilon}}_{\mathrm{el}}} = \frac{\mathrm{d}\lambda_0^{\pm 2}Y^{\pm}}{\mathrm{d}\hat{\boldsymbol{\varepsilon}}_{\mathrm{el}}} = 2\frac{\mathrm{d}\lambda_0^{\pm}}{\mathrm{d}\hat{\boldsymbol{\varepsilon}}_{\mathrm{el}}}Y^{\pm} + \lambda_0^{\pm 2}\frac{\mathrm{d}Y^{\pm}}{\mathrm{d}\hat{\boldsymbol{\varepsilon}}_{\mathrm{el}}}. \tag{A.60}$$

Next the derivative of trial damage driving force $Y^{\pm}$ and the derivative of the scaling factor $\lambda_0^{\pm}$ are needed. Using Equations (3.74) and (A.50) the derivatives are defined as following

$$\begin{aligned}\frac{\mathrm{d}Y^{\pm}}{\mathrm{d}\hat{\boldsymbol{\varepsilon}}_{\mathrm{el}}} &= \frac{\mathrm{d}Y^{\pm}}{\mathrm{d}\hat{\boldsymbol{\sigma}}} : \frac{\mathrm{d}\hat{\boldsymbol{\sigma}}}{\mathrm{d}\hat{\boldsymbol{\varepsilon}}_{\mathrm{el}}} + \frac{\mathrm{d}Y^{\pm}}{\mathrm{d}\boldsymbol{\varepsilon}_{\mathrm{el}}} : \frac{\mathrm{d}\boldsymbol{\varepsilon}_{\mathrm{el}}}{\mathrm{d}\hat{\boldsymbol{\varepsilon}}_{\mathrm{el}}} \\ &= \frac{1}{2}\mathbb{P}^{\pm} : \boldsymbol{\varepsilon}_{\mathrm{el}} : \frac{\mathrm{d}\hat{\boldsymbol{\sigma}}}{\mathrm{d}\hat{\boldsymbol{\varepsilon}}_{\mathrm{el}}} + \frac{1}{2}\mathbb{P}^{\pm} : \hat{\boldsymbol{\sigma}} : \frac{\mathrm{d}\boldsymbol{\varepsilon}_{\mathrm{el}}}{\mathrm{d}\hat{\boldsymbol{\varepsilon}}_{\mathrm{el}}}\end{aligned} \tag{A.61}$$

$$\begin{aligned}\frac{\mathrm{d}\lambda_0^{\pm}}{\mathrm{d}\hat{\boldsymbol{\varepsilon}}_{\mathrm{el}}} &= \frac{\mathrm{d}\lambda_0^{\pm}}{\mathrm{d}\hat{J}_2^{\pm}}\frac{\mathrm{d}\hat{J}_2^{\pm}}{\mathrm{d}\hat{\boldsymbol{\varepsilon}}_{\mathrm{el}}} + \frac{\mathrm{d}\lambda_0^{\pm}}{\mathrm{d}\hat{I}_1^{\pm}}\frac{\mathrm{d}\hat{I}_1^{\pm}}{\mathrm{d}\hat{\boldsymbol{\varepsilon}}_{\mathrm{el}}} \\ &= \frac{\mathrm{d}\lambda_0^{\pm}}{\mathrm{d}\hat{J}_2^{\pm}}\hat{\boldsymbol{\sigma}}_{\mathrm{dev}}^{\pm} : \mathbb{P}^{\pm} : \frac{\mathrm{d}\hat{\boldsymbol{\sigma}}}{\mathrm{d}\hat{\boldsymbol{\varepsilon}}_{\mathrm{el}}} + \frac{\mathrm{d}\lambda_0^{\pm}}{\mathrm{d}\hat{I}_1^{\pm}}\boldsymbol{I} : \mathbb{P}^{\pm} : \frac{\mathrm{d}\hat{\boldsymbol{\sigma}}}{\mathrm{d}\hat{\boldsymbol{\varepsilon}}_{\mathrm{el}}}\end{aligned} \tag{A.62}$$

Since the derivative of the trial stress $\hat{\boldsymbol{\sigma}}$ to the trial elastic strain $\hat{\boldsymbol{\varepsilon}}_{\mathrm{el}}$ results to the undamaged material stiffness $\mathbb{C}$ all parameters of the consistent tangent modulus are known.

A.1.2 Fiber Material

A.1.2.1 Consistent Tangent Operator

In the case of pure linear elastic stress only the material stiffness $\mathbb{C}^{\mathrm{TI}}$ as the consistent tangent operator ${}^{\mathrm{d}\Delta\sigma}/_{\mathrm{d}\Delta\varepsilon}$ would be returned. However, two sources of nonlinear behavior of the fiber are present: nonlinearity of the modulus in fiber direction and damage evolution after failure initiation. The derivative of the resulting stress leads to the following expression

$$\frac{\mathrm{d}\boldsymbol{\sigma}}{\mathrm{d}\hat{\boldsymbol{\varepsilon}}_{\mathrm{el}}} = -\frac{\mathrm{d}d_{\mathrm{v}}^{\pm}}{\mathrm{d}\hat{\boldsymbol{\varepsilon}}_{\mathrm{el}}} \otimes \hat{\boldsymbol{\sigma}} + \left(1 - d_{\mathrm{v}}^{\pm}\right) \frac{\mathrm{d}\mathbb{C}^{\mathrm{TI}}}{\mathrm{d}\hat{\boldsymbol{\varepsilon}}_{\mathrm{el}}} : \hat{\boldsymbol{\varepsilon}}_{\mathrm{el}} + \left(1 - d_{\mathrm{v}}^{\pm}\right) \mathbb{C}^{\mathrm{TI}}. \tag{A.63}$$

In the following the subscript 'el' is dropped. Since the definition of the viscous damage variable is equal to the matrix material, the derivative of it is also the same and is given by Equation (A.58). Since the true damage variable $d^{\pm}$ is dependent on the damage driving forces $Y^{\pm}$ and $Y_0^{\pm}$ the derivative of $d^{\pm}$ results to

$$\frac{\mathrm{d}d^{\pm}}{\mathrm{d}\hat{\boldsymbol{\varepsilon}}} = \frac{\mathrm{d}d^{\pm}}{\mathrm{d}Y^{\pm}} \frac{\mathrm{d}Y^{\pm}}{\mathrm{d}\hat{\boldsymbol{\varepsilon}}} + \frac{\mathrm{d}d^{\pm}}{\mathrm{d}Y_0^{\pm}} \frac{\mathrm{d}Y_0^{\pm}}{\mathrm{d}\hat{\boldsymbol{\varepsilon}}} \tag{A.64}$$

with

$$\frac{\mathrm{d}Y_0^{\pm}}{\mathrm{d}\hat{\boldsymbol{\varepsilon}}} = \frac{\mathrm{d}Y_0^{\pm}}{\mathrm{d}\lambda_0^{\pm}} \frac{\mathrm{d}\lambda_0^{\pm}}{\mathrm{d}\hat{\boldsymbol{\varepsilon}}} + \frac{\mathrm{d}Y_0^{\pm}}{\mathrm{d}Y^{\pm}} \frac{\mathrm{d}Y^{\pm}}{\mathrm{d}\hat{\boldsymbol{\varepsilon}}} = -\frac{2\lambda_0^{\pm} Y^{\pm} X_{\mathrm{T,C}}}{\hat{\sigma}_{11}^2} \frac{\mathrm{d}\hat{\sigma}_{11}}{\mathrm{d}\hat{\boldsymbol{\varepsilon}}} + \lambda_0^{\pm 2} \frac{\mathrm{d}Y^{\pm}}{\mathrm{d}\hat{\boldsymbol{\varepsilon}}}, \tag{A.65}$$

$$\frac{\mathrm{d}Y^{\pm}}{\mathrm{d}\hat{\boldsymbol{\varepsilon}}} = \frac{\mathrm{d}Y^{\pm}}{\mathrm{d}\hat{\sigma}_{11}} \frac{\mathrm{d}\hat{\sigma}_{11}}{\mathrm{d}\hat{\boldsymbol{\varepsilon}}} + \frac{\mathrm{d}Y^{\pm}}{\mathrm{d}\hat{\varepsilon}_{11}} \frac{\mathrm{d}\hat{\varepsilon}_{11}}{\mathrm{d}\hat{\boldsymbol{\varepsilon}}} = \frac{1}{2}\hat{\varepsilon}_{11} \frac{\mathrm{d}\hat{\sigma}_{11}}{\mathrm{d}\hat{\boldsymbol{\varepsilon}}} + \frac{1}{2}\hat{\sigma}_{11} \frac{\mathrm{d}\hat{\varepsilon}_{11}}{\mathrm{d}\hat{\boldsymbol{\varepsilon}}}. \tag{A.66}$$

As the stress $\hat{\sigma}_{11}$ depends on the material stiffness $\mathbb{C}^{\mathrm{TI}}$, which itself is dependent on the strain, the resulting derivative can be summarized in index notation to

$$\frac{\mathrm{d}\hat{\sigma}_{11}}{\mathrm{d}\hat{\varepsilon}_{mn}} = \left.\frac{\mathrm{d}C_{ijkl}^{\mathrm{TI}}}{\mathrm{d}\hat{\varepsilon}_{mn}}\right|_{i=1,j=1} \hat{\varepsilon}_{kl} + C_{11mn}^{\mathrm{TI}}. \tag{A.67}$$

Although the material stiffness $\mathbb{C}^{\mathrm{TI}}$ is dependent on five invariant material constants, only λ^{TI}, α^{TI} and β^{TI} are affected by the change of the Young's modulus E_1. The derivative of $\mathbb{C}^{\mathrm{TI}}$ is therefore given by

$$\frac{\mathrm{d}\mathbb{C}^{\mathrm{TI}}}{\mathrm{d}\hat{\boldsymbol{\varepsilon}}} = \frac{\mathrm{d}\mathbb{C}^{\mathrm{TI}}}{\mathrm{d}\lambda^{\mathrm{TI}}} \otimes \frac{\mathrm{d}\lambda^{\mathrm{TI}}}{\mathrm{d}\hat{\boldsymbol{\varepsilon}}} + \frac{\mathrm{d}\mathbb{C}^{\mathrm{TI}}}{\mathrm{d}\alpha^{\mathrm{TI}}} \otimes \frac{\mathrm{d}\alpha^{\mathrm{TI}}}{\mathrm{d}\hat{\boldsymbol{\varepsilon}}} + \frac{\mathrm{d}\mathbb{C}^{\mathrm{TI}}}{\mathrm{d}\beta^{\mathrm{TI}}} \otimes \frac{\mathrm{d}\beta^{\mathrm{TI}}}{\mathrm{d}\hat{\boldsymbol{\varepsilon}}} \tag{A.68}$$

where the derivatives of λ^{TI}, α^{TI} and β^{TI} are defined as

$$\frac{\mathrm{d}\lambda^{\mathrm{TI}}}{\mathrm{d}\hat{\boldsymbol{\varepsilon}}} = \frac{\mathrm{d}\lambda^{\mathrm{TI}}}{\mathrm{d}D} \frac{\mathrm{d}D}{\mathrm{d}\hat{\boldsymbol{\varepsilon}}} + \frac{\mathrm{d}\lambda^{\mathrm{TI}}}{\mathrm{d}\nu_{12}} \frac{\mathrm{d}\nu_{12}}{\mathrm{d}\hat{\boldsymbol{\varepsilon}}} \tag{A.69}$$

$$\frac{\mathrm{d}\alpha^{\mathrm{TI}}}{\mathrm{d}\hat{\boldsymbol{\varepsilon}}} = \frac{\mathrm{d}\alpha^{\mathrm{TI}}}{\mathrm{d}\lambda^{\mathrm{TI}}}\frac{\mathrm{d}\lambda^{\mathrm{TI}}}{\mathrm{d}\hat{\boldsymbol{\varepsilon}}} + \frac{\mathrm{d}\alpha^{\mathrm{TI}}}{\mathrm{d}D}\frac{\mathrm{d}D}{\mathrm{d}\hat{\boldsymbol{\varepsilon}}} + \frac{\mathrm{d}\alpha^{\mathrm{TI}}}{\mathrm{d}\nu_{12}}\frac{\mathrm{d}\nu_{12}}{\mathrm{d}\hat{\boldsymbol{\varepsilon}}} \tag{A.70}$$

$$\frac{\mathrm{d}\beta^{\mathrm{TI}}}{\mathrm{d}\hat{\boldsymbol{\varepsilon}}} = \frac{\mathrm{d}\beta^{\mathrm{TI}}}{\mathrm{d}D}\frac{\mathrm{d}D}{\mathrm{d}\hat{\boldsymbol{\varepsilon}}} + \frac{\mathrm{d}\beta^{\mathrm{TI}}}{\mathrm{d}\nu_{12}}\frac{\mathrm{d}\nu_{12}}{\mathrm{d}\hat{\boldsymbol{\varepsilon}}} + \frac{\mathrm{d}\beta^{\mathrm{TI}}}{\mathrm{d}E_1}\frac{\mathrm{d}E_1}{\mathrm{d}\hat{\boldsymbol{\varepsilon}}} \tag{A.71}$$

with

$$\frac{\mathrm{d}D}{\mathrm{d}\hat{\boldsymbol{\varepsilon}}} = \frac{\mathrm{d}D}{\mathrm{d}\nu_{12}}\frac{\mathrm{d}\nu_{12}}{\mathrm{d}\hat{\boldsymbol{\varepsilon}}}. \tag{A.72}$$

Finally, the derivatives of the Poisson's ratio ν_{12} and E_1 remains as the only unknown. From the definition of ν_{12} and E_1 (cf. Equation (3.102) and (3.104)) the derivatives results to

$$\frac{\mathrm{d}\nu_{12}}{\mathrm{d}\hat{\boldsymbol{\varepsilon}}} = \frac{\nu_{12}^{\mathrm{init}}}{E_1^{\mathrm{init}}}\frac{\mathrm{d}E_1}{\mathrm{d}\hat{\boldsymbol{\varepsilon}}} \quad \text{and} \quad \frac{\mathrm{d}E_1}{\mathrm{d}\hat{\boldsymbol{\varepsilon}}} = m_{\mathrm{f}}\frac{\mathrm{d}\hat{\varepsilon}_{11}}{\mathrm{d}\hat{\boldsymbol{\varepsilon}}} \tag{A.73}$$

and the derivative of the strain component $\hat{\varepsilon}_{11}$ yields to

$$\frac{\mathrm{d}\hat{\varepsilon}_{11}}{\mathrm{d}\hat{\boldsymbol{\varepsilon}}} = \begin{pmatrix} 1 & 0 & 0 \\ 0 & 0 & 0 \\ 0 & 0 & 0 \end{pmatrix}. \tag{A.74}$$

Substituting these results in Equations (A.66) and (A.67) together with the definition of the derivative of $\mathbb{C}^{\mathrm{TI}}$ (cf. Equation (A.68)) and d (cf. Equation (A.64)) lead to a fully defined consistent tangent operator.

A.1.3 Composite Material

A.1.3.1 Material Stiffness Matrix of a Transversely Isotropic Material

The inverse of the composite material compliance $\boldsymbol{S}$ leads to the material stiffness $\boldsymbol{C}$. If the compliance is defined in matrix notation, the resulting material stiffness is then given as

$$\boldsymbol{C} = \begin{pmatrix} \frac{E_1(1-\nu_{23}\nu_{32})}{D} & \frac{E_1(\nu_{31}\nu_{23}+\nu_{21})}{D} & \frac{E_1(\nu_{21}\nu_{32}+\nu_{31})}{D} & 0 & 0 & 0 \\ \frac{E_2(\nu_{32}\nu_{13}+\nu_{12})}{D} & \frac{E_2(1-\nu_{13}\nu_{31})}{D} & \frac{E_2(\nu_{12}\nu_{31}+\nu_{32})}{D} & 0 & 0 & 0 \\ \frac{E_3(\nu_{12}\nu_{23}+\nu_{13})}{D} & \frac{E_3(\nu_{13}\nu_{21}+\nu_{23})}{D} & \frac{E_3(1-\nu_{12}\nu_{21})}{D} & 0 & 0 & 0 \\ 0 & 0 & 0 & G_{12} & 0 & 0 \\ 0 & 0 & 0 & 0 & G_{12} & 0 \\ 0 & 0 & 0 & 0 & 0 & G_{23} \end{pmatrix} \tag{A.75}$$

where the parameter D is defined as

$$D = 1 - \nu_{12}\nu_{23}\nu_{31} - \nu_{13}\nu_{32}\nu_{21} - \nu_{12}\nu_{21} - \nu_{13}\nu_{31} - \nu_{23}\nu_{32}. \tag{A.76}$$

Additionally, the damaged stiffness matrix as a result of the inverse of the damaged compliance matrix $\boldsymbol{S}_\mathrm{D}$ yields to

$$\boldsymbol{C}_\mathrm{D} = \begin{pmatrix} \frac{\phi_1 E_1(1-\phi_2\phi_3\nu_{23}\nu_{32})}{\Delta} & \frac{\phi_1\phi_2 E_1(\phi_3\nu_{31}\nu_{23}+\nu_{21})}{\Delta} & \frac{\phi_1\phi_3 E_1(\phi_2\nu_{21}\nu_{32}+\nu_{31})}{\Delta} & 0 & 0 & 0 \\ \frac{\phi_1\phi_2 E_2(\phi_3\nu_{32}\nu_{13}+\nu_{12})}{\Delta} & \frac{\phi_2 E_2(1-\phi_1\phi_3\nu_{13}\nu_{31})}{\Delta} & \frac{\phi_2\phi_3 E_2(\phi_1\nu_{12}\nu_{31}+\nu_{32})}{\Delta} & 0 & 0 & 0 \\ \frac{\phi_1\phi_3 E_3(\phi_2\nu_{12}\nu_{23}+\nu_{13})}{\Delta} & \frac{\phi_2\phi_3 E_3(\phi_1\nu_{13}\nu_{21}+\nu_{23})}{\Delta} & \frac{\phi_3 E_3(1-\phi_1\phi_2\nu_{12}\nu_{21})}{\Delta} & 0 & 0 & 0 \\ 0 & 0 & 0 & \phi_4 G_{12} & 0 & 0 \\ 0 & 0 & 0 & 0 & \phi_5 G_{12} & 0 \\ 0 & 0 & 0 & 0 & 0 & \phi_6 G_{23} \end{pmatrix} \tag{A.77}$$

where the damaged parameter Δ is defined as

$$\Delta = 1 - \phi_1\phi_2\phi_3\left(\nu_{12}\nu_{23}\nu_{31} + \nu_{13}\nu_{32}\nu_{21}\right) - \phi_1\phi_2\nu_{12}\nu_{21} - \phi_1\phi_3\nu_{13}\nu_{31} - \phi_2\phi_3\nu_{23}\nu_{32}. \tag{A.78}$$

with the damage vector $\boldsymbol{\phi}$

$$\boldsymbol{\phi} = \begin{pmatrix} 1 - d_1^{\pm} & 1 - d_2^{\pm} & 1 - d_3^{\pm} & 1 - d_{12} & 1 - d_{13} & 1 - d_{23} \end{pmatrix}^\top. \tag{A.79}$$

A.1.3.2 Action Plane Plasticity Return Mapping Algorithm

The return mapping algorithm is performed similar to Appendix A.1.1.1. Considering that the material stiffness $\mathbb{C}^{\mathrm{TI}}$ of a transversely isotropic material does not change if it is rotated along the fiber direction and by rewriting stress and plastic strain increment into vector notation, the relation between trial stress and resulting stress is given by

$$\boldsymbol{\sigma}_{\mathrm{ap}} = \hat{\boldsymbol{\sigma}}_{\mathrm{ap}} - \Delta\lambda_{\mathrm{ap}} \mathbb{C}^{\mathrm{TI}} \frac{\partial g_{\mathrm{ap}}}{\partial \boldsymbol{\sigma}_{\mathrm{ap}}}. \tag{A.80}$$

Since the plastic strain affects only the σ_{n}, τ_{n1} and τ_{nt} stress components, a direct relation between the resulting stresses and the trial stress is summarized to

$$\sigma_{\mathrm{n}} = \hat{\sigma}_{\mathrm{n}} - \Delta\lambda_{\mathrm{ap}} C_{22} \beta_{\mathrm{ap}} \tag{A.81}$$

$$\tau_{\mathrm{n1}} = \hat{\tau}_{\mathrm{n1}} - \Delta\lambda_{\mathrm{ap}} C_{44} \frac{\tau_{\mathrm{n1}}}{\sqrt{\tau_{\mathrm{n1}}^2 + f_{\mathrm{ap}} \tau_{\mathrm{nt}}^2}} \tag{A.82}$$

$$\tau_{\mathrm{nt}} = \hat{\tau}_{\mathrm{nt}} - \Delta\lambda_{\mathrm{ap}} C_{66} \frac{f_{\mathrm{ap}} \tau_{\mathrm{nt}}}{\sqrt{\tau_{\mathrm{n1}}^2 + f_{\mathrm{ap}} \tau_{\mathrm{nt}}^2}} \tag{A.83}$$

where C_{22}, C_{44} and C_{66} are components of the material stiffness matrix. From Equations (A.82) and (A.83) it is obvious that the resulting stresses depend on each other. By inserting the square root term of these equations into each other, two possible cases as solution for τ_{n1} and τ_{nt} can be determined

$$\begin{aligned} \tau_{\mathrm{nt}} &= \frac{\hat{\tau}_{\mathrm{nt}} \tau_{\mathrm{n1}} C_{44}}{\tau_{\mathrm{n1}} C_{44} + (\hat{\tau}_{\mathrm{n1}} - \tau_{\mathrm{n1}})\, C_{66} f_{\mathrm{ap}}}, \quad && \hat{\tau}_{\mathrm{n1}} \geq \hat{\tau}_{\mathrm{nt}} \\ \tau_{\mathrm{n1}} &= \frac{\hat{\tau}_{\mathrm{n1}} f_{\mathrm{ap}} \tau_{\mathrm{nt}} C_{66}}{f_{\mathrm{ap}} \tau_{\mathrm{nt}} C_{66} + (\hat{\tau}_{\mathrm{nt}} - \tau_{\mathrm{nt}})\, C_{44}}, \quad && \hat{\tau}_{\mathrm{nt}} \geq \hat{\tau}_{\mathrm{n1}}. \end{aligned} \tag{A.84}$$

In case of $\hat{\tau}_{\mathrm{n1}} \geq \hat{\tau}_{\mathrm{nt}}$ the solution for τ_{nt} is substituted in Equation (A.82) or in the other case τ_{n1} into Equation (A.83). The resulting definition of τ_{n1} or τ_{nt} depends then only on trial stresses $\hat{\tau}_{\mathrm{n1}}$ and $\hat{\tau}_{\mathrm{nt}}$, the material stiffness matrix components C_{44} and C_{66}, the parameter f_{ap} and the plastic corrector $\Delta\lambda_{\mathrm{ap}}$. For a given $\Delta\lambda_{\mathrm{ap}}$ the resulting stress τ_{n1} or τ_{nt} can then be solved by using Newton-Raphson scheme. To determine $\Delta\lambda_{\mathrm{ap}}$ the definition of the yield surface (cf.

Equation (3.113)) is utilized. Since the result of $\Delta\lambda_{ap}$ can be highly nonlinear, the Newton-Raphson scheme is suited to solve such condition. The derivative of the yield surface to the plastic corrector is given by

$$\frac{\partial \Phi_{ap}}{\partial \Delta\lambda_{ap}} = \frac{\partial \bar{\sigma}_{ap}}{\partial \Delta\lambda_{ap}} - \frac{\partial \tau_{y}}{\partial \Delta\lambda_{ap}}. \tag{A.85}$$

The stress components σ_{n}, τ_{n1} and τ_{nt} of the equivalent stress $\bar{\sigma}_{ap}$ are dependent on the plastic corrector. Therefore, its derivative results to:

$$\begin{aligned}\frac{\partial \bar{\sigma}_{ap}}{\partial \Delta\lambda_{ap}} &= \frac{\partial \bar{\sigma}_{ap}}{\partial \sigma_{n}}\frac{\partial \sigma_{n}}{\partial \Delta\lambda_{ap}} + \frac{\partial \bar{\sigma}_{ap}}{\partial \tau_{n1}}\frac{\partial \tau_{n1}}{\partial \Delta\lambda_{ap}} + \frac{\partial \bar{\sigma}_{ap}}{\partial \tau_{nt}}\frac{\partial \tau_{nt}}{\partial \Delta\lambda_{ap}} \\ &= \alpha_{ap}\frac{\partial \sigma_{n}}{\partial \Delta\lambda_{ap}} + \frac{1}{\sqrt{\tau_{n1}^2 + e_{ap}\tau_{nt}^2}}\left(\tau_{n1}\frac{\partial \tau_{n1}}{\partial \Delta\lambda_{ap}} + e_{ap}\tau_{nt}\frac{\partial \tau_{nt}}{\partial \Delta\lambda_{ap}}\right)\end{aligned} \tag{A.86}$$

Due to two possible cases $\hat{\tau}_{n1} \geq \hat{\tau}_{nt}$ or $\hat{\tau}_{nt} \geq \hat{\tau}_{n1}$, the solution of the derivatives of the action plane shear stresses τ_{n1} and τ_{nt} yield also in two cases. However, the resulting derivatives have a similar structure. Using the definitions of τ_{n1} and τ_{nt} according to Equation (A.84) the derivatives for each case result to

$$\begin{aligned}\frac{\partial \tau_{nt}}{\partial \Delta\lambda_{ap}} &= \frac{\partial \tau_{nt}}{\partial \tau_{n1}}\frac{\partial \tau_{n1}}{\partial \Delta\lambda_{ap}} = \xi_1\frac{\partial \tau_{n1}}{\partial \Delta\lambda_{ap}}, \quad \hat{\tau}_{n1} \geq \hat{\tau}_{nt} \\ \frac{\partial \tau_{n1}}{\partial \Delta\lambda_{ap}} &= \frac{\partial \tau_{n1}}{\partial \tau_{nt}}\frac{\partial \tau_{nt}}{\partial \Delta\lambda_{ap}} = \xi_1\frac{\partial \tau_{nt}}{\partial \Delta\lambda_{ap}}, \quad \hat{\tau}_{nt} \geq \hat{\tau}_{n1}\end{aligned} \tag{A.87}$$

where the result of ξ_1 is also dependent on the specific case. Since the shear stresses τ_{n1} and τ_{nt} are self dependent on the plastic corrector $\Delta\lambda_{ap}$ their derivatives yield in conjunction with Equation (A.87) to

$$\begin{aligned}\frac{\partial \tau_{n1}}{\partial \Delta\lambda_{ap}} &= \underbrace{\frac{\partial \tau_{n1}}{\partial \tau_{nt}}}_{\kappa_1}\frac{\partial \tau_{nt}}{\partial \Delta\lambda_{ap}} + \underbrace{\frac{\partial \tau_{n1}}{\partial \tau_{n1}}}_{\kappa_2}\frac{\partial \tau_{n1}}{\partial \Delta\lambda_{ap}} + \underbrace{\frac{\partial \tau_{n1}}{\partial \Delta\lambda_{ap}}}_{\kappa_3}, \quad \hat{\tau}_{n1} \geq \hat{\tau}_{nt} \\ \frac{\partial \tau_{nt}}{\partial \Delta\lambda_{ap}} &= \underbrace{\frac{\partial \tau_{nt}}{\partial \tau_{nt}}}_{\kappa_2}\frac{\partial \tau_{nt}}{\partial \Delta\lambda_{ap}} + \underbrace{\frac{\partial \tau_{nt}}{\partial \tau_{n1}}}_{\kappa_1}\frac{\partial \tau_{n1}}{\partial \Delta\lambda_{ap}} + \underbrace{\frac{\partial \tau_{nt}}{\partial \Delta\lambda_{ap}}}_{\kappa_3}, \quad \hat{\tau}_{nt} \geq \hat{\tau}_{n1} \\ \Rightarrow \frac{\partial \tau_{n1}}{\partial \Delta\lambda_{ap}} &= \frac{\partial \tau_{nt}}{\partial \Delta\lambda_{ap}} = \frac{\kappa_3}{1 - \kappa_1\xi_1 - \kappa_2},\end{aligned} \tag{A.88}$$

where the full definition of the case-dependent factors κ_1, κ_2 and κ_3 is given in Appendix A.1.3.3. Next the derivative of the hardening function τ_y needs to be determined. Similar to the hardening function of the matrix material only the equivalent plastic strain is dependent on the plastic corrector $\Delta\lambda_{ap}$. Therefore, the resulting derivative of τ_y yields a function dependent on the hardening rate H_{ap} and the derivative of the equivalent plastic strain $\Delta\bar{\varepsilon}_{pl,ap}$

$$\frac{\partial \tau_y}{\partial \Delta\lambda_{ap}} = \frac{\partial \tau_y}{\partial \Delta\bar{\varepsilon}_{pl,ap}} \frac{\partial \Delta\bar{\varepsilon}_{pl,ap}}{\partial \Delta\lambda_{ap}} = H_{ap} \frac{\partial \Delta\bar{\varepsilon}_{pl,ap}}{\partial \Delta\lambda_{ap}}. \tag{A.89}$$

Since the plastic corrector $\Delta\lambda_{ap}$ affects only the stress values at the end of the time increment, the derivative of the equivalent plastic strain is applied also only to them. The derivative is then given by

$$\frac{\partial \Delta\bar{\varepsilon}_{pl,ap}}{\partial \Delta\lambda_{ap}} = \chi_1 \frac{\partial \sigma_n}{\partial \Delta\lambda_{ap}} + \chi_2 \frac{\partial \tau_{n1}}{\partial \Delta\lambda_{ap}} + \chi_3 \frac{\partial \tau_{nt}}{\partial \Delta\lambda_{ap}} + \chi_4 \frac{\partial \bar{\sigma}_{ap}}{\partial \Delta\lambda_{ap}} + \chi_5. \tag{A.90}$$

The full definition of the factors χ_1 to χ_5 is given in Appendix A.1.3.3. While the derivatives of τ_{n1}, τ_{nt} and $\bar{\sigma}_{ap}$ to the plastic corrector are given by Equations (A.86) to (A.88), the derivative of σ_n can be obtained by using Equation (A.81)

$$\frac{\partial \sigma_n}{\partial \Delta\lambda_{ap}} = -C_{22}\beta_{ap}. \tag{A.91}$$

A.1.3.3 Parameters of the Action Plane Based Plasticity

Due to two separate cases of τ_{n1} and τ_{nt} the corresponding parameters of the derivatives of each action shear stress lead to the following definition of the parameters ξ_1, κ_1 , κ_2 and κ_3. By using Equation (A.84) the parameter ξ_1 yield to

$$\xi_1 = \begin{cases} \left(1 - \frac{\tau_{n1}\left(e_{ap}C_{66} - C_{44}\right)}{(\hat{\tau}_{n1} - \tau_{n1})e_{ap}C_{66} + \tau_{n1}C_{44}}\right) \frac{\hat{\tau}_{nt}C_{44}}{(\hat{\tau}_{n1} - \tau_{n1})e_{ap}C_{66} + \tau_{n1}C_{44}}, & \hat{\tau}_{n1} \geq \hat{\tau}_{nt} \\ \left(1 - \frac{\tau_{nt}\left(e_{ap}C_{66} - C_{44}\right)}{(\hat{\tau}_{nt} - \tau_{nt})C_{44} + \tau_{nt}e_{ap}C_{66}}\right) \frac{\hat{\tau}_{n1}e_{ap}C_{66}}{(\hat{\tau}_{nt} - \tau_{nt})C_{44} + \tau_{nt}e_{ap}C_{66}}, & \hat{\tau}_{nt} \geq \hat{\tau}_{n1}. \end{cases} \tag{A.92}$$

The remaining parameters κ_1, κ_2 and κ_3 are obtained from derivatives of Equations (A.82) and (A.83) which are summarized to

$$\kappa_1 = \begin{cases} \frac{f_{\mathrm{ap}}\tau_{\mathrm{nt}}\tau_{\mathrm{n1}}C_{44}\Delta\lambda_{\mathrm{ap}}}{\sqrt{\left(\tau_{\mathrm{n1}}^2+f_{\mathrm{ap}}\tau_{\mathrm{nt}}^2\right)^3}}, & \hat{\tau}_{\mathrm{n1}} \geq \hat{\tau}_{\mathrm{nt}} \\ \frac{f_{\mathrm{ap}}\tau_{\mathrm{nt}}\tau_{\mathrm{n1}}C_{66}\Delta\lambda_{\mathrm{ap}}}{\sqrt{\left(\tau_{\mathrm{n1}}^2+f_{\mathrm{ap}}\tau_{\mathrm{nt}}^2\right)^3}}, & \hat{\tau}_{\mathrm{nt}} \geq \hat{\tau}_{\mathrm{n1}} \end{cases} \tag{A.93}$$

$$\kappa_2 = \begin{cases} \left(\frac{\tau_{\mathrm{n1}}^2}{\tau_{\mathrm{n1}}^2+f_{\mathrm{ap}}\tau_{\mathrm{nt}}^2} - 1\right) \frac{C_{44}\Delta\lambda_{\mathrm{ap}}}{\sqrt{\tau_{\mathrm{n1}}^2+f_{\mathrm{ap}}\tau_{\mathrm{nt}}^2}}, & \hat{\tau}_{\mathrm{n1}} \geq \hat{\tau}_{\mathrm{nt}} \\ \left(\frac{f_{\mathrm{ap}}\tau_{\mathrm{nt}}^2}{\tau_{\mathrm{n1}}^2+f_{\mathrm{ap}}\tau_{\mathrm{nt}}^2} - 1\right) \frac{f_{\mathrm{ap}}C_{66}\Delta\lambda_{\mathrm{ap}}}{\sqrt{\tau_{\mathrm{n1}}^2+f_{\mathrm{ap}}\tau_{\mathrm{nt}}^2}}, & \hat{\tau}_{\mathrm{nt}} \geq \hat{\tau}_{\mathrm{n1}} \end{cases} \tag{A.94}$$

$$\kappa_3 = \begin{cases} -C_{44}\frac{\tau_{\mathrm{n1}}}{\sqrt{\tau_{\mathrm{n1}}^2+f_{\mathrm{ap}}\tau_{\mathrm{nt}}^2}}, & \hat{\tau}_{\mathrm{n1}} \geq \hat{\tau}_{\mathrm{nt}} \\ -C_{66}\frac{f_{\mathrm{ap}}\tau_{\mathrm{nt}}}{\sqrt{\tau_{\mathrm{n1}}^2+f_{\mathrm{ap}}\tau_{\mathrm{nt}}^2}}, & \hat{\tau}_{\mathrm{nt}} \geq \hat{\tau}_{\mathrm{n1}}. \end{cases} \tag{A.95}$$

Additionally, from the derivative of the equivalent action plane based plastic strain increment $\Delta\bar{\varepsilon}_{\mathrm{pl,ap}}$ the factors χ_1 to χ_5 are defined as following (for the sake of clarity the indication $t + \Delta t$ is dropped)

$$\chi_1 = \frac{\beta_{\mathrm{ap}}\Delta\lambda_{\mathrm{ap}}}{\bar{\sigma}_{\mathrm{ap}} + \bar{\sigma}_{\mathrm{ap}}\big|_t} \tag{A.96}$$

$$\begin{aligned} \chi_2 = \frac{\Delta\lambda_{\mathrm{ap}}}{\bar{\sigma}_{\mathrm{ap}} + \bar{\sigma}_{\mathrm{ap}}\big|_t} \Bigg(& \frac{2\tau_{\mathrm{n1}} + \tau_{\mathrm{n1}}|_t}{\sqrt{\tau_{\mathrm{n1}}^2 + f_{\mathrm{ap}}\tau_{\mathrm{nt}}^2}} \\ & - \frac{\tau_{\mathrm{n1}}\left(\left(\tau_{\mathrm{nt}} + \tau_{\mathrm{nt}}|_t\right) f_{\mathrm{ap}}\tau_{\mathrm{nt}} + \left(\tau_{\mathrm{n1}} + \tau_{\mathrm{n1}}|_t\right)\tau_{\mathrm{n1}}\right)}{\sqrt{\left(\tau_{\mathrm{n1}}^2 + f_{\mathrm{ap}}\tau_{\mathrm{nt}}^2\right)^3}} \Bigg) \end{aligned} \tag{A.97}$$

$$\begin{aligned} \chi_3 = \frac{\Delta\lambda_{\mathrm{ap}}f_{\mathrm{ap}}}{\bar{\sigma}_{\mathrm{ap}} + \bar{\sigma}_{\mathrm{ap}}\big|_t} \Bigg(& \frac{2\tau_{\mathrm{nt}} + \tau_{\mathrm{nt}}|_t}{\sqrt{\tau_{\mathrm{n1}}^2 + f_{\mathrm{ap}}\tau_{\mathrm{nt}}^2}} \\ & - \frac{\tau_{\mathrm{nt}}\left(\left(\tau_{\mathrm{nt}} + \tau_{\mathrm{nt}}|_t\right) f_{\mathrm{ap}}\tau_{\mathrm{nt}} + \left(\tau_{\mathrm{n1}} + \tau_{\mathrm{n1}}|_t\right)\tau_{\mathrm{n1}}\right)}{\sqrt{\left(\tau_{\mathrm{n1}}^2 + f_{\mathrm{ap}}\tau_{\mathrm{nt}}^2\right)^3}} \Bigg) \end{aligned} \tag{A.98}$$

$$\chi_4 = -\frac{\Delta\lambda_{\mathrm{ap}}}{\left(\bar{\sigma}_{\mathrm{ap}} + \bar{\sigma}_{\mathrm{ap}}\big|_t\right)^2}\left(\beta_{\mathrm{ap}}\ \sigma_{\mathrm{n}}\big|_t + \frac{\tau_{\mathrm{n1}}\big|_t\ \tau_{\mathrm{n1}} + f_{\mathrm{ap}}\ \tau_{\mathrm{nt}}\big|_t\ \tau_{\mathrm{nt}}}{\sqrt{\tau_{\mathrm{n1}}^2 + f_{\mathrm{ap}}\tau_{\mathrm{nt}}^2}} + g_{\mathrm{ap}}\right) \tag{A.99}$$

$$\chi_5 = \frac{1}{\left(\bar{\sigma}_{\mathrm{ap}} + \bar{\sigma}_{\mathrm{ap}}\big|_t\right)}\left(\beta_{\mathrm{ap}}\ \sigma_{\mathrm{n}}\big|_t + \frac{\tau_{\mathrm{n1}}\big|_t\ \tau_{\mathrm{n1}} + f_{\mathrm{ap}}\ \tau_{\mathrm{nt}}\big|_t\ \tau_{\mathrm{nt}}}{\sqrt{\tau_{\mathrm{n1}}^2 + f_{\mathrm{ap}}\tau_{\mathrm{nt}}^2}} + g_{\mathrm{ap}}\right) \tag{A.100}$$

A.1.3.4 Analytical Models for Fiber Volume Content dependent Strength Values

To evaluate the suitability of the different analytical models [20, 88–90] to predict the Y_{T}, Y_{C} and S_{12} strength values at specific fiber volume content, each one is introduced and afterwards all models are compared. Although the strength values of Y_{T}, Y_{C} and S_{12} differs, each proposed model use the same structure of the formula but replace the material properties to the corresponding load (e.g., use of E_2 for transverse tension load and G_{12} for a shear load). Therefore, only the formulas for transverse tensile strengths are presented here, since the trends for the other strength values are the same. Using a 2D approach Kaw [90] suggest that a transverse load leads to a strain distribution ε_{22} via series-connected model using the fiber and matrix transverse strain. Furthermore, by using the diameter of the fiber d and the distance s between center of two fibers, the relation of the fiber volume content to these two values is given by

$$\frac{d}{s} = \begin{cases} \sqrt{\frac{4\varphi}{\pi}}, & \text{for square array packing} \\ \sqrt{\frac{2\sqrt{3}\varphi}{\pi}}, & \text{for hexagonal array packing.} \end{cases} \tag{A.101}$$

By combining fiber and matrix strain ($\varepsilon_{22}^{\mathrm{f}}$ and $\varepsilon_{22}^{\mathrm{m}}$) over the ratio d/s, while assuming an equal stress distribution in fiber and matrix $E_2^{\mathrm{f}}\varepsilon_{22}^{\mathrm{f}} = E_m\varepsilon_{22}^{\mathrm{m}}$, the composite strain results to

$$\varepsilon_{22} = \frac{d}{s}\varepsilon_{22}^{\mathrm{f}} + \left(1 - \frac{d}{s}\right)\varepsilon_{22}^{\mathrm{m}} = \left(\frac{d}{s}\frac{E_{\mathrm{m}}}{E_2^{\mathrm{f}}} + \left(1 - \frac{d}{s}\right)\right)\varepsilon_{22}^{\mathrm{m}}. \tag{A.102}$$

In case of linear elasticity, the transverse stress σ_{22} results as a product of E_2 and ε_{22}. By defining the transverse modulus E_2 as a function of fiber volume content φ and set $\varepsilon_{22}^{\mathrm{m}}$ to $\varepsilon_{22,\max}^{\mathrm{m}}$ as the matrix failure strain in transverse direction, the transverse tensile strength is defined by

$$Y_{\mathrm{T}} = E_2(\varphi)\left(\left(\frac{d}{s}\frac{E_m}{E_2^{\mathrm{f}}} + \left(1 - \frac{d}{s}\right)\right)\varepsilon_{22,\max}^{\mathrm{m}}\right). \tag{A.103}$$

According to Barbero [89] tensile strength is a fracture mechanics problem and depends on the energy release rate G_{Ic}, the geometry (in particular ply thickness t_{L}) and the material parameters E_1, E_2 and ν_{12}. This leads to the following tensile strength definition

$$Y_{\mathrm{T}} = \sqrt{\frac{G_{\mathrm{Ic}}\Lambda_{22}}{1.12^2\pi\left(t/4\right)}} \tag{A.104}$$

with

$$\Lambda_{22} = \frac{E_2E_1^3}{2\left(E_1^3 - \nu_{12}^2E_2^3\right)}. \tag{A.105}$$

The corresponding material parameters E_1, E_2 and ν_{12} are functions of the fiber volume content φ, while it is assumed that the G_{Ic} is constant within the evaluated fiber volume content range. An older empirical approach by Barbero assumed that transverse tensile strength is the result of the void volume fraction φ_{v} and the matrix tensile strength $X_{\mathrm{T}}^{\mathrm{m}}$. Such approach is summarized by the following formula

$$Y_{\mathrm{T}} = X_{\mathrm{T}}^{\mathrm{m}}C_{\mathrm{v}}\left(1 + \left(\varphi - \sqrt{\varphi}\right)\left(1 - \frac{E_m}{E_2^{\mathrm{f}}}\right)\right) \tag{A.106}$$

with

$$C_{\mathrm{v}} = 1 - \sqrt{\frac{4\varphi_{\mathrm{v}}}{\pi\left(1 - \varphi\right)}}. \tag{A.107}$$

It should be noted that in case of $\varphi_{\mathrm{v}} = 0\,\%$ the definition of tensile strength is equal to the one proposed by Chamis [88]. The model proposed by Huang [20] distinguishes between transverse tensile fiber or matrix failure ($Y_{\mathrm{T}}^{\mathrm{f}}$ or $X_{\mathrm{T}}^{\mathrm{m}}$). Therefore, the resulting tensile strength yields from the comparison of these two possible failure modes by choosing the first one which reaches failure for given $Y_{\mathrm{T}}^{\mathrm{f}}$ and $X_{\mathrm{T}}^{\mathrm{m}}$. Additionally, nonlinearity resulting due to yielding of the matrix is considered by introducing a matrix hardening modulus $E_{\mathrm{m}}^{\mathrm{T}}$ which defines the tangent to a uniaxial stress-strain curve in a plastic region. The transverse tensile strength is then defined by

$$Y_{\mathrm{T}} = \min\left\{ \frac{Y_{\mathrm{T}}^{\mathrm{f}} - \left(\alpha_{\mathrm{el}}^{\mathrm{f}} - \alpha_{\mathrm{pl}}^{\mathrm{f}}\right) \sigma_{22}^{\mathrm{init}}}{\alpha_{\mathrm{pl}}^{\mathrm{f}}}, \frac{X_{\mathrm{T}}^{\mathrm{m}} - \left(\alpha_{\mathrm{el}}^{\mathrm{m}} - \alpha_{\mathrm{pl}}^{\mathrm{m}}\right) \sigma_{22}^{\mathrm{init}}}{\alpha_{\mathrm{pl}}^{\mathrm{m}}} \right\} \tag{A.108}$$

with

$$\sigma_{22}^{\mathrm{init}} = \min\left\{ \frac{X_{\mathrm{T}}^{\mathrm{m}}}{\alpha_{\mathrm{el}}^{\mathrm{m}}}, \frac{Y_{\mathrm{T}}^{\mathrm{f}}}{\alpha_{\mathrm{el}}^{\mathrm{f}}} \right\}, \tag{A.109}$$

$$\alpha_{\mathrm{el}}^{\mathrm{f}} = \frac{E_2^{\mathrm{f}}}{\varphi E_2^{\mathrm{f}} + 0.5\,(1-\varphi)\left(E_{\mathrm{m}} + E_2^{\mathrm{f}}\right)}, \tag{A.110}$$

$$\alpha_{\mathrm{el}}^{\mathrm{m}} = \frac{0.5\left(E_2^{\mathrm{f}} + E_{\mathrm{m}}\right)}{\varphi E_2^{\mathrm{f}} + 0.5\,(1-\varphi)\left(E_{\mathrm{m}} + E_2^{\mathrm{f}}\right)}, \tag{A.111}$$

$$\alpha_{\mathrm{pl}}^{\mathrm{f}} = \frac{E_2^{\mathrm{f}}}{\varphi E_2^{\mathrm{f}} + 0.5\,(1-\varphi)\left(E_{\mathrm{m}}^{\mathrm{T}} + E_2^{\mathrm{f}}\right)}, \tag{A.112}$$

$$\alpha_{\mathrm{pl}}^{\mathrm{m}} = \frac{0.5\left(E_2^{\mathrm{f}} + E_{\mathrm{m}}\right)}{\varphi E_2^{\mathrm{f}} + 0.5\,(1-\varphi)\left(E_{\mathrm{m}}^{\mathrm{T}} + E_2^{\mathrm{f}}\right)}. \tag{A.113}$$

To compare these models a common set of material parameters need to be defined. To obtain fiber volume content specific material properties such as E_1, E_2 and ν_{12} Equations (3.148), (3.149) and (3.152) are used. The necessary parameters for those equations are given in Table A.1. Using the material properties for each fiber volume content, a variation of model specific parameters is performed to evaluate the effect of each parameter on the resulting transverse

Table A.1: Common set of material properties for comparison of different approaches to determine transverse tensile strength Y_{T}

E_1^{f} /GPa	E_2^{f} /GPa	E_{m} /GPa	ν_{12}^{f} /-	ν_{m} /-	ζ_{E_2} /-
200	20	3	0.2	0.4	2

tensile strength. The varied parameters for each model are summarized in Table A.2. It should be noted that to enforce fiber or matrix failure only using the HUANG model, the corresponding strength Y_T^f or X_T^m should be set to a very high value to provoke the result of the minimum function to the desired failure mode. The results for each model are given in Figure A.1. In general the results can be divided in two groups: tensile strength increases or decreases with increasing fiber volume content. Only the results of the KAW and BARBERO void volume content models predict a decrease of the strength while fiber volume content increases. Comparing the results of the KAW model for square and hexagonal array packing at different matrix failure strains $\varepsilon_{22,\mathrm{max}}^\mathrm{m}$ in Figure A.1a and A.1b show that the packing has a significant effect on the strength gradient. Since square and hexagonal array packing represent two ideal limits, the real fiber distribution will be somewhere in between. With increasing maximum matrix strains $\varepsilon_{22,\mathrm{max}}^\mathrm{m}$ the resulting tensile strength also increases, since the strain serves as a factor to a scalar value. Using BARBERO's void volume content model (cf. Figure A.1d) leads to a drastic drop of the

Table A.2: Transverse tensile strength models and the corresponding model type and parameter set variation

Proposed by	Model type	Parameter set to vary
KAW	square array packing	$\varepsilon_{22,\mathrm{max}}^\mathrm{m} = 2.0\,\%$ $\varepsilon_{22,\mathrm{max}}^\mathrm{m} = 2.5\,\%$
KAW	hexagonal array packing	$\varepsilon_{22,\mathrm{max}}^\mathrm{m} = 2.0\,\%$ $\varepsilon_{22,\mathrm{max}}^\mathrm{m} = 2.5\,\%$
BARBERO	energy release rate	$G_\mathrm{Ic} = 0.17\,\mathrm{kJ\,m^{-2}}, t = 0.25\,\mathrm{mm}$ $G_\mathrm{Ic} = 0.20\,\mathrm{kJ\,m^{-2}}, t = 0.30\,\mathrm{mm}$
BARBERO	void volume content	$\varphi_\mathrm{v} = 0.0\,\%, X_\mathrm{T}^\mathrm{m} = 68\,\mathrm{MPa}$ $\varphi_\mathrm{v} = 2.5\,\%, X_\mathrm{T}^\mathrm{m} = 72\,\mathrm{MPa}$
HUANG	fiber failure only	$Y_\mathrm{T}^\mathrm{f} = 60\,\mathrm{MPa}, E_\mathrm{m}^\mathrm{T} = 0.3\,\mathrm{GPa}$ $Y_\mathrm{T}^\mathrm{f} = 70\,\mathrm{MPa}, E_\mathrm{m}^\mathrm{T} = 3.0\,\mathrm{GPa}$
HUANG	matrix failure only	$X_\mathrm{T}^\mathrm{m} = 35\,\mathrm{MPa}, E_\mathrm{m}^\mathrm{T} = 0.3\,\mathrm{GPa}$ $X_\mathrm{T}^\mathrm{m} = 70\,\mathrm{MPa}, E_\mathrm{m}^\mathrm{T} = 3.0\,\mathrm{GPa}$

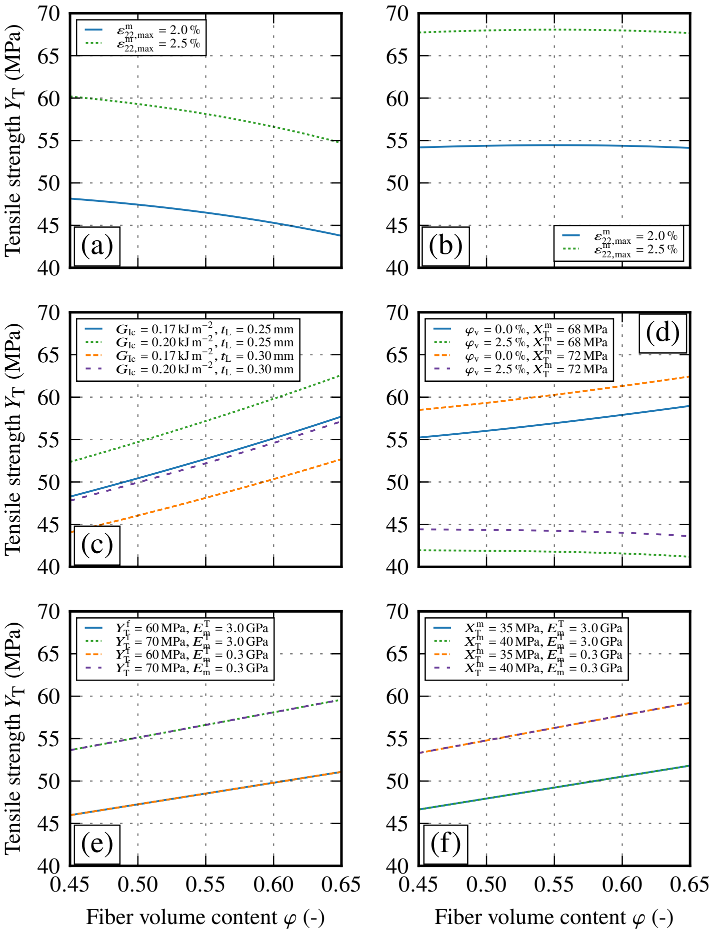

Figure A.1: Comparison of different analytical approaches to determine transverse tensile strength Y_T depending on the fiber volume content and their sensitivity to model specific parameters: KAW model (square array packing (a), hexagonal array packing (b)), BARBERO model (energy release rate G_{Ic} and thickness t_L (c), void volume content φ_V and matrix tensile strength X^{m}_{T} (d)) and HUANG model (only transverse fiber failure Y^{f}_{T} and matrix hardening modulus E^{T}_{m} (e), only matrix failure X^{m}_{T} and matrix hardening modulus E^{T}_{m} (f)) strength with increasing void volume content. However, optimized manufacturing processes, such as HP-RTM process, allow reducing trapped air in the fabric while simultaneously using high pressure forces to impregnate the fabric and avoid entrapped voids within the ply. Other models such as BARBERO's energy release rate model (cf. Figure A.1c) or HUANG's model (cf. Figure A.1e and A.1f) predict an increase towards high transverse tensile strength for high fiber volume contents. The model fracture specific parameters, such as energy release rate G_{Ic} or transverse fiber and matrix strength ($Y_{\mathrm{T}}^{\mathrm{f}}$ and $X_{\mathrm{T}}^{\mathrm{m}}$), are the direct proportional parameters which function as an offset for the resulting tensile strength of the composite. Furthermore, the thickness t_{L} in BARBERO's energy release rate model has the same effect as the energy release rate G_{Ic}. The matrix hardening modulus $E_{\mathrm{m}}^{\mathrm{T}}$ in HUANG's model is not sensitive at all for the evaluated fiber volume content and the chosen material properties of fiber and matrix. As mentioned previously these models predicts the same trends for each strength component.

A.1.3.5 Homogenized Parameters for Composites with Waviness

From the definition of the homogenized material compliance $\bar{\boldsymbol{S}}$ (cf. Equation (3.168)) each component which is dependent on x can be integrated by using the method described in Section 3.5.6 and the results are summarized to

$$\Upsilon_2 = \frac{1}{\lambda}\int_0^{\lambda} \sin^4\theta \mathrm{dx} = 1 - \frac{1 + \frac{3}{2}\left(2\pi A/\lambda\right)^2}{\left(1 + \left(2\pi A/\lambda\right)^2\right)^{3/2}} \tag{A.114}$$

$$\Upsilon_3 = \frac{1}{\lambda}\int_0^{\lambda} \cos^2\theta \mathrm{dx} = \frac{1}{\sqrt{1 + \left(2\pi A/\lambda\right)^2}} \tag{A.115}$$

$$\Upsilon_4 = \frac{1}{\lambda}\int_0^{\lambda} \sin^2\theta \mathrm{dx} = 1 - \frac{1}{\sqrt{1 + \left(2\pi A/\lambda\right)^2}} \tag{A.116}$$

$$\Upsilon_5 = \frac{1}{\lambda}\int_0^{\lambda} \sin^2\cos^2\theta \mathrm{dx} = \frac{\frac{1}{2}\left(2\pi A/\lambda\right)^2}{\left(1 + \left(2\pi A/\lambda\right)^2\right)^{3/2}} \tag{A.117}$$

$$\frac{1}{\lambda}\int_0^\lambda \sin^3\cos\theta \mathrm{dx} = \frac{1}{\lambda}\int_0^\lambda \sin\cos^3\theta \mathrm{dx} = \frac{1}{\lambda}\int_0^\lambda \sin\cos\theta \mathrm{dx} = 0. \quad (A.118)$$

Furthermore, the effective material properties of a composite with waviness can be obtained by applying uniaxial stress loads. Utilizing Equations (3.173), (A.114) to (A.117) the effective material properties are given by

$$E_{\mathrm{x}} = \frac{1}{\left(2\hat{S}_{12} + \hat{S}_{44}\right)\Upsilon_5 + \Upsilon_1\hat{S}_{11} + \Upsilon_2\hat{S}_{22}} \quad (A.119)$$

$$E_{\mathrm{y}} = \frac{1}{\left(2\hat{S}_{12} + \hat{S}_{44}\right)\Upsilon_5 + \Upsilon_1\hat{S}_{22} + \Upsilon_2\hat{S}_{11}} \quad (A.120)$$

$$E_{\mathrm{z}} = \frac{1}{\hat{S}_{33}} \quad (A.121)$$

$$\nu_{\mathrm{xy}} = -\frac{\left(\hat{S}_{11} + \hat{S}_{22} - \hat{S}_{44}\right)\Upsilon_5 + \hat{S}_{12}\left(\Upsilon_1 + \Upsilon_2\right)}{\left(2\hat{S}_{12} + \hat{S}_{44}\right)\Upsilon_5 + \Upsilon_1\hat{S}_{11} + \Upsilon_2\hat{S}_{22}} \quad (A.122)$$

$$\nu_{\mathrm{xz}} = -\frac{\Upsilon_3\hat{S}_{13} + \Upsilon_4\hat{S}_{23}}{\left(2\hat{S}_{12} + \hat{S}_{44}\right)\Upsilon_5 + \Upsilon_1\hat{S}_{11} + \Upsilon_2\hat{S}_{22}} \quad (A.123)$$

$$\nu_{\mathrm{zx}} = -\frac{\Upsilon_3\hat{S}_{13} + \Upsilon_4\hat{S}_{23}}{\hat{S}_{33}} \quad (A.124)$$

$$\nu_{\mathrm{zy}} = -\frac{\Upsilon_3\hat{S}_{23} + \Upsilon_4\hat{S}_{13}}{\hat{S}_{33}} \quad (A.125)$$

$$G_{\mathrm{xy}} = \frac{1}{\left(\Upsilon_1 + \Upsilon_2 - 2\Upsilon_5\right)\hat{S}_{44} + 4\left(\hat{S}_{11} - 2\hat{S}_{12} + \hat{S}_{22}\right)\Upsilon_5} \quad (A.126)$$

$$G_{\mathrm{xz}} = \frac{1}{\Upsilon_3\hat{S}_{55} + \Upsilon_4\hat{S}_{66}} \quad (A.127)$$

$$G_{\mathrm{yz}} = \frac{1}{\Upsilon_3\hat{S}_{66} + \Upsilon_4\hat{S}_{55}}, \quad (A.128)$$

where $\hat{S}_{ij}$ are components of the transversely isotropic material compliance matrix (cf. Equation (3.110))

A.1.3.6 Consistent Tangent Operator

Due to high nonlinear behavior of the composite material the convergence of the solver is highly affected by the accuracy of the consistent tangent operator. While some derivations of the tangent operator are similar to the matrix or fiber material, there are several differences due to failure initiation, damage propagation etc. First the consistent tangent operator of the transversely isotropic material is derived. Afterwards the resulting tangent operator is used within the constitutive model which considers draping effects. The derivative of the resulting stress of a transversely isotropic material to strain yields

$$\frac{\mathrm{d}\boldsymbol{\sigma}}{\mathrm{d}\boldsymbol{\varepsilon}} = \frac{\mathrm{d}\boldsymbol{C}_{\mathrm{D}}\boldsymbol{\varepsilon}_{\mathrm{el}}}{\mathrm{d}\boldsymbol{\varepsilon}} = \frac{\mathrm{d}\boldsymbol{C}_{\mathrm{D}}}{\mathrm{d}\boldsymbol{\varepsilon}}\boldsymbol{\varepsilon}_{\mathrm{el}} + \boldsymbol{C}_{\mathrm{D}}\frac{\mathrm{d}\boldsymbol{\varepsilon}_{\mathrm{el}}}{\mathrm{d}\boldsymbol{\varepsilon}}. \tag{A.129}$$

To determine the derivative of the elastic strain $\boldsymbol{\varepsilon}_{\mathrm{el}}$ its definition is used $\boldsymbol{\varepsilon}_{\mathrm{el}} = \boldsymbol{\varepsilon} - \boldsymbol{\varepsilon}_{\mathrm{pl}}$, where only the plastic strain increment is dependent on the current strain. Therefore, the derivative is given as

$$\frac{\mathrm{d}\boldsymbol{\varepsilon}_{\mathrm{el}}}{\mathrm{d}\boldsymbol{\varepsilon}} = \boldsymbol{I} - \frac{\mathrm{d}\Delta\boldsymbol{\varepsilon}_{\mathrm{pl}}}{\mathrm{d}\boldsymbol{\varepsilon}} \tag{A.130}$$

where $\boldsymbol{I}$ is a 6×6 unity matrix and $\Delta\boldsymbol{\varepsilon}_{\mathrm{pl}}$ is the plastic strain increment rotated from the $(1, n, t)$-space into $(1, 2, 3)$-space. As for the matrix material the derivative of the plastic strain increment $\Delta\boldsymbol{\varepsilon}_{\mathrm{pl}}$ can be obtained by using Equation (3.115). The necessary derivative of the plastic corrector $\Delta\lambda_{\mathrm{ap}}$ can be obtained by derivation of Equation (3.113) to the strain $\boldsymbol{\varepsilon}$ and solving to $\mathrm{d}\Delta\lambda_{\mathrm{ap}}/\mathrm{d}\boldsymbol{\varepsilon}$. The final definition yields an expression with the following structure

$$\frac{\mathrm{d}\Delta\lambda_{\mathrm{ap}}}{\mathrm{d}\boldsymbol{\varepsilon}} = (\cdots)\frac{\mathrm{d}\hat{\sigma}_{\mathrm{n}}}{\mathrm{d}\boldsymbol{\varepsilon}} + (\cdots)\frac{\mathrm{d}\hat{\tau}_{\mathrm{n1}}}{\mathrm{d}\boldsymbol{\varepsilon}} + (\cdots)\frac{\mathrm{d}\hat{\tau}_{\mathrm{nt}}}{\mathrm{d}\boldsymbol{\varepsilon}} \tag{A.131}$$

where the derivatives $\mathrm{d}\hat{\sigma}_{\mathrm{n}}/\mathrm{d}\boldsymbol{\varepsilon}$,$\mathrm{d}\hat{\tau}_{\mathrm{n1}}/\mathrm{d}\boldsymbol{\varepsilon}$ and $\mathrm{d}\hat{\tau}_{\mathrm{nt}}/\mathrm{d}\boldsymbol{\varepsilon}$ are equal to the second, forth and sixth rows of the product $\boldsymbol{T}_{\mathrm{ap}}\boldsymbol{C}$, where $\boldsymbol{T}_{\mathrm{ap}}$ is a 6×6 rotation matrix using θ_{ap} to rotate the initial stress vector $\boldsymbol{\sigma}$ to obtain $\boldsymbol{\sigma}_{\mathrm{ap}}$.

On other hand the derivative of $\boldsymbol{C}_\mathrm{D}$ can be separated into two parts which are dependent on the strain $\boldsymbol{\varepsilon}$: the E_1 modulus (and therefore of ν_{12}) and the damage variables d_i. Therefore, the derivative results to

$$\frac{\mathrm{d}\boldsymbol{C}_\mathrm{D}}{\mathrm{d}\boldsymbol{\varepsilon}} = \frac{\mathrm{d}\boldsymbol{C}_\mathrm{D}}{\mathrm{d}E_1}\frac{\mathrm{d}E_1}{\mathrm{d}\boldsymbol{\varepsilon}} + \frac{\mathrm{d}\boldsymbol{C}_\mathrm{D}}{\mathrm{d}\nu_{12}}\frac{\mathrm{d}\nu_{12}}{\mathrm{d}\boldsymbol{\varepsilon}} + \sum_i \frac{\mathrm{d}\boldsymbol{C}_\mathrm{D}}{\mathrm{d}d_i}\frac{\mathrm{d}d_i}{\mathrm{d}\boldsymbol{\varepsilon}} \tag{A.132}$$

for $i \in \{1, 2, 3, 12, 13, 23\}$ and where ${}^{\mathrm{d}\nu_{12}}/_{\mathrm{d}\boldsymbol{\varepsilon}}$ is also a function of E_1 and is given in Equation (A.73). It should be noted that the damage variables d_1, d_2 and d_3 are dependent on the loading direction as shown in Section 3.5.3 and the corresponding derivatives result from the use of Macaulay bracket operator. Since the damage variable $d_1^\pm$ is a function of $f_\mathrm{FF}^\pm$ (which is self a function of the $\hat{\sigma}_{11}$ stress) the corresponding derivative yields

$$\frac{\mathrm{d}d_1^\pm}{\mathrm{d}\boldsymbol{\varepsilon}} = \frac{\mathrm{d}d_1^\pm}{\mathrm{d}f_\mathrm{FF}^\pm}\frac{\mathrm{d}f_\mathrm{FF}^\pm}{\mathrm{d}\hat{\sigma}_{11}}\frac{\mathrm{d}\hat{\sigma}_{11}}{\mathrm{d}\boldsymbol{\varepsilon}} \tag{A.133}$$

where the distinction between positive and negative damage is obtained by using Equations (3.136) to (3.137). While the damage variable d_{23} remains zero as discussed in Section 3.5.3 and its derivative is also zero, the derivatives of the remaining damage variables are all functions of d_n and f_IFF

$$\frac{\mathrm{d}d_i}{\mathrm{d}\boldsymbol{\varepsilon}} = \frac{\mathrm{d}d_i}{\mathrm{d}d_\mathrm{n}}\frac{\mathrm{d}d_\mathrm{n}}{\mathrm{d}f_\mathrm{IFF}}\frac{\mathrm{d}f_\mathrm{IFF}}{\mathrm{d}\tilde{\boldsymbol{\sigma}}}\frac{\mathrm{d}\tilde{\boldsymbol{\sigma}}}{\mathrm{d}\boldsymbol{\varepsilon}} \tag{A.134}$$

for $i \in \{2, 3, 12, 13\}$ and since $\tilde{\boldsymbol{\sigma}} = \hat{\boldsymbol{\sigma}} - \boldsymbol{C}\Delta\boldsymbol{\varepsilon}_\mathrm{pl}$ the corresponding derivative is given by

$$\frac{\mathrm{d}\tilde{\boldsymbol{\sigma}}}{\mathrm{d}\boldsymbol{\varepsilon}} = \boldsymbol{C} + \frac{\mathrm{d}\boldsymbol{C}}{\mathrm{d}\boldsymbol{\varepsilon}}\boldsymbol{\varepsilon} - \left(\frac{\mathrm{d}\boldsymbol{C}}{\mathrm{d}\boldsymbol{\varepsilon}}\Delta\boldsymbol{\varepsilon}_\mathrm{pl} + \boldsymbol{C}\frac{\mathrm{d}\Delta\boldsymbol{\varepsilon}_\mathrm{pl}}{\mathrm{d}\boldsymbol{\varepsilon}}\right). \tag{A.135}$$

Since the only strain dependent parameters of the trial material stiffness $\boldsymbol{C}$ are E_1 and ν_{12}, the corresponding derivative can be obtained as previously described. If the results are plugged into Equation (A.129) the fully defined consistent tangent operator of the transversely isotropic material is obtained.

By considering draping effects like fiber volume content or waviness, the tangent operator of the transversely isotropic material can be utilized. If no waviness is present and only the fiber volume content changes, the derivative of the transversely isotropic stress corresponds to the required tangent operator. However, in case of waviness the applied strain needs to be rotated to the misalignment angles. In every time increment a strain increment $\Delta\boldsymbol{\varepsilon}$ is calculated and added to the previously present strain $\boldsymbol{\varepsilon}^{\mathrm{t}}$. The sum of both represents the applied effective strain $\boldsymbol{\varepsilon}_{\mathrm{x}}$ on the homogenized volume with present waviness. The resulting stress, if waviness is present, is given by Equation (3.179). The corresponding derivative is then defined as

$$\frac{\mathrm{d}\boldsymbol{\sigma}_{\mathrm{x}}}{\mathrm{d}\boldsymbol{\varepsilon}_{\mathrm{x}}} = \frac{1}{2}\left(\frac{\mathrm{d}\boldsymbol{\sigma}_1^{\mathrm{x}}}{\mathrm{d}\boldsymbol{\varepsilon}_{\mathrm{x}}} + \frac{\mathrm{d}\boldsymbol{\sigma}_2^{\mathrm{x}}}{\mathrm{d}\boldsymbol{\varepsilon}_{\mathrm{x}}}\right). \tag{A.136}$$

Using Equation (3.180) both derivatives ${}^{\mathrm{d}\boldsymbol{\sigma}_1^{\mathrm{x}}}/{\boldsymbol{\varepsilon}_{\mathrm{x}}}$ and ${}^{\mathrm{d}\boldsymbol{\sigma}_2^{\mathrm{x}}}/{\boldsymbol{\varepsilon}_{\mathrm{x}}}$ for a linear elastic behavior of the transversely isotropic material can be obtained. However, during loading nonlinearity occurs and needs to be considered. Luckily such behavior is already captured by the tangent operator of the transversely isotropic material (cf. Equation (A.129)). Therefore, the derivative of $\boldsymbol{\sigma}_1^{\mathrm{x}}$ (or $\boldsymbol{\sigma}_2^{\mathrm{x}}$ respectively) in vector form is given by

$$\frac{\mathrm{d}\boldsymbol{\sigma}_1^{\mathrm{x}}}{\mathrm{d}\boldsymbol{\varepsilon}_{\mathrm{x}}} = \boldsymbol{T}_1\frac{\mathrm{d}\boldsymbol{\sigma}}{\mathrm{d}\boldsymbol{\varepsilon}}\frac{\mathrm{d}\boldsymbol{\varepsilon}}{\mathrm{d}\boldsymbol{\varepsilon}_{\mathrm{x}}} = \boldsymbol{T}_1\frac{\mathrm{d}\boldsymbol{\sigma}}{\mathrm{d}\boldsymbol{\varepsilon}}\boldsymbol{S}\tilde{\boldsymbol{T}}_1\bar{\boldsymbol{C}} \tag{A.137}$$

where $\boldsymbol{T}_1$ and $\tilde{\boldsymbol{T}}_1$ are 6×6 rotation matrices as discussed in Section 3.5.6, $\boldsymbol{S}$ is the undamaged material compliance according to Equation (3.110) and $\bar{\boldsymbol{C}}$ is the effective material stiffness with present waviness. If the results of each derivative are plugged into Equation (A.136) the tangent operator of the constitutive model which considers draping effects is fully defined.

A.2 Impact of the Matrix on the Failure Envelopes yielding from Micromodels

A.2.1 Influence of the Matrix Strength on the Composite Strength

According to the used matrix failure criteria (see Equation (3.59)) the failure initiation is not dependent on the used coordinate system as it is based on invariants. In such case the coordinate system to evaluate the acting stresses can be arbitrary. To obtain failure points in the transverse stress vs in-plane shear plane different load combinations are applied to the micro-scale models.

By evaluating the acting matrix stresses, the only nonzero stresses are the normal stresses $(\sigma_{11}, \sigma_{22}, \sigma_{33})$ and the shear stress σ_{12}. As long as linear elastic behavior of the matrix is present, the normal stresses are also convertible into each other due to interdependence of the elasticity parameters of fiber and matrix. Therefore, the matrix failure criteria can be rewritten in terms of the transverse stress σ_{22} and σ_{12} alone. For a given tensile and compressive strength the failure shear stress can be expressed as following

$$\sigma_{12} = \left\{ \frac{1}{6} \Big(2X_\mathrm{T}X_\mathrm{C} - \Big((\sigma_{11} - \sigma_{22})^2 + (\sigma_{22} - \sigma_{33})^2 + (\sigma_{33} - \sigma_{11})^2 + 2\,(X_\mathrm{C} - X_\mathrm{T})\,(\sigma_{11} + \sigma_{22} + \sigma_{33}) \Big) \Big) \right\}^{1/2} \tag{A.138}$$

where in case of a pure shear load of the matrix $(\sigma_{11} = \sigma_{22} = \sigma_{33} = 0)$ the shear strength yields

$$S_\mathrm{m} = \sqrt{\frac{X_\mathrm{T}X_\mathrm{C}}{3}}. \tag{A.139}$$

In the $(\sigma_{22}$,$\sigma_{12})$-plane the equation above defines a parabolic curve. By setting σ_{11} and σ_{33} to zero, a midpoint of the curve at $\sigma_{22} = {}^1\!/_2\,(X_\mathrm{T} - X_\mathrm{C})$ can be defined. If the midpoint is plugged into Equation (A.138) the maximum shear stress value in the $(\sigma_{22}$,$\sigma_{12})$-plane can be determined (Figure A.2). It should be noted that the failure envelope of the matrix in Figure A.2 does not represent the failure envelope of a composite material. However, they are related as the local failure of the matrix determines the resulting shape of the failure envelope of a composite. Since the matrix tensile strength is smaller as the compressive strength, the shear stress at the midpoint $\sigma_{12}^{(\mathrm{max})}$ is larger as the shear strength itself. Such failure envelope is comparable with the one for composites (cf. Figure 3.26). The ratio between the maximum shear stress and shear strength $\sigma_{12}^{(\mathrm{max})}/S_\mathrm{m}$ is an indicator how the tensile and compressive strength are related. In case of an increasing compressive strength or a decreasing tensile strength the ratio will increase. It is obvious that if both strength values are equal the ratio yields one. In order to analyze how this ratio affects the shape of the composite failure envelope, the matrix strength has been varied. For fixed matrix tensile strength values $(X_\mathrm{T} = \{75\,\mathrm{MPa}, 87\,\mathrm{MPa}, 105\,\mathrm{MPa}, 123\,\mathrm{MPa}\})$, the corresponding compressive strength values are determined from the $\sigma_{12}^{(\mathrm{max})}/S_\mathrm{m} = \{1.05, 1.1, 1.15, 1.2, 1.25\}$ ratios. For each parameter combination several load combinations are applied

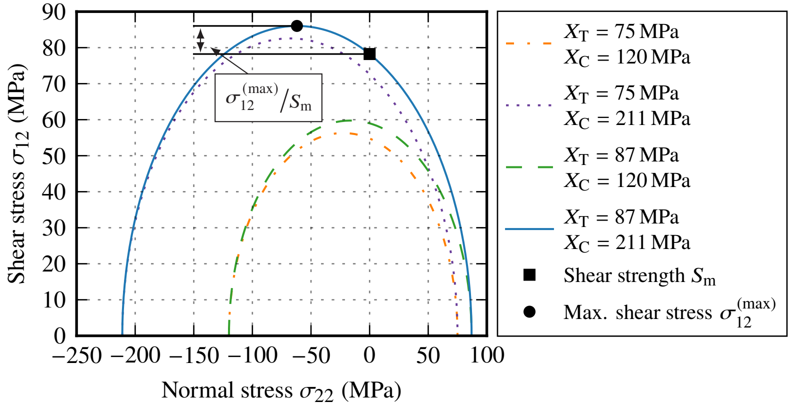

Figure A.2: Matrix failure envelope in the (σ_{22},σ_{12})-plane for different matrix strength values

to achieve different failure points in the (σ_{22}, σ_{12})-plane. All models have a fiber volume content of around 60 %. Besides the strength values all material parameters from Tables A.3 and A.7 are not changed. The obtained results are given in Figure A.3. For all failure envelopes several similarities can be observed. For example, by increasing the $\sigma_{12}^{(\max)}/S_m$ ratio, the slope of the curve at negative σ_{22} values increases. With increasing matrix tensile strength values (cf. Figure A.3c and A.3d) the impact on the slope at $\sigma_{12}^{(\max)}/S_m = 1.05$, which corresponds to the lower value of the compressive strength of the matrix, continues to decrease. By increasing the $\sigma_{12}^{(\max)}/S_m$ ratio, the obtained compressive strength Y_C of the composite increases while the tensile strength Y_T decreases (cf. Figure A.4). Although the compressive strength of the matrix is more than doubled for a constant matrix tensile strength, it has not the same effect on the resulting compressive strength of the composite. Similar observations can be made in regard to the yielding tensile strengths. Furthermore, it can be observed that with increasing matrix tensile strength values, the band of the obtained composite strength values narrow down. In conclusion, it can be seen that the slope of the failure envelope in the mode B region is highly affected by the combination of the matrix strength values. The percentual increase of the matrix strength values does not correlate directly with the resulting composite failure strength values. If additionally the interface between fiber matrix

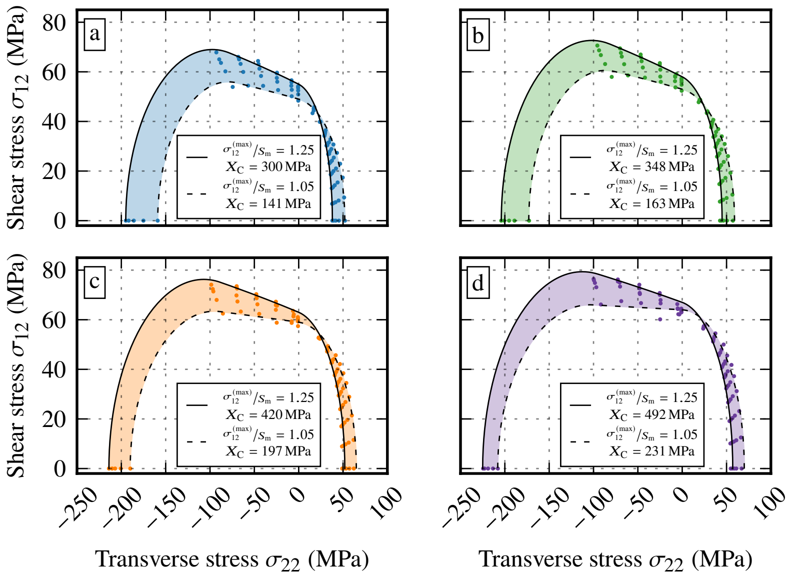

Figure A.3: Failure envelopes for unidirectional composites yielding from micro-scale models for different matrix strength values: (a) $X_T = 75$ MPa, (b) $X_T = 87$ MPa, (c) $X_T = 105$ MPa and (d) $X_T = 123$ MPa

would be considered, inducing a transverse failure due to interface failure, the resulting transverse tensile strength Y_T would be even lower. In the end the usage of micro-scale models to predict composite failure envelopes becomes even more a challenge.

A.2.2 Influence of the Matrix Energy Release Rate on the Composite Strength

In addition to the obvious impact of the matrix strengths on the resulting composite strengths and the failure envelope, the influence of the energy release rate is equally crucial. Based on the previous results, the energy release rate is varied and the resulting composite strength is investigated. The chosen

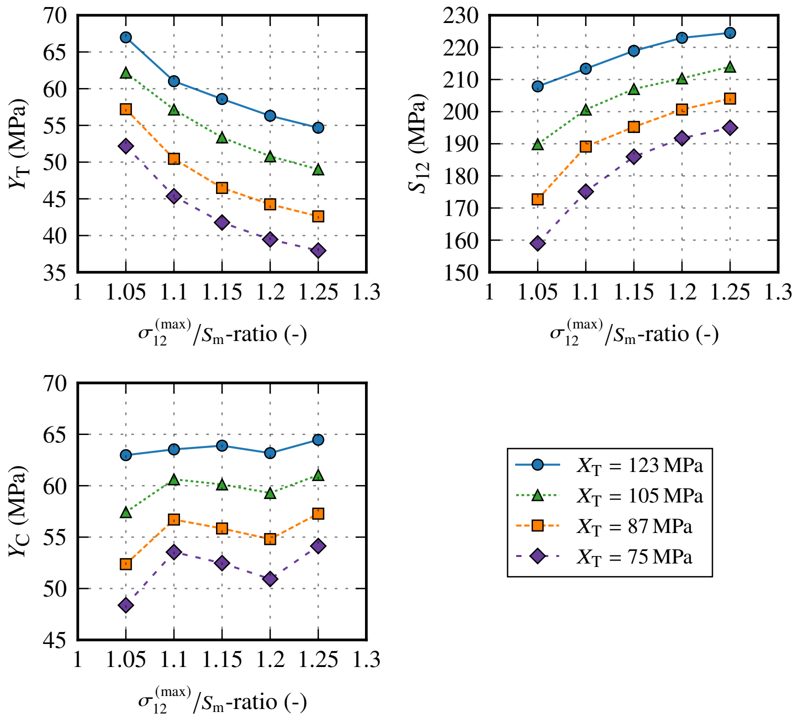

Figure A.4: Resulting composite strength values from micro-scale models at different $\sigma_{12}^{(max)}/S_m$-ratios and matrix strength values X_T

matrix strengths are $X_T = 87\,\mathrm{MPa}$ and $X_C = 257\,\mathrm{MPa}$, which corresponds to a $\sigma_{12}^{(max)}/S_m$-ratio of 1.15. The numerical results are summarized in Figure A.5. As expected, the composite strengths increase with increasing energy release rate. However, the increase is nonlinear. For example, the transverse tensile strength Y_T increases by just one megapascal with a tenfold increase in the energy release rate from $G_f = 0.1\,\mathrm{J\,m^{-2}}$ to $G_f = 1\,\mathrm{J\,m^{-2}}$. The reason for this lies in used damage model. As the energy release rate increases, the damage will leads to a constant stress (see Section 3.3.2.4). Therefore, for any combination of matrix strengths X_T and X_C, above a certain value for the energy release rate, no increase in composite strength is achieved. On the

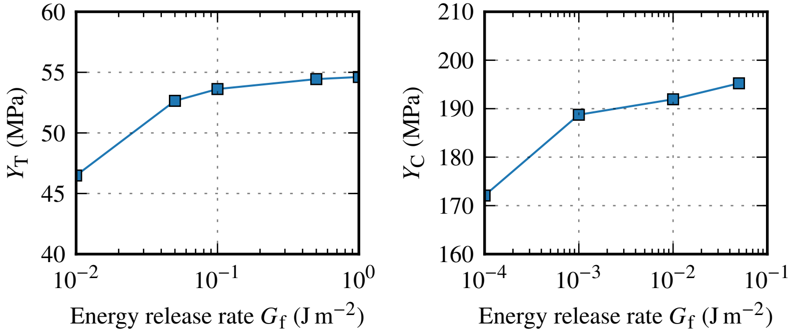

Figure A.5: Resulting composite strength values Y_T and Y_C from micro-scale models at different energy release rates

other hand, the composite strength decreases drastically with decreasing energy release rate. Taking into account that the energy release rates determined in the experiments for isotropic materials are subject to a natural scatter, this variation in the simulation can lead to considerable differences in the resulting composite strengths. Thus, the choice of material parameters for the matrix is very dominant in determining the composite strengths. However, based on the numerical results a most appropriate set of material parameters can be identified by varying the different matrix strengths and energy release rates to perform a virtual material characterization from the composite.

A.3 Material Parameters

A.3.1 Matrix Material Parameters

Table A.3: Matrix elastic material properties and strength values

Young's modulus E /GPa	Poisson's ratio ν /–	Tensile strength X_T /MPa	Compressive strength X_C /MPa
2.8	0.435	87	211

Table A.4: Plasticity parameters for the matrix under tensile loads

Coupling term	Yield onset	Voce parameters		Swift parameters	
m_t /–	$\bar{\sigma}_{0t}$ /MPa	$\bar{\sigma}_{st}$ /MPa	H_{0t} /GPa	A_t /MPa	n_t /–
0.915	18.61	69.26	33.92	187.28	0.251

Table A.5: Plasticity parameters for the matrix under compression loads

Coupling term	Yield onset	Voce parameters		Swift parameters	
m_c /–	$\bar{\sigma}_{0c}$ /MPa	$\bar{\sigma}_{sc}$ /MPa	H_{0c} /GPa	A_c /MPa	n_c /–
0.852	36.47	121	73.62	439.17	0.481

Table A.6: Rate dependent plasticitiy parameters of the matrix and the direction-dependent energy release rates

Perzyna parameters		Damage parameters	
μ /s	h /–	G_f^+ /J m^{-2}	G_f^- /J m^{-2}
7.956	0.289	50	10

A.3.2 Fiber Material Parameters

Table A.7: Fiber elastic material properties and strength values

Material parameter		Value
Static Young's modulus fiber direction	$E_1^{\mathrm{f,init}}$ /GPa	200
Young's modulus fiber direction slope	m_{f} /TPa	6.2 [61]
Young's modulus transverse direction	E_2^{f} /GPa	19
Poisson's ratio 12-plane	ν_{12}^{f} /–	0.2
Shear modulus 12-plane	G_{12}^{f} /GPa	22.5
Poisson's ratio 23-plane	ν_{23}^{f} /–	0.4
Tensile strength	$X_{\mathrm{T}}^{\mathrm{f}}$ /MPa	3000
Compressive strength	$X_{\mathrm{C}}^{\mathrm{f}}$ /MPa	3000
Tensile energy release rate	G_{f}^{+} /J m^{-2}	30
Compressive energy release rate	G_{f}^{-} /J m^{-2}	30

A.3.3 Composite Material Parameters

Table A.8: Linear elasticity material parameters

Material parameter		Value
Matrix Young's modulus	E_{m} /GPa	2.8
Matrix Poisson's ratio	ν_{m} /–	0.435
Fiber longitudinal static modulus	E_1^{f} /GPa	178
Fiber longitudinal modulus slope	$\mathrm{d}E_1/\mathrm{d}\varepsilon_{11}$ /TPa	2.15
Fiber transverse modulus	E_2^{f} /GPa	19
Fiber Poisson's ratio 12-plane	ν_{12}^{f} /–	0.26
Fiber Shear modulus 12-plane	G_{12}^{f} /GPa	22.5
Fiber Poisson's ratio 23-plane	ν_{23}^{f} /–	0.4
Halpin-Tsai transverse modulus parameter	ζ_{E_2} /–	2.5
Halpin-Tsai in-plane shear modulus parameter	$\zeta_{G_{12}}$ /–	2.53
Halpin-Tsai out-of-plane shear modulus parameter	$\zeta_{G_{23}}$ /–	1.3

Table A.9: Plasticity model parameters

Material parameter		Value
Yield surface slope	α_{ap} /–	0.175
Ellipticity of the yield surface	e_{ap} /–	0.95
Dilatancy coefficient	β_{ap} /–	0
Flow rate parameter	f_{ap} /–	1.5
Yield onset	$\tau_{\mathrm{y}}^{\mathrm{init}}$ /MPa	15.94
Voce saturation flow stress	τ_{s} /GPa	45.87
Voce hardening modulus	$H_{0\mathrm{t,c}}$ /TPa	9.99
Swift hardening rate	$A_{\mathrm{t,c}}$ /MPa	108.57
Swift hardening decrement	$n_{\mathrm{t,c}}$ /–	0.207
Voce-Swift balance weight parameter	$m_{\mathrm{t,c}}$ /–	0.999

Table A.10: Failure and damage parameters

Material parameter		Value
Fiber tensile strength	$X_{\mathrm{T}}^{\mathrm{f}}$ /MPa	2675
Fiber maximum longitudinal tensile strain	$\varepsilon_{11,\max}^{\mathrm{f}}$ /%	2.16
Fiber compressive strength ratio parameter	$\bar{\phi}/\gamma_{\mathrm{y}}$ /–	1.346
Transverse tensile strength	Y_{T} /MPa	60
Transverse compressive strength at $\varphi = 50\,\%$	$Y_{\mathrm{C}}\vert_{\varphi=50\,\%}$ /MPa	151.4
Transverse compressive strength slope over FVC	$\mathrm{d}Y_{\mathrm{C}}/\mathrm{d}\varphi$ /MPa $\%^{-1}$	308
Shear strength at $\varphi = 50\,\%$	$S_{12}\vert_{\varphi=50\,\%}$ /MPa	66.4
Shear strength slope over FVC	$\mathrm{d}S_{12}/\mathrm{d}\varphi$ /MPa $\%^{-1}$	51.2
Incline parameter at $\varphi = 50\,\%$	$p\vert_{\varphi=50\,\%}$ /–	0.31
Incline parameter slope over FVC	$\mathrm{d}p/\mathrm{d}\varphi$ /$\%^{-1}$	0.569
Parameter impact of f_{FF} on f_{IFF}	m /-	0
Parameter impact of f_{FF} on f_{IFF}	s /-	0
Tensile energy release rate in fiber direction	G_{d}^{+} /kJ m^{-2}	240
Compressive energy release rate in fiber direction	G_{d}^{-} /kJ m^{-2}	30

A.4 Further Numerical Firewall Results

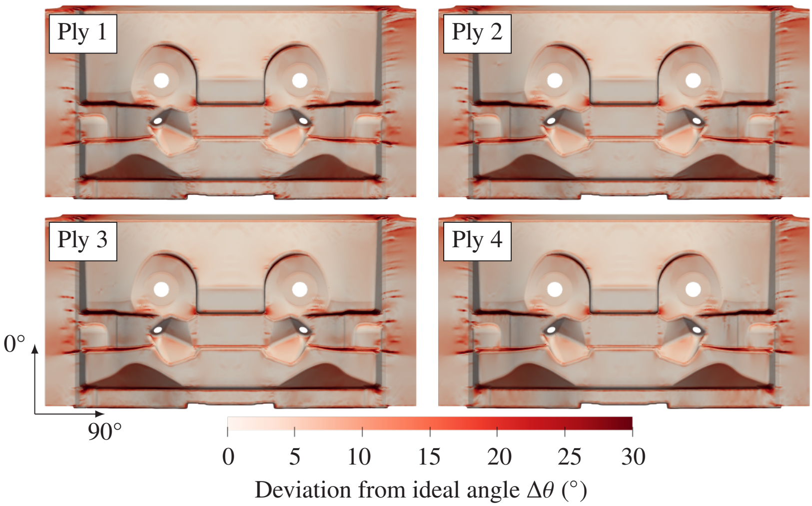

Figure A.6: Deviation of the ideal fiber direction angle for each ply of the (0°_{4}) unidirectional laminate

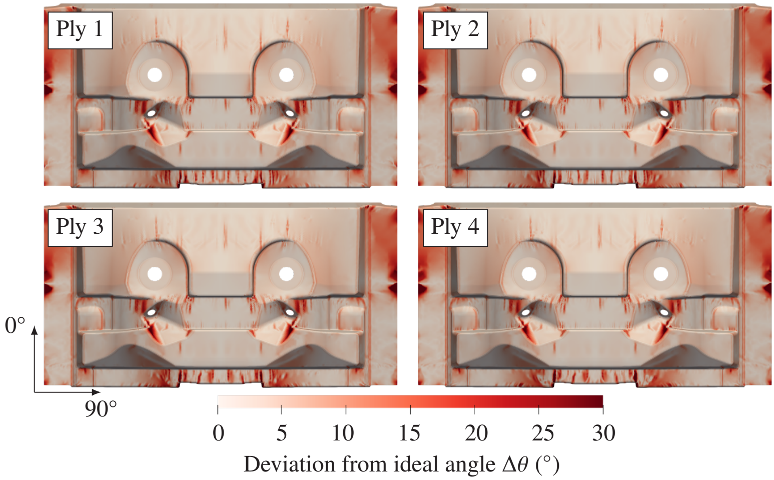

Figure A.7: Deviation of the ideal fiber direction angle for each ply of the (90°_4) unidirectional laminate

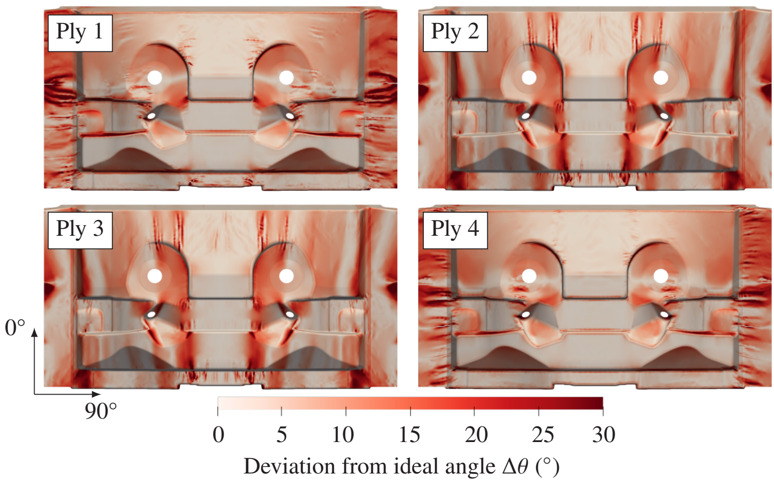

Figure A.8: Deviation of the ideal fiber direction angle for each ply of the $(0^\circ/90^\circ)|_s$ cross-ply laminate

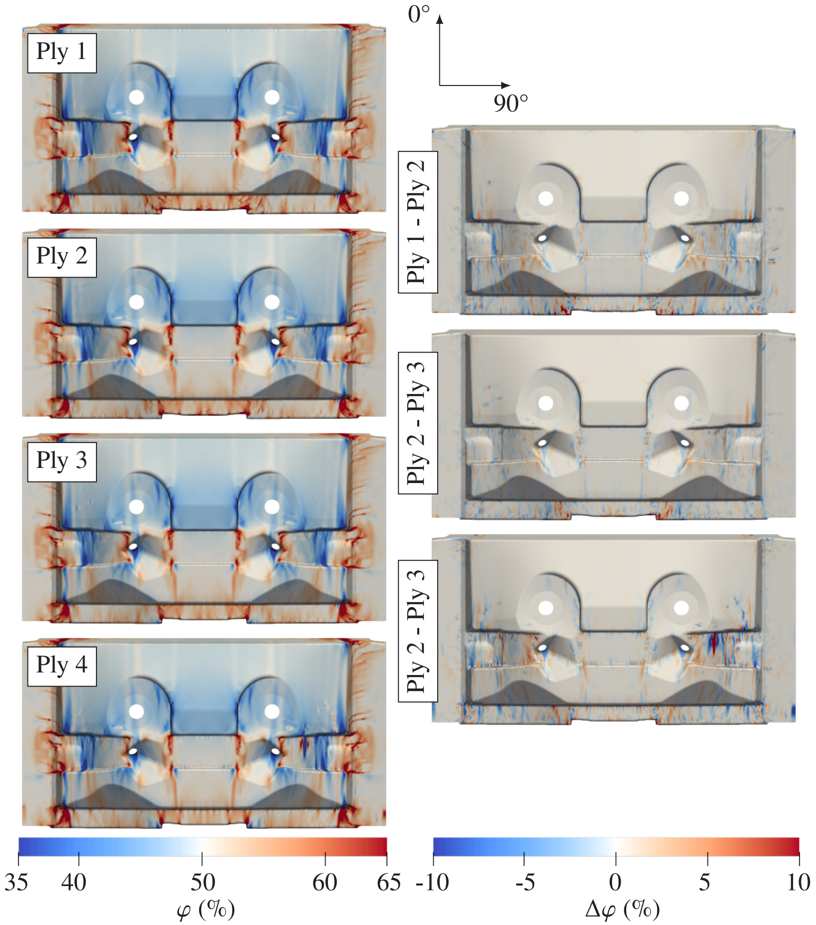

Figure A.9: Distribution of the fiber volume content and the difference between adjacent layers for a (0°_4) unidirectional laminate

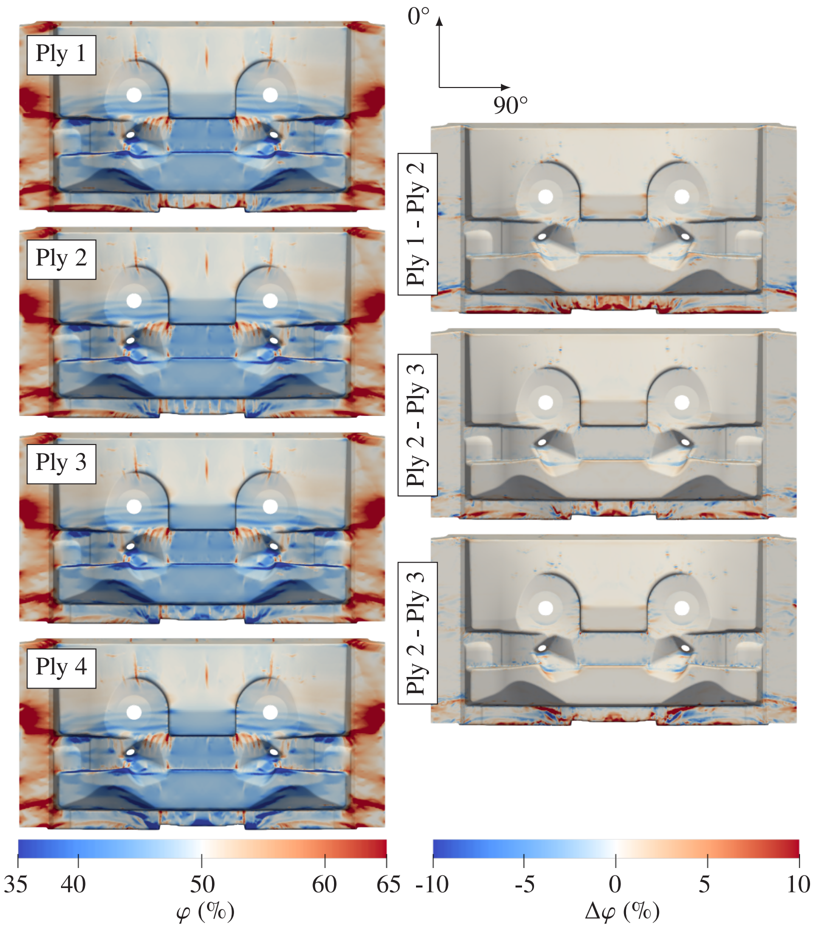

Figure A.10: Distribution of the fiber volume content and the difference between adjacent layers for a (90°_4) unidirectional laminate

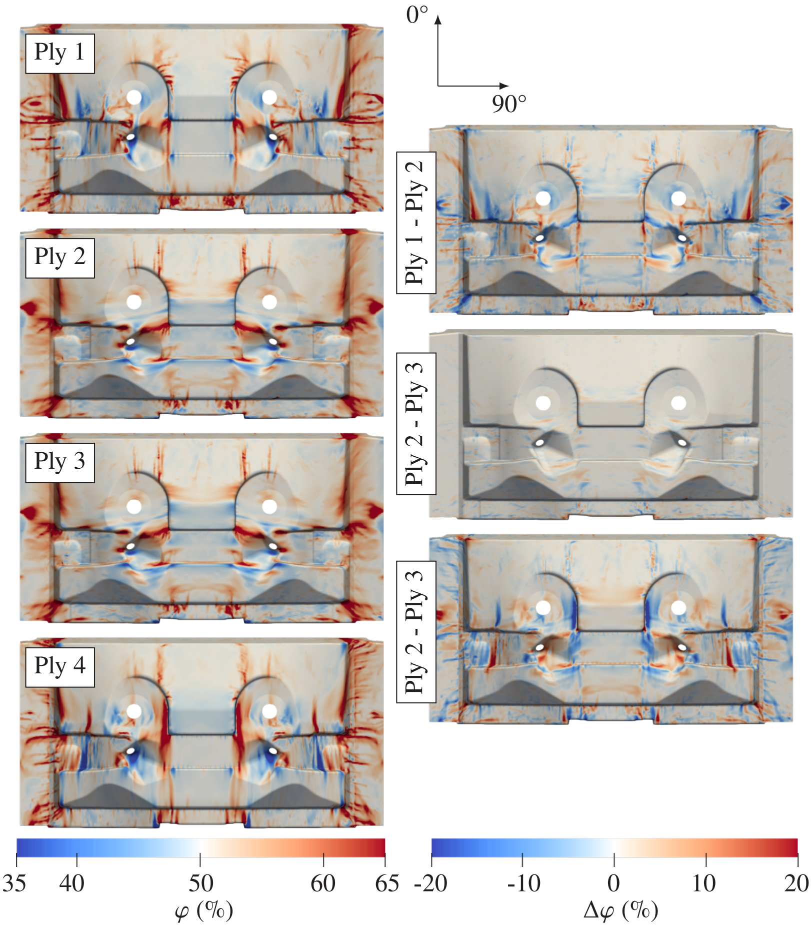

Figure A.11: Distribution of the fiber volume content and the difference between adjacent layers for a $(0°/90°)|_s$ cross-ply laminate

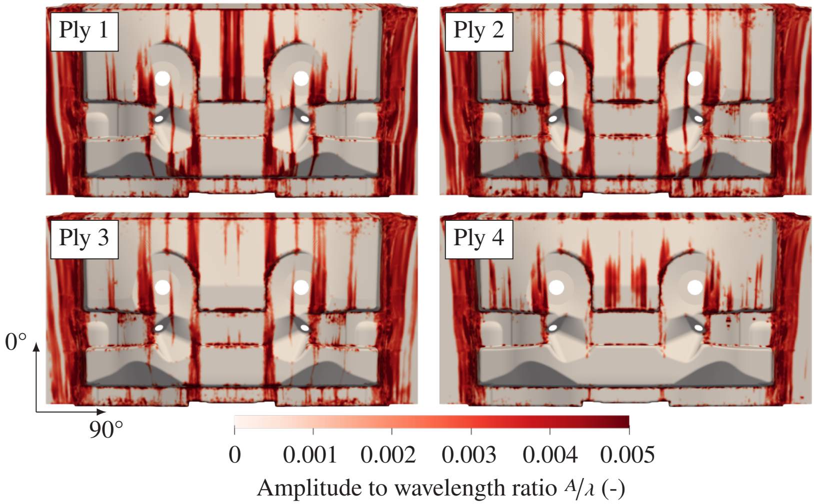

Figure A.12: Areas with a predicted waviness for a (0°_4) unidirectional laminate

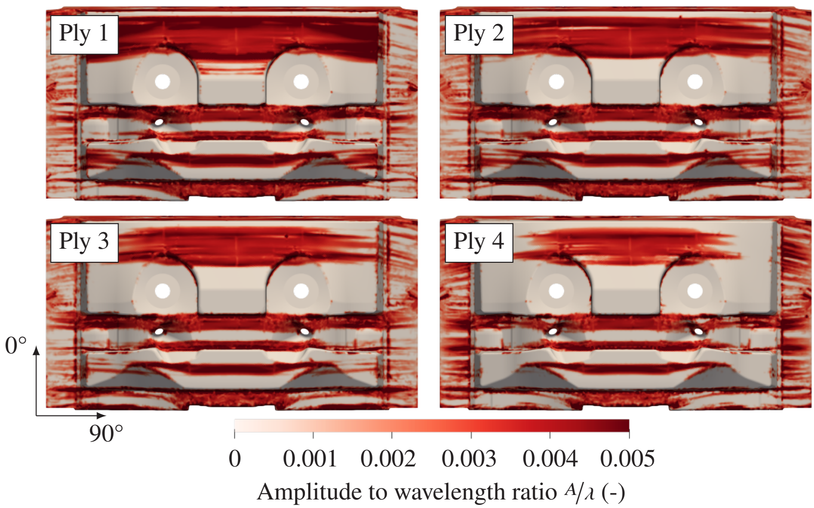

Figure A.13: Areas with a predicted waviness for a (90°_4) unidirectional laminate

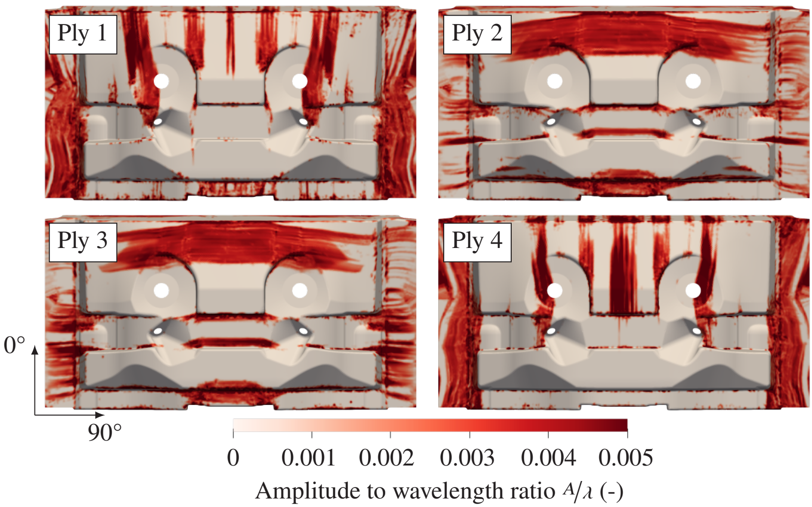

Figure A.14: Areas with a predicted waviness for a $(0°/90°)|_s$ cross-ply laminate

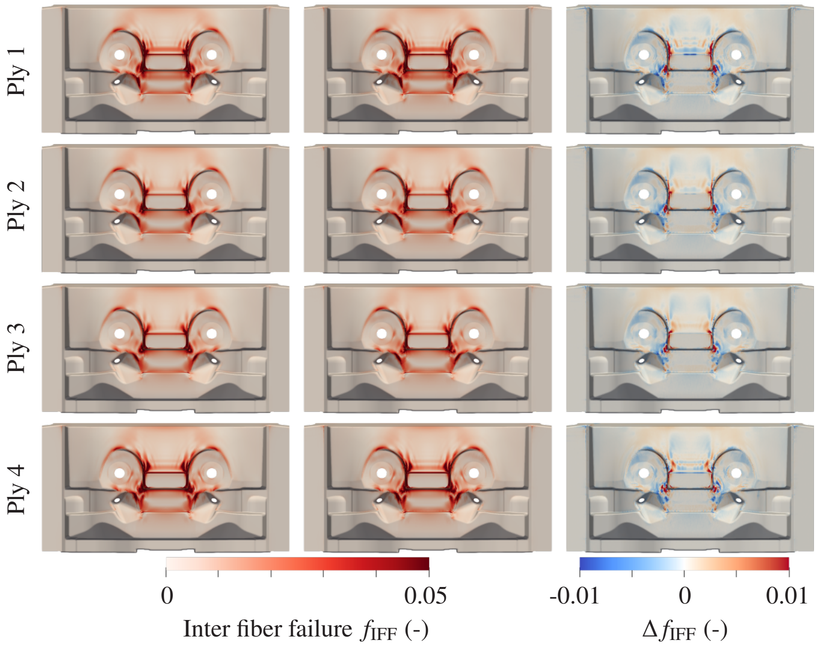

Figure A.15: Distribution of inter-fiber failure if the draping effects are neglected (left) or considered (middle) and the corresponding difference of the inter-fiber failure criterion for a (0°_4) unidirectional laminate

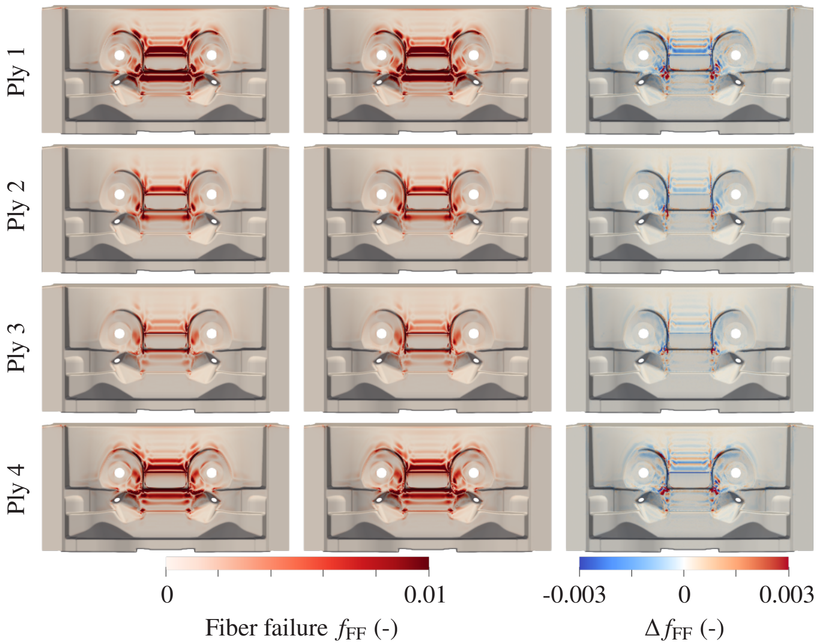

Figure A.16: Distribution of fiber failure if the draping effects are neglected (left) or considered (middle) and the corresponding difference of the inter-fiber failure criterion for a (0°_4) unidirectional laminate

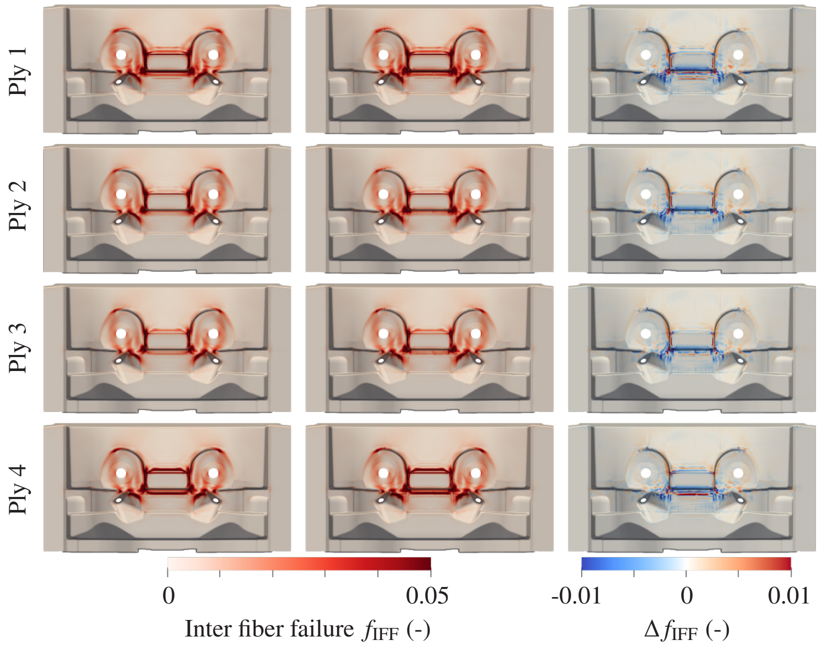

Figure A.17: Distribution of inter-fiber failure if the draping effects are neglected (left) or considered (middle) and the corresponding difference of the inter-fiber failure criterion for a (90°_4) unidirectional laminate

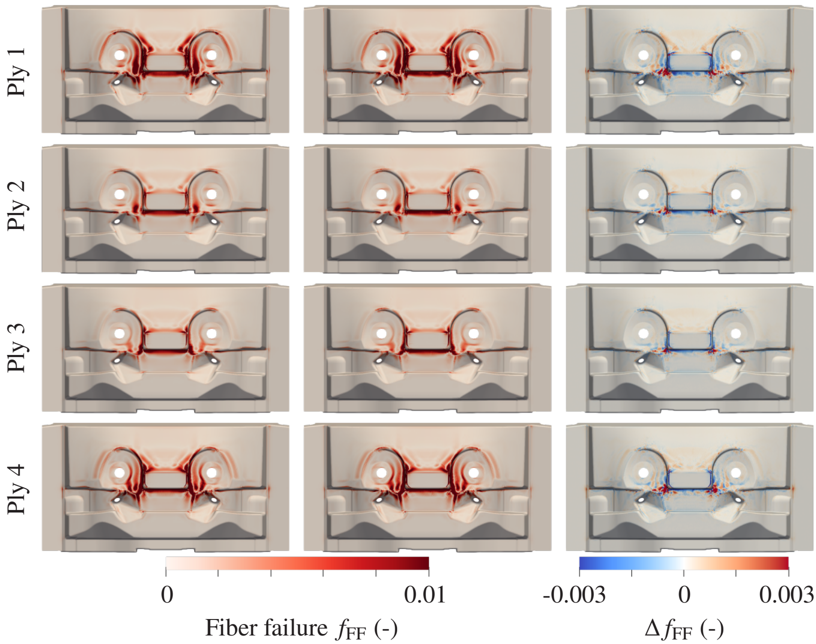

Figure A.18: Distribution of fiber failure if the draping effects are neglected (left) or considered (middle) and the corresponding difference of the inter-fiber failure criterion for a (0°_4) unidirectional laminate

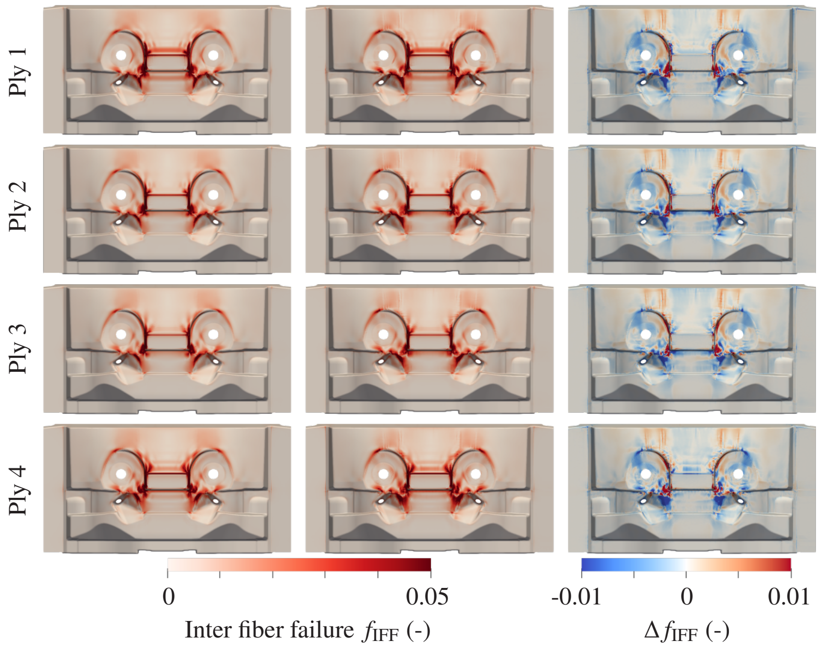

Figure A.19: Distribution of inter-fiber failure if the draping effects are neglected (left) or considered (middle) and the corresponding difference of the inter-fiber failure criterion for a $(0°/90°)|_s$ cross-ply laminate

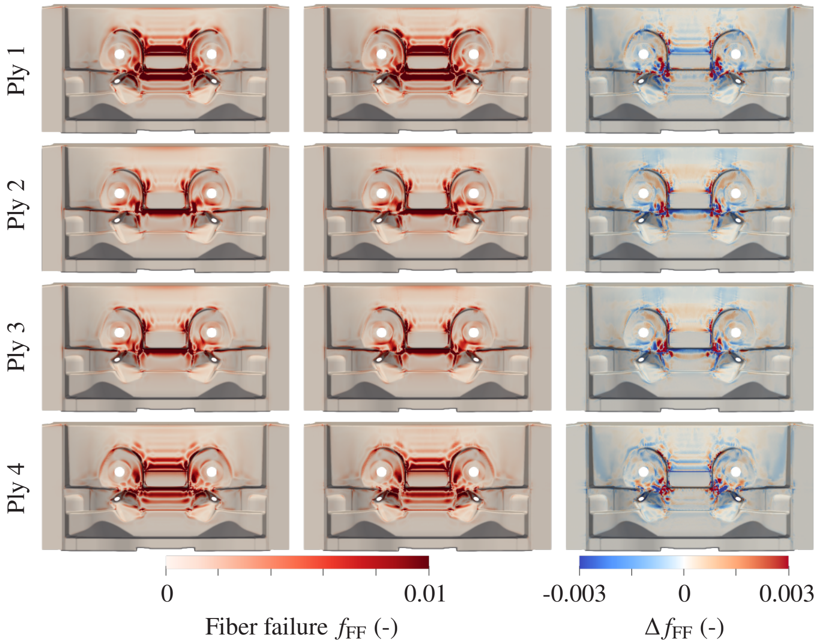

Figure A.20: Distribution of fiber failure if the draping effects are neglected (left) or considered (middle) and the corresponding difference of the inter-fiber failure criterion for a $(0°/90°)|_s$ cross-ply laminate

Technical Datasheet

ZOLTEK™ PX35 Uni-Directional Fabrics

Stitch-Bonded Uni-Directional Carbon Fabrics

DESCRIPTION

ZOLTEK PX35 Stitch-Bonded Uni-Directional Carbon Fabrics are produced from our ZOLTEK PX35 50K Continuous Tow Carbon Fiber. Unique fiber spreading techniques are utilized to obtain a wide range of UD fabric weights for a varied set of composite part applications. Quick composite part build-up is cost effectively achieved with our diverse weight range of low-cost carbon fabric products.

MATERIAL OVERVIEW	UD150	UD200	UD300	UD400	UD500	UD600	UD900V
0° Carbon ZOLTEK'S™ PX35 50K	158	200	309	403	500	600	865
90° Glass 34 dtex	10	10	10	10	10	10	—
Polyester Veil	—	—	—	—	—	—	30
Polyester Stitch 76 dtex	6	6	6	6	6	6	5
Total Fabric Weight	182 g/m² 5.37 oz/yd²	224 g/m² 6.61 oz/yd²	333 g/m² 9.82 oz/yd²	419 g/m² 12.36 oz/yd²	516 g/m² 15.22 oz/yd²	624 g/m² 18.40 oz/yd²	900 g/m² 26.54 oz/yd²

Average Values Shown

**Epoxy resin binder available upon customer request.*

FABRIC CONSTRUCTION	UD150	UD200	UD300	UD400	UD500	UD600	UD900V
Stitch Length	A variety of stitch lengths are available to meet application requirements.						
Stitch Pattern	A variety of stitch patterns are available to meet application requirements.						
Cured Thickness/Ply	.21 mm	.25 mm	.37 mm	.46 mm	.57 mm	.69 mm	1.00 mm
Roll Width	30 cm - 61 cm - 122 cm						122 cm
Roll Length	100 m				50 m		30 m

Average Values Shown

The properties listed in this datasheet do not constitute any warranty or guarantee of values. This information should only used for the purposes of material selection. Please contact us for more details.

ZOLTEK™ PX35

ZOLTEK Corporation | 3101 McKelvey Road | Bridgeton, MO 63044
P: 314-291-5110 | F: 314-291-8536 | www.zoltek.com

Technical Datasheet

ZOLTEK™ PX35 Uni-Directional Fabrics

Stitch-Bonded Uni-Directional Carbon Fabrics

COMPOSITE PROPERTIES	SI	US	METHOD
Tensile Strength	1,600 MPa	232 ksi	DIN EN ISO 527
Tensile Modulus	120 GPa	17.4 msi	DIN EN ISO 527
Compressive Strength	1,000 MPa	145 ksi	ASTM D694
Compressive Modulus	110 GPa	16.0 msi	ASTM D695

Typical Fiber Volume Fraction (FVF) is 55%.
Standard Epoxy Resin System

The properties listed in this datasheet do not constitute any warranty or guarantee of values. This information should only used for the purposes of material selection. Please contact us for more details.

TYPICAL PACKAGING

Wound on cardboard cone, sealed in polyethylene bag, and placed in cardboard box. Rolls stacked horizontally on pallets when shipping.

+ Requirements other than standard widths and roll lengths should be specified by purchase order.

APPROVAL

DNV-GL has granted approval to ZOLTEK PX35 Uni-Directional Fabrics for use in wind energy applications.

DNV·GL

Approval No. WP 1030011 HH

CERTIFICATION

ZOLTEK PX35 Fabrics are manufactured in accordance with ZOLTEK'S written and published data. A Certificate of Conformance is provided with each shipment.

SAFETY

Obtain, read, and understand the Material Safety Data Sheet (SDS) before use of this or any other ZOLTEK product.

June 07, 2017

ZOLTEK
Toray Group

CERTIFICATE OF ANALYSIS

KARLSRUHER INSTITUT FÜR TECHNOLOGIE
GERMANY - KARLSRUHE
FAST-LBT, R 115
76131

ATTN: Quality Assurance / Gabriele Hentschel

This document certifies that the content of this shipment have been manufactured in accordance with Zoltek's written and published data.

A) **IDENTIFICATION**

Product Description	ZOLTEK™ PX35 UD Fabric
Product Code	**PX35 UD0300-1221**
Quantity Shipped	488,00 m2
P.O. Number	400/27087350/FAST/UB
Zoltek Order Number	110029
Shipment Date	June 07, 2017
Production Date Lot# 1626017	2016.06.27-07.08

B) **MATERIAL PROPERTIES**

	Lot Avg. Acceptance	Lot Average
Lot #		1626017
Quantity per Lot (m2)		488,0
Total Areal wt.(g/m^2)	315-349	334
Carbon Fiber content 0° Warp (g/m^2)	294-324	309
Glass yarn content 90° (g/m^2)	6,5-11,5	9,5
Binder (g/m^2)	5-10	7,41
Width (cm)	120,5-123,5	122,3
Thickness (mm)	0,40-0,74	0,55

Szilágyi

Mrs Szilágyi
Quality Administrator

Tooling & Composites

Product Data Sheet
Version 04 / 2016

Biresin® CR170 and Biresin® CH150-3 Hardener

Composite resin system

Product Description

Biresin® CR170 resin (A) cured with Biresin® CH150-3 hardener (B) is an epoxy resin system suitable for the production of high performance fibre reinforced components by the RTM process.

Areas of Application

Biresin® CR170/CH150-3 is especially suited to injection processes due to its viscosity range and reactivity. It can be used in areas where short cycle times are required, perhaps in the production of automotive parts.

Features / Advantages

- Reduced cycle times for RTM processing are possible with this resin system especially where dynamic curing cycles are used.
- Glass transition temperatures up to 143°C are possible depending on cure conditions

Physical Data		Resin (A)	Hardener (B)
Individual Components		**Biresin® CR170**	**Biresin® CH150-3**
Mixing Ratio, parts by	**Weight**	100	24
Mixing Ratio, parts by	**Volume**	100	29
Colour		translucent	colourless
Viscosity, 25°C	mPa.s	~13,000	~20
Density, 25°C	g/ml	1.14	0.94
		Mixture	
Potlife, 100 g / RT, approx. values	min	60	
Mixed viscosity, 25°C, approx.	mPa.s	1,600	
Mixed viscosity, 60°C, approx.	mPa.s	160	
Mixed viscosity, 80°C, approx.	mPa.s	90	

Processing and processing properties

- The material and processing temperatures should be in the range 18 - 35°C.
- The mixing ratio must be followed accurately to obtain best results. Deviating from the correct mix ratio will lead to lower performance.
- Before demoulding precuring of at least 2 h at 60°C is recommended.
- The final mechanical and thermal values are dependent on the applied postcuring cycles.
- It is recommended to clean brushes or tools immediately after use with Sika Reinigungsmittel 5.
- Additional information is available in “Processing Instructions for Composite Resins”.

.

BUILDING TRUST

Tooling & Composites

Typical Mechanical Properties of Fully Cured Neat Resin			
Biresin® CR170 resin (A)		with hardener (B)	**Biresin® CH150-3**
Tensile strength	ISO 527	MPa	87
Tensile E-Modulus	ISO 527	MPa	2,700
Elongation at break	ISO 527	%	6.6
Flexural strength	ISO 178	MPa	133
Flexural E-Modulus	ISO 178	MPa	2,800
Compressive Strength	ISO 604	MPa	120
Density	ISO 1183	g/cm³	1.15
Shore hardness	ISO 868	-	D 84
Impact resistance	ISO 179	kJ/m²	42

Typical Thermal Properties of Cured Neat Resin (approx. values after 4 h / 140°C)			
Biresin® CR170 resin (A)		with hardener (B)	**Biresin® CH150-3**
Heat distortion temperature	ISO 75B	°C	139
Glass transition temperature	ISO 11357	°C	143

Glass Transition Temperature vs. Cure Cycle

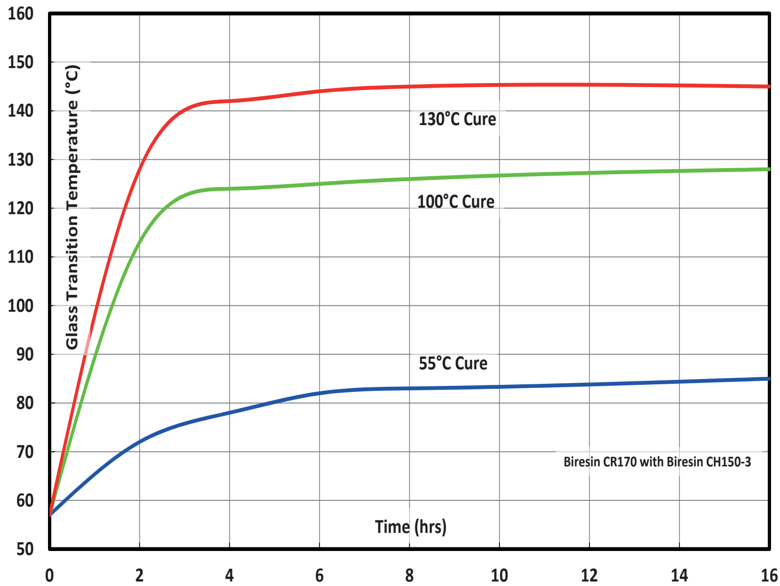

When curing a composite part, the whole of the part (including the very middle of the laminate) needs to see the cure temperature.

Packaging (net weight, kg)

Biresin® CR170 resin (A)	1,000	200		10
Biresin® CH150-3 hardener (B)	900	180	20	2.4

Storage

- Minimum shelf life of Biresin® CR170 resin (A) is 24 month and of Biresin® CH150-3 hardener (B) is 12 month under room conditions (18 - 25°C), when stored in original unopened containers.
- After prolonged storage crystallisation of resin (A) may occur. This is easily removed by warming up for a sufficient time at a minimum of 60°C.
- Containers must be closed tightly immediately after use to prevent moisture ingress. The residual material needs to be used up as soon as possible.

Health and Safety Information

For information and advice on the safe handling, storage and disposal of chemical products, users shall refer to the most recent Safety Data Sheet (SDS) containing physical, ecological, toxicological and other safety related data.

Disposal considerations

Product Recommendations: Must be disposed of in a special waste disposal unit in accordance with the corresponding regulations.
Packaging Recommendations: Completely emptied packagings can be given for recycling. Packaging that cannot be cleaned should be disposed of as product waste.

Value Bases

All technical data stated in this Product Data Sheet are based on laboratory tests. Actual measured data may vary due to circumstances beyond our control.

Legal Notice

The information, and, in particular, the recommendations relating to the application and end-use of Sika products, are given in good faith based on Sika's current knowledge and experience of the products when properly stored, handled and applied under normal conditions in accordance with Sika's recommendations. In practice, the differences in materials, substrates and actual site conditions are such that no warranty in respect of merchantability or of fitness for a particular purpose, nor any liability arising out of any legal relationship whatsoever, can be inferred either from this information, or from any written recommendations, or from any other advice offered. The user of the product must test the product's suitability for the intended application and purpose. Sika reserves the right to change the properties of its products. The proprietary rights of third parties must be observed. All orders are accepted subject to our current terms of sale and delivery. Users must always refer to the most recent issue of the local Product Data Sheet for the product concerned, copies of which will be supplied on request.

Further information available at:

Sika Deutschland GmbH
Subsidiary Bad Urach
Stuttgarter Str. 139
D - 72574 Bad Urach
Germany

Tel: +49 (0) 7125 940 492
Fax: +49 (0) 7125 940 401
Email: tooling@de.sika.com
Internet: www.sika.com

BUILDING TRUST

Bibliography

[1] Kärger L., Bernath A., Fritz F., Galkin S., Magagnato D., Oeckerath A., Schön A., and Henning F. "Development and validation of a CAE chain for unidirectional fibre reinforced composite components". In: *Composite Structures* 132 (2015), pp. 350–358.

[2] Schirmaier F. J., Dörr D., Henning F., and Kärger L. "A macroscopic approach to simulate the forming behaviour of stitched unidirectional non-crimp fabrics (UD-NCF)". In: *Composites Part A: Applied Science and Manufacturing* 102 (2017), pp. 322–335.

[3] Schirmaier F. "Experimentelle Untersuchung und Simulation des Umformverhaltens nähgewirkter unidirektionaler Kohlenstofffasergelege". German. Dissertation. Karlsruher Institut für Technologie (KIT), 2017.

[4] Kärger L., Galkin S., Dörr D., and Poppe C. "Capabilities of Macroscopic Forming Simulation for Large-Scale Forming Processes of Dry and Impregnated Textiles". In: *Procedia Manufacturing* 47 (2020), pp. 140–147.

[5] Bing Q. and Sun C. T. "Specimen size effect in off-axis compression tests of fiber composites". In: *Composites Part B: Engineering* 39.1 (2008), pp. 20–26.

[6] Kawai M., Morishita M., Satoh H., Tomura S., and Kemmochi K. "Effects of end-tab shape on strain field of unidirectional carbon/epoxy composite specimens subjected to off-axis tension". In: *Composites Part A: Applied Science and Manufacturing* 28.3 (1997), pp. 267–275.

[7] Pipes R. B. and Cole B. W. "On the Off-Axis Strength Test for Anisotropic Materials1". In: *Journal of Composite Materials* 7.2 (1973), pp. 246–256.

[8] Koerber H., Kuhn P., Ploeckl M., Otero F., Gerbaud P.-W., Rolfes R., and Camanho P. P. “Experimental characterization and constitutive modeling of the non-linear stress–strain behavior of unidirectional carbon–epoxy under high strain rate loading”. In: *Advanced Modeling and Simulation in Engineering Sciences* 5.1 (2018), p. 50.

[9] Knops M. *Analysis of failure in fiber polymer laminates: The theory of Alfred Puck*. Berlin and New York: Springer, 2008.

[10] Fuller J. D. and Wisnom M. R. “Pseudo-ductility and damage suppression in thin ply CFRP angle-ply laminates”. In: *Composites Part A: Applied Science and Manufacturing* 69 (2015), pp. 64–71.

[11] Mandel U., Taubert R., and Hinterhölzl R. “Mechanism based non-linear constitutive model for composite laminates subjected to large deformations”. In: *Composite Structures* 132 (2015), pp. 98–108.

[12] Cui H., Thomson D., Pellegrino A., Wiegand J., and Petrinic N. “Effect of strain rate and fibre rotation on the in-plane shear response of ±45° laminates in tension and compression tests”. In: *Composites Science and Technology* 135 (2016), pp. 106–115.

[13] Dumanskii A. M., Komarov V. A., Alimov M. A., and Radchenko A. A. “On the effect of fiber rotation upon deformation of carbon-fiber angle-ply laminates”. In: *Polymer Science, Series D* 10.2 (2017), pp. 197–199.

[14] Herakovich C. “Damage evolution in [±45]s laminates with fiber rotation”. In: *Composites Science and Technology* 60.15 (2000), pp. 2781–2789.

[15] Sun C. “The effect of deformation-induced change of fiber orientation on the non-linear behavior of polymeric composite laminates”. In: *Composites Science and Technology* 60.12-13 (2000), pp. 2337–2345.

[16] Taubert R. “Einfluss von nichtlinearem Materialverhalten auf die Entwicklung und Auswirkung von Zwischenfaserbrüchen in Verbundlaminaten”. Dissertation. München: Universitätsbibliothek der TU München, 2017.

[17] Schürmann H. *Konstruieren mit Faser-Kunststoff-Verbunden*. 2., bearb. und erw. Aufl. VDI. Berlin, Heidelberg, and New York, NY: Springer, 2007.

[18] Bleier A. “Prüfverfahren zur Ermittlung exakter Werkstoffkennwerte einer unidirektionalen Schicht unter besonderer Berücksichtigung physikalischer Nichtlinearitäten”. Dissertation. Aachen: RWTH Aachen University, 2011.

[19] Heidari-Rarani M., Bashandeh-Khodaei-Naeini K., and Mirkhalaf S. M. “Micromechanical modeling of the mechanical behavior of unidirectional composites – A comparative study”. In: *Journal of Reinforced Plastics and Composites* 37.16 (2018), pp. 1051–1071.

[20] Huang Z. M. “Micromechanical strength formulae of unidirectional composites”. In: *Materials Letters* 40.4 (1999), pp. 164–169.

[21] Djordjevic I., Sekulic D., and Stevanovic M. “Non-linear elastic behavior of carbon fibres of different structural and mechanical characteristic”. In: *Journal of the Serbian Chemical Society* 72.5 (2007), pp. 513–521.

[22] Djordjević I. M., Sekulić D. R., Mitrić M. N., and Stevanović M. M. “Non-Hookean Elastic Behavior and Crystallite Orientation in Carbon Fibers”. In: *Journal of Composite Materials* 44.14 (2009), pp. 1717–1727.

[23] Kant M. and Penumadu D. “Dynamic mechanical characterization for nonlinear behavior of single carbon fibers”. In: *Composites Part A: Applied Science and Manufacturing* 66 (2014), pp. 201–208.

[24] Piggott M. R. “Compressive Properties of Resins and Composites”. In: *Developments in Reinforced Plastics—4*. Ed. by Pritchard G. Vol. 56. Dordrecht: Springer Netherlands, 1984, pp. 131–163.

[25] Naik N. K. and Kumar R. S. “Compressive strength of unidirectional composites: evaluation and comparison of prediction models”. In: *Composite Structures* 46.3 (1999), pp. 299–308.

[26] Mishra A. and Naik N. K. “Inverse Micromechanical Models for Compressive Strength of Unidirectional Composites”. In: *Journal of Composite Materials* 43.10 (2009), pp. 1199–1211.

[27] Fuhr J.-P. *Schichtbasierte Modellierung von Fertigungseffekten in der Struktursimulation von Faserverbundwerkstoffen*. Luftfahrt. München: Dr. Hut, 2017.

[28] Brunbauer J. and Pinter G. “Effects of mean stress and fibre volume content on the fatigue-induced damage mechanisms in CFRP”. In: *International Journal of Fatigue* 75 (2015), pp. 28–38.

[29] Brunbauer J., Stadler H., and Pinter G. “Mechanical properties, fatigue damage and microstructure of carbon/epoxy laminates depending on fibre volume content”. In: *International Journal of Fatigue* 70 (2015), pp. 85–92.

[30] Hsiao H. M. and Daniel I. M. “Effect of fiber waviness on stiffness and strength reduction of unidirectional composites under compressive loading”. In: *Composites Science and Technology* 56.5 (1996), pp. 581–593.

[31] Adams D. O. and Bell S. J. “Compression strength reductions in composite laminates due to multiple-layer waviness”. In: *Composites Science and Technology* 53.2 (1995), pp. 207–212.

[32] Altmann A., Taubert R., Mandel U., Hinterhoelzl R., and Drechsler K. “A continuum damage model to predict the influence of ply waviness on stiffness and strength in ultra-thick unidirectional Fiber-reinforced Plastics”. In: *Journal of Composite Materials* 50.20 (2016), pp. 2739–2755.

[33] Chun H.-J., Shin J.-Y., and Daniel I. M. “Effects of material and geometric nonlinearities on the tensile and compressive behavior of composite materials with fiber waviness”. In: *Composites Science and Technology* 61.1 (2001), pp. 125–134.

[34] Karayaka M. and Kurath P. “Deformation and Failure Behavior of Woven Composite Laminates”. In: *Journal of Engineering Materials and Technology* 116.2 (1994), p. 222.

[35] Piggott M. R. “The effect of fibre waviness on the mechanical properties of unidirectional fibre composites: A review”. In: *Composites Science and Technology* 53.2 (1995), pp. 201–205.

[36] Lemanski S. L. and Sutcliffe M. “Compressive failure of finite size unidirectional composite laminates with a region of fibre waviness”. In: *Composites Part A: Applied Science and Manufacturing* 43.3 (2012), pp. 435–444.

[37] Wilhelmsson D. and Asp L. E. “A high resolution method for characterisation of fibre misalignment angles in composites”. In: *Composites Science and Technology* 165 (2018), pp. 214–221.

[38] Chou T. W. and Takahashi K. “Non-linear elastic behaviour of flexible fibre composites”. In: *Composites* 18.1 (1987), pp. 25–34.

[39] Highsmith A. L., Davis J. J., and Helms K. L. “The Influence of Fiber Waviness on the Compressive Behavior of Unidirectional Continuous Fiber Composites”. In: *Composite Materials: Testing and Design (Tenth Volume)*. Ed. by Grimes G. C. 100 Barr Harbor Drive, PO Box C700, West Conshohocken, PA 19428-2959: ASTM International, 1992, pp. 20-20–17.

[40] Hsiao H. M. and Daniel I. M. “Nonlinear Elastic Behavior of Unidirectional Composites With Fiber Waviness Under Compressive Loading”. In: *Journal of Reinforced Plastics and Composites* 118.4 (1996), p. 561.

[41] Fiedler B., Hojo M., Ochiai S., Schulte K., and Ando M. “Failure behavior of an epoxy matrix under different kinds of static loading”. In: *Composites Science and Technology* 61.11 (2001), pp. 1615–1624.

[42] Liebig W. V., Schulte K., and Fiedler B. “Hierarchical analysis of the degradation of fibre-reinforced polymers under the presence of void imperfections”. In: *Philosophical transactions. Series A, Mathematical, physical, and engineering sciences* 374.2071 (2016), p. 20150279.

[43] Eberl C. *Digital Image Correlation and Tracking*. `https://www.mathworks.com/matlabcentral/fileexchange/12413-digital-image-correlation-and-tracking`. Accessed: 2018-01-30. 2010.

[44] Blaber J., Adair B., and Antoniou A. “Ncorr: Open-Source 2D Digital Image Correlation Matlab Software”. In: *Experimental Mechanics* 55.6 (2015), pp. 1105–1122.

[45] Jones E. *Improved Digital Image Correlation (DIC)*. `https://de.mathworks.com/matlabcentral/fileexchange/43073-improved-digital-image-correlation--dic-`. Accessed: 2015-05-12. 2015.

[46] Solav D., Moerman K. M., Jaeger A. M., Genovese K., and Herr H. M. “MultiDIC: An Open-Source Toolbox for Multi-View 3D Digital Image Correlation”. In: *IEEE Access* 6 (2018), pp. 30520–30535.

[47] Kunze E., Galkin S., Böhm R., Gude M., and Kärger L. “The Impact of Draping Effects on the Stiffness and Failure Behavior of Unidirectional Non-Crimp Fabric Fiber Reinforced Composites”. In: *Materials (Basel, Switzerland)* 13(13).2959 (2020).

[48] Chaudhari R. “Characterization of high-pressure resin transfer molding process variants for manufacturing high-performance composites”. Dissertation. Karlsruher Institut für Technologie (KIT), 2014.

[49] Rosenberg P. “Entwicklung einer RTM Prozessvariante zur kavitätsdruckgeregelten Herstellung von Faserverbundstrukturbauteilen”. German. Dissertation. Karlsruher Institut für Technologie (KIT), 2018.

[50] Galkin S., Kunze E., Kärger L., Böhm R., and Gude M. “Experimental and Numerical Determination of the Local Fiber Volume Content of Unidirectional Non-Crimp Fabrics with Forming Effects”. In: *Journal of Composites Science* 3.1 (2019), p. 19.

[51] Basan R. *Untersuchung der intralaminaren Schubeigenschaften von Faserverbundwerkstoffen mit Epoxidharzmatrix unter Berücksichtigung nichtlinearer Effekte: Zugl.: Berlin, Techn. Univ., Diss., 2011*. Vol. 74. BAM-Dissertationsreihe. Berlin: Bundesanstalt für Materialforschung und -prüfung (BAM), 2011.

[52] *Fracture mechanics evaluation of RTM-CFRP materials for large-scale production of automotive structures*. 7th International Conference on Fracture of Polymers, Composites and Adhesives. Les Diablerets, Switzerland, 2014.

[53] Koerber H., Xavier J., and Camanho P. P. “High strain rate characterisation of unidirectional carbon-epoxy IM7-8552 in transverse compression and in-plane shear using digital image correlation”. In: *Mechanics of Materials* 42.11 (2010), pp. 1004–1019.

[54] Körber H. “Mechanical response of advanced composites under high strain rates”. PhD thesis. Universidade do Porto (Portugal), 2010.

[55] Schäfer B., Dörr D., and Kärger L. “Reduced-Integrated 8-Node Hexahedral Solid-Shell Element for the Macroscopic Forming Simulation of Continuous Fibre-Reinforced Polymers”. In: *Procedia Manufacturing* 47.1 (2020), pp. 134–139.

[56] *Potential and challenges of a solid-shell element for the macroscopic forming simulation of engineering textiles.* 24th International Conference on Material Forming. ESAFORM 2021 (Online, Apr. 14–16, 2021). ULiège Library, 2021.

[57] *Prediction of forming effects in UD-NCF by macroscopic forming simulation – Capabilities and limitations.* 24th International Conference on Material Forming. ESAFORM 2021 (Online, Apr. 14–16, 2021). ULiège Library, 2021.

[58] Hummelberger D. “Hybride Werkstoffsysteme: Systematische Betrachtung und Bewertung der physikalischen Wirkmechanismen”. German. Dissertation. Karlsruher Institut für Technologie (KIT), 2019.

[59] Poppe C., Dörr D., Henning F., and Kärger L. “Experimental and numerical investigation of the shear behaviour of infiltrated woven fabrics”. In: *Composites Part A: Applied Science and Manufacturing* 114 (2018), pp. 327–337.

[60] Kies J. A. *Maximum strains in the resin of fiberglass composites.* Washington, D.C. and Alexandria, VA: U.S. Naval Research Laboratory and U.S. Department of Commerce, National Technical Information Service, 1962.

[61] Huether J., Esse D., Rupp P., Seitz M., and Weidenmann K. A. “Enhanced strain and stiffness evaluation of virgin and recycled single carbon fibres by means of one-dimensional digital image correlation”. In: *Measurement Science and Technology* 30.3 (Feb. 2019), p. 035201.

[62] Ueda M., Saito W., Imahori R., Kanazawa D., and Jeong T.-K. “Longitudinal direct compression test of a single carbon fiber in a scanning electron microscope”. In: *Composites Part A: Applied Science and Manufacturing* 67 (2014), pp. 96–101.

[63] Ueda M. and Akiyama M. “Compression test of a single carbon fiber in a scanning electron microscope and its evaluation via finite element analysis”. In: *Advanced Composite Materials* 28.1 (2019), pp. 57–71.

[64] Leopold C., Liebig W. V., Wittich H., and Fiedler B. “Size effect of graphene nanoparticle modified epoxy matrix”. In: *Composites Science and Technology* 134 (2016), pp. 217–225.

[65] Hobbiebrunken T., Fiedler B., Hojo M., Ochiai S., and Schulte K. “Microscopic yielding of CF/epoxy composites and the effect on the formation of thermal residual stresses”. In: *Composites Science and Technology* 65.10 (2005), pp. 1626–1635.

[66] Littell J. D., Ruggeri C. R., Goldberg R. K., Roberts G. D., Arnold W. A., and Binienda W. K. “Measurement of Epoxy Resin Tension, Compression, and Shear Stress–Strain Curves over a Wide Range of Strain Rates Using Small Test Specimens”. In: *Journal of Aerospace Engineering* 21.3 (2008), pp. 162–173.

[67] Simonovsky M. *Ellipse Detection Using 1D Hough Transform*. `https://de.mathworks.com/matlabcentral/fileexchange/33970-ellipse-detection-using-1d-hough-transform`. Accessed: 2019-02-04. 2013.

[68] Soden P., Hinton M. J., and Kaddour A. S. “Lamina properties, lay-up configurations and loading conditions for a range of fibre-reinforced composite laminates”. In: *Composites Science and Technology* 58.7 (1998), pp. 1011–1022.

[69] Kaddour A. S. and Hinton M. J. “Input data for test cases used in benchmarking triaxial failure theories of composites”. In: *Journal of Composite Materials* 46.19-20 (2012), pp. 2295–2312.

[70] Kaddour A. S., Hinton M. J., Smith P. A., and Li S. “Mechanical properties and details of composite laminates for the test cases used in the third world-wide failure exercise”. In: *Journal of Composite Materials* 47.20-21 (2013), pp. 2427–2442.

[71] Liebig W. V., Leopold C., Hobbiebrunken T., and Fiedler B. “New test approach to determine the transverse tensile strength of CFRP with regard to the size effect”. In: *Composites Communications* 1 (2016), pp. 54–59.

[72] A. Puck and H. Schürmann. “Failure analysis of FRP laminates by means of physically based phenomenological models”. In: *Composites Science and Technology* 58.7 (1998), pp. 1045–1067.

[73] Pinho S., Darvizeh R., Robinson P., Schuecker C., and Camanho P. “Material and structural response of polymer-matrix fibre-reinforced composites”. In: *Journal of Composite Materials* 46.19-20 (2012), pp. 2313–2341.

[74] Soden P. D., Hinton M. J., and Kaddour A. S. “Biaxial test results for strength and deformation of a range of E-glass and carbon fibre reinforced composite laminates: failure exercise benchmark data”. In: *Composites Science and Technology* 62.12-13 (2002), pp. 1489–1514.

[75] Kärger L., Galkin S., Zimmerling C., Dörr D., Linden J., Oeckerath A., and Wolf K. “Forming optimisation embedded in a CAE chain to assess and enhance the structural performance of composite components”. In: *Composite Structures* 192 (2018), pp. 143–152.

[76] Mayer N., Prowe J., Havar T., Hinterhölzl R., and Drechsler K. “Structural analysis of composite components considering manufacturing effect”. In: *Composite Structures* 140 (2016), pp. 776–782.

[77] Mayer N., Van Den Broucke, Björn, Prowe J., Havar T., and Hinterhölzl R. “Finite element mapping for incompatible FE meshes of composite structures”. In: *Advances in Engineering Software* 99 (2016), pp. 81–88.

[78] Taubert R., Mandel U., and Hartmann M. “Influence of nonlinear material behavior on the effect of inter-fiber cracks in composite laminates”. In: *Journal of Composite Materials* 51.27 (2017), pp. 3819–3833.

[79] Eskandari S., Andrade Pires F. M., Camanho P. P., and Marques A. T. “Intralaminar damage in polymer composites in the presence of finite fiber rotation: Part II – Numerical analysis and validation”. In: *Composite Structures* 151 (2016), pp. 127–141.

[80] Eskandari S., Andrade Pires F. M., Camanho P. P., and Marques A. T. “Intralaminar damage in polymer composites in the presence of finite fiber rotation: Part I – Constitutive model”. In: *Composite Structures* 151 (2016), pp. 114–126.

[81] Chae H. G., Newcomb B. A., Gulgunje P. V., Liu Y., Gupta K. K., Kamath M. G., Lyons K. M., Ghoshal S., Pramanik C., Giannuzzi L., Şahin K., Chasiotis I., and Kumar S. “High strength and high modulus carbon fibers”. In: *Carbon* 93 (2015), pp. 81–87.

[82] Meng M., Le H. R., Rizvi M. J., and Grove S. M. “The effects of unequal compressive/tensile moduli of composites”. In: *Composite Structures* 126 (2015), pp. 207–215.

[83] U.S. Dept. of Defense. *Composite Materials Handbook: Polymer Matrix Composites Materials Properties*. Vol. v. 2. Department of defense handbook. Composite materials handbook. Washington, D.C.: U.S. Dept. of Defense, 2002.

[84] Halpin J. C. *Effects of Environmental Factors on Composite Materials*. Fort Belvoir: Defense Technical Information Center, 1969.

[85] Affdl J. C. H. and Kardos J. L. "The Halpin-Tsai equations: A review". In: *Polymer Engineering & Science* 16.5 (1976), pp. 344–352.

[86] Hill R. "A self-consistent mechanics of composite materials". In: *Journal of the Mechanics and Physics of Solids* 13.4 (1965), pp. 213–222.

[87] Mori T. and Tanaka K. "Average stress in matrix and average elastic energy of materials with misfitting inclusions". In: *Acta Metallurgica* 21.5 (1973), pp. 571–574.

[88] Chamis C. C. *Simplified Composite Micromechanics Equations for Strength, Fracture Toughness, Impact Resistance and Environmental Effects*. Ft. Belvoir: Defense Technical Information Center, 1984.

[89] Barbero E. J. *Introduction to Composite Materials Design, Third Edition*. 3rd ed. Composite Materials. Milton: CRC Press, 2017.

[90] Kaw A. K. *Mechanics of composite materials*. 2. ed. Vol. 29. Mechanical engineering series. Boca Raton: CRC Taylor & Francis, 2006.

[91] Rosen B. W. "Mechanics of composite strengthening". In: *Fiber composite materials*. Metals Park, Ohio: American Society for Metals, 1965.

[92] Budiansky B. "Micromechanics". In: *Computers & Structures* 16.1-4 (1983), pp. 3–12.

[93] Matthias Deuschle H. and Kröplin B.-H. "Finite element implementation of Puck's failure theory for fibre-reinforced composites under three-dimensional stress". In: *Journal of Composite Materials* 46.19-20 (2012), pp. 2485–2513.

[94] Kress G. "Examination of Hashin's failure criteria for the second worldwide failure exercise". In: *Journal of Composite Materials* 46.19-20 (2012), pp. 2539–2561.

[95] Cuntze R. "The predictive capability of failure mode concept-based strength conditions for laminates composed of unidirectional laminae under static triaxial stress states". In: *Journal of Composite Materials* 46.19-20 (2012), pp. 2563–2594.

[96] Flatscher T., Schuecker C., and Pettermann H. E. "Prediction of plastic strain accumulation in continuous fiber reinforced laminates by a constitutive ply model". In: *International Journal of Fracture* 158.2 (2009), pp. 145–156.

[97] Laux T., Gan K. W., Dulieu-Barton J. M., and Thomsen O. T. "A simple nonlinear constitutive model based on non-associative plasticity for UD composites: Development and calibration using a Modified Arcan Fixture". In: *International Journal of Solids and Structures* 162 (2019), pp. 135–147.

[98] Vyas G. M., Pinho S. T., and Robinson P. "Constitutive modelling of fibre-reinforced composites with unidirectional plies using a plasticity-based approach". In: *Composites Science and Technology* 71.8 (2011), pp. 1068–1074.

[99] Vogler M., Rolfes R., and Camanho P. P. "Modeling the inelastic deformation and fracture of polymer composites – Part I: Plasticity model". In: *Mechanics of Materials* 59 (2013), pp. 50–64.

[100] Mandel U., Taubert R., and Hinterhölzl R. "Three-dimensional nonlinear constitutive model for composites". In: *Composite Structures* 142 (2016), pp. 78–86.

[101] Thomson D. M., Erice B., Cui H., Hoffmann J., Wiegand J., and Petrinic N. "A Puck-based localisation plane theory for rate- and pressure-dependent constitutive modelling of unidirectional fibre-reinforced polymers". In: *Composite Structures* 184 (2018), pp. 299–305.

[102] Galkin S., Schirmaier F. J., and Kärger L. "Simplified phenomenological model of the nonlinear behavior of FRPs under combined stress states". In: *Journal of Composite Materials* 52.4 (2018), pp. 475–485. eprint: `https://doi.org/10.1177/0021998317709332`.

[103] Böhm R., Gude M., and Hufenbach W. "A phenomenologically based damage model for textile composites with crimped reinforcement". In: *Composites Science and Technology* 70.1 (2010), pp. 81–87.

[104] Böhm R., Gude M., and Hufenbach W. “A phenomenologically based damage model for 2D and 3D-textile composites with non-crimp reinforcement”. In: *Materials & Design* 32.5 (2011), pp. 2532–2544.

[105] Daghia F. and Ladeveze P. “Identification and validation of an enhanced mesomodel for laminated composites within the WWFE-III”. In: *Journal of Composite Materials* 47.20-21 (2013), pp. 2675–2693.

[106] Puck, A., Mannigel, M. “Physically based non-linear stress–strain relations for the inter-fibre fracture analysis of FRP laminates”. In: *Composites Science and Technology* 67.9 (2007), pp. 1955–1964.

[107] Kaddour A. S., Hinton M. J., Smith P. A., and Li S. “A comparison between the predictive capability of matrix cracking, damage and failure criteria for fibre reinforced composite laminates: Part A of the third world-wide failure exercise”. In: *Journal of Composite Materials* 47.20-21 (2013), pp. 2749–2779.

[108] Catalanotti G., Arteiro A., Hayati M., and Camanho P. P. “Determination of the mode I crack resistance curve of polymer composites using the size-effect law”. In: *Engineering Fracture Mechanics* 118 (2014), pp. 49–65.

[109] Catalanotti G. and Xavier J. “Measurement of the mode II intralaminar fracture toughness and R-curve of polymer composites using a modified Iosipescu specimen and the size effect law”. In: *Engineering Fracture Mechanics* 138 (2015), pp. 202–214.

[110] Catalanotti G., Xavier J., and Camanho P. P. “Measurement of the compressive crack resistance curve of composites using the size effect law”. In: *Composites Part A: Applied Science and Manufacturing* 56 (2014), pp. 300–307.

[111] Laffan M. J., Pinho S. T., Robinson P., Iannucci L., and McMillan A. J. “Measurement of the fracture toughness associated with the longitudinal fibre compressive failure mode of laminated composites”. In: *Composites Part A: Applied Science and Manufacturing* 43.11 (2012), pp. 1930–1938.

[112] Pinho S. T., Robinson P., and Iannucci L. “Fracture toughness of the tensile and compressive fibre failure modes in laminated composites”. In: *Composites Science and Technology* 66.13 (2006), pp. 2069–2079.

[113] Bradley W. L. and Cohen R. N. “Matrix Deformation and Fracture in Graphite-Reinforced Epoxies”. In: *Delamination and Debonding of Materials*. Ed. by Johnson W. S. 100 Barr Harbor Drive, PO Box C700, West Conshohocken, PA 19428-2959: ASTM International, 1985, pp. 389–410.

[114] Russell A. J. “Micromechanisms of interlaminar fracture and fatigue”. In: *Polymer Composites* 8.5 (1987), pp. 342–351.

[115] Compston P. and Jar P.-Y. B. “The Influence of Fibre Volume Fraction on the Mode I Interlaminar Fracture Toughness of a Glass-Fibre/Vinyl Ester Composite”. In: *Applied Composite Materials* 6.6 (1999), pp. 353–368.

[116] Hunston D. L., Moulton R. J., Johnston N. J., and Bascom W. D. “Matrix Resin Effects in Composite Delamination: Mode I Fracture Aspects”. In: *Toughened Composites*. Ed. by Johnston N. J. 100 Barr Harbor Drive, PO Box C700, West Conshohocken, PA 19428-2959: ASTM International, 1987, pp. 74-74–21.

[117] Chen J. H., Schulz E., Bohse J., and Hinrichsen G. “Effect of fibre content on the interlaminar fracture toughness of unidirectional glass-fibre/polyamide composite”. In: *Composites Part A: Applied Science and Manufacturing* 30.6 (1999), pp. 747–755.

[118] Hsiao H. M. and Daniel I. M. “Elastic properties of composites with fiber waviness”. In: *Composites Part A: Applied Science and Manufacturing* 27.10 (1996), pp. 931–941.

[119] Zhu J., Wang J., and Zu L. “Influence of out-of-plane ply waviness on elastic properties of composite laminates under uniaxial loading”. In: *Composite Structures* 132 (2015), pp. 440–450.

[120] Takeda T. “Micromechanics Model for Three-dimensional Effective Elastic Properties of Composite Laminates with Ply Wrinkles”. In: *Composite Structures* 189 (2018), pp. 419–427.

[121] Karami G. and Garnich M. “Effective moduli and failure considerations for composites with periodic fiber waviness”. In: *Composite Structures* 67.4 (2005), pp. 461–475.

[122] Karami G. and Garnich M. “Micromechanical study of thermoelastic behavior of composites with periodic fiber waviness”. In: *Composites Part B: Engineering* 36.3 (2005), pp. 241–248.

[123] Garnich M. R. and Karami G. “Finite Element Micromechanics for Stiffness and Strength of Wavy Fiber Composites”. In: *Journal of Composite Materials* 38.4 (2004), pp. 273–292.

[124] Belytschko T., Liu W. K., Moran B., and Elkhodary K. I. *Nonlinear finite elements for continua and structures*. Second edition. CourseSmart. Hoboken, New Jersey: John Wiley & Sons Inc, 2014.

[125] Willems A. “Forming Simulation of Textile Reinforced Composite Shell Structures (Vormgevingssimulatie van textielversterkte composiet schaalproducten)”. PhD thesis. Leuven: KU Leuven, 2008.

[126] Seth B. R. *Generalized strain measure with applications to physical problems*. Ft. Belvoir: Defense Technical Information Center, 1961.

[127] Hill R. “On constitutive inequalities for simple materials—I”. In: *Journal of the Mechanics and Physics of Solids* 16.4 (1968), pp. 229–242.

[128] Onaka S. “Appropriateness of the Hencky Equivalent Strain as the Quantity to Represent the Degree of Severe Plastic Deformation”. In: *Materials Transactions* 53.8 (2012), pp. 1547–1548.

[129] Ji W., Waas A. M., and Bazant Z. P. “On the Importance of Work-Conjugacy and Objective Stress Rates in Finite Deformation Incremental Finite Element Analysis”. In: *Journal of Applied Mechanics* 80.4 (2013), p. 041024.

[130] Crisfield M. A. and Borst R. d. *Non-linear finite element analysis of solids and structures*. 2nd ed. Wiley series in computational mechanics. Chichester, West Sussex, U.K: Wiley, 2012.

[131] Boubakar M. L., Boisse P., and Gelin J. C. “Numerical implementation of orthotropic plasticity for sheet-metal forming analysis”. In: *Journal of Materials Processing Technology* 65.1-3 (1997), pp. 143–152.

[132] Xiao H., Bruhns O. T., and Meyers A. “Hypo-Elasticity Model Based upon the Logarithmic Stress Rate”. In: *Journal of Elasticity* 47.1 (1997), pp. 51–68.

[133] Badel P., Vidal-Sallé E., and Boisse P. “Large deformation analysis of fibrous materials using rate constitutive equations”. In: *Computers & Structures* 86.11-12 (2008), pp. 1164–1175.

[134] Hughes T. J. R. and Winget J. "Finite rotation effects in numerical integration of rate constitutive equations arising in large-deformation analysis". In: *International Journal for Numerical Methods in Engineering* 15.12 (1980), pp. 1862–1867.

[135] Maimí P., Camanho P. P., Mayugo J. A., and Dávila C. G. "A continuum damage model for composite laminates: Part I – Constitutive model". In: *Mechanics of Materials* 39.10 (2007), pp. 897–908.

[136] Maimí P., Camanho P. P., Mayugo J. A., and Dávila C. G. "A continuum damage model for composite laminates: Part II – Computational implementation and validation". In: *Mechanics of Materials* 39.10 (2007), pp. 909–919.

[137] Pinho S. T., Iannucci L., and Robinson P. "Physically based failure models and criteria for laminated fibre-reinforced composites with emphasis on fibre kinking. Part II: FE implementation". In: *Composites Part A: Applied Science and Manufacturing* 37.5 (2006), pp. 766–777.

[138] Pinho S. T., Iannucci L., and Robinson P. "Physically-based failure models and criteria for laminated fibre-reinforced composites with emphasis on fibre kinking: Part I: Development". In: *Composites Part A: Applied Science and Manufacturing* 37.1 (2006), pp. 63–73.

[139] Puck A. and Schürmann H. "Failure analysis of FRP laminates by means of physically based phenomenological models". In: *Composites Science and Technology* 62.12-13 (2002), pp. 1633–1662.

[140] Dong L., Lekakou C., and Bader M. G. "Processing of Composites: Simulations of the Draping of Fabrics with Updated Material Behaviour Law". In: *Journal of Composite Materials* 35.2 (2001), pp. 138–163.

[141] Xue P., Peng X., and Cao J. "A non-orthogonal constitutive model for characterizing woven composites". In: *Composites Part A: Applied Science and Manufacturing* 34.2 (2003), pp. 183–193.

[142] Peng X. Q. and Cao J. "A continuum mechanics-based non-orthogonal constitutive model for woven composite fabrics". In: *Composites Part A: Applied Science and Manufacturing* 36.6 (2005), pp. 859–874.

[143] Melro A. R. "Analytical and numerical modelling of damage and fracture of advanced composites". PhD Thesis. Porto: University of Porto, 2011.

[144] Zhang J., Lin Z., Wong A., Kikuchi N., Li V. C., Yee A. F., and Nusholtz G. S. "Constitutive Modeling and Material Characterization of Polymeric Foams". In: *Journal of Engineering Materials and Technology* 119.3 (1997), pp. 284–291.

[145] *A semi-analytical model for polymers subjected to high strain rates*. 5th European LS-DYNA Conference. Birmingham, ARUP, UK, 2005.

[146] Rolfes R., Ernst G., Vogler M., and Hühne C. "Material and Failure Models for Textile Composites". In: *Mechanical Response of Composites*. Ed. by Oñate E., Camanho P. P., Dávila C. G., Pinho S. T., and Remmers J. J. C. Vol. 10. Computational Methods in Applied Sciences. Dordrecht: Springer Netherlands, 2008, pp. 27–56.

[147] Perzyna P. "Fundamental Problems in Viscoplasticity". In: *Advances in Applied Mechanics* 9 (1966), pp. 243–377.

[148] Perzyna P. "Thermodynamic Theory of Viscoplasticity". In: *Advances in Applied Mechanics* 11 (1971), pp. 313–354.

[149] Tschoegl N. W. "Failure surfaces in principal stress space". In: *Journal of Polymer Science Part C: Polymer Symposia* 32.1 (1971), pp. 239–267.

[150] Cicekli U., Voyiadjis G. Z., and Abu Al-Rub R. K. "A plasticity and anisotropic damage model for plain concrete". In: *International Journal of Plasticity* 23.10-11 (2007), pp. 1874–1900.

[151] Kachanov L. M. *Fundamentals of the Theory of Plasticity*. North-Holland series in applied mathematics and mechanics, v. 12. US.: Courier Corporation, 2014.

[152] Hill R. *The mathematical theory of plasticity*. Repr. Vol. 11. Oxford classic texts in the physical sciences. Oxford: Clarendon Press and Oxford University Press, 2009.

[153] Asp L. E., Berglund L. A., and Talreja R. "A criterion for crack initiation in glassy polymers subjected to a composite-like stress state". In: *Composites Science and Technology* 56.11 (1996), pp. 1291–1301.

[154] Asp L. E., Berglund L. A., and Gudmundson P. "Effects of a composite-like stress state on the fracture of epoxies". In: *Composites Science and Technology* 53.1 (1995), pp. 27–37.

[155] Fiedler B., Hojo M., Ochiai S., Schulte K., and Ochi M. “Finite-element modeling of initial matrix failure in CFRP under static transverse tensile load”. In: *Composites Science and Technology* 61.1 (2001), pp. 95–105.

[156] Naik N. K., Gadipatri R., Thoram N. M., Kavala V. R., and Ch. V. “Shear properties of epoxy under high strain rate loading”. In: *Polymer Engineering & Science* 50.4 (2010), pp. 780–788.

[157] Naik N. K., Shankar P. J., Kavala V. R., Ravikumar G., Pothnis J. R., and Arya H. “High strain rate mechanical behavior of epoxy under compressive loading: Experimental and modeling studies”. In: *Materials Science and Engineering: A* 528.3 (2011), pp. 846–854.

[158] Raghava R., Caddell R. M., and Yeh, Gregory S. Y. “The macroscopic yield behaviour of polymers”. In: *Journal of Materials Science* 8.2 (1973), pp. 225–232.

[159] Voce E. “The relationship between stress and strain for homogeneous deformation”. In: *Journal of the Institute of Metals* 74.74 (1948), pp. 537–562.

[160] Swift H. W. “Plastic instability under plane stress”. In: *Journal of the Mechanics and Physics of Solids* 1.1 (1952), pp. 1–18.

[161] Larour P. “Strain rate sensitivity of automotive sheet steels: influence of plastic strain, strain rate, temperature, microstructure, bake hardening and pre-strain”. Zugl.: Aachen, Techn. Hochsch., Diss., 2010. Aachen: Shaker, 2010.

[162] Souza Neto E. A. de, Peri D., and Owen D. R. J. *Computational Methods for Plasticity*. Chichester, UK: John Wiley & Sons, Ltd, 2008.

[163] Simo J. C. and Ju J. W. “Strain- and stress-based continuum damage models—I. Formulation”. In: *International Journal of Solids and Structures* 23.7 (1987), pp. 821–840.

[164] Simo J. C. and Ju J. W. “Strain- and stress-based continuum damage models—II. Computational aspects”. In: *International Journal of Solids and Structures* 23.7 (1987), pp. 841–869.

[165] Abu Al-Rub R. K. and Voyiadjis G. Z. “Gradient-enhanced Coupled Plasticity-anisotropic Damage Model for Concrete Fracture: Computational Aspects and Applications”. In: *International Journal of Damage Mechanics* 18.2 (2009), pp. 115–154.

[166] Abu Al-Rub R. K. and Kim S.-M. "Computational applications of a coupled plasticity-damage constitutive model for simulating plain concrete fracture". In: *Engineering Fracture Mechanics* 77.10 (2010), pp. 1577–1603.

[167] Kim S.-M. and Abu Al-Rub R. K. "Meso-scale computational modeling of the plastic-damage response of cementitious composites". In: *Cement and Concrete Research* 41.3 (2011), pp. 339–358.

[168] Voyiadjis G. Z., Taqieddin Z. N., and Kattan P. I. "Anisotropic damage–plasticity model for concrete". In: *International Journal of Plasticity* 24.10 (2008), pp. 1946–1965.

[169] Duvaut G. and Lions J. L. *Inequalities in Mechanics and Physics*. Vol. 219. Grundlehren der mathematischen Wissenschaften, A Series of Comprehensive Studies in Mathematics. Berlin and Heidelberg: Springer, 1976.

[170] Wilhelmsson D., Gutkin R., Edgren F., and Asp L. E. "An experimental study of fibre waviness and its effects on compressive properties of unidirectional NCF composites". In: *Composites Part A: Applied Science and Manufacturing* 107 (2018), pp. 665–674.

[171] Shin E. S. and Pae K. D. "Effects of Hydrostatic Pressure on In-Plane Shear Properties of Graphite/Epoxy Composites". In: *Journal of Composite Materials* 26.6 (1992), pp. 828–868.

[172] Shin E. S. and Pae K. D. "Effects of Hydrostatic Pressure on the Torsional Shear Behavior of Graphite/Epoxy Composites". In: *Journal of Composite Materials* 26.4 (1992), pp. 462–485.

[173] Pae K. D. and Rhee K. Y. "Effects of hydrostatic pressure on the compressive behavior of thick laminated 45 ° and 90 ° unidirectional graphite-fiber/epoxy-matrix composites". In: *Composites Science and Technology* 53.3 (1995), pp. 281–287.

[174] Hine P. J., Duckett R. A., Kaddour A. S., Hinton M. J., and Wells G. M. "The effect of hydrostatic pressure on the mechanical properties of glass fibre/epoxy unidirectional composites". In: *Composites Part A: Applied Science and Manufacturing* 36.2 (2005), pp. 279–289.

[175] Mohr O. “Welche Umstände bedingen die Elastizitätsgrenze und den Bruch eines Materials? (Which circumstances are causing yield limit and fracture of a material?)” In: *Zeitschrift des Vereins Deutscher Ingenieure* 44,45.44,45 (1900), 1524–1530 (44), 1572–1577(45).

[176] Hashin Z. “Failure Criteria for Unidirectional Fiber Composites”. In: *Journal of Applied Mechanics* 47.2 (1980), p. 329.

[177] Cuntze R. G. and Freund A. “The predictive capability of failure mode concept-based strength criteria for multidirectional laminates”. In: *Composites Science and Technology* 64.3-4 (2004), pp. 343–377.

[178] Soden P., Hinton M. J., and Kaddour A. S. “A comparison of the predictive capabilities of current failure theories for composite laminates”. In: *Composites Science and Technology* 58.7 (1998), pp. 1225–1254.

[179] Kaddour A. S. and Hinton M. J. “Benchmarking of triaxial failure criteria for composite laminates: Comparison between models of ‘Part (A)’ of ‘WWFE-II’”. In: *Journal of Composite Materials* 46.19-20 (2012), pp. 2595–2634.

[180] Kaddour A. S. and Hinton M. J. “Maturity of 3D failure criteria for fibre-reinforced composites: Comparison between theories and experiments: Part B of WWFE-II”. In: *Journal of Composite Materials* 47.6-7 (2013), pp. 925–966.

[181] Wiegand J., Petrinic N., and Elliott B. “An algorithm for determination of the fracture angle for the three-dimensional Puck matrix failure criterion for UD composites”. In: *Composites Science and Technology* 68.12 (2008), pp. 2511–2517.

[182] Schirmaier F. J., Weiland J., Kärger L., and Henning F. “A new efficient and reliable algorithm to determine the fracture angle for Puck’s 3D matrix failure criterion for UD composites”. In: *Composites Science and Technology* 100 (2014), pp. 19–25.

[183] VDI-Gesellschaft Materials Engineering. *Development of Fibre-Reinforced Plastics components - Analysis*. Berlin, 2014.

[184] Costa S., Bru T., Olsson R., and Portugal A. “Improvement and validation of a physically based model for the shear and transverse crushing of orthotropic composites”. In: *Journal of Composite Materials* 53.12 (2019), pp. 1681–1696.

[185] Schuecker C. and Pettermann H. E. “A continuum damage model for fiber reinforced laminates based on ply failure mechanisms”. In: *Composite Structures* 76.1-2 (2006), pp. 162–173.

[186] Zhou Y., Yazdani Nezhad H., Hou C., Wan X., McCarthy C., and McCarthy M. “A three dimensional implicit finite element damage model and its application to single-lap multi-bolt composite joints with variable clearance”. In: *Composite Structures* 131 (2015), pp. 1060–1072.

[187] Reinoso J., Catalanotti G., Blázquez A., Areias P., Camanho P., and París F. “A consistent anisotropic damage model for laminated fiber-reinforced composites using the 3D-version of the Puck failure criterion”. In: *International Journal of Solids and Structures* 126-127 (2017), pp. 37–53.

[188] Naake D. R. “Simulation of damage mechanisms in weave reinforced materials based on multiscale modeling”. Dissertation. Karlsruher Institut für Technologie (KIT), 2019.

[189] Deuschle H. M. “3D failure analysis of UD fibre reinforced composites”. Zugl.: Stuttgart, Univ., Diss., 2010. Stuttgart: Inst. für Statik und Dynamik der Luft- und Raumfahrtkonstruktionen, 2010.

[190] Lapczyk I. and Hurtado J. A. “Progressive damage modeling in fiber-reinforced materials”. In: *Composites Part A: Applied Science and Manufacturing* 38.11 (2007), pp. 2333–2341.

[191] Dvorak G. J., Laws N., and Hejazi M. “Analysis of Progressive Matrix Cracking in Composite Laminates I. Thermoelastic Properties of a Ply with Cracks”. In: *Journal of Composite Materials* 19.3 (1985), pp. 216–234.

[192] Laws N., Dvorak G. J., and Hejazi M. “Stiffness changes in unidirectional composites caused by crack systems”. In: *Mechanics of Materials* 2.2 (1983), pp. 123–137.

[193] Tan S. C. and Nuismer R. J. “A Theory for Progressive Matrix Cracking in Composite Laminates”. In: *Journal of Composite Materials* 23.10 (1989), pp. 1029–1047.

[194] Salavatian M. and Smith L. V. “An investigation of matrix damage in composite laminates using continuum damage mechanics”. In: *Composite Structures* 131 (2015), pp. 565–573.

[195] Salavatian M. and Smith L. V. “The effect of transverse damage on the shear response of fiber reinforced laminates”. In: *Composites Science and Technology* 95 (2014), pp. 44–49.

[196] Lager J. R. and June R. R. “Compressive Strength of Boron-Epoxy Composites”. In: *Journal of Composite Materials* 3.1 (1969), pp. 48–56.

[197] Argon A. S. “Fracture of Composites”. In: *Treatise on Materials Science & Technology*. Vol. 1. Cambridge, Massachusetts: Massachusetts Institute of Technology, 1972, pp. 79–114.

[198] Fleck N. A. and Budiansky B. “Compressive Failure of Fibre Composites Due to Microbuckling”. In: *Inelastic Deformation of Composite Materials*. Ed. by Dvorak G. J. Vol. 18. New York, NY: Springer New York, 1991, pp. 235–273.

[199] Bogetti T. A., Gillespie J. W., and Lamontia M. A. “Influence of Ply Waviness on the Stiffness and Strength Reduction on Composite Laminates”. In: *Journal of Thermoplastic Composite Materials* 5.4 (1992), pp. 344–369.

[200] Eskandari S., Andrade Pires F. M., Camanho P. P., and Marques A. T. “Damage analysis of out of plane undulated fiber composites”. In: *Composite Structures* 152 (2016), pp. 464–476.

[201] Reddy J. N. *Mechanics of laminated composite plates and shells: Theory and analysis*. 2nd ed. Boca Raton: CRC Press, 2004.

[202] Mallach A., Härtel F., Heieck F., Fuhr J.-P., Middendorf P., and Gude M. “Experimental comparison of a macroscopic draping simulation for dry non-crimp fabric preforming on a complex geometry by means of optical measurement”. In: *Journal of Composite Materials* 51.16 (2017), pp. 2363–2375.

[203] Christ M., Miene A., and Mörschel U. “Measurement and Analysis of Drapeability Effects of Warp-Knit NCF with a Standardised, Automated Testing Device”. In: *Applied Composite Materials* 24.4 (2017), pp. 803–820.

[204] Stender S., Magura N., Fischer K., and Emonts M. “Funktionsorientierte Fertigung von FVK-Bauteilen”. In: *Lightweight Design* 12.1 (2019), pp. 18–25.

[205] Bardl G., Nocke A., Hübner M., Gereke T., Pooch M., Schulze M., Heuer H., Schiller M., Kupke R., Klein M., and Cherif C. "Analysis of the 3D draping behavior of carbon fiber non-crimp fabrics with eddy current technique". In: *Composites Part B: Engineering* 132 (2018), pp. 49–60.

[206] Kunze E., Schwarz B., Weber T., Müller M., Böhm R., and Gude M. "Forming Analysis of Internal Plies of Multi-Layer Unidirectional Textile Preforms using Projectional Radiography". In: *Procedia Manufacturing* 47 (2020), pp. 17–23.

[207] Dörr D., Schirmaier F. J., Henning F., and Kärger L. "A viscoelastic approach for modeling bending behavior in finite element forming simulation of continuously fiber reinforced composites". In: *Composites Part A: Applied Science and Manufacturing* 94 (2017), pp. 113–123.

[208] Dörr D., Henning F., and Kärger L. "Nonlinear hyperviscoelastic modelling of intra-ply deformation behaviour in finite element forming simulation of continuously fibre-reinforced thermoplastics". In: *Composites Part A: Applied Science and Manufacturing* 109 (2018), pp. 585–596.

[209] Yu X., Cartwright B., McGuckin D., Ye L., and Mai Y.-W. "Intra-ply shear locking in finite element analyses of woven fabric forming processes". In: *Composites Part A: Applied Science and Manufacturing* 37.5 (2006), pp. 790–803.

[210] Boisse P., ZOUARI B., and GASSER A. "A mesoscopic approach for the simulation of woven fibre composite forming". In: *Composites Science and Technology* 65.3-4 (2005), pp. 429–436.

[211] Lomov S. V. and Verpoest I. "Model of shear of woven fabric and parametric description of shear resistance of glass woven reinforcements". In: *Composites Science and Technology* 66.7-8 (2006), pp. 919–933.

[212] Swery E. E., Hans T., Bultez M., Wijaya W., Kelly P., Hinterhölzl R., and Bickerton S. "Complete simulation process chain for the manufacturing of braided composite parts". In: *Composites Part A: Applied Science and Manufacturing* 102 (2017), pp. 378–390.

[213] Afazov S. M., Becker A. A., and Hyde T. H. "Development of a Finite Element Data Exchange System for chain simulation of manufacturing processes". In: *Advances in Engineering Software* 47.1 (2012), pp. 104–113.

[214] Spiess H., Oeckerath A., and Landvogt B. *Mapping Library Manual Version 2010.1*. Sankt Augustin: Fraunhofer SCAI, 2012.

[215] Ernst G., Vogler M., Hühne C., and Rolfes R. "Multiscale progressive failure analysis of textile composites". In: *Composites Science and Technology* 70.1 (2010), pp. 61–72.

[216] Sarac O. "Berücksichtigung des Faservolumengehalts als Feldgröße in der Struktursimulation von Faserverbund-bauteilen in ABAQUS". Bachelor Thesis. Institut für Fahrzeugsystemtechnik, Teilinstitut Leichtbautechnologie, Karlsruhe Institute of Technology, 2013.

[217] Fengler B., Kärger L., Henning F., and Hrymak A. "Multi-Objective Patch Optimization with Integrated Kinematic Draping Simulation for Continuous–Discontinuous Fiber-Reinforced Composite Structures". In: *Journal of Composites Science* 2.2 (2018).

[218] Schroeder W., Martin K., and Lorensen B. *The visualization toolkit: An object-oriented approach to 3D graphics ; [visualize data in 3D - medical, engineering or scientific ; build your own applications with C++, Tcl, Java or Python ; includes source code for VTK (supports Unix, Windows and Mac)*. 4. ed. Clifton Park, NY: Kitware Inc, 2006.

[219] Melro A. R., Camanho P. P., Andrade Pires F. M., and Pinho S. T. "Micromechanical analysis of polymer composites reinforced by unidirectional fibres: Part II – Micromechanical analyses". In: *International Journal of Solids and Structures* 50.11-12 (2013), pp. 1906–1915.

[220] Arefi A., van der Meer F. P., Forouzan M. R., Silani M., and Salimi M. "Micromechanical evaluation of failure models for unidirectional fiber-reinforced composites". In: *Journal of Composite Materials* 54.6 (2020), pp. 791–800.

[221] Bai X., Bessa M. A., Melro A. R., Camanho P. P., Guo L., and Liu W. K. "High-fidelity micro-scale modeling of the thermo-visco-plastic behavior of carbon fiber polymer matrix composites". In: *Composite Structures* 134 (2015), pp. 132–141.

[222] Melro A., Camanho P., and Pinho S. "Generation of random distribution of fibres in long-fibre reinforced composites". In: *Composites Science and Technology* 68.9 (2008), pp. 2092–2102.

[223] Barbero E. J. *Finite element analysis of composite materials using Abaqus*. Composite materials: analysis and design. Boca Raton Fla. u.a.: CRC Press, 2013.

[224] Melro A. R., Camanho P. P., and Pinho S. T. “Influence of geometrical parameters on the elastic response of unidirectional composite materials”. In: *Composite Structures* 94.11 (2012), pp. 3223–3231.

[225] Trias Mansilla. “Analysis and Simulation of Transverse Random Fracture of Long Fibre Reinforced Composites”. Dissertation. Girona: Universitat de Girona. Departament d’Enginyeria mecànica i de la construcció industrial, 2005.

[226] Danzi F., Fanteria D., Panettieri E., and Mancino M. C. “A numerical micro-mechanical study on damage induced by the curing process in carbon/epoxy unidirectional material”. In: *Composite Structures* 210 (2019), pp. 755–766.

[227] Puck A., Kopp J., and Knops M. “Guidelines for the determination of the parameters in Puck’s action plane strength criterion”. In: *Composites Science and Technology* 62.3 (2002), pp. 371–378.

[228] *Failure and Damage Analysis of Undulated Fiber Composites depending on the Fiber Volume Content*. 6th European Conference on Computational Mechanics (ECCM 2018). Glasgow, Great Britain, 2018.

[229] Salavatian M. and Smith L. “An improved analytical model for shear modulus of fiber reinforced laminates with damage”. In: *Composites Science and Technology* 105 (2014), pp. 9–14.

[230] Salavatian M. and Smith L. V. “A novel experimental technique for biaxial testing of a composite laminate with matrix damage”. In: *Journal of Composite Materials* 50.20 (2016), pp. 2783–2792.

[231] Kunze E., Böhm R., Geller S., and Gude M. “Experimental analysis of process induced draping effects in textile preforms”. In: *AIP Conference Proceedings*. Vol. 2113. 2019, p. 020012.

[232] Witmer T. R. and Cardano G., eds. *Ars magna, or, The rules of algebra*. New York and London: Dover and Constable, 1993.

Publications

Journal Papers

Kunze E., Galkin S., Böhm R., Gude M., and Kärger L. “The Impact of Draping Effects on the Stiffness and Failure Behavior of Unidirectional Non-Crimp Fabric Fiber Reinforced Composites”. In: *Materials (Basel, Switzerland)* 13.13 (2020).

Galkin S., Kunze E., Kärger L., Böhm R., and Gude M. “Experimental and Numerical Determination of the Local Fiber Volume Content of Unidirectional Non-Crimp Fabrics with Forming Effects”. In: *Journal of Composites Science* 3.1 (2019), p. 19.

Galkin S., Schirmaier F. J., and Kärger L. “Simplified phenomenological model of the nonlinear behavior of FRPs under combined stress states”. In: *Journal of Composite Materials* 52 (2018), pp. 475–485.

Co-authored Journal Papers

Kärger L., Galkin S., Zimmerling C., Dörr D., Linden J., Oeckerath A., and Wolf K. “Forming optimisation embedded in a CAE chain to assess and enhance the structural performance of composite components”. In: *Composite Structures* 192 (2018), pp. 143–152.

Botzkowski T., Galkin S., Wagner S., Sikora S. P., and Kärger L. “Experimental and numerical analysis of bolt-loaded open-hole laminates reinforced by winded carbon rovings”. In: *Composite Structures* 141 (2016), pp. 194–202.

Kärger L., Bernath A., Fritz F., Galkin S., Magagnato D., Oeckerath A., Schön A., and Henning F. "Development and validation of a CAE chain for unidirectional fibre reinforced composite components". In: *Composite Structures* 132 (2015), pp. 350–358.

Conference Contributions

Galkin S. and Kärger L. "Strength of UD-laminates depending on the fiber volume content: experimental tests and modelling". In: *18th European Conference on Composite Materials (ECCM18)*. Athens, 2018.

Galkin S., Fürst T., Henning F., and Kärger L. "Testing, modelling and evaluation of different joint designs for CFRP sub-preforms regarding their loading capacity under three point bending". In: *ICCS19 – 19th International Conference on Composite Structures*. Porto, 2016.

Galkin S., Brylka B., Ruck J., Häfele P., Gall M., Mohrmann H., and Fey P. "Experimentelle und virtuelle Strukturbewertung von FVW unter statischer Belastung - vom Coupon zum finalen Bauteil anhand der CAE-Kette". In: *Abschlussworkshop Technologie-Cluster Composites Baden-Württemberg TC*^{2}. Pfinztal, Feb. 2015.

Galkin S., Schirmaier F., and Kärger L. "Application of a virtual shear stress model and comparison with WWFE-III prediction to describe the non-linear behavior of composite materials". In: *20th International Conference on Composite Materials (ICCM)*. Kopenhagen, 2015.

Galkin S., Kärger L., Häfele P., Gall M., Voß H., and Henning F. "Parametrisierung und Evaluierung von Schädigungsmodellen für Faserverbundkunststoffe auf Basis umfangreicher Charakterisierungs- und Validierungsversuche". In: *NAFEMS 2014 Berechnung und Simulation – Anwendungen, Entwicklungen, Trends*. Bamberg, May 2014, pp. 133–137.

Co-authored Conference Contributions

Kärger L., Galkin S., Kunze E., Gude M., and Schäfer B. “Prediction of forming effects in UD-NCF by macroscopic forming simulation – Capabilities and limitations”. In: *ESAFORM 2021* (2021).

Kärger L., Galkin S., Dörr D., and Poppe C. “Capabilities of Macroscopic Forming Simulation for Large-Scale Forming Processes of Dry and Impregnated Textiles”. In: *Procedia Manufacturing* 47 (2020), pp. 140–147.

Krauß C., Dörr D., Seuffert J., Bernath A., Galkin S., and Kärger L. “Interface Challenges and Solution Approaches with Regard to the New VMAP Standard in a Continuous CAE-Chain for the Holistic Manufacturing Simulation of High Performance Composites”. In: *NAFEMS World Congress 2019*. Quebec City, Canada, 2019.

Kunze E., Galkin S., Gröger B., Böhm R., Kärger L., and Gude M. “Experimental Description of Draping Effects and their Influence on the Structural Behavior of Fiber Reinforced Composites”. In: *22nd International Conference on Composites Materials (ICCM22)*. Melbourne, 2019.

Kärger L., Dörr D., Poppe C., Seuffert J., Bernath A., Galkin S., Zimmerling C., and Henning F. “Continuous Process Simulation for Continuous Fiber Reinforced Composites”. In: *International VDI Conference*. Amsterdam, 2018.

Kärger L. and Galkin S. “Failure and Damage Analysis of Undulated Fiber Composites depending on the Fiber Volume Content”. In: *6th European Conference on Computational Mechanics (ECCM 2018)*. Glasgow, Great Britain, 2018.

Krauß C., Galkin S., and Kärger L. “Generation of Reliable Input Data for a Damage Model Taking Use of a Closed CAE-Chain Containing Material Interfaces”. In: *13th World Congress on Computational Mechanics*. New York, 2018.

Kärger L., Galkin S., Zimmerling C., Dörr D., Schirmaier F., Oeckerath A., Wolf K., and Linden J. “Continuous CAE chain for composite design, established on an HPC system and accessible via web-based user-interfaces”. In: *NAFEMS World Congress*. Stockholm, 2017.

Sikora S. P., Wagner S., Galkin S., and Kopp G. “Innovative load application into oscillation-loaded fibre-reinforced plastic structures”. In: *FiMPART*. Bordeaux, 2017.

Wagner S., Sikora S. P., Hummel J., and Galkin S. “Testing of novel joining concepts for improved load application into oscillation-loaded fibre-reinforced plastic structures”. In: *SAMPE Europe*. Stuttgart, 2017.

Kärger L., Dörr D., Fengler B., Galkin S., Naake D., Poppe C., and Zimmerling C. “Tailored Composite Materials for Lightweight Vehicles”. In: *BRAGFOST*. Potsdam, 2017.

Kärger L., Dörr D., Galkin S., Schirmaier F., and Henning F. “Forming simulation for process design of curved CFRP structures”. In: *19. Airbus Workshop: Tooling for CFRP Production and Assembly*. Augsburg, 2016.

Kärger L., Bernath A., Dörr D., Galkin S., Magagnato D., Schirmaier F., and Henning F. “Simulation methods for process design of structural composite components”. In: *asc(s simpulseday greenCAE*. Weissach, 2016.

Kärger L., Botzkowski T., Galkin S., Wagner S., and Sikora S. P. “Stress analysis and design suggestions for multi-loop carbon roving rosettes to reinforce bolt-loaded open-hole laminates”. In: *ECCM17 - 17th European Conference on Composite Materials*. Munich, 2016.

Henning F., Bernath A., Galkin S., Kärger L., Magagnato D., Schirmaier F., and Thoma B. “Holistic Development of High-Pressure RTM Composite Structures”. In: *31st International Conference of the Polymer Processing Society*. Jeju Island, Korea, June 2015.

Kärger L., Fritz F., Magagnato D., Galkin S., Schön A., Oeckerath A., Wolf K., and Henning F. “Virtuelle Prozesskette für Bauteile aus Hochleistungsfaserverbunden”. In: *CCeV-Veranstaltung der AGs „Engineering, Klebtechnik, ZFP“*. Augsburg, Nov. 2014.

Kärger L., Fritz F., Magagnato D., Galkin S., Schön A., Wolf K., and Henning F. “Entwicklungsstand und Anwendungsbeispiele einer virtuellen Prozesskette für RTM-Bauteile”. In: *NAFEMS Seminar Simulation von Composites – Eine geschlossene Prozesskette*. Leipzig, Oct. 2014.

Gall M., Hohe J., Kärger L., and Galkin S. “Fracture mechanics evaluation of RTM-CFRP materials for large-scale production of automotive structures”. In: *7th International Conference on Fracture of Polymers, Composites and Adhesives*. Les Diablerets, Switzerland, 2014.